Contents

Chapter 1

Introduction

1.1 The wind-driven ocean circulation

The ocean circulation is forced at the sea surface, partly by the frictional stress exerted by the wind and partly by heat- and freshwater fluxes. The wind stress is the main driving force for the surface currents, but its direct influence on the circulation is limited to the upper thousand meters of the ocean. In contrast, the heat- and freshwater fluxes change the density and thus the buoyancy of the water column, which may result in mixing and deep convection. This buoyancy-driven circulation, known as the thermohaline circulation, sets the deeper waters in motion (e.g., Stommel, 1957; Broecker, 1991). Due to the large heat capacity of the oceans, the ocean circulation and variations therein have a significant impact on climate (Peixoto and Oort, 1992). Thus, knowledge of the (variability of the) ocean circulation and its sensitivity to for example changing forcing conditions is crucial for climate studies.

Figure 1.1 schematically shows the primarily wind-driven surface circulation. In all oceans, the circulation in both the northern and southern hemisphere is characterized by basin-wide cell-like patterns known as gyres. These gyres are strongest on the western side of the basin, where narrow boundary currents are found. Eastward flowing mid-ocean jets emerge where two such boundary currents meet. Examples of such western boundary currents and their mid-ocean extensions are the Gulf Stream in the North Atlantic Ocean, the Kuroshio in the North Pacific Ocean and the Agulhas Current in the Indian Ocean (the latter is not explicitly named in Fig. 1.1). Typical velocities in these narrow currents are on the order of 1 m/s, whereas the velocities at the heart of the gyres are much slower (~ 0.01 m/s). Although the main features of the surface circulation are fairly well known, many details are still unexplored. This is partly due to the limited availability of direct observations of ocean currents. Over large parts of the ocean, the horizontal and vertical motions have been deduced from the distribution of temperature and salinity, based on dynamical and thermodynamical considerations (Niiler, 1987). Direct measurements of the circulation away from the coasts and outside main shipping routes are still hardly performed on a regular basis. As a consequence of this sparseness of the oceanographic data set, in particular

the characteristics of the variability of the flow are poorly known. The recent introduction of satellites that measure for example the sea surface temperature and sea surface height over the whole globe have partly resolved this data sampling problem. Currently, a valuable time series of the variability of the surface circulation is thus being composed. However, subsurface observations still remain scarce and difficult to collect.

The physical laws that dictate the ocean circulation are well known. The fluid motions are governed by the Navier-Stokes equations, which basically represent the laws of conservation of mass and momentum (e.g., Acheson, 1990). When applied to the ocean circulation, the Coriolis force (the deflective force that results from the earth's rotation) has to be taken into account. In addition, equations that describes the transport and mixing of heat and salt can be derived. In this way, a set of coupled non-linear differential equations is obtained that describe the evolution of the flow. However, the resulting mathematical problem is complex and can only be solved analytically for specific, idealized cases. Oceanographers have therefore put much effort in simulating the circulation numerically. Although the thermohaline and the wind-driven component of the circulation interact, they are often treated separately in modelling studies. This is justified by the notion that the characteristic time scales for variability are much longer for the thermohaline component than for the wind-driven component of the flow (on the order of centuries versus months to years). Hence, the purely wind-driven circulation can be studied by *prescribing* a specific density distribution (the stratification), which is thought to be established by the thermohaline circulation. In this way, the basic processes that determine the characteristics of the wind-driven circulation can be studied. Naturally, for realistic long-term simulations of the observed ocean circulation both wind- and buoyancy forcing have to be considered.

1.1.1 Large-scale ocean gyres

To understand what causes the large-scale circulation patterns shown in Figure 1.1, oceanographers started by studying stationary wind-driven flows. Idealized circumstances were investigated, so that the mathematical problem could be handled analytically. Ekman (1905) showed how the wind stress at the sea surface is a source of momentum for the ocean, and directly drives a flow in a thin boundary layer of approximately 10 to 100 meters thick. Non-uniform winds lead to convergence or divergence in this thin Ekman layer, which induces weak vertical motions at the base of this boundary layer (e.g., Apel, 1988). In a homogeneous ocean, this so-called Ekman pumping would drive a flow throughout the whole depth of the water column. In reality, the vertical density gradient limits the wind-driven motions to the upper thousand meters.

An explanation for the existence of large-scale gyres was first given by Sverdrup (1947), who demonstrated that the spatial pattern of the surface wind stress controls the mass transport of the circulation. He simplified the wind-driven circulation problem by assuming that the ocean is hydrostatic, i.e., that the vertical pressure gradient is determined by the density distribution of the water column. In addition,

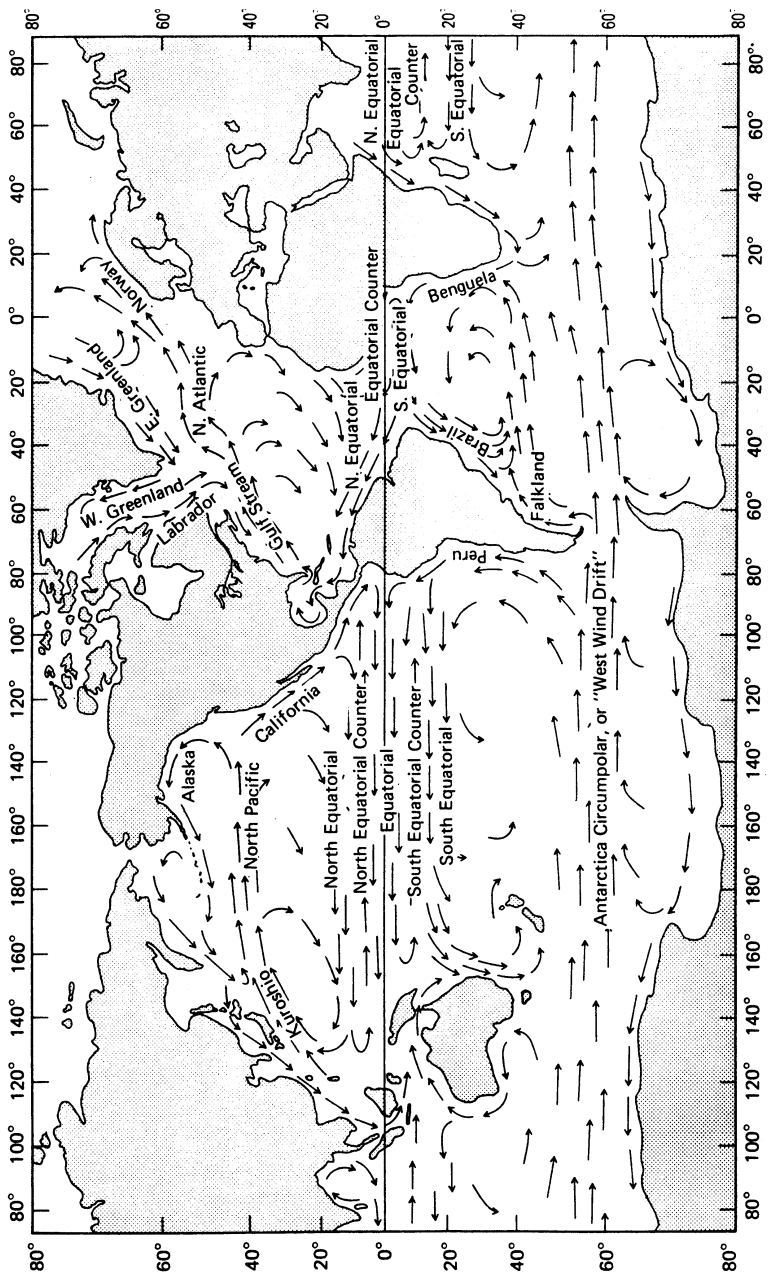

Figure 1.1: *Large-scale circulation patterns at the ocean surface (adapted from Stowe, 1979).*

he neglected advective and frictional effects, so that the horizontal momentum equations reduce to the geostrophic balance, which is a balance between the horizontal pressure gradient and the Coriolis force. From this, Sverdrup (1947) derived that the vertically integrated *meridional* mass transport is proportional to the curl of the surface wind stress. When a negative (positive) torque is exercised by the surface wind stress, the resulting Sverdrup transport is southward (northward). At latitudes where the curl of the wind stress vanishes, the resulting wind-driven flow is purely zonal, and mid-ocean jets appear that form the northern and southern boundaries of the gyres (see Fig. 1.1). Furthermore, Sverdrup (1947) demonstrated that the vertically integrated *zonal* mass transport depends linearly on longitude. In a closed basin, it is required that this zonal mass transport vanishes at coastal boundaries in the east and west. Obviously, the Sverdrup solution can not satisfy this condition and is thus only applicable to the open ocean.

By including frictional effects, Stommel (1948) derived a solution for the wind-driven flow in a closed, rectangular basin. He calculated the stationary circulation for a homogeneous ocean driven by a negative wind stress torque at the surface and decelerated by bottom friction. Over a large part of the basin, the meridional mass transport is indeed southward, as predicted by Sverdrup (1947). The Sverdrup flow is compensated in a narrow northward boundary current in the western part of the basin. This westward intensification of the gyre flow appears to be a consequence of the variation of the Coriolis force with latitude. Munk (1950) studied a similar homogeneous circulation problem in a confined basin. He deduced a solution for the wind-driven circulation slowed down by lateral friction rather than bottom friction. This closure also gives rise to a western boundary current, now flanked by a weak countercurrent. In both cases, the width of the western boundary current is determined by the relative strength of the friction. This linear Munk model was extended by Munk *et al.* (1950), who introduced weak non-linear effects. These non-linearities were found to induce a north-south asymmetry, as the centers of (anti-)clockwise rotating wind-driven gyres shift to the north (south).

To solve the full non-linear equations, numerical models are required. The earliest numerical models were direct extensions of the analytical studies discussed above, and were applied to study homogeneous wind-driven flows in idealized configurations (see Holland, 1977, for an overview). Starting from a state of rest, the response of the ocean to a surface wind stress is determined by a numerical integration of the governing differential equations. Bryan (1963) extended the study of Munk *et al.* (1950), and investigated the characteristics of single-gyre flows for changing physical parameters. He explored the sensitivity of the circulation to both the strength of the lateral friction and to the relative size of the non-linear terms in the momentum equations. A similar study was performed by Veronis (1966), but for single-gyre flows braked by bottom friction rather than lateral friction. That is, he solved a non-linear version of the Stommel model.

1.1.2 The deep sea circulation

The wind-driven gyres only extend down to approximately thousand meters. At larger depths, the ocean circulation is mainly buoyancy driven, and is generally much weaker than the wind-driven surface circulation (typical velocities are on the order of cm/s). As a consequence, typical time scales for the internal variability of the thermohaline circulation are relatively long. However, in the North Atlantic Ocean, a swift subsurface current known as the Deep Western Boundary Current exists, with characteristic velocities up to 20 cm/s. This Deep Western Boundary Current originates from the northern parts of the North Atlantic, and flows southward along the American continent. Near Cape Hatteras, at $35°N$, it crosses underneath the Gulf Stream, which separates from the American coast there and turns (north-)eastward. Both observations and modelling studies indicate that the two currents interact strongly in this cross-over region (Pickart and Smethie Jr., 1993; Thompson and Schmitz Jr., 1989). More specifically, the characteristic time- and spatial scales of the variability of the Gulf Stream seem to be affected by the presence of this Deep Western Boundary Current (Spall, 1996b; Tansley and Marshall, 2000).

The existence of this deep, thermohaline driven current was derived theoretically by Stommel in 1958. At that time, very little was known about the subsurface flows. It was known, though, that the deep ocean waters are very cold, also in tropical regions. The dividing-line between the warm surface waters and the colder subsurface waters is a sharp vertical temperature gradient known as the ocean thermocline, which is clearly present over large areas of the ocean (Worthington, 1981). The presence of a thermocline indicates that the cold deep waters must be slowly rising. Otherwise, the downward diffusion of heat would result in a much smoother vertical temperature gradient. Stommel (1958) argued that, to compensate for this upwelling, at some locations the thermocline had 'spring a leak' and allow for downward motions. He presumed these source regions for deep water existed in polar areas, where the atmosphere cools the surface waters and thus reduces the vertical density gradient of the water column. This would also account for the low temperature of the deep waters. Indeed, the oxygen content of the subsurface waters in the northern parts of the Atlantic Ocean and close to the Antarctic continent appeared to be very high, which indicates that they have recently been in contact with the atmosphere. These areas are the source regions for the deep waters of the oceans. Stommel (1958) considered a simple two-layer system of the flow below and above the thermocline, in which he forced a circulation by prescribing two equal sources of deep water in the North and South Atlantic, and homogeneous upwelling elsewhere. In the North Atlantic, the resulting deep meridional circulation appeared to be directed poleward, i.e., *towards* the source of deep water. Stommel (1958) concluded that a relatively fast western boundary current is needed to close the circulation, which flows southward along the American continent. A few years after the publication of the theory, this Deep Western Boundary Current was actually measured for the first time (Swallow and Worthington, 1961), using acoustically tracked subsurface floats. Since then, this subsurface current has been the subject of many observational campaigns (e.g., Richardson, 1977; Bower and Hunt, 2000a,b).

1.2 Variability of the wind-driven circulation

In the analytical studies performed by Sverdrup (1947), Stommel (1948) and Munk (1950), only stationary flows were considered. In reality, the wind-driven ocean currents are highly variable. In fact, the energy contained in the varying part of the circulation is larger than that of the mean circulation (Robinson, 1983). Fluctuations in the surface circulation, referred to by the generic term 'eddies', have typical time scales of weeks to years and spatial scales of a few hundred kilometers. Eddies directly affect the large-scale circulation, through interactions with the mean flow and through the averaged effects of eddy-eddy interactions. In addition, the eddies are important for the global heat transport, for mixing and for the dissipation of energy (Gill, 1983; Haidvogel *et al.*, 1983). Associated with ocean currents are gradients in the sea surface height. For example, the sea level changes by approximately 60 *cm* across the Gulf Stream. Variations in the circulation will thus be reflected in observations of the sea surface height, which can be measured by satellite altimetry. From Figure 1.2, a picture of the variability of such observations of the sea surface height, it is clear that the largest variations in the surface circulation (the darkest areas) coincide with the mean positions of mid-ocean jets like the Gulf Stream, the Kuroshio and the Agulhas Current. So, when studying the variability of the wind-driven ocean circulation, one naturally focuses on these mid-ocean jet systems.

In general, three different physical mechanisms can be distinguished that all give rise to variability of the ocean circulation. A first possibility is that the fluctuations are caused by feedbacks between the atmospheric and the ocean circulation. A well-known example of such coupled ocean-atmosphere variability is the El Niño/Southern Oscillation phenomenon in the equatorial Pacific Ocean (Philander, 1989). Second, variability in the ocean circulation may arise as a result of external processes. Transient weather regimes, for example, are responsible for variations in the atmospheric forcing on time scales of a few days. The ocean acts as an integrator of these high-frequency excitations (Hasselmann, 1976), and displays variability on longer time scales (typically on the order of weeks to months) in response. Third, internal processes in the ocean may cause variability of the ocean circulation. Whereas in nature all three processes act together to produce the observed variability, the latter is the only possible mechanism in an ocean model driven by a constant wind forcing.

Internal variability of the wind-driven ocean circulation is a consequence of hydrodynamic instabilities. Both in reality and in numerical analyses, small perturbations are always present on the flow. The flow is stable when these perturbations eventually all die out, and unstable when they are able to extract energy from the large-scale circulation and grow with time. The time and spatial scale of these growing perturbations is determined by the dynamics of the interaction between the large-scale circulation and the perturbations (Pedlosky, 1987). A distinction can be made between *barotropic* and *baroclinic* instability. The instability process is called barotropic when the perturbations feed on the kinetic energy of the unstable large-scale circulation. Hence, barotropic instability occurs when the horizontal shear of the large-scale flow is strong. In contrast, baroclinic instability of the flow may arise as a result of a strong vertical shear of the circulation. During the instability process, available

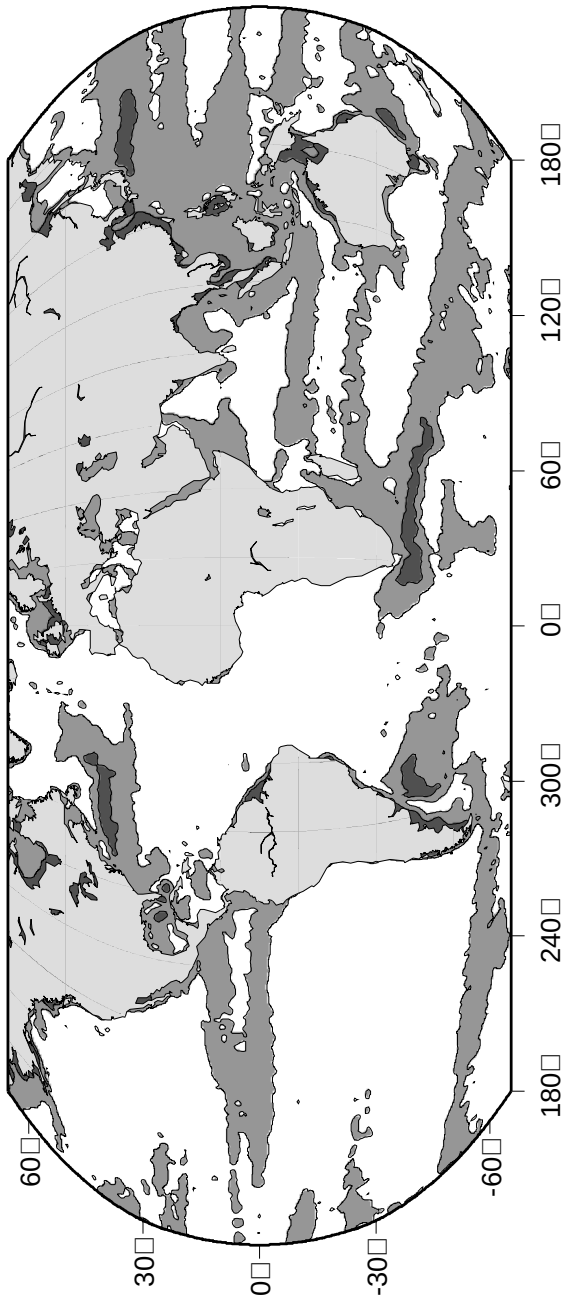

Figure 1.2: *Variability of the sea surface height over the oceans, as measured by the TOPEX/Poseidon satellite. The white, gray and dark-gray areas indicate where the root mean square of the variations is less than 15 cm, between 15 and 30 cm and larger than 30 cm, respectively. Mid-ocean jets as the Gulf Stream, the Kuroshio and the Agulhas Current clearly stand out as regions of intense variability (dark-grey areas). Courtesy of M. W. Schouten (IMAU).*

potential energy of the large-scale circulation is transferred to kinetic energy for the perturbations (Cushman-Roisin, 1994). In general, both horizontal and vertical shear will be present in oceanic flows, so that instabilities can also be of mixed type, that is, due to both barotropic and baroclinic processes. Barotropic and baroclinic instability are dominant mechanisms in large-scale flows through which energy is transferred between different scales of motion, and in particular from the large gyre scale down to the smaller eddy scales.

When the ratio of forcing to friction is high enough, and thus the shear of the circulation is strong, instabilities are expected to occur spontaneously in numerical simulations. Indeed, Bryan (1963) already noticed this in his simple numerical calculations of the wind-driven circulation, while varying the strength of the lateral friction. When the lateral friction was relatively strong, the circulation asymptotically approached a stationary solution. Transient oscillations appeared during spin-up, but their amplitude decreased rapidly. When he reduced the strength of the lateral friction, the oscillations persisted. Bryan (1963) demonstrated that these oscillations were a consequence of barotropic instabilities, and not a numerical artifact of the model.

Since then, many numerical studies have explicitly focused on the internal variability of the wind-driven circulation. Pioneering work was done by Holland and Lin (1975a,b), who used an eddy-resolving general circulation model on a rectangular domain. They used a two-layer configuration, in which the vertical density distribution of the ocean is approximated by two inmiscible layers, each of constant density. As in Bryan (1963), eddies appeared spontaneously in their simulations at small enough lateral friction. A transient ocean circulation emerged, which reached a statistical equilibrium a few years after the onset of the wind forcing. The eddies were found to play an important role in determining the character of the mean flow. Holland and Lin (1975a,b) explored a wide range of parameter settings, and described the eddy statistics of the transient flows. In single-gyre flows, westward propagating eddies formed in the westward return current of the gyre. These eddies have spatial scales of a few hundred kilometers, time scales of a few months, and were found to be generated by baroclinic instability processes. Holland and Lin (1975b) also performed numerical analyses with a double-gyre wind stress forcing pattern. The resulting circulation displayed a free eastward jet at the central latitude of the basin, flanked by a subtropical and a subpolar gyre, and served as an idealization of the large-scale gyres and mid-ocean jets shown in Figure 1.1. In contrast to the single-gyre cases, eddies now appeared in the eastward jet as well as in the westward return flow. The eddy characteristics were similar to the single-gyre simulations, and an energy analysis indicated that also the eastward jet becomes baroclinically unstable.

Many studies followed, in which for example the effects of increased vertical resolution, bottom topography, spatial distribution of the wind stress and coastal geometry were investigated (e.g., Holland, 1978; Holland *et al.*, 1983; Schmitz Jr. and Holland, 1986; Rhines and Schopp, 1991). In all these simulations, eddies with spatial scales of a few hundred kilometers appear spontaneously when the ratio of forcing to dissipation is high enough. They arise primarily as a result of growing instabilities on mid-ocean jets, and are responsible for variability on intermonthly time scales. In

addition, when the friction in the numerical simulations is decreased further, the transient flows display variability on interannual time scales, associated with changes in the large-scale circulation patterns (e.g., McCalpin and Haidvogel, 1996; Berloff and McWilliams, 1999). The origin of this relatively low-frequency variability in purely wind-driven flows is not yet fully understood.

The recent increase in computer power allows for studies at very high resolution nowadays, so that the circulation and its variability can be simulated in more detail and in more realistic model configurations. Examples of such state-of-the-art simulations are described in the recent study by Hurlburt and Hogan (2000), in which the wind-driven circulation in the North Atlantic Ocean is studied at a horizontal resolution of $1/8^\circ$ to $1/64^\circ$ ($\sim 14-1.8\ km$), with five layers in the vertical. A Deep Western Boundary Current, forced by in- and outflow conditions at the lateral boundaries, is also incorporated. The authors analyzed the mean circulation pattern and the eddy statistics of simulations at various resolutions. The results demonstrate that sufficient resolution is critical for realistic simulations of the Gulf Stream system. Fairly realistic simulations were obtainable at $1/16^\circ$ resolution, but major improvement was found up to $1/32^\circ$ resolution, and more modest improvement with a further increase to $1/16^\circ$ resolution. A major drawback of such high-resolution models is that they require so much computer time that usually only one simulation can be performed. Hence, such studies remain mainly descriptive in nature. The statistical properties of the transient part of the flow are summed up and compared to observations and other modelling studies. Sensitivity studies, to trace the dominant physical processes that determine this simulated variability, are practically impossible. For such process studies, idealized models which capture the basic physics of the flow are more useful. They can be applied to investigate the eddy characteristics of transient flows at different parameter settings (e.g., Holland, 1978; McCalpin, 1995). In addition, energy analyses of the flow can provide some information on the instability processes. But even then, finding physical explanations for different regimes of transient behavior remains difficult on the basis of time integrations alone.

1.3 Scope of this thesis

The main objective of this thesis is to explore the dynamical behavior of the wind-driven ocean circulation in a systematic way. In particular, the characteristics and the origin of the internal variability are investigated. For this study, an idealized two-layer ocean model is used, driven by a steady zonal wind stress at the surface. The forcing pattern is chosen such that a mid-ocean jet is generated at the central latitude of the basin, which is flanked by a subpolar and a subtropical gyre. This double-gyre circulation is a prototype for the major ocean gyres shown in Figure 1.1, and is subject to both barotropic and baroclinic instability processes. The model is designed for performing detailed process studies of the internal variability of the flow, and not for realistic simulations of the observed ocean circulation. Hence, the results are discussed qualitatively rather than quantitatively (see also Section 2.3).

As discussed in Section 1.2, in most studies of the variability of the wind-driven

circulation, the time-dependent equations describing the fluid motions are integrated forward in time with some time-stepping technique. The resulting time series are analyzed in detail, to extract the statistical properties of the variability. In contrast, in this thesis the subject is approached using mathematical tools based on the theory of dynamical systems (Guckenheimer and Holmes, 1983). Within this approach, the link between the internal variability of the flow and its instabilities is exploited. First, the stationary solutions for the wind-driven flow are calculated while continuously varying a physical parameter (the control parameter). Meanwhile, their stability with respect to infinitesimally small perturbations is determined. In this way, an overview of the possible stationary solutions and their stability characteristics is obtained in parameter space. Critical boundaries for instability can be derived, and the characteristics of the specific perturbations or *internal modes* that successively destabilize the flow are calculated.

Near the stability boundary, these modes control the dominant time and spatial scales of the variability. But also further from criticality, in the unstable regime, they are expected to play an important role. The results of this dynamical systems analysis will thus provide a framework for the interpretation of the time-dependent behavior of the circulation. Since the physical parameters are changed continuously, parameter regimes with differing model physics can be connected. Meanwhile, changes in the stability characteristics can be monitored to explain the origin of differences in the behavior of the flow. Second, the knowledge of the internal modes of variability allows for a detailed study of the destabilization process and its sensitivity to physical parameters. The impacts of eddy-mean flow and eddy-eddy interactions can be studied in 'controlled circumstances' near the stability boundary, where only one or a few modes interact. This provides a more transparent view of the physical processes involved than an analysis at highly unstable conditions, where many modes determine the final mean circulation pattern. Finally, the results of this dynamical systems analysis can be applied to identify the contributions of various internal modes to the variability displayed by transient flows.

In this thesis, the following questions are addressed:

- What are the characteristics of the stationary solutions of the wind-driven double-gyre system and of the internal modes that destabilize them?
- How do the instabilities of the flow modify the large-scale circulation?
- How does the presence of a Deep Western Boundary Current affect the dynamics of the wind-driven double-gyre circulation?
- Can the variability in transient flows be understood on the basis of the results of the dynamical systems analysis?

The outline of this thesis is as follows. The two-layer ocean model and the applied methodology are discussed extensively in Chapter 2. In Chapter 3, the dynamics of the idealized wind-driven double-gyre system are explored. The stationary flows for this system are calculated using the strength of the lateral friction as the control parameter. Furthermore, the characteristics of the internal modes that destabilize

them are discussed in detail. The results will not only provide insight in the qualitative features of the double-gyre circulation and its variability, but will also provide a starting-point for studies of less idealized, non-symmetric systems. To assess the impact of baroclinic instability processes, a barotropic system is approached by changing the vertical stratification of the model continuously. Also for this barotropic system, the stationary flows and their stability characteristics are determined, and compared to the baroclinic results.

On the basis of the results presented in Chapter 3, the impact of eddy-eddy interactions on the large-scale flow is studied in Chapter 4. In layer models, such interactions are known to be responsible for the flow in subsurface layers which are not directly forced by the wind (Pedlosky, 1996). The mechanism by which the eddies drive this deep flow is elaborated in this chapter. The results of the dynamical systems analysis are combined with the results of time integrations to derive a clear picture of the rectification of the flow by the instabilities.

Next, the focus of this thesis is turned specifically towards the circulation in the North Atlantic Ocean, by investigating the interaction between a Deep Western Boundary Current and the wind-driven gyres. To this end, a Deep Western Boundary Current is introduced in the symmetric wind-driven double-gyre system in Chapter 5. The stationary solutions for this coupled wind-driven/Deep Western Boundary Current system and the most unstable internal modes are calculated, again using the lateral friction as control parameter. They are compared to the results for the purely wind-driven system presented in Chapter 3. In addition, the strength of the Deep Western Boundary Current is used as a control parameter to explore the origin of changes induced by the presence of this subsurface current.

In Chapter 6, a series of transient flow computations is discussed, both for purely wind-driven and for coupled wind-driven/Deep Western Boundary Current flows. With the help of a statistical analysis, the most dominant time scales and spatial patterns of variability in these transient flows are determined. These are compared to the results of the dynamical systems analysis, to identify the contributions of various internal modes to the time-dependent behavior. In particular, the origin of low-frequency (interannual time scale) variability in wind-driven flows is explored in this way. In addition, the impact of the presence of a Deep Western Boundary Current on this type of variability is addressed. Finally, a discussion of the results follows in Chapter 7.

Chapter 2

Formulation and Approach

Throughout this thesis, an idealized numerical model is used to study the dynamical behavior of wind-driven flows. In this chapter, this model is defined, and the governing equations for the flow are formulated. The basic principles of the methodology used for this study were discussed in the previous chapter. Here, its numerical implementation is described.

2.1 The two-layer quasi-geostrophic model

In this thesis, a quasi-geostrophic model is used to study the variability of the wind-driven ocean circulation. The derivation of the quasi-geostrophic equations that describe the flow in such a model is only briefly outlined here, as details can be found in for example Pedlosky (1987). The oceanic motions are governed by the (non-linear) Navier-Stokes equations, which express the laws of conservation of mass and momentum (Acheson, 1990). For the large-scale ocean circulation, it is natural to use a frame of reference that rotates with the earth. Using typical scales appropriate for this circulation, it can be derived that, to lowest order, the flow is hydrostatic and geostrophic. That is, the vertical pressure gradient is determined by the density distribution of the water column, and horizontal pressure gradients are balanced by the Coriolis force. However, small deviations from this pure geostrophic flow are important for the dynamics of the circulation. These deviations can be (partly) incorporated by making an expansion in a small parameter known as the Rossby number Ro. This Rossby number is defined as the ratio of the non-linear terms and the Coriolis term in the equations, and thus measures to what extent the circulation differs from a linear, pure geostrophic flow. Small non-geostrophic effects can be taken into account by considering only the $\mathcal{O}(Ro)$ terms in the Navier-Stokes equations, and neglecting the terms that are higher order in Ro.

A further simplification of the full Navier-Stokes equations can be made by assuming that the horizontal scale of the motions L is small with respect to the radius of the earth r_0. Then it is justified to linearize the variation of the Coriolis parameter

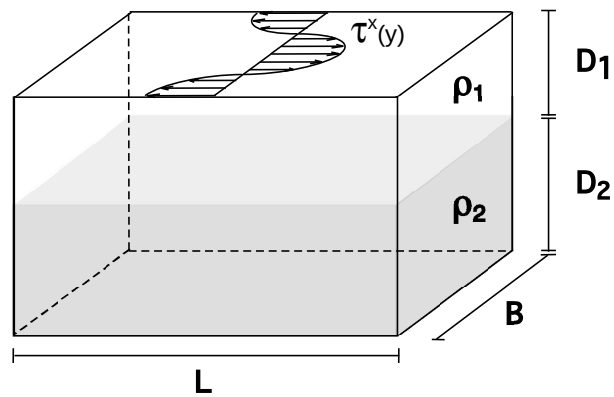

Figure 2.1: *Schematic picture of the two-layer quasi-geostrophic model.*

f with latitude around a central latitude ϕ_0 ($y = 0$ at the southern boundary):

$$f = f_0 + \beta_0(y - 0.5)$$

with $f_0 = 2\Omega \; sin \; \phi_0$ and $\beta_0 = \Omega / r_0 \; cos \; \phi_0$. In these expressions, Ω is the angular speed of rotation of the earth, and ϕ_0 is taken here as $45°N$.

These simplifications of the Navier-Stokes equations yield the so-called quasi-geostrophic equations of motion. These are formulated entirely in terms of the stream-function ψ and the vorticity ζ of the flow, which are related to the horizontal velocities u and v:

$$u = -\frac{\partial \psi}{\partial y}; \qquad v = \frac{\partial \psi}{\partial x}; \qquad \zeta = \frac{\partial v}{\partial x} - \frac{\partial u}{\partial y} = \nabla^2 \psi \tag{2.1}$$

For a homogeneous ocean, one equation (the quasi-geostrophic vorticity equation) describes the –vertically uniform– circulation. To represent the mean stratification of the ocean, a layer model consisting of n homogeneous layers with slightly different densities ρ_n can be constructed. For each layer, a quasi-geostrophic vorticity equation can be derived. Within each layer, the circulation is again uniform in the vertical, whereas movements of the layer interfaces couple the motions in adjacent layers.

The simplest layer model that incorporates the effects of the stratification is a two-layer model, which can be seen as a crude representation of warm upper ocean waters separated from colder deep waters by the ocean thermocline. In this thesis, such a two-layer quasi-geostrophic model is used to study the dynamics of the wind-driven double-gyre circulation. This circulation serves as a prototype for the observed large-scale wind-driven gyres (Fig. 1.1). A schematic picture of the model is shown in Figure 2.1. It uses an idealized rectangular domain of horizontal dimensions $L \times B$ and of constant depth D. The surface layer has a homogeneous density ρ_1 and equilibrium depth D_1, the second layer has density $\rho_2 = \rho_1 + \Delta\rho$ and depth D_2 ($D = D_1 + D_2$).

The pattern of the surface wind stress forcing $\tau = \tau_0(\tau^x, \tau^y)$ is steady, and chosen such that a double-gyre circulation arises (see also Fig. 2.1)

$$\tau^x(y) = -\frac{1}{2\pi}\, cos\left(\frac{2\pi y}{A}\right); \qquad \tau^y = 0$$

where $A = B/L$ is the aspect ratio of the basin. In all calculations, $B = L$ so that $A = 1$. Dissipation is through friction at the lateral boundaries only, no bottom or interfacial friction is applied. As a consequence, the second layer of the model is unforced when the flow is stationary.

In the vorticity-streamfunction formulation, there are four unknowns in the two-layer system: ζ_1, ψ_1, ζ_2 and ψ_2. The quasi-geostrophic equations can be non-dimensionalized using the horizontal and vertical length scales L and D, a characteristic horizontal velocity scale U, a time scale L/U and the maximum amplitude of the wind stress τ_0. The dimensionless quasi-geostrophic vorticity equations then become (Pedlosky, 1987):

$$\left[\frac{\partial}{\partial t} + u_1\frac{\partial}{\partial x} + v_1\frac{\partial}{\partial y}\right](\zeta_1 - F_1(\psi_1 - \psi_2) + \beta y) = \frac{1}{Re}\nabla^2\zeta_1 + \alpha_\tau\left(\frac{\partial \tau^y}{\partial x} - \frac{\partial \tau^x}{\partial y}\right) \quad (2.2a)$$

$$\zeta_1 = \nabla^2\psi_1 \quad (2.2b)$$

$$\left[\frac{\partial}{\partial t} + u_2\frac{\partial}{\partial x} + v_2\frac{\partial}{\partial y}\right](\zeta_2 + F_2(\psi_1 - \psi_2) + \beta y) = \frac{1}{Re}\nabla^2\zeta_2 \quad (2.2c)$$

$$\zeta_2 = \nabla^2\psi_2 \quad (2.2d)$$

These equations contain five dimensionless parameters: the Reynolds number Re, the strength of the planetary vorticity gradient β, the strength of the wind stress forcing α_τ and the rotational Froude numbers based on the depth of the first and the second layer, F_1 and F_2, respectively. They are defined as

$$Re = \frac{UL}{A_H};\ \beta = \frac{\beta_0 L^2}{U};\ \alpha_\tau = \frac{\tau_0 L}{\rho_1 D_1 U^2};\ F_1 = \frac{f_0^2 L^2}{g' D_1};\ F_2 = \delta F_1 = \frac{f_0^2 L^2}{g' D_2} \quad (2.3)$$

where $g' = g\,(1 - \rho_1/\rho_2)$ is the reduced gravity, $\delta = D_1/D_2$ is the layer thickness ratio and A_H is the lateral friction coefficient. This coefficient, the eddy viscosity, includes the effects of small-scale turbulent motions not resolved in the model and is much larger than the molecular viscosity. The parameter β is in fact an inverse Rossby number, since it is defined as the ratio of the non-linear terms (which are of order $\mathcal{O}(U^2/L)$) and Coriolis effects (of order $\mathcal{O}(\beta_0 LU)$):

$$\beta = \frac{\beta_0 L^2}{U} = \frac{\beta_0 LU}{U^2/L} = \frac{1}{Ro}$$

The Froude numbers F_1 and F_2 are linked to the internal Rossby deformation radius $R_D = \sqrt{g'D}/f_0$ by

$$\frac{1}{F_1} + \frac{1}{F_2} = \left(\frac{R_D}{L}\right)^2$$

When $F_2 = 0$, the second layer is infinitely deep and hence dynamically inactive. In that case, there is no coupling between the first layer and the second layer, and an equivalent barotropic model or 1.5-layer model is obtained. In the limit of F_1 and $F_2 = 0$, the equations (2.2) reduce to those for the circulation in a barotropic (homogeneous), single-layer model.

A set of standard parameter values is used throughout this thesis, which is stated in Table 2.1. The choice of the horizontal velocity scale U is based on the notion that in the open ocean, the circulation is governed by a balance between the input of vorticity by the wind stress and the planetary vorticity (Sverdrup, 1947). By assuming that $\alpha_\tau = \beta$, the Sverdrup balance is indeed the main balance in equation (2.2). This assumption yields a velocity scale U

$$U = \frac{\tau_0}{\rho_1 D_1 \beta_0 L}$$

Thin boundary layers are expected in the western part of the basin, in which frictional and/or inertial effects are important (Section 1.1.1). Typical length scales for the width of these boundary layers can be derived on the basis of the vorticity equations (2.2). Since bottom friction is not incorporated in the model, only the (dimensionless) inertial boundary layer thickness δ_I and the Munk boundary layer thickness δ_M are relevant. These boundary layer thicknesses are given by $\delta_I = \beta^{-1/2}$ and $\delta_M = (Re\beta)^{-1/3}$, respectively (e.g., Pedlosky, 1987). For the standard value of $\beta = 10^3$, the inertial boundary layer thickness $\delta_I = 0.032$, or in dimensional units $\delta_I^* = \delta_I L = 32\ km$. The Munk boundary layer thickness δ_M is varied in the range $[0.02, 0.04]$ by changing Re (δ_M^* between 20 and 40 km). With the choice of parameters as in Table 2.1, the advective time scale of the gyre $L/U = 6.25 \cdot 10^7\ s$ or 2.0 $years$. The internal Rossby deformation radius $R_D = 63\ km$. The Reynolds number is not stated in Table 2.1, since it is used as the main control parameter in the calculations.

No-slip conditions are prescribed at the eastern and western boundaries of the domain to represent the continents. At the northern and southern sides, free-slip conditions are imposed to simulate the edges of the gyres. In Chapter 5, a Deep Western Boundary Current is prescribed in the second layer of the model through in- and outflow conditions. The specification of the new boundary conditions is postponed until Section 5.2.

2.1.1 Discretization

The set of partial differential equations (2.2) is discretized by a finite volume method. To assure that enough grid points lie within the thin western boundary layers and near the mid-ocean jet forced by the double-gyre wind stress pattern, a non-equidistant grid is used. The stretched grid is obtained by transforming the x-and y-coordinates $\bar{x}$ and $\bar{y}$ of an equidistant grid according to

$$x = 1 - \frac{tanh(q_x(1-\bar{x}))}{tanh(q_x)}$$

$$y = \frac{1}{2}\left[1 + \frac{tanh(q_y\bar{y}) - tanh(q_y(1-\bar{y}))}{tanh(q_y)}\right]$$

f_0	$=$	$1.0 \cdot 10^{-4}$	s^{-1}	β_0	$=$	$1.6 \cdot 10^{-11}$	$(ms)^{-1}$
τ_0	$=$	$1.5 \cdot 10^{-1}$	N/m^2	U	$=$	$1.6 \cdot 10^{-2}$	m/s
L	$=$	$1.0 \cdot 10^{6}$	m	B	$=$	$1.0 \cdot 10^{6}$	m
D_1	$=$	$0.6 \cdot 10^{3}$	m	D_2	$=$	$1.4 \cdot 10^{3}$	m
ρ_1	$=$	$1.0 \cdot 10^{3}$	kg/m^3	$\Delta\rho$	$=$	2.0	kg/m^3
α_τ	$=$	$1.0 \cdot 10^{3}$		β	$=$	$1.0 \cdot 10^{3}$	
F_1	$=$	$8.5 \cdot 10^{2}$		F_2	$=$	$3.5 \cdot 10^{2}$	

Table 2.1: *Standard dimensional and non-dimensional parameters for the two-layer model.*

with stretching parameters q_x and q_y. A grid of 49×33 points is used for all the computations, with $q_x = q_y = 2$. As a result, the grid size varies between 3 and 43 km zonally and between 27 and 35 km in the meridional direction for the standard basin size of $L = B = 1000$ km.

2.1.2 The evolution of perturbations

The internal variability of the wind-driven circulation is studied on the basis of the stability of stationary solutions (Section 1.3). It can be assumed that a stationary solution of (2.2), which will be denoted by $\Psi = (\Psi_1, Z_1, \Psi_2, Z_2)$, is disturbed by perturbations $\boldsymbol{\varphi} = (\phi_1, \eta_1, \phi_2, \eta_2)$ of the form

$$\boldsymbol{\varphi}(x, y, t) = \hat{\boldsymbol{\varphi}}(x, y)\ e^{\sigma t} = \hat{\boldsymbol{\varphi}}(x, y)\ e^{(\lambda + i\nu)t} \tag{2.4}$$

As long as the perturbations $\boldsymbol{\varphi}$ are small, their evolution is governed by the equations (2.2), linearized around the stationary solution Ψ:

$$\begin{aligned}
&\left[\sigma + U_1 \frac{\partial}{\partial x} + V_1 \frac{\partial}{\partial y}\right](\eta_1 - F_1(\phi_1 - \phi_2)) + \\
&\qquad + \left[u_1' \frac{\partial}{\partial x} + v_1' \frac{\partial}{\partial y}\right](Z_1 - F_1(\Psi_1 - \Psi_2) + \beta y) &= \frac{1}{Re}\nabla^2 \eta_1 && \text{(2.5a)}\\
&\qquad\qquad \eta_1 &= \nabla^2 \phi_1 && \text{(2.5b)}\\
&\left[\sigma + U_2 \frac{\partial}{\partial x} + V_2 \frac{\partial}{\partial y}\right](\eta_2 + F_2(\phi_1 - \phi_2)) + \\
&\qquad + \left[u_2' \frac{\partial}{\partial x} + v_2' \frac{\partial}{\partial y}\right](Z_2 + F_2(\Psi_1 - \Psi_2) + \beta y) &= \frac{1}{Re}\nabla^2 \eta_2 && \text{(2.5c)}\\
&\qquad\qquad \eta_2 &= \nabla^2 \phi_2 && \text{(2.5d)}
\end{aligned}$$

where

$$U_n = -\frac{\partial \Psi_n}{\partial y}; \qquad V_n = \frac{\partial \Psi_n}{\partial x}; \qquad u_n' = -\frac{\partial \phi_n}{\partial y}; \qquad v_n' = \frac{\partial \phi_n}{\partial x}$$

for $n = 1, 2$. The real part of the growth rate σ determines whether perturbations $\boldsymbol{\varphi}$ will grow or decay with time, and thus whether the stationary flow Ψ is stable or unstable with respect to these perturbations.

2.2 Numerical implementation

The basic principles of the dynamical systems approach that is used in this thesis were outlined in Section 1.3. It is based on the notion that the internal variability of the flow is linked to its stability. Hence, it is of interest to calculate stationary solutions* for the flow, and subsequently determine the stability properties of the circulation. The applied numerical algorithm consists of two main parts. The first part is a continuation algorithm (Section 2.2.2), with which branches of stationary solutions can be traced for changing values of a model parameter (the control parameter). The second part of the numerical algorithm consists of an eigenvalue solver to determine the linear stability of the computed stationary solutions (Section 2.2.3). The growth rates σ of the perturbations are monitored for changing values of the control parameter. A point in parameter space where the growth rate of a specific perturbation changes sign is called a bifurcation point, and marks a qualitative change in the behavior of the flow (Nayfeh and Balachandran, 1995). It is advantageous to start in a low-forcing regime where the flow is stable. Subsequently, one can detect the successive bifurcation points along a branch of stationary solutions while progressing towards a high-forcing regime. The simplest type of bifurcations are those that involve only one parameter in the system under study, the so-called codimension-one bifurcations. In the next section, it is first illustrated on the basis of simple, low-dimensional dynamical systems how bifurcation points can be detected, before turning to the details of the numerical method.

2.2.1 Simple bifurcations

The evolution of a variable u can in general be described by the one-dimensional autonomous dynamical system

$$u' = f(u, \mu) \tag{2.6}$$

where μ is the control parameter and the prime indicates the time-derivative. Suppose that a branch of stationary solutions $\bar{u}$ of (2.6) is known as a function of μ. To determine the stability of these stationary solutions with respect to infinitesimally small perturbations φ of the form $\varphi = \hat{\varphi}(x, y)e^{\sigma t}$, one has to consider the evolution of $u = \bar{u} + \varphi$. Equation (2.6) yields that (using that φ is small)

$$\begin{aligned} u' \equiv \sigma\varphi &= f(\bar{u} + \varphi, \mu) = f(\bar{u}, \mu) + \frac{\partial f(\bar{u}, \mu)}{\partial u}\varphi + \dots \\ &\simeq \frac{\partial f(\bar{u}, \mu)}{\partial u}\varphi \end{aligned} \tag{2.7}$$

*For clarity, the use of the phrase "steady state" is avoided in this thesis, since it can be a confusing choice of words. In the terminology of dynamical systems theory, all solutions of the stationary equations are steady (that is, time-independent) states. However, it is common practice among oceanographers to define the steady state of an ocean model run as the transient circulation, averaged over a certain integration period. In this thesis, such an average is explicitly called a "mean state", whereas solutions of stationary equations will consistently be called "stationary solutions".

where the dots represent higher order terms in the Taylor expansion around $\bar{u}$. To assess the stability of the flow, one needs to determine the (real part of the) growth rate σ of the perturbation, which, according to (2.7), can be approximated by the derivative $\partial f/\partial u$ evaluated at the stationary solution $(\bar{u}, \mu)$. The bifurcation point is the specific value of μ for which $\partial f(\bar{u}, \mu)/\partial u = 0$, so that the stationary solution is neutrally stable with respect to the perturbation φ.

As an example of a simple system in which a codimension-one bifurcation occurs, consider

$$u' = \mu u - u^3 \tag{2.8}$$

For $\mu < 0$, equation (2.8) has only one stationary solution: $\bar{u} = 0$. For $\mu > 0$, three stationary solutions exist ($\bar{u} = 0$, $\bar{u} = \sqrt{\mu}$ and $\bar{u} = -\sqrt{\mu}$). To assess the stability of these solutions, the derivative $\partial f/\partial u = \mu - 3u^2$ must be evaluated at the stationary solutions. For $\bar{u} = 0$ it follows that $\partial f/\partial u = \mu$, indicating that this solution is stable for $\mu < 0$ but unstable for $\mu > 0$. For the two additional stationary solutions $\bar{u} = \pm\sqrt{\mu}$ that exist for positive μ it follows that $\partial f/\partial u = -2\mu$, showing that these are both stable.

The results of this stability analysis can be visualized in a bifurcation diagram. In such a diagram, the stationary solutions for the flow are plotted as a function of the control parameter. A particular measure of the stationary solutions is plotted on the vertical axis. The bifurcation diagram for the one-dimensional system (2.8) is shown in Figure 2.2a, with in this case the stationary solution $\bar{u}$ on the vertical axis. The stability of the stationary solutions is indicated by the line style: stable solutions are drawn and unstable solutions are dashed. Bifurcation points are indicated by markers. At $\mu = 0$, the system undergoes a qualitative change, since the number of stationary solutions changes from one to three. Moreover, the stability of the stationary solution $\bar{u} = 0$ changes. The corresponding bifurcation is called a pitchfork bifurcation. Two other bifurcation diagrams, those for a saddle node and a transcritical bifurcation, are shown in Figures 2.2b and 2.2c. The simplest one-dimensional system which exhibits such a bifurcation is provided in the caption. For reasons obvious from Figure 2.2b, a saddle node bifurcation is often called a limit point: it determines the limit of the existence of certain stationary solutions.

Whereas for the bifurcations in Figures 2.2a-c the number of stationary solutions changes as the control parameter μ is varied, it is also possible that the character of the solution changes from stationary to oscillatory. An example of a simple dynamical system undergoing such a transition is the two-dimensional autonomous system given by

$$u_1' = \mu u_1 - \omega u_2 - u_1(u_1^2 + u_2^2) \tag{2.9a}$$
$$u_2' = \mu u_2 + \omega u_1 - u_2(u_1^2 + u_2^2) \tag{2.9b}$$

By substituting $u_1 = r\,cos\,\theta$ and $u_2 = r\,sin\,\theta$, (2.9) is transformed into polar coordinates

$$r' = \mu r - r^3 \tag{2.10a}$$
$$\theta' = \omega \tag{2.10b}$$

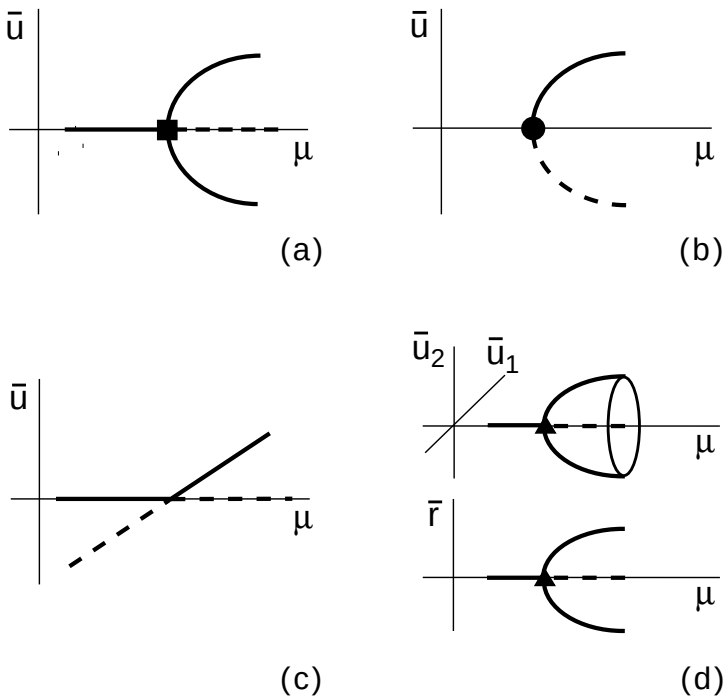

Figure 2.2: *Overview of codimension-one bifurcations and the simplest dynamical system exhibiting this bifurcation. (a) pitchfork bifurcation,* $u' = \mu\, u - u^3$*; (b) saddle node bifurcation or limit point,* $u' = \mu - u^2$*; (c) transcritical bifurcation,* $u' = \mu\, u - u^2$*; (d) Hopf bifurcation,* $u_1' = \mu\, u_1 - \omega\, u_2 - u_1(u_1^2 + u_2^2); u_2' = \mu\, u_2 + \omega\, u_1 - u_2(u_1^2 + u_2^2)$*.*

Comparing (2.10a) with (2.8), it can be seen that a pitchfork bifurcation occurs at $\mu = 0$ in the (r, μ)-plane. Hence, stationary solutions for the amplitude r are $\bar{r} = 0$ for $\mu < 0$ and $\bar{r} = 0, \pm\sqrt{\mu}$ for $\mu > 0$. The stationary solution for $\mu < 0$ is stable, and corresponds to the trivial stationary solution $\bar{u} = (\bar{u}_1, \bar{u}_2) = (0, 0)$ of the original equations (2.9). For $\mu > 0$, this particular solution is unstable, whereas the two additional stationary solutions for $\bar{r}$ are stable. They correspond to a limit cycle or periodic orbit of the original equations (2.9): $\bar{u} = (u_1, u_2) = \pm(\sqrt{\mu}\ cos(\omega t), \sqrt{\mu}\ sin(\omega t)\ )$. The bifurcation diagram for this case is shown in Figure 2.2d.

From these examples it is clear that multiple stationary solutions can occur due to pitchfork, transcritical or saddle node bifurcations, whereas Hopf bifurcations introduce temporal variability in the system. More complicated bifurcations may arise as more than one parameter in the system is changed (Nayfeh and Balachandran, 1995). Detecting Hopf bifurcation points and analyzing the associated oscillatory modes is an important element of this study, since these modes determine the characteristics of the internal variability near critical conditions. Moreover, they are expected to be of importance for the internal variability far into the unstable regime as well.

2.2.2 Continuation method

The discretized stationary equations (2.2) can be written in a general form as a set of nonlinear algebraic equations

$$\mathbf{F}(\mathbf{u}, \mathbf{p}) = 0 \tag{2.11}$$

In (2.11), $\mathbf{u}$ is a d-dimensional vector consisting of the unknowns at all grid points. The p-dimensional vector $\mathbf{p}$ contains the physical parameters of the model, and $\mathbf{F}$ is a nonlinear mapping from $R^d \times R^p \rightarrow R^d$. For the standard configuration of the two-layer quasi-geostrophic model, $d = 4$ unknowns $\times$ 49 $\times$ 33 grid points = 6468 and the parameter vector $\mathbf{p}$ is five-dimensional.

To determine branches of stationary solutions for the flow as one of the parameters in $\mathbf{p}$ (say μ) is varied, a numerical technique is needed with which a new stationary solution $(\mathbf{u_n}, \mu_n)$ of (2.11) can be calculated, using a previously computed stationary solution $(\mathbf{u_o}, \mu_o)$. Here, pseudo-arclength continuation is used, a numerical technique described extensively in literature (Keller, 1977; Seydel, 1988). The procedure is sketched in Figure 2.3. In this bifurcation diagram, a certain measure $|u|$ of the stationary solution $\mathbf{u_n}$ is plotted on the vertical axis.

The (yet unknown) branch of stationary solutions is parameterized by an arc-length parameter s, and stationary solutions are denoted as $(\mathbf{u}(s), \mu(s))$. Suppose a stationary solution $(\mathbf{u_o}, \mu_o)$ of the system under study is known (the black squares in Fig. 2.3). A first guess for a new solution $(\hat{\mathbf{u}}, \hat{\mu})$ can be obtained by taking a step Δs along the tangent to the branch of stationary solutions:

$$\hat{\mathbf{u}} = \mathbf{u_o} + \Delta s \frac{\partial \mathbf{u_o}}{\partial s}; \qquad \hat{\mu} = \mu_o + \Delta s \frac{\partial \mu_o}{\partial s} \tag{2.12}$$

These estimates for the new solutions are indicated by gray squares in Figure 2.3. Since in general $(\hat{\mathbf{u}}, \hat{\mu})$ is not a solution of (2.11), a Newton-Raphson process is initiated, visualized by the thin line in Figure 2.3, to arrive at a new stationary solution

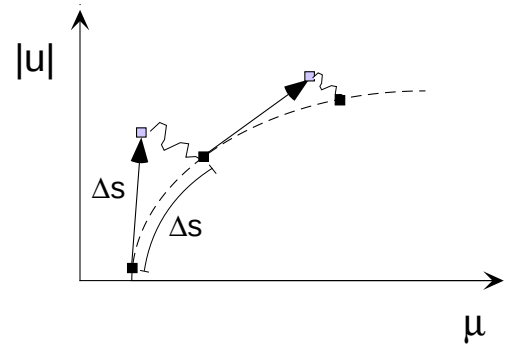

Figure 2.3: *Sketch of the pseudo-arclength continuation procedure. Starting from a known stationary solution (black square), a first guess of a new solution is obtained (gray square) by taking a step in the direction of the tangent to the solution branch. Using an iterative technique and keeping the step length Δs fixed, a new stationary solution is obtained. In this diagram, $|u|$ is used as a measure for the stationary solution $\mathbf{u_n}$.*

iteratively. Meanwhile, the step length Δs is kept fixed. Often, the stationary solution for the unforced system (2.11) can be derived analytically and can serve as a starting-point for the continuation procedure. The arclength parameter s is introduced to assure that the branch of stationary solutions can be traced around a limit point. Near a limit point, simply taking a step in μ will fail to produce a new stationary solution. An additional equation is required to close the system of equations (2.11), that relates this extra parameter s to $\mathbf{u}$ and μ (see for example Dijkstra, 2000). Hence, finding a stationary solution by pseudo-arclength continuation requires solving a non-linear system of $d+1$ algebraic equations.

2.2.3 Linear stability analysis

Once a stationary solution of (2.11) is known, sufficient conditions for instability can be determined by presuming that infinitesimally small perturbations $\boldsymbol{\varphi} = \hat{\boldsymbol{\varphi}}(x,y)e^{\sigma t}$ are present on this stationary solution. The evolution of these perturbations is governed by the discretized equations (2.5). A generalized eigenvalue problem for σ of the form

$$\mathcal{A}\boldsymbol{\varphi} = \sigma\mathcal{B}\boldsymbol{\varphi} \tag{2.13}$$

emerges, where $\mathcal{A}$ and $\mathcal{B}$ are $d \times d$ matrices. The eigenvectors associated with the eigenvalues σ determine the spatial patterns $\hat{\boldsymbol{\varphi}}$ of the specific perturbations or internal modes that destabilize the flow. Of interest are the bifurcation points, where the real part of one or more eigenvalues changes sign and the stability characteristics of the flow are altered (Section 2.2.1). At pitchfork bifurcations and limit points, one real

eigenvalue $\sigma = \lambda$ crosses the imaginary axis. At a Hopf bifurcation point, the real part λ of a complex conjugated pair of eigenvalues $\sigma_{1,2} = \lambda \pm i\nu$ changes sign, so that the stationary solution becomes unstable to an oscillatory mode. The time-dependent behavior of the mode $\boldsymbol{\varphi}$ is described by the two eigenvectors $\boldsymbol{\varphi}_1$ and $\boldsymbol{\varphi}_2$ associated with σ_1 and σ_2:

$$\boldsymbol{\varphi}(x, y, t) = [\boldsymbol{\varphi}_1(x, y)cos(\nu t) - \boldsymbol{\varphi}_2(x, y)sin(\nu t)]\ e^{\lambda t} \tag{2.14}$$

The imaginary part ν of the eigenvalue determines the frequency of the oscillation, the period $p = 2\pi/\nu$.

Traditional eigenvalue solvers that determine all eigenvalues and all eigenvectors are in practice impossible to use for a large-dimensional system (recall that $d = \mathcal{O}(10^4)$). However, to determine the initial destabilization of the flow, only the first few bifurcation points need to be detected, which involve only a small number of modes. That is, the eigenmodes that have eigenvalues closest to the imaginary axis (the 'most dangerous' modes) are the ones of interest to compute. To this end, the eigenvalue problem is transformed in such a way that the most dangerous modes become the most dominant modes (i.e., those with eigenvalues with largest norm). The eigenmodes for the transformed problem can be solved by applying a generalized power method (see Dijkstra *et al.*, 1995, for details on the numerical implementation).

2.3 Qualitative remarks

In this chapter, the idealized quasi-geostrophic model that is used in this thesis was introduced, as well as the methodology with which the internal variability of the wind-driven circulation in this model is studied. Before discussing the results of this analysis, a few remarks on both the model set-up and the approach need to be made.

Idealized model set-up

The numerical model used in this thesis is highly idealized, both with regard to the computational domain, the wind forcing as well as the representation of the stratification by only two layers. This choice is motivated by the main objective of this study, which is to understand the physical mechanisms that determine the variability of the wind-driven ocean circulation qualitatively, rather than to provide a detailed, quantitative description of this circulation. The reverse side of the medal is that a comparison with observations and the results of more realistic ocean simulations is difficult.

In this thesis, a simplified set of equations, the quasi-geostrophic equations, is used to describe the (evolution of the) circulation. Formally, for the quasi-geostrophic approximation to be valid, the deviations of the layer interfaces with respect to their mean value need to be relatively small. However, earlier eddy-resolving studies have shown that there is a qualitative agreement between the results of time integrations obtained with quasi-geostrophic layer models and shallow-water models, in which the amplitude of the interface deformations is not restricted by a priori assumptions. Examples are the two-layer study by Holland (1978), the results of which are compared

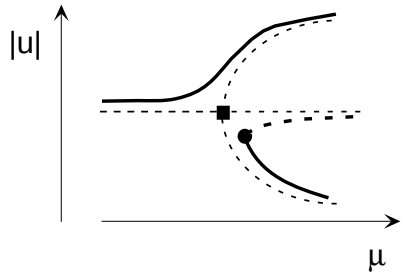

Figure 2.4: *Schematic bifurcation diagram of a perturbed pitchfork bifurcation (thick solid and dashed lines). Solution branches associated with an unperturbed pitchfork bifurcation are shown as thin dashed lines.*

to those presented by Holland and Lin (1975a, b), and the five-layer study by Semtner and Holland (1978). Since the goal of this study is to investigate the basic physical mechanisms that cause internal variability qualitatively, using a quasi-geostrophic model seems legitimate.

Internal symmetry of the quasi-geostrophic system
When applying continuation techniques, an important advantage of a quasi-geostrophic model is that the system of quasi-geostrophic equations (2.2) has a reflection symmetry with respect to the mid-axis of the basin. Since the applied wind stress curl and the boundary conditions were defined in such a way that they also have this property, the system allows for solutions that display the symmetry

$$\psi(x, y) = -\psi(x, 1 - y)$$

In a system with internal symmetry, branches of stationary solutions are connected through bifurcation points (e.g., Dijkstra, 2000), which is a large advantage from a computational point of view: branches of solutions are much easier to track, as is illustrated in Figure 2.4. In this figure, the thin dashed lines represent branches of solutions in a system with internal symmetry, connected by a pitchfork bifurcation (black square). With the continuation technique, one can easily switch to one of the new branches that come into existence at the bifurcation point by taking a step *normal* to the branch in stead of along the branch to obtain a first guess for a new solution. Then, the Newton-Raphson procedure will converge to one of the new branches. In contrast, when a so-called imperfection is present that destroys the internal symmetry of the system, branches of stationary solutions are not connected. In such an imperfect system, a perturbed pitchfork bifurcation can be encountered (thick solid and dashed lines in Figure 2.4). The branch with the limit point can not be reached directly from the low-forcing regime, and switching to it is difficult since its position is not known a priori. So, it is advantageous to start by tracking down the solution branches for a system which displays a high degree of internal symmetry first, and subsequently introduce more complex features which destroy this symmetry. A quasi-geostrophic model is therefore better suited as a starting-point for a dynamical systems analysis

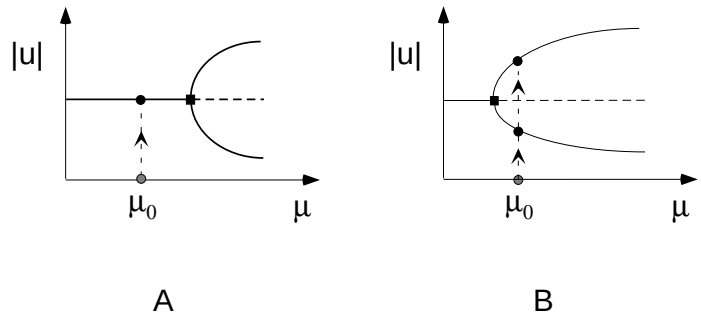

Figure 2.5: *Illustration of how quantitative changes can be distinguished from qualitative changes, once the bifurcation diagram is constructed. Shown are two bifurcation diagrams, for model versions A and B. The trajectory of model A, when initialized at parameter value μ_0, will reach a stationary, symmetric solution. In contrast, for model B an asymmetric solution will be obtained. From the bifurcation diagram, it is obvious this is a consequence of a quantitative change.*

than for example a shallow-water model, which does not have this internal symmetry property (Dijkstra and Molemaker, 1999).

An interesting feature of the applied two-layer quasi-geostrophic model is that there is no flow in the second layer for any of the stationary solutions because the wind stress forcing only acts on the upper layer and no interfacial friction is incorporated. As a result, the stationary solutions for the two-layer model are the same as the stationary solutions for an equivalent barotropic model with otherwise the same set of parameters. However, the second layer is of importance for the stability of the wind-driven flows, as will be demonstrated in Chapter 3. When the flow in the upper layer is time-dependent, a non-zero mean flow does develop in the second model layer. The mechanism by which this deep mean flow is generated is the subject of Chapter 4.

Distinguishing qualitative from quantitative changes

It is of interest to be able to distinguish whether changes in for example the model set-up result in qualitative changes in the behavior of the flow, or whether they merely induce quantitative effects. In the former case, the changes are essential to the physical processes that determine the circulation. This distinction is often easier from continuation results than from the results of time integrations. To illustrate this, two bifurcation diagrams are sketched in Figure 2.5, which may display results obtained with two models with different boundary conditions, for example. From the bifurcation diagram, it is obvious that the changes to the model only affect the location of the pitchfork bifurcation point, and thus only induce quantitative effects. However, the results of time integrations for the parameter value μ_0 may give the impression that a qualitative change has occurred, since the stationary solution reached with model A is very different from the one reached with model B.

The contributions of internal modes to the variability

In this thesis, the variability of the wind-driven circulation is studied on the basis of the characteristics of the most unstable internal modes. These modes are assumed to determine the internal variability of the flow. Close to the stability boundary, this assumption is certainly valid. When a stationary solution is unstable to a specific oscillatory mode, a time integration at slightly supercritical conditions will show a regularly oscillating flow. Further into the unstable regime, the time-dependent behavior can no longer be predicted on the basis of the results of the dynamical systems analysis. A second mode may destabilize the (already unstable) stationary solution for higher forcing, but this does not guarantee that this second mode will contribute to the variability of the transient flow. Ideally, in stead of calculating the stability of the unstable stationary solution, one would like to study the stability of the periodic flow associated with the first mode. Unfortunately, no feasible numerical methods exist (yet) with which this can be done for large-dimensional problems. The only choice is thus to determine the stability of the stationary solution, which is in general not too different from the (mean state of the) periodic flow, and thus can be expected to display qualitatively the same stability characteristics. Nonetheless, the contributions of various unstable modes to the variability needs to be analyzed by performing 'traditional' time integrations at selected parameter settings.

In this thesis, the results of time integrations at various parameter settings are discussed in both Chapters 4 and 6. For this, an implicit time-stepping code is developed, on the basis of the continuation code and the linear stability analysis (Dijkstra, 2000). When the continuation method is used to calculate (unstable) stationary solutions first, these can be used as an initial condition for the time integrations. This is often far more efficient than letting the flow spin up from rest. Moreover, the initial solution can be perturbed with the most unstable eigenmode for this specific solution, to assure a fast deviation of the time-dependent flow away from this stationary solution.

Chapter 3

Stationary wind-driven flows and their variability*

In this chapter, it is explored how temporal variability arises through successive bifurcations of the symmetric wind-driven double-gyre circulation as lateral friction is decreased. The characteristics of the destabilizing perturbations are discussed in detail. Subsequently, results for the two-layer model are linked and compared to those obtained with a barotropic version of the model.

3.1 Introduction

The stability problem for the wind-driven ocean circulation in a confined basin is mathematically complex, since the spatial pattern of both the stationary solution as well as of the destabilizing perturbation are both functions of the zonal and the meridional coordinate. In contrast, the stability problem for a zonal jet in a channel is relatively easy to solve, when it is assumed that the basic stationary jet only varies in the cross-channel direction. Therefore, the stability of channel flows has been studied extensively. Such zonal flows can serve as an idealization of both the jet stream in the atmosphere and of narrow wind-driven surface currents in the ocean. Various stationary jet profiles, designed to study barotropic, baroclinic or mixed instability processes, have been analyzed analytically (see Pedlosky, 1987, for a comprehensive review). Eady (1949) studied the stability of a jet in a continuously stratified inviscid fluid. The basic flow in his model comprises only vertical shear, and was shown to become baroclinically unstable to perturbations with wavelengths larger than the internal Rossby deformation radius. Phillips (1954) studied a similar baroclinic instability problem in a simpler two-layer set-up. Zonal flows with both horizontal and vertical shear were studied by Pedlosky (1964), who found that the stability charac-

*This chapter is based on the paper "*Temporal variability of the wind-driven quasi-geostrophic double gyre ocean circulation: Basic bifurcation diagrams*" by H. A. Dijkstra and C. A. Katsman, *Geophys. and Astrophys. Fluid Dynamics*, vol. **85**, pp. 195-232, 1997

teristics may change significantly once the flow is susceptible to both barotropic and baroclinic instability processes. Slightly non-zonal flows, for which the variation of the Coriolis parameter with latitude starts playing a role, were considered by Robinson and McWilliams (1974). They demonstrated that slight deviations from zonality considerably destabilize the flow.

In reality, the large-scale ocean circulation is certainly non-zonal and non-parallel, in particular near the continental boundaries where the flow is forced to turn. This turning effect may very well influence the stability characteristics of the flow. In this chapter, the stationary solutions for the wind-driven flow in the two-layer model are presented. Moreover, the problem of the (mixed) instability of a non-parallel double-gyre flow is addressed by solving the linear stability problem. The flows that are forced within this model are subject to both baroclinic and barotropic instability processes, as in reality, and instabilities are expected to be of mixed type. In this study, the basic stationary gyre flow depends on the physical parameters of the system, such as the lateral friction. This in contrast to the zonal channel flow studies described above, where the basic state jet of which the stability was studied was prescribed.

The stationary solutions for flows in a closed basin can be calculated by solving the stationary vorticity equations (Section 2.1). Solutions of the (linearized) barotropic vorticity equation were originally studied to explain the western intensification observed in ocean gyres (Section 1.1.1). In a series of studies, Moro (Moro, 1987, 1988, 1990) addressed the stability and variability of the double-gyre flow within an equivalent barotropic quasi-geostrophic model in a systematic way. He was one of the first to directly solve the stationary vorticity equations by applying an iterative method, and to determine stationary solutions as a function of the physical parameters. He considered the stability of these solutions by adding specific perturbations to the double-gyre stationary solutions, and monitoring their evolution by time integration. He found that below a certain critical Reynolds number, which was different for no-slip and slip boundary conditions, only stationary flow appears. Above criticality, the temporal behavior contains more and more time scales as the Reynolds number is increased. Far above the critical value, the flow shows much variability with dominant signals on an intermonthly (160 days) and an interannual time scale (1600 days).

Mathematical tools based on the theory of dynamical systems have been applied to climate models of relatively small degrees of freedom. For example, Legras and Ghil (1985) studied the physics of intraseasonal variability of the atmosphere in this way, whereas Dijkstra and Neelin (1995) considered interannual variability in the tropics. In both studies, successive bifurcation points were detected. A few years ago, the methodology was extended so that dynamical systems with a large number of degrees of freedom could be handled as well (Dijkstra *et al.*, 1995). Using these tools, the successive bifurcations of the double-gyre wind-driven circulation were studied within an equivalent barotropic shallow-water model (Speich *et al.*, 1995). It was found that interannual variability arises due to an oscillatory instability of the double-gyre circulation. The dominant bifurcation structure within this model is an imperfect pitchfork bifurcation (Section 2.3). Each of the stable branches of solutions is destabilized by an oscillatory mode at large enough forcing. Jiang *et al.* (1995) explored the larger forcing regime, and found all kinds of complicated temporal behavior. However, to

understand the physical mechanisms of the oscillatory modes proved to be difficult within the results of the shallow-water model.

In Jiang *et al.* (1995), a simpler truncated quasi-geostrophic model was shown to exhibit similar behavior as the shallow-water model. Motivated by this result, the appearance of internal variability is explored here within the two-layer quasi-geostrophic model, and within its reduction, the barotropic model. A systematic study of the possible stationary solutions of the quasi-geostrophic barotropic vorticity equation was initiated by Cessi and Ierley (1995). They found that the symmetry of the double-gyre flow is spontaneously broken at a pitchfork bifurcation when the forcing is high enough. They presented regime diagrams, showing the areas in parameter space where multiple stable stationary solutions occur. Ierley and Sheremet (1995) performed a similar study for barotropic flows with single-gyre forcing, and also discovered parameter regimes where multiple stationary solutions exist. However, the temporal variability arising through Hopf bifurcations was not considered by these authors.

In this chapter, the first stages of a systematic study of the internal variability of the double-gyre wind-driven circulation are presented. The stationary solutions for the flow are calculated as a function of the Reynolds number Re, using the two-layer quasi-geostrophic model in its standard, symmetric set-up (Section 3.2). Furthermore, sufficient conditions for their instability are determined. In particular, the determination of Hopf bifurcations and the corresponding time scales of internal variability which are introduced through these bifurcations are discussed (Section 3.3). This perfectly symmetric system is not only interesting to study as a prototype for the large-scale gyre systems in the ocean, but it also provides a starting-point for further studies of less idealized, non-symmetric cases. To assess the importance of the possibility of baroclinic instabilities, the results for the two-layer model are compared to those obtained with a barotropic model configuration, otherwise using the same parameter setting (Section 3.4). In Section 3.5, the symmetry-breaking mechanism through which multiple equilibria arise is explained, which is followed by a discussion of the results (Section 3.6).

3.2 Stationary solutions for the two-layer model

First, the possible stationary solutions and their spatial patterns are considered. The relative strength of the lateral friction, measured by the Reynolds number $Re = UL/A_H$, is used as the control parameter, and other parameter values are as in Table 2.1. Re is varied between 15 and 50, so the Munk boundary layer thickness $\delta_M = (Re\beta)^{-1/3}$ ranges from 0.027 to 0.041 ($\delta_M^* \in [27, 41]\ km$). The dimensionless inertial boundary layer thickness is $\delta_I = \beta^{-1/2} = 0.032$, or in dimensional units $\delta_I^* = 32\ km$.

In Figure 3.1a, the computed bifurcation diagram for the wind-driven flow in the two-layer model is presented as a function of the Reynolds number. A detail between $Re = 36$ and $Re = 37$ shown in Figure 3.1b. On the vertical axis, a measure of the stationary solutions is plotted, which is chosen such that individual branches of stationary solutions can be distinguished. Here, the value of the upper layer stream-

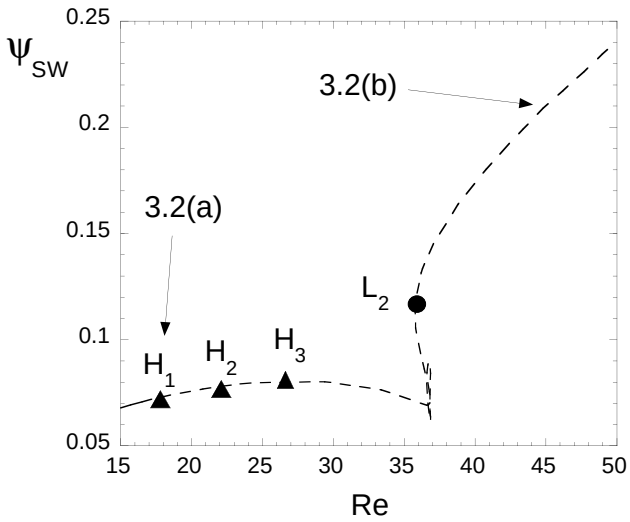

(a)

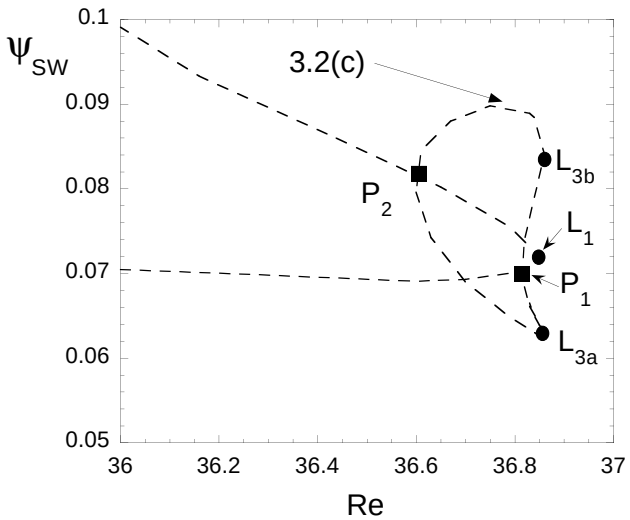

(b)

Figure 3.1: *(a) Bifurcation diagram for the wind-driven flow in the two-layer model as a function of Re. (b) Detail of (a) for the interval* $Re \in [36, 37]$. *Standard values of the parameters are used (see Table 2.1). On the vertical axis,* Ψ_1 *at a grid point in the southwest of the domain is plotted as the measure* ψ_{SW} *of the stationary solutions. Drawn (dashed) branches indicate stable (unstable) stationary solutions and bifurcation points are indicated by markers. Arrows marked 3.2(a)-(c) point to locations for which flow patterns are presented in Fig. 3.2 as a contour plot of the upper layer streamfunction* Ψ_1.

function Ψ_1 at a grid point in the southwest of the domain is used, denoted by ψ_{SW}. This measure will be used in all the bifurcation diagrams presented in this thesis. Drawn (dashed) branches indicate (un-)stable stationary solutions, bifurcation points are indicated by different markers. The arrows marked 3.2(a)-(c) in the diagram point to locations for which flow patterns are presented as a contour plot of the upper layer streamfunction Ψ_1 in Figure 3.2.

For low values of Re (large lateral friction), a unique branch of stationary solutions is found to exist. An example of a stationary solution on this branch (at $Re = 17$) is shown in Figure 3.2a. The stationary flow is directed along the lines of constant Ψ_1, the streamlines. Positive (negative) values of Ψ_1 denote (anti-)clockwise flows. The grid point that is used to define ψ_{SW} is marked by an asterisk in Figure 3.2a. The streamfunction is anti-symmetric with respect to the mid-axis of the basin, as expected from the symmetry properties of the model (Section 2.3). The separation point of the jet lies exactly at the zero wind stress curl line ($y = 0.5$). Since the zonal velocity (and therefore the eastward jet) is symmetric, this type of solutions will be referred to as a symmetric double gyre-flow. The stationary solution displays the characteristic westward intensification of the gyres caused by the variation of the Coriolis force with latitude and the north-south asymmetry induced by non-linearities (Section 1.1.1). As a result, pronounced western boundary currents and a free mid-ocean jet appear.

Three Hopf bifurcation points (marked H_1, H_2 and H_3 in Fig. 3.1a), occur on the symmetric branch at quite small values of Re ($Re = 17.2$, $Re = 21.0$ and $Re = 26.5$, respectively). At each of these points the flow becomes unstable to a specific oscillatory mode, determined by the eigenvectors of the linear stability problem. So, the double-gyre flow is linearly stable for high lateral friction only ($A_H > 930\ m^2/s$). The variability introduced by the modes associated with these Hopf bifurcations will be discussed in the next section. First, the other stationary solution branches in the bifurcation diagram are discussed.

Two limit points are detected on the symmetric branch. The first limit point is found at $Re = 36.85$ (L_1 in Fig. 3.1b). A second limit point is found at $Re = 35.7$, and is marked L_2. Between these two limit points, multiple symmetric solutions exist for one value of the lateral friction coefficient. The stationary solution at $Re = 45$ is shown in Figure 3.2b. Its two gyres are almost symmetric in east-west direction, and the transport of the flow is an order of magnitude larger than predicted by Sverdrup theory (recall that the scale for U is chosen such that Ψ_1 is $\mathcal{O}(1)$ for a flow primarily in Sverdrup balance). This increase in transport, which is also reflected in the value of ψ_{SW} along the branch, is indicative of changes in the dominant balances in the vorticity equation, which will be discussed in Section 3.2.1.

Two symmetry-breaking pitchfork bifurcations are also encountered along the symmetric branch, at $Re = 36.82$ and $Re = 36.60$. At the pitchfork bifurcation P_1 (Fig. 3.1b), two asymmetric branches come into existence. The solutions on these two branches are exact mirror-images. At the second pitchfork bifurcation, P_2, again two asymmetric branches arise. The asymmetric solutions originating from P_1 and P_2 are connected by two limit points, marked L_{3a} and L_{3b} (Fig. 3.1b). As a result of this connection, asymmetric solutions exist only over a small range in Re, between

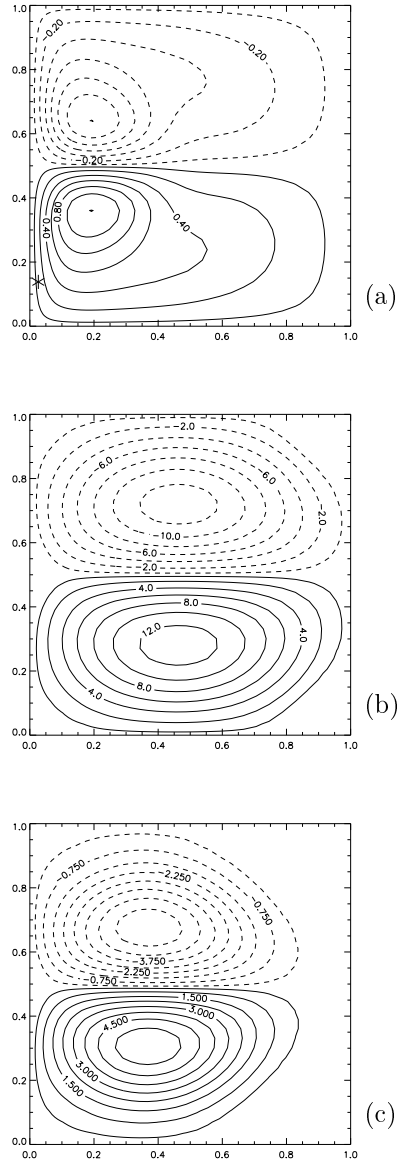

Figure 3.2: *Contour plots of Ψ_1 at the selected points marked 3.2(a)-(c) in Fig. 3.1: (a) symmetric solution at $Re = 17$ (contour interval=0.2); (b) symmetric solution at $Re = 45$ (contour interval=2.0); (c) asymmetric solution at $Re = 36.8$ (contour interval=0.75). In (c), the mid-ocean jet separates slightly south of the zero wind stress curl line, at $y = 0.48$. The grid point that is used to define ψ_{SW} is marked by an asterisk in (a). Note that Ψ_1 is scaled with $UL = 1.6 \cdot 10^4\ m^2/s$.*

$Re_{P_2} = 36.60$ and Re_{L_3}=36.86. The solutions on these asymmetric branches have either a stronger subtropical or subpolar gyre, and a midlatitude jet that separates south or north of the mid-axis of the basin, respectively (ψ_{SW} is larger or smaller). As an example, the solution at $Re = 36.8$ on the upper branch in Fig. 3.1a is shown in Figure 3.2c. Its separation point is located at $y = 0.48$, and the subpolar gyre is slightly stronger than the subtropical gyre. However, the asymmetry of the solution is not very pronounced this close to P_1.

3.2.1 Vorticity balance

Between the two limit points L_1 and L_2, the symmetric solution branch rescales over a small interval in Re. Along the branch, the spatial pattern of the symmetric solution changes significantly (compare Figs. 3.2a and b). These changes in the solution are indicative of a change in the dominant quasi-geostrophic vorticity balance. In Figure 3.3, different terms in the vorticity balance are plotted for the stationary solution shown in Figure 3.2a ($Re = 17$). For this value of Re, the Munk boundary layer thickness is $\delta_M = 0.039$ and slightly larger than $\delta_I = 0.032$. Only the vorticity balance in the upper layer is considered, since the lower layer is motionless. Plotted are the input of vorticity by the wind INP, the advection of planetary vorticity $BETA$, the advection of relative vorticity ADV and the dissipation $DISS$ for a stationary solution $\Psi = (Z_1, \Psi_1, Z_2, \Psi_2)$, defined as

$$\begin{aligned} INP &= \alpha_\tau \frac{\partial \tau^x}{\partial y} \qquad & BETA &= \beta \frac{\partial \Psi_1}{\partial x} \\ ADV &= \mathbf{U_1} \cdot \nabla Z_1 \qquad & DISS &= -\frac{1}{Re} \nabla^2 Z_1 \end{aligned} \tag{3.1}$$

with $\mathbf{U_1} = (-\partial\Psi_1/\partial y, \partial\Psi_1/\partial x)$. The vorticity balance in the upper layer (equation (2.2a)) yields

$$BETA + ADV + STR + DISS + INP = 0.0$$

The stretching term STR, defined as $-F_1 \mathbf{U_1} \cdot \nabla(\Psi_1 - \Psi_2)$, is not shown since it is zero for flows with $\Psi_2 = 0$. Note that the contour interval in Figure 3.3 is $4 \cdot 10^2$ for absolute values lower than $2 \cdot 10^3$, and $2 \cdot 10^3$ otherwise. Three different regions can be indicated, where different vorticity balances hold. For $x > 0.5$, the eastern half of the basin, the input of vorticity INP is mainly balanced by the advection of planetary vorticity $BETA$ (Figs. 3.3a and b), so there the flow is primarily in Sverdrup balance. More to the west, for $x \in [0.1, 0.5]$, an approximate balance exists between the advection of planetary and of relative vorticity. The contribution of the dissipation is of lesser importance. Finally, in the western boundary layer, $BETA$ and ADV (Figs. 3.3b and c) are compensated by the dissipation $DISS$ (Fig. 3.3d).

For the solution at $Re = 45$, shown in Figure 3.2b, the vorticity balance is very different (Fig. 3.4). For this value of Re, $\delta_M = 0.028$, so smaller than δ_I. There is no region in the basin where the flow is in Sverdrup balance. The advection of planetary vorticity and of relative vorticity approximately balance over most of the

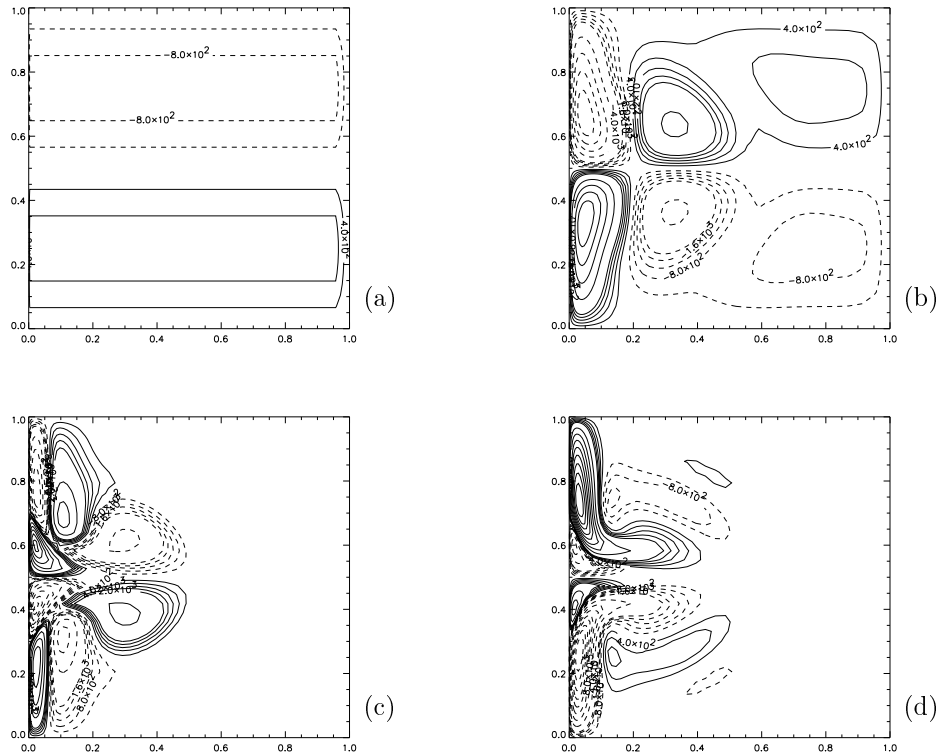

Figure 3.3: *Various terms in the upper layer vorticity balance for the stationary solution at* $Re = 17$ *in Fig. 3.2a: (a) the input of vorticity by the wind* INP*; (b) the advection of planetary vorticity* $BETA$*; (c) the advection of relative vorticity* ADV*; (d) the dissipation of vorticity* $DISS$ *(see (3.1) for definitions). The contour interval is* $4 \cdot 10^2$ *for absolute values lower than* $2 \cdot 10^3$*, and* $2 \cdot 10^3$ *otherwise. The stretching term* STR *is not shown, since it is zero for stationary flows with a motionless second layer.*

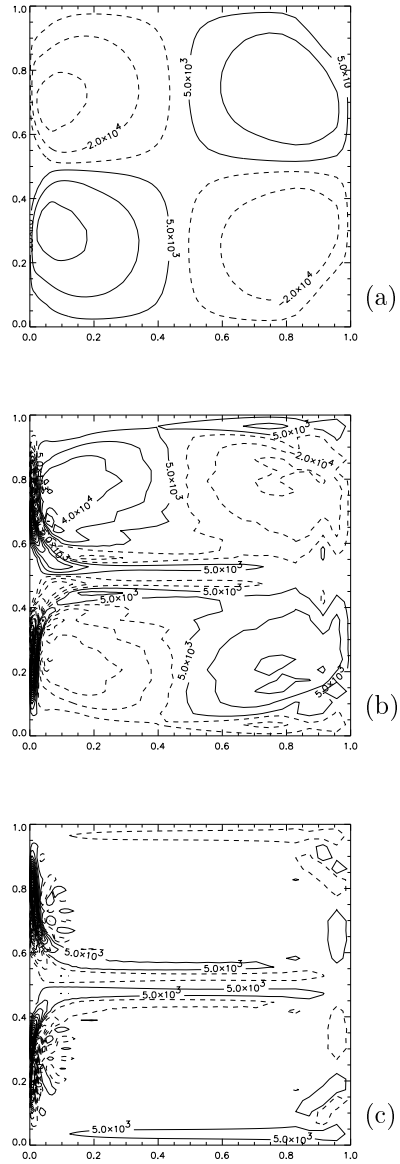

Figure 3.4: *Various terms in the upper layer vorticity balance for the stationary solution at* $Re = 45$ *in Fig. 3.2b: (a) the advection of planetary vorticity* $BETA$*; (b) the advection of relative vorticity* ADV*; (c) the dissipation of vorticity* $DISS$ *(contour interval is* $3.0 \cdot 10^4$*). The input of vorticity by the wind* INP *is the same as in Fig. 3.3a, the stretching term* STR *is again zero and not shown.*

basin ($BETA \simeq -ADV$, see Figs. 3.4a-b), except very close to the western boundary ($x < 0.05$) and in a narrow strip around the mid-axis of the basin. There, the dominant balance is between the advection of relative vorticity and the dissipation, while the advection of planetary vorticity is negligible.

The rescaling of the solutions between the two limit points is a manifestation of the transition towards a regime where the flow is inertially dominated. This type of stationary solutions is characteristic for perfectly symmetric flows, and they were also found by Cessi and Ierley (1995) in a barotropic quasi-geostrophic model. The large transports are a result of the fact that the stationary flows in the quasi-geostrophic model are perfectly symmetric with respect to the mid-axis of the basin. As a consequence, there is no transport of vorticity across the zero wind stress curl line so that the input of vorticity by the wind stress needs to be dissipated in each gyre separately, as is the case in single-gyre flows (Ierley and Sheremet, 1995). For low Re, this input of vorticity is dissipated in the Munk boundary layer. This Munk boundary layer becomes thinner as Re is increased, while the advection increases. As a consequence, the input of vorticity by the wind can no longer be dissipated in the viscous boundary layer alone. The flow then spins up until a new balance is reached, with large velocities over the whole basin to establish the large vorticity gradients needed for dissipating the input of vorticity. Such a transition to 'inertial runaway' solutions is unavoidable when δ_I/δ_M becomes sufficiently large (Primeau, 1998b). Solutions that are non-symmetric with respect to the wind forcing are able to transport vorticity across the line of zero wind stress curl. As a result, the input of vorticity in each half of the basin is partly balanced by the advection of vorticity across the zero wind stress curl line, so that there is no need for spinning up to a solution with much larger transports than predicted by Sverdrup theory as δ_M is decreased. This also holds for stationary solutions of the circulation in wind-driven shallow-water models, which do not have the internal symmetry the quasi-geostrophic models have (Speich *et al.*, 1995). Transient flows in a symmetric quasi-geostrophic model will not display such high transports either, as vorticity will be advected across the zero wind stress curl line. In Chapter 4, examples of this will be shown, when stationary solutions and the mean states of time integrations are compared (Fig. 4.1).

3.3 Characteristics of the modes of variability

The wind-driven double-gyre flow is destabilized by oscillatory modes at the Hopf bifurcations H_1, H_2 and H_3 in Figure 3.1a. Their characteristics, like their spatial pattern and time scale, can be determined from the solution of the linear stability problem (Section 2.2.3). The wind-driven flow is first destabilized at H_1 ($Re = 17.2$). The stationary solution for this Reynolds number was already shown in Figure 3.2a. The oscillatory mode that destabilizes this stationary flow has a dimensional period $p^* = 2\pi L/\nu U$ of 4.7 months (its dimensionless frequency $\nu = 32.4$). Its spatial pattern is shown in Figure 3.5, at four phases of the oscillation 1/8 period apart, for both the upper and lower layer. Note that the amplitude of the mode is arbitrary, but that the ratio of the amplitude in the upper and lower layer can be obtained from the linear

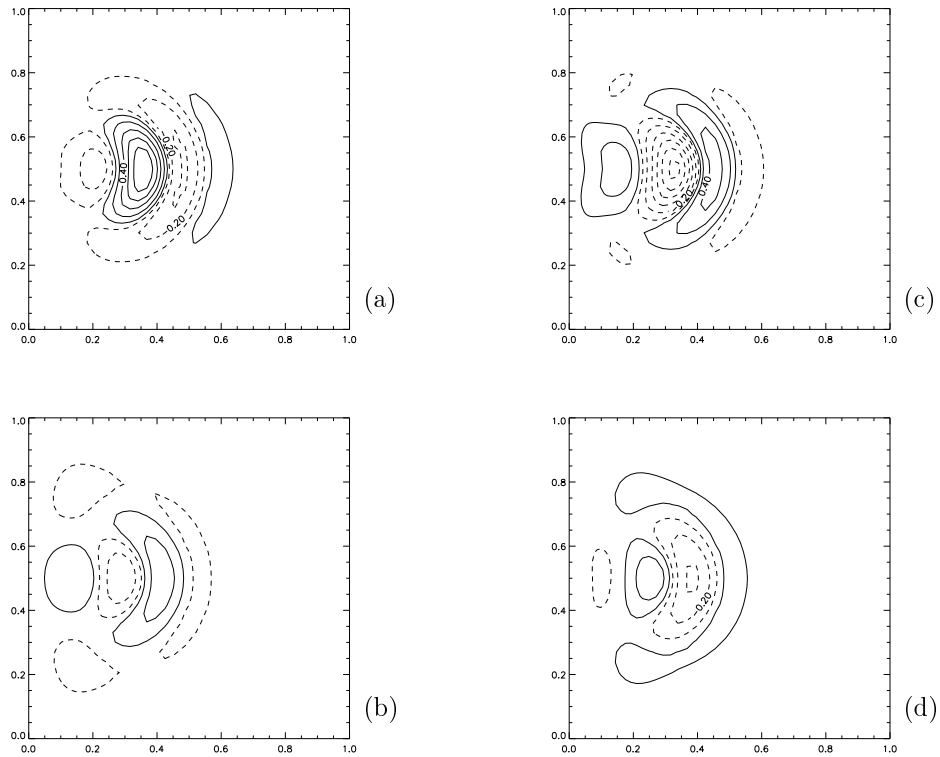

Figure 3.5: *Contour plot of the streamfunction of the mode that destabilizes the double-gyre flow at Hopf bifurcation H_1 in Fig. 3.1a, for the upper and lower layer (upper and lower panels), at four phases of the oscillation, 1/8 period apart: (a-b) $\nu t = 0.0$; (c-d) $\nu t = 0.125$; (e-f) $\nu t = 0.25$; (g-h) $\nu t = 0.375$. Since the amplitude of the mode is arbitrary, all plots are scaled with the maximum of (a), the perturbation in the upper layer at phase $\nu t = 0.0$. The contour interval is 0.2.*

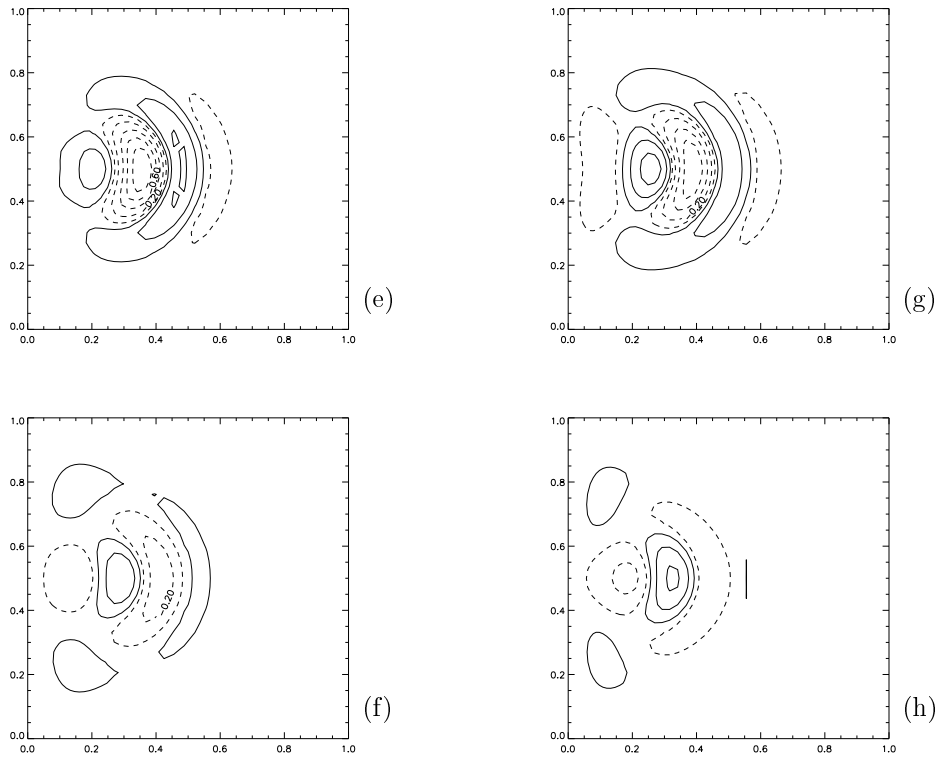

Fig. 3.5, continued.

stability analysis. Hence, each field is scaled with the maximum of the upper layer perturbation streamfunction ϕ_1 at phase $\nu t = 0.0$ (Fig. 3.5a). The spatial pattern at $\nu t = 0.5$, which would be the next panel after Figure 3.5g-h, has the same spatial pattern as the one for $\nu t = 0.0$ (Fig. 3.5a-b), but with a minus-sign.

First note that, although the stationary solution has a motionless second layer, the mode that destabilizes the double-gyre flow does show a response in both layers. The zonal velocity of the mode is anti-symmetric with respect to $y = 0.5$ (the streamfunction is symmetric). In the upper layer, the mode is localized within the $x - y$ region $[0.0, 0.7] \times [0.2, 0.8]$, and in the lower layer within $[0.0, 0.7] \times [0.1, 0.9]$. The perturbation structure displays 'banana-shaped' patterns near the zonal jet. There is a phase difference between the response in the two layers: the lower layer leads the upper layer by approximately 1/4 period. So, the mode tilts against the direction of the stationary flow, which demonstrates the baroclinic nature of the mode (Pedlosky, 1987). When added to the basic stationary flow (Fig. 3.2a), the mode causes the jet to meander. The mode propagates eastward at a speed of approximately 2 cm/s, which is much slower than the speed of the midlatitude jet of the stationary solution (about 22 cm/s). The zonal wavelength of the disturbance is approximately 250 km, which is much larger than the Rossby deformation radius of the two-layer model ($R_D = 63$ km).

A second Hopf bifurcation (H_2 in Fig. 3.1a) occurs at $Re = 21.0$. The period of this oscillation is $p^* = 8.5$ months ($\nu = 17.7$), and the destabilizing perturbation is shown in Figure 3.6, again at four phases 1/8 period apart. The basic stationary flow has not changed much compared to Figure 3.2a and is therefore not shown. The zonal velocity of this mode is symmetric with respect to $y = 0.5$, in contrast to the mode at H_1. The mode rotates (anti-)clockwise in the region below (above) the symmetry axis. It fills the basin in north-south direction: it is localized in the $x - y$ region $[0.0, 0.65] \times [0.1, 0.9]$ and $[0.0, 0.6] \times [0.0, 1.0]$ for the upper and lower layer, respectively. The spatial pattern of this mode results in local and temporary weakening or strengthening of the midlatitude jet. Again, there is a phase difference between the upper and lower layer response, characteristic of baroclinic instability. In this case, the lower layer leads by 1/2 cycle.

On the symmetric branch, a third Hopf bifurcation point is detected at $Re = 26.5^\dagger$. Its time scale p^* is 6.0 months at criticality, and its spatial pattern is shown in Figure 3.7. As for the mode associated with H_1, the perturbation streamfunction of this mode is symmetric with respect to the mid-axis of the domain, so that it also causes meandering of the midlatitude jet. However, the typical zonal wavelength of the disturbance is 450 km and thus larger than that of the mode shown in Figure 3.5. It propagates eastward at a speed of 3 cm/s, which is again considerably slower than the velocity of the jet of the stationary solution at this Reynolds number, which is about 32 cm/s. The phase difference between the two layers is slightly less than half a cycle, with the lower layer leading the upper layer.

Based on Figure 3.1, the following time-dependent behavior of the double-gyre flow is expected. For values of Re below H_1, the symmetric double-gyre solution is

†This third Hopf bifurcation and its associated mode were not discussed in Dijkstra and Katsman (1997)

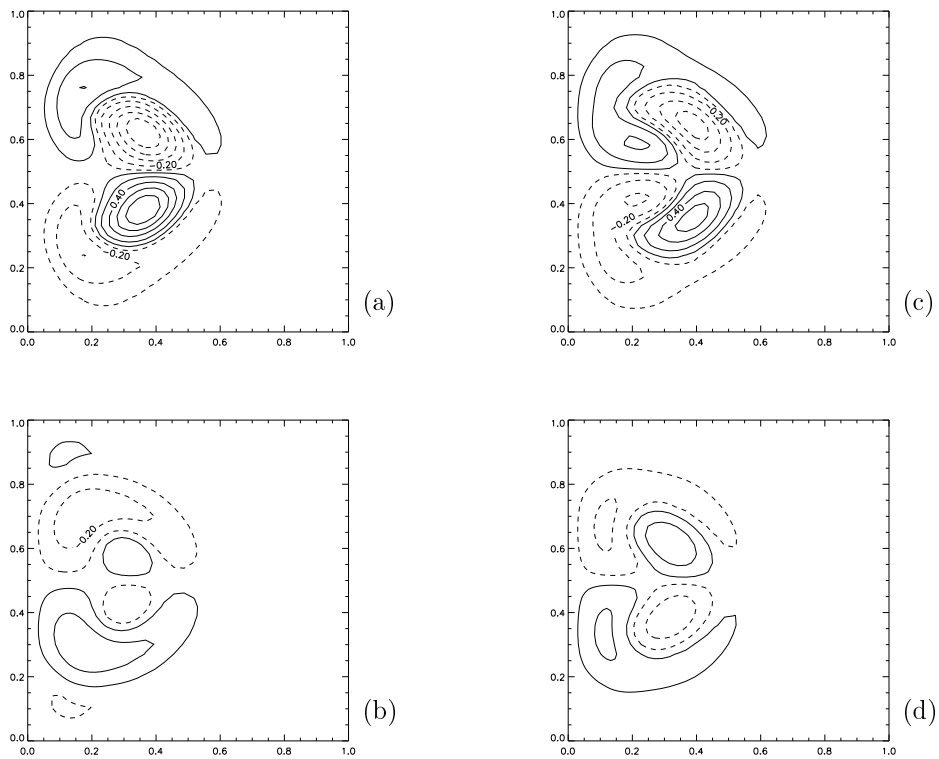

Figure 3.6: *As in Fig. 3.5, but for the mode that destabilizes the flow at the bifurcation point H_2 in Fig. 3.1a. (a-b) $\nu t = 0.0$; (c-d) $\nu t = 0.125$; (e-f) $\nu t = 0.25$; (g-h) $\nu t = 0.375$.*

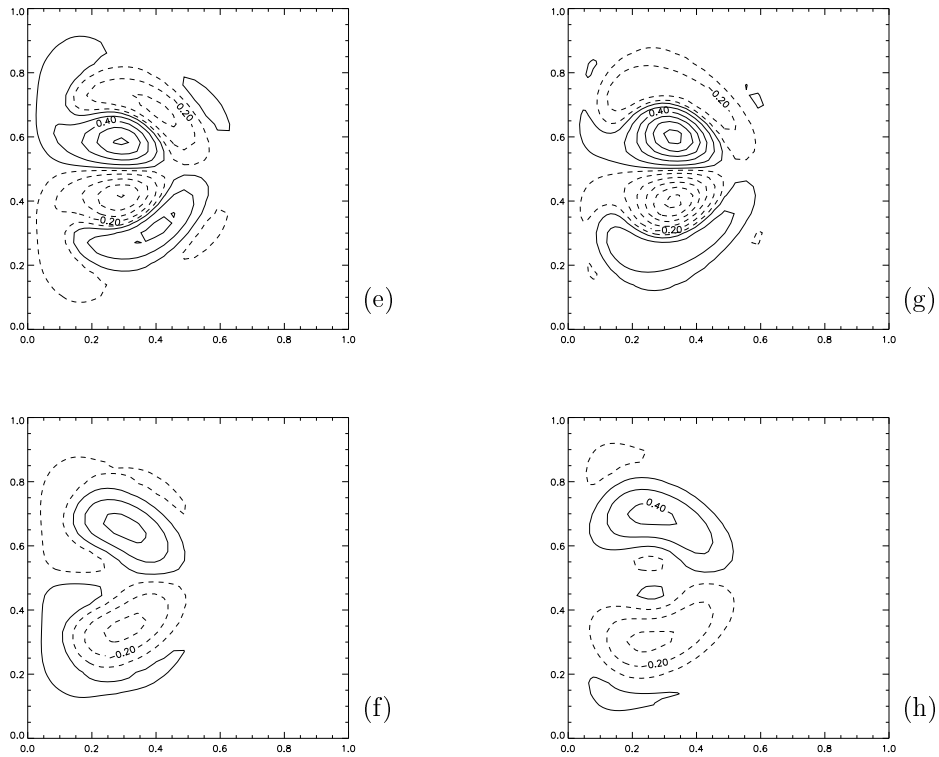

Fig. 3.6, continued.

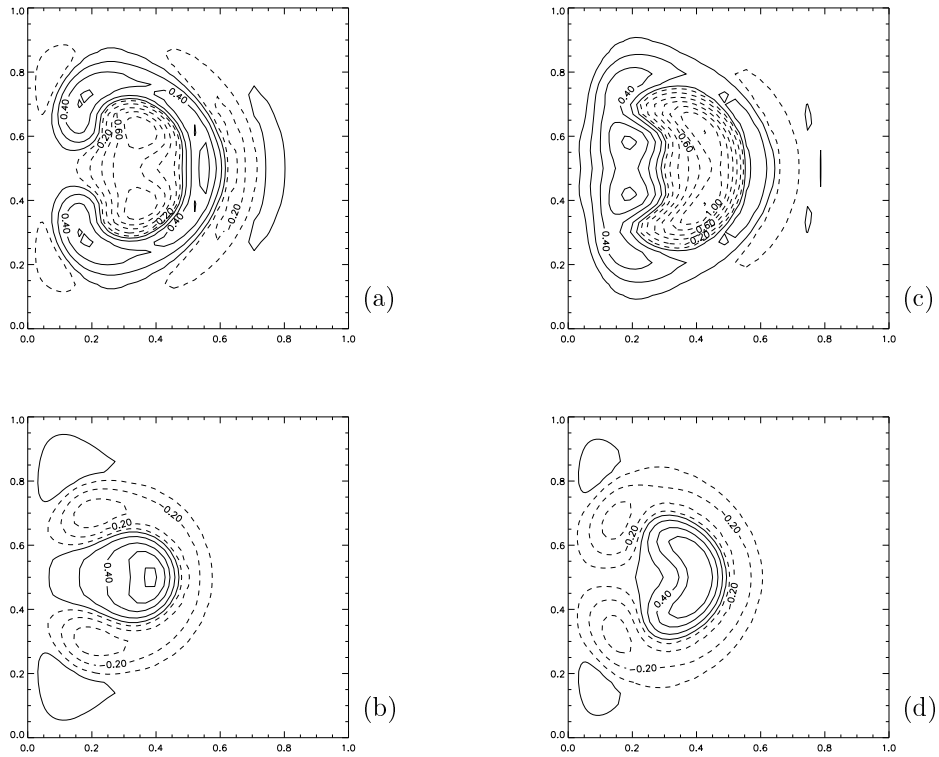

Figure 3.7: *As in Figs. 3.5 and 3.6, but for the mode that destabilizes the flow at the bifurcation point H_3 in Fig. 3.1a. (a-b) $\nu t = 0.0$; (c-d) $\nu t = 0.125$; (e-f) $\nu t = 0.25$; (g-h) $\nu t = 0.375$.*

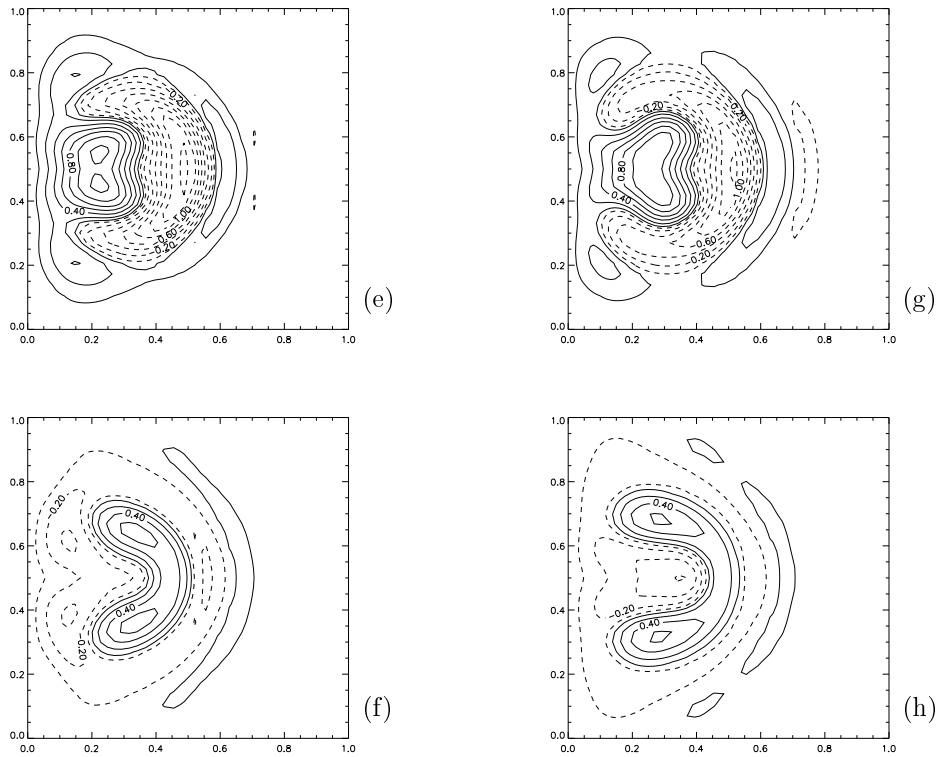

Fig. 3.7, continued.

linearly stable. Hence, this solution will be approached with a time-stepping code. For values of Re slightly above $Re_{H_1} = 17.2$, it is expected that a periodic orbit is approached, which has the characteristics of the mode associated with H_1 (Fig. 3.5). That is, we expect a double-gyre solution with an eastward jet that meanders on an intermonthly time scale and with a spatial scale of about 250 km. The time-dependent behavior at higher Re can not be predicted from the results presented here, since the stability from the periodic orbit associated with H_1 is not analyzed (see also Section 2.3). Numerical simulations for time-dependent flows in the two-layer model will be discussed in Chapters 4 and 6.

3.3.1 Energy analysis

To determine the dominant instability process responsible for the growth of the modes, the mechanical energy balance can be analyzed. When the instability mechanism is purely barotropic, energy is transferred from the stationary flow to the mode through the kinetic energy, whereas the baroclinic path is through the available potential energy. The energy equation for perturbations on the stationary flow is derived by multiplying the vorticity equations describing the evolution of the perturbations (2.5) by $-D_n\phi_n/D$ for each layer n, summing over the two layers and finally integrating over the domain (Pedlosky, 1987). The change in the energy E of the mode is given by the barotropic energy conversions due to the Reynolds stresses in each layer (BT_1 and BT_2), the conversion of available potential energy BC and the dissipation D:

$$\frac{\partial E}{\partial t} \equiv \sigma E = BT_1 + BT_2 + BC - D \tag{3.2}$$

where

$$BT_1 = d_1 \iint \phi_1 \left[\mathbf{U_1} \cdot \nabla\eta_1 + \mathbf{u_1'} \cdot \nabla Z_1\right] dx\, dy \tag{3.3a}$$

$$BT_2 = d_2 \iint \phi_2 \left[\mathbf{U_2} \cdot \nabla\eta_2 + \mathbf{u_2'} \cdot \nabla Z_2\right] dx\, dy \tag{3.3b}$$

$$\begin{aligned} BC &= -F_0 \iint \phi_1 \left[\mathbf{U_1} \cdot \nabla(\phi_1 - \phi_2) + \mathbf{u_1'} \cdot \nabla(\Psi_1 - \Psi_2)\right] dx\, dy \\ &\quad + F_0 \iint \phi_2 \left[\mathbf{U_2} \cdot \nabla(\phi_1 - \phi_2) + \mathbf{u_2'} \cdot \nabla(\Psi_1 - \Psi_2)\right] dx\, dy \end{aligned} \tag{3.3c}$$

$$-D = -\frac{d_1}{Re} \iint \phi_1 \nabla^4 \phi_1 \; dx\, dy - \frac{d_2}{Re} \iint \phi_2 \nabla^4 \phi_2 \; dx\, dy \tag{3.3d}$$

with $\mathbf{U_n} = (-\partial\Psi_n/\partial y, \partial\Psi_n/\partial x)$, $\mathbf{u_n'} = (-\partial\phi_n/\partial y, \partial\phi_n/\partial x)$, $d_n = D_n/D$ and $F_0 = f_0^2 L^2/g'D$. The net energy production term $\partial E/\partial t$ is calculated by averaging (3.2) over the oscillation period. Since the second layer is motionless for the stationary flows considered here, BT_2 is always zero. In Figure 3.8, the other terms in (3.3) are plotted as a function of the Reynolds number, in the neighborhood of the three bifurcation points. On the horizontal axis, the Reynolds number scaled with the critical Reynolds number for that specific mode is plotted. The scale on the vertical axis is in arbitrary units, since the amplitude of the modes is undetermined.

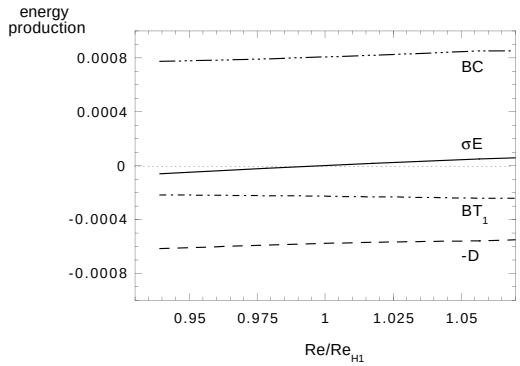

(a)

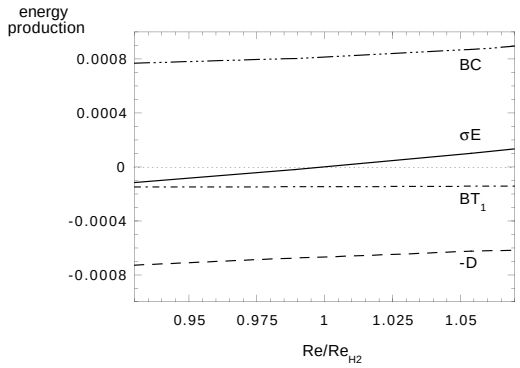

(b)

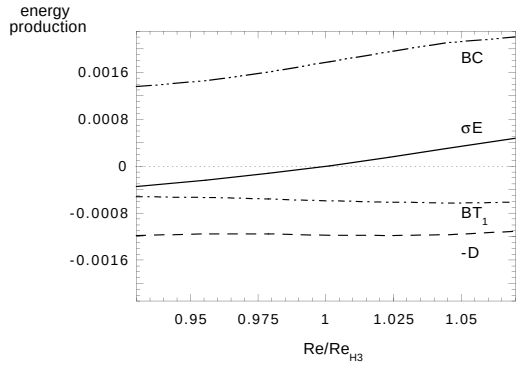

(c)

Figure 3.8: *Energy production terms averaged over a complete oscillation, for (a) the mode shown in Fig. 3.5; (b) the mode shown in Fig. 3.6 and (c) the mode shown in Fig. 3.7. Plotted are the barotropic energy conversion in the first layer* BT_1*, the baroclinic energy conversion* BC*, the dissipation* $-D$ *and the net production term* σE *defined in (3.2) and (3.3). The Reynolds number on the horizontal axis is scaled with the critical Reynolds number for that specific mode. The scale on the vertical axis is in arbitrary units, since the amplitude of the modes is unknown.*

Figure 3.8a illustrates a classical baroclinic instability process. BC is the largest production term for the mode shown in Figure 3.5, whereas the barotropic production due to the Reynolds stresses is negative. That is, the mode loses energy to the stationary solution through the barotropic energy conversion BT_1. This is in agreement with the analytical results derived for the barotropic energy transfer by Reynolds stresses in zonal jets (Pedlosky, 1987, pages 502-503). When the perturbation is tilted in the direction of the zonal flow, as is the case here, it acts to accelerate the jet and loses energy to the basic flow through the Reynolds stresses. To gain additional insight in the destabilization process, the terms (3.3a) and (3.3c) can both be split into two parts. The first part describes the energy production due to the advection of perturbation properties by the large-scale flow, whereas the second part describes the energy production that results from the advection of the properties of the large-scale flow by the perturbation. For both terms, the second part is at least two orders of magnitude smaller than the first part. That is, the main source of energy for the mode is the second part of (3.3c): the advection of anomalous layer thickness $\tilde{h}_1$ (which is proportional to $\phi_1 - \phi_2$) by the large-scale circulation. As Re is increased, the perturbation hardly changes, but the large-scale flow accelerates. As a consequence, the magnitude of both BT_1 and BC increases. Meanwhile, the dissipation (which is proportional to $1/Re$) decreases so that $Re/Re_{H_1} > 1$ the baroclinic energy production BC is able to overcome the dissipation D and the loss of energy through BT_1.

A similar picture is derived for the energy production of the modes associated with H_2 and H_3 (Figs. 3.8b and c). Both modes gain energy through the conversion of available potential energy BC, which increases with increasing Re, and lose energy through the barotropic energy conversion term BT_1. Again, the energy production due to the advection of the properties of the large-scale flow by the perturbation is much smaller than the advection of perturbation properties by the large-scale flow.

3.4 The baroclinic versus the barotropic model

To assess the impact of the presence of a second model layer, a similar analysis of the solution structure and stability characteristics as presented in Sections 3.2 and 3.3 was carried out for a barotropic version of the model. The same standard parameter set is used, except that now $F_1 = F_2 = 0$. This barotropic model version is similar to the model used by Cessi and Ierley (1995), so the stationary solutions can be compared to their results. Moreover, by applying the continuation technique to vary F_1 and F_2, the results of the barotropic and the baroclinic model can be connected.

3.4.1 Results for the barotropic model

The basic bifurcation diagram for $F_1 = F_2 = 0$ is shown in Figure 3.9a, again as a plot of Re versus the measure for the stationary solution ψ_{SW}. Drawn (dash-dotted) branches indicate (un-)stable stationary solutions, and bifurcation points are indicated by markers. The Reynolds number is varied between 20 and 100, so the investigated range in δ_M is from 0.022 to 0.037 ($\delta_M^* \in [22, 37]\ km$).

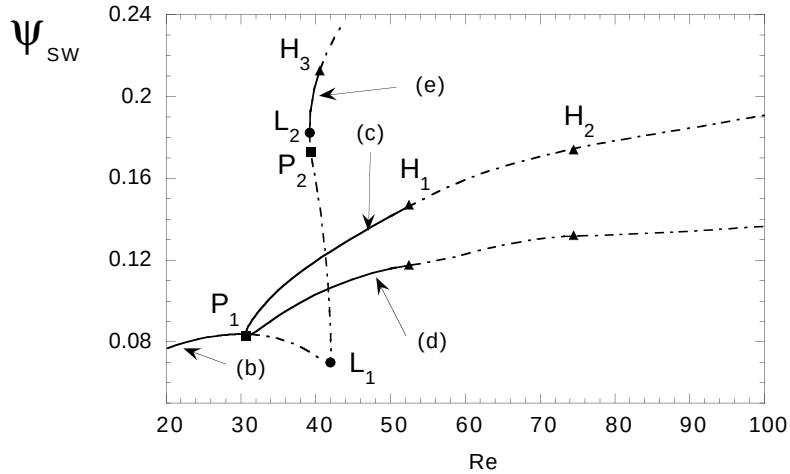

(a)

Figure 3.9: *(a) Bifurcation diagram as a function of Re for the barotropic model ($F_1 = F_2 = 0$ and values of the other parameters as in Table 2.1). On the vertical axis, the same measure ψ_{SW} of the stationary solutions as plotted in Fig. 3.1 is used. Drawn (dash-dotted) branches indicate stable (unstable) stationary solutions and bifurcation points are indicated by markers. (b-e) Contour plots of the barotropic streamfunction ψ at selected points (marked (b)-(e)) on the branches in (a). Contours are with respect to the absolute maximum of the field (from Dijkstra and Katsman, 1997).*

As for the two-layer model, one symmetric solution branch exists for low Re. As an example, the stationary solution for $Re = 20$ is shown in Figure 3.9b. At $Re = 31$, the double-gyre flow becomes unstable through a pitchfork bifurcation P_1 (Fig. 3.9a), and two asymmetric branches emerge. So, the barotropic symmetric solutions are stable over a much larger regime in Re than the baroclinic ones (recall that the critical value for instability for the two-layer model is $Re = 17.2$). In contrast to the results for the two-layer model, no Hopf bifurcations are found on the symmetric branch before encountering the pitchfork bifurcation, which is consistent with the conclusion drawn from the energy analysis in that the modes shown in Figures 3.5, 3.6 and 3.7 are pure baroclinic instabilities (Section 3.3.1).

First, consider the two asymmetric solution branches that bifurcate from the symmetric solution branch at P_1. The solution on the branch with larger ψ_{SW} (Fig. 3.9c) has a stronger subtropical gyre, and a southeastward flowing jet that separates south of the zero wind stress curl line. Its mirror-image is found on the branch with smaller ψ_{SW} (Fig. 3.9d). Both the symmetric and the asymmetric solutions are similar to those found in Cessi and Ierley (1995). The asymmetric solutions destabilize through two Hopf bifurcations (H_1 and H_2 in Fig. 3.9a) at $Re = 52$ and $Re = 74$, respectively. Hence, for the barotropic model, there is a considerable interval in Re for which the asymmetric solutions are (linearly) stable, whereas for the two-layer model all asym-

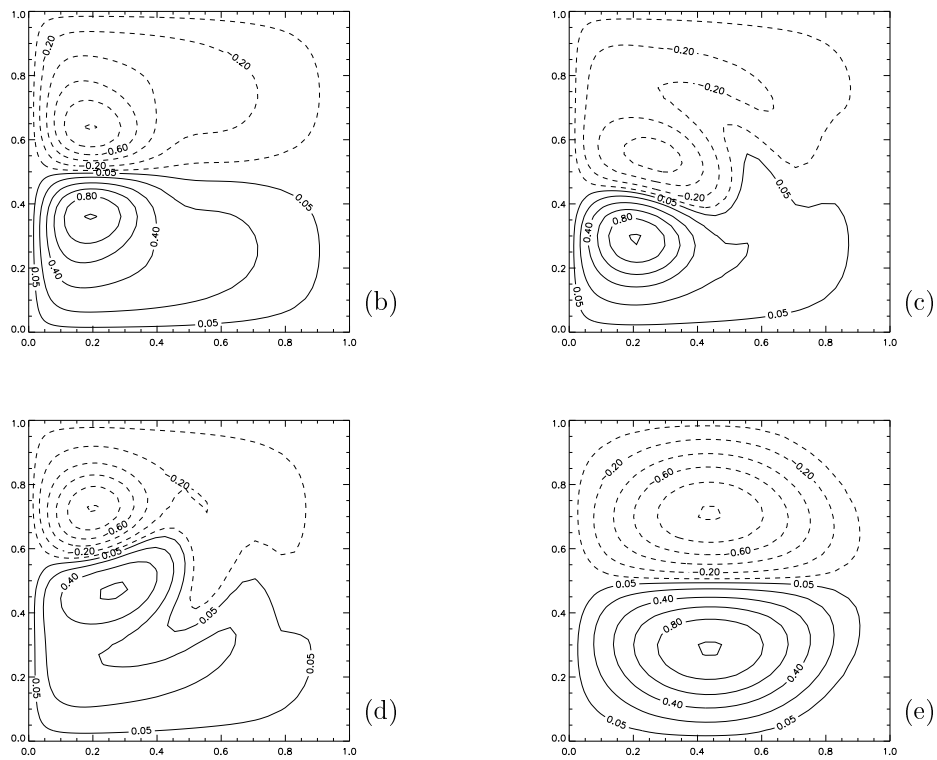

Fig. 3.9, continued.

metric solutions are unstable. Second, consider the symmetric solution branch after it is destabilized at P_1. The symmetric solution destabilizes once more through a Hopf bifurcation at $Re = 40.8$ (not shown in Fig. 3.9a), very near L_1. Due to the change in dominant balances in the vorticity equation as discussed in Section 3.2.1, the solution rescales between L_1 and L_2. A reverse Hopf bifurcation, where a complex pair of eigenvalues moves back to the left half of the complex plane, occurs at $Re = 40.2$ (not shown). A second pitchfork bifurcation, P_2, occurs very near L_2 at $Re = 39.39$. Here, an additional set of asymmetric solutions appears, similar to those found in Cessi and Ierley (1995). These solutions are unstable and to make Figure 3.9a not too complicated, these have not been drawn. The asymmetric solution branches emerging from P_1 and P_2 do not connect through a limit point within the range in Re that was explored (Re up to 100). The symmetric solution then stabilizes at the limit point L_2 and is stable only over a very short interval in Re. A solution just in the stable regime is shown in Figure 3.9e. The symmetric branch destabilizes again at $Re = 40.57$ through a Hopf bifurcation (H_3 in Fig. 3.9a) and then remains unstable for larger Re.

The oscillatory mode associated with the Hopf bifurcation H_1 on the upper branch

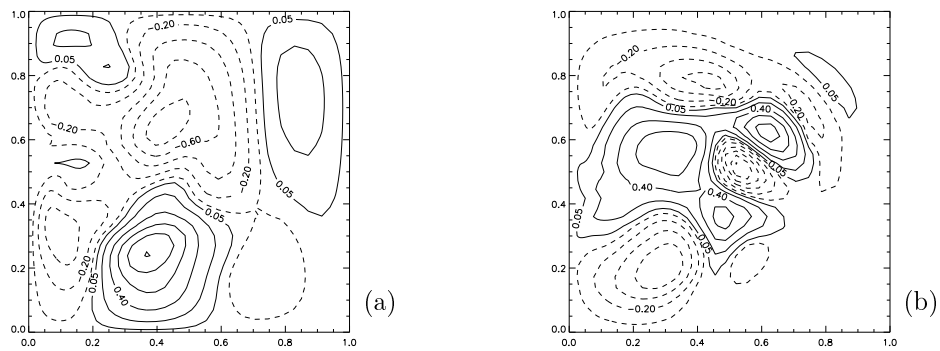

Figure 3.10: *(a) Contour plot of the streamfunction of the mode that destabilizes the barotropic flow at the Hopf bifurcation H_1 on the upper asymmetric branch in Fig. 3.9a, at phase $\nu t = 0.0$. (b) As in (a), but for the mode that destabilizes the barotropic flow at the Hopf bifurcation H_2.*

in Figure 3.9a consists of a basin scale perturbation. A snapshot of this mode is shown in Figure 3.10a, for $\nu t = 0.0$. It has a dimensionless frequency $\nu = 75.0$, which corresponds to a period p^* of 2.0 months. When this oscillatory mode is followed to very small forcing by using α_τ (the relative strength of the wind forcing) as the control parameter, it can be shown to modify into an ocean basin mode (Dijkstra and Katsman, 1997). These modes are the frictional modifications of the inviscid basin modes considered in Pedlosky (1987), which have oscillation periods with a similar time scale. Therefore, the propagation mechanism of the oscillatory instability can be deduced from that of the (inviscid) ocean basin modes, and is similar to that of free Rossby waves. The growth of the mode is related to the strength of the horizontal shear within the double-gyre flow.

The oscillatory mode associated with H_2 on the upper asymmetric branch in Figure 3.9a is shown in Figure 3.10b, also at phase $\nu t = 0.0$. For this mode, $\nu = 5.43$, which corresponds to an interannual period $p^* = 2.3$ years. It has similar signatures as the mode found in Speich *et al.* (1995): the modes both align with the (asymmetric) jet, and the time scales are similar. The mode strengthens and weakens the jet during the different phases of the oscillation.

To study the robustness of the bifurcation diagram constructed for the barotropic mode, the effect of different conditions on the meridional boundaries of the basin were considered in Dijkstra and Katsman (1997). To this end, a new parameter γ_{EW} was introduced to distinguish between no-slip ($\gamma_{EW} = 1$ implying $\psi = \partial\psi/\partial x = 0$) and slip ($\gamma_{EW} = 0$ implying $\zeta = \psi = 0$) east-west boundaries. The bifurcation diagram in Figure 3.9a was constructed for $\gamma_{EW} = 1$. Not unexpectedly, for $\gamma_{EW} = 0$ (corresponding to slip meridional boundaries, not shown) the pitchfork P_1 shifts to a smaller value of Re ($Re_{P_1} = 20.2$) in the bifurcation diagram.

This decrease in stability with slip boundaries, reflected by the shift in P_1 to

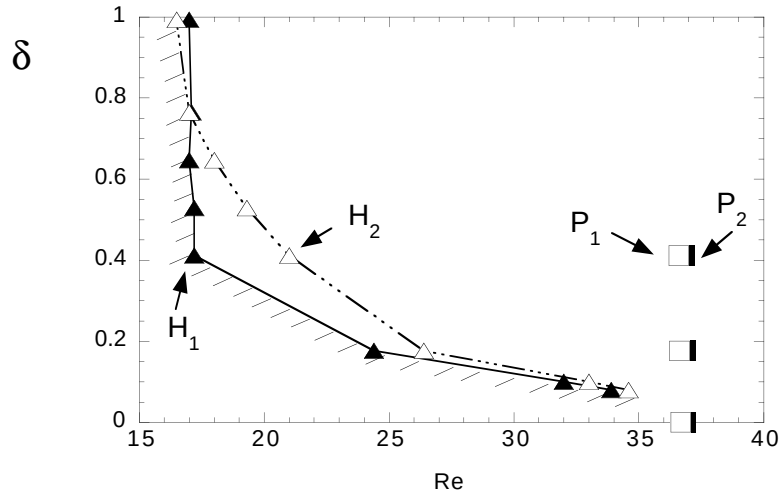

Figure 3.11: *Path of the Hopf bifurcation points H_1 and H_2 and pitchfork bifurcation points P_1 and P_2 (as in Fig. 3.1) in the (Re, δ)-plane. The neutral curve (linear stability boundary) for the baroclinic instabilities of the wind-driven symmetric double gyre flow is indicated by the hatched curve, the hatching points into the stable region. The pitchfork bifurcations were only followed for $\delta < 0.4$.*

smaller Re, is due to a larger energy of the basic flow (Jiang *et al.*, 1995). With the same wind stress input, no-slip boundaries constrain the flow more than slip boundaries, lower its mean energy and make it more stable. The position of the first Hopf bifurcation, associated with the ocean basin mode, hardly changes with γ_{EW}, nor does its time scale of oscillation. However, the second Hopf bifurcation, associated with the gyre mode, shifts to much larger values of Re for slip meridional boundaries and is therefore strongly stabilized. Qualitatively, the bifurcation diagram for the barotropic model is thus robust for changes in the meridional boundary conditions.

3.4.2 Connecting the baroclinic and the barotropic results

Comparing the results obtained with the two-layer and the barotropic model (Figs. 3.1 and 3.9), the effect of the presence of the second layer is two-fold. First, the baroclinic modes destabilize the symmetric solution already at much larger lateral friction (lower Re) than the strength for which symmetry-breaking occurs in the barotropic model. Second, the range in Re where multiple stationary equilibria exist is significantly reduced in the baroclinic case, and the asymmetric equilibria are all unstable. By changing F_1 and F_2 continuously, a connection can be made between the results obtained with the baroclinic and with the barotropic model (that is, the results discussed in Sections 3.2 and 3.4.1). In this way, the fate of the baroclinic Hopf bifurcations in Figure 3.1a can be investigated, as well as the disappearance of the limit point L_3, which results in the disconnection of the asymmetric solutions. It appears that H_1

and H_2 are sensitive to changes in F_2, whereas the position of L_3 is mainly affected by changes in F_1.

In the two-layer model, the linear stability boundary for the double-gyre flow is determined by the value of Re at the bifurcation point H_1 in Figure 3.1a. This boundary separates stationary from oscillatory behavior, and can be followed in other parameters to construct a regime diagram. First, the path of the linear stability boundary is determined in the (Re, δ)-plane, where $\delta = D_1/D_2 = F_2/F_1$ is the layer depth ratio. Since F_1 is kept fixed at its standard value, changing δ corresponds to changing the thickness of the second layer D_2 while g' and D_1 are kept constant. The standard value for the two-layer model is $\delta = 0.4$. In Figure 3.11, the locations of the first two Hopf bifurcations H_1 and H_2 and of the pitchfork bifurcations P_1 and P_2 are plotted in the (Re, δ)-plane (the pitchfork bifurcations were only followed for $\delta < 0.4$). When δ is increased from its standard value ($\delta > 0.4$), the first Hopf bifurcation hardly changes position. The second Hopf bifurcation moves to lower values of Re, and becomes the most unstable one for $\delta > 0.752$. Hence, the resulting neutral curve in Figure 3.11 is composed of parts of the paths of both Hopf bifurcations H_1 and H_2 (the hatching along this neutral curve points into the stable region). At $(Re, \delta) = (17, 0.752)$ the flow becomes unstable to both oscillatory modes simultaneously in a so-called double Hopf bifurcation. The frequencies ν of the two modes associated with H_1 and H_2 are different for this parameter setting. Hence, rather complex temporal behavior can be expected near this point (Nayfeh and Balachandran, 1995).

In the limit $\delta \to 0$ ($F_2 \to 0$), the equivalent barotropic model is reached. Then, the second layer is so deep that it is no longer dynamically active. When δ is decreased from its standard value, the pitchfork bifurcations P_1 and P_2 stay at approximately the same position in the (Re, δ)-plane. However, the Hopf bifurcations H_1 and H_2 move to larger values of Re and closer to each other (Fig. 3.11). So, the double-gyre flow stabilizes as δ is decreased. The Hopf bifurcations can be detected down to $\delta = 0.08$ ($D_2 = 7500\ m$), but not for lower values of δ. The patterns of the most unstable modes associated with the Hopf bifurcations do not change with δ, but the period of both the oscillations approaches 6.6 months ($\nu = 23$). Apparently, for small but finite δ there is a so-called cusp in parameter space where the two Hopf bifurcations coalesce (Nayfeh and Balachandran, 1995). This cusp marks the lower limit in δ of the regime with oscillatory behavior. For smaller δ, the first bifurcation point that is detected is the pitchfork bifurcation P_1 (H_3 was not detected either). Also Figure 3.11 reflects the baroclinic nature of the oscillatory modes associated with the Hopf bifurcations: they can only destabilize the double-gyre flow when the second layer is dynamically active.

To connect the results obtained with the two-layer model to those of the barotropic model, the bifurcation points are followed in the (Re, F_1)-plane for $\delta = 0$. That is, the model configuration is changed from equivalent barotropic to barotropic. Reducing F_1 corresponds to increasing g', and thus to increasing the density difference $\Delta\rho$ between the layers. In this way, the 'soft' interface between the layers that can be deformed by pressure differences is continuously transformed into a 'hard' solid bottom. Decreasing F_1 mainly affects the positions of the pitchfork bifurcations P_1 and P_2 and of the limit point L_3, whereas the limit points L_1 and L_2 remain at the same position (not shown).

For the equivalent barotropic case, $Re_{L_3} = 36.9$ as for the two-layer configuration. With decreasing F_1 it moves to larger values of Re, whereas the pitchfork bifurcations move away from each other on the symmetric branch. As a consequence, the region in Re where multiple (asymmetric) equilibria exist increases. For $F_1 = 650$, the limit point L_3 is found at $Re = 48$. For values of $F_1 \leq 450$, L_3 is not found within the computational domain (Re up to 100): the asymmetric solutions branching from P_1 and P_2 are then disconnected, as was the case for the barotropic model (Fig. 3.9a).

3.5 The symmetry-breaking mechanism

As Re is increased, symmetry breaking occurs spontaneously in both the barotropic and the baroclinic model. At the pitchfork bifurcation P_1 in Figures 3.1b and 3.9a, a stationary mode destabilizes the symmetric, stationary solution. The symmetry-breaking mechanism can be derived by studying the interaction between the stationary solution at P_1 and this mode. It is discussed here for the barotropic model, since in that case it marks the destabilization of the symmetric branch. For the baroclinic model, the stationary mode and thus the symmetry-breaking mechanism is similar.

The streamfunction, vorticity and the horizontal velocities of the barotropic stationary solution just at the pitchfork P_1 in Figure 3.9a are presented in Figure 3.12. The spatial patterns of the corresponding quantities of the mode that destabilizes this stationary solution are shown in Figure 3.13. The perturbation streamfunction (Fig. 3.13a) has a symmetric tripole like structure, with a negative vorticity center along the jet-axis and two positive vorticity centers at either side (Fig. 3.13b). The special property of this mode is that the center structure is exactly localized within the recirculation cells of the double-gyre stationary solution (Fig. 3.12a). In the region just above the symmetry line of the eastward jet ($y = 0.5$), the perturbation zonal flow (Fig. 3.13c) is eastward, and therefore in the same direction as that of the stationary solution (Fig. 3.12c). More northward (north of $y = 0.7$), the perturbation flow is westward thus again in the same direction as the stationary solution. In contrast, if the flow just below the symmetry line is considered, the flow perturbations are in the opposite direction to that of the stationary solution. Hence, the flow perturbation weakens the subtropical gyre and strengthens the subpolar gyre. The asymmetric change in the strength of the basic flow due to the perturbations leads to increased horizontal shear in the eastward jet, which leads to additional negative vorticity. This extra vorticity just amplifies the original perturbation flow in this region, leading to instability.

Next, consider the region of positive vorticity with its maximum near $[x, y] = [0.3, 0.7]$ in Figure 3.13b. In this area, the perturbation meridional velocity (Fig. 3.13d) is in the same direction as that of the stationary solution (Fig. 3.12d) and northward (southward) to the right (left) of the vorticity maximum. Hence, the changes in the stationary solution, as mentioned above, generate an additional horizontal shear leading to increased positive vorticity. To the left of this area, in the region where the perturbation vorticity (Fig. 3.13b) is negative, the strengthening of the subpolar gyre (both meridional velocities of stationary solution and perturbation

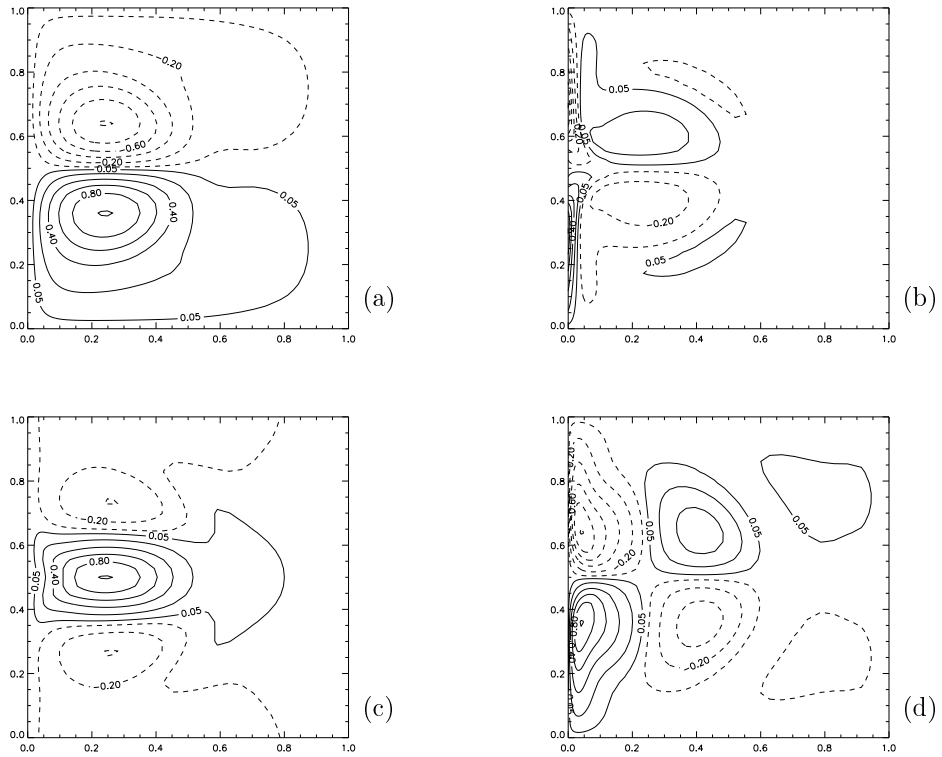

Figure 3.12: *Contour plot of the characteristics of the barotropic stationary solution at P_1 in Fig. 3.9a: (a) the streamfunction Ψ; (b) the vorticity Z; (c) the zonal velocity U; (d) the meridional velocity V.*

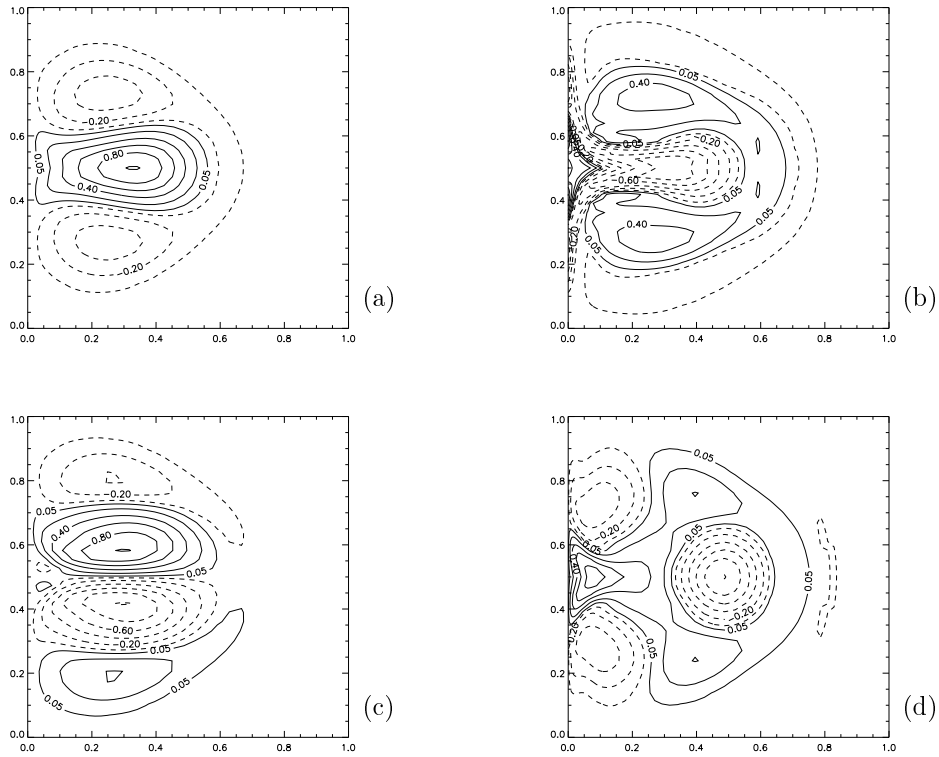

Figure 3.13: *As in Fig. 3.12, but for the stationary mode* $\boldsymbol{\varphi}$ *that destabilizes the flow at* P_1 *in Fig. 3.9a: (a) the perturbation streamfunction* ϕ*; (b) the perturbation vorticity* η*; (c) the perturbation zonal velocity* u*; (d) the perturbation meridional velocity* v*.*

are negative) leads to enhanced shear because the meridional velocity at the western boundary is zero. Consequently, the original negative vorticity anomaly in that region is also amplified.

3.6 Discussion

In this chapter, stationary wind-driven flows were studied in both a baroclinic and a barotropic model, for varying strength of the lateral friction. For the two-layer model in a square basin, the linear stability boundary of the symmetric double-gyre flow is marked by a Hopf bifurcation. There, oscillatory behavior is introduced at an intermonthly time scale. Two more Hopf bifurcations are identified, which mark the destabilization of the flow by oscillatory modes with intermonthly periods. The oscillatory modes cause meandering and local and temporal weakening of the midlatitude jet. An energy analysis showed that all three modes gain energy through the baroclinic conversion of available potential energy, and are thus baroclinic instabilities. Two of the oscillatory modes were shown to determine the neutral curve in the (Re, δ)-plane and to interact at some particular location in this plane. The baroclinic instabilities appear at much larger lateral friction (lower Re) than symmetry-breaking pitchfork bifurcations. The latter lead to an interval where multiple asymmetric equilibria exist. As a consequence, these asymmetric multiple equilibria are all unstable for the baroclinic case.

In contrast, the linear stability boundary for the barotropic double-gyre model is determined by a pitchfork bifurcation. At the symmetry-breaking pitchfork bifurcation, stable asymmetric equilibria come into existence. As the lateral friction is decreased, these stationary solutions become unstable to oscillatory instabilities. One mode, having a monthly to intermonthly period, was shown to originate from ocean basin modes, as known from inviscid linear theory (Pedlosky, 1987). The second mode that destabilizes the stationary flow was found to exist only due to the presence of the gyres. It has an interannual period, on the order of the advective time scale of the gyre circulation. To connect the results of both models, the two-layer model was continuously transformed into the barotropic model by subsequently reducing the control parameters $\delta = F_2/F_1$ and F_1 to zero. Meanwhile, the positions of bifurcation points were followed in parameter space. Increasing the lower layer thickness (reducing δ) was found to stabilize the flow. The apparent cusp of the Hopf bifurcations H_1 and H_2 for small δ, which marks the lowest value for δ for which these Hopf bifurcations were found to exist, demonstrates the existence of a critical boundary in δ for the occurrence of baroclinic instability. That the oscillatory modes that destabilize the flow in the two-layer case are baroclinic was also confirmed by an energy analysis.

For the quasi-geostrophic approximation to be valid, it is required that deformations of the interface between the layers are relatively small with respect to the mean thickness of the layers. In the quasi-geostrophic formulation, the dimensionless interface deformation h_2 is given by (with $\Psi_2 = 0$)

$$h_2 = \frac{H_2}{D}(1 + \varepsilon F_2 \Psi_1)$$

(see Pedlosky, 1987). For most the symmetric and asymmetric solutions that are displayed in the bifurcation diagram in Figure 3.1 Ψ_1 is of order $\mathcal{O}(1)$ so that the deviations of the interface are fairly small ($\varepsilon F_2 \Psi_1 = \mathcal{O}(10^{-2})$). An exception are the symmetric 'inertial runaway' solutions for higher values of the Reynolds number, for which Ψ_1 is of order $\mathcal{O}(10)$. As explained in Section 3.2.1, these solutions exist as a consequence of the symmetric set-up of the model and are therefore of lesser importance.

As a first step towards a more realistic situation, an asymmetric wind stress as prescribed by Moro (e.g., Moro, 1988) was considered, which induces a jet that is displaced northward. Within both the barotropic and the two-layer model, this causes the pitchfork bifurcations to break up, since the internal symmetry of the system is destroyed (see Section 2.3). For the two-layer model forced with such an asymmetric wind stress, the first two bifurcations are still Hopf bifurcations. They have a similar time scale as for the case of symmetric wind stress, and their spatial patterns are still localized within the (now asymmetric) jet, just as in Figures 3.5 and 3.6. Hence, the transition to time-dependence is very similar to that derived from Figure 3.1. Within the barotropic model ($F_1 = F_2 = 0$), the branch of asymmetric solutions associated with northward jet displacement now connects continuously to the trivial solution at zero forcing. The other branch only exists for large Re. A Hopf bifurcation is detected at about $Re = 70$, with an associated intermonthly time scale. This Hopf bifurcation identifies the critical Reynolds number as considered by Moro (1990) by performing time integrations. It is located nicely between his values of $Re = 40$ and $Re = 100$, determined for slip and no-slip conditions on all four boundaries, respectively. The spatial pattern of this mode is again a basin wide oscillation, as in Figure 3.10a.

Chapter 4

The rectification of wind-driven flows by instabilities*

In the previous chapter it was demonstrated that when lateral friction is large enough, the wind-driven flow in the two-layer model is stationary, and characterized by a motionless lower layer. As friction is decreased, the flow undergoes a transition to time-dependence as it becomes unstable to a baroclinic oscillatory mode. In this chapter, it is shown that the non-linear self-interaction of this mode induces a non-zero time-mean response in the lower layer. The origin of this deep flow is clarified through a weakly non-linear analysis near critical conditions. Results deduced from time-dependent numerical simulations at supercritical conditions support the conclusions from the weakly non-linear analysis.

4.1 Introduction

In the two-layer quasi-geostrophic model introduced in Section 2.1, the flow is forced by a steady zonal wind stress. When there is no explicit friction between the layers, stationary wind-driven flows are characterized by motionless subsurface layers. This also applies to the mean states of time integrations at high friction, as shown by for example Holland (1978). When the vertical resolution of the model is increased by introducing more and thinner layers, one consequently ends up with an absurd result, as pointed out by Pedlosky (1996). In the limiting case of an infinite number of layers the total Sverdrup transport is still carried by the uppermost layer, so that the velocity distribution becomes a delta function with depth. Obviously, this contradicts the expectation that enhancing the resolution leads to a more realistic representation

*This chapter is based on the paper "*The rectification of wind-driven flow due to its instabilities*", by C.A. Katsman, H.A. Dijkstra and S.S. Drijfhout, *J. Mar. Res.*, vol. **56**, pp. 559-587, 1998

of the flow. However, when layer models are run in a realistic parameter regime, the statistically stationary solutions do show a mean subsurface response (e.g., Holland, 1978; Holland and Haidvogel, 1980; Barnier *et al.*, 1991). An important issue, therefore, is to understand how the deep circulation in such layer models is driven.

In Rhines and Young (1982), the stationary (nearly) inviscid problem of a mid-ocean wind-driven gyre is taken as an example to point out how a deep flow can be induced. Although the wind stress that forces the gyre flow only provides an input of vorticity in the surface layer, it also deforms the contours of constant potential vorticity (the geostrophic contours) in the deeper layer(s). For sufficiently strong forcing, these contours may close upon themselves, such that within the regions bounded by the contours the flow is no longer constrained to be motionless by the boundary conditions. In the inviscid limit, the only constraint on the flow in these regions is that streamlines coincide with geostrophic contours. These contours thus determine the paths of motion in the unforced layer, and weak viscous stresses between the layers are sufficient to induce a deep flow in these regions. In the case of weak dissipation, the integrated vorticity equation provides the information on the amplitude of the lower layer flow. This theoretical result was elaborated in two papers studying the inertial recirculation in a two-layer model (Cessi *et al.*, 1987; Cessi, 1988). The necessary conditions for abyssal circulation to occur as formulated by Rhines and Young (1982), i.e. the closing of geostrophic contours, were translated to the existence of a critical value for the ratio of the layer depths. Furthermore, predictions of the north-south extent of the recirculation gyres could be made, which were found to depend on the surface forcing.

The view on how a deep flow can be induced in a layer model presented by Rhines and Young (1982) is based essentially on stationary-state theory, and assumes that weak interfacial friction is present. In contrast, it is clear from eddy-resolving general circulation models in which interfacial friction is absent that transient properties of the flow can give rise to the appearance of a subsurface circulation (Holland, 1978; Rhines and Holland, 1979). The origin of these transient features is the instability of the mean flow to perturbations, which evolve to a finite amplitude and modify the mean flow in a fundamental way. They induce a momentum flux on the interface between the first and subsequent layers, effectively driving a flow in the deeper ocean. Consequently, eddies play an important role in shaping the ocean circulation (e.g., Robinson, 1983). In particular, the homogenization of potential vorticity by eddies was demonstrated by McDowell *et al.* (1982) and Keffer (1985). Observations of eddy-driven deep recirculations were discussed by Hogg (1983) and Lozier (1997).

It is by no means exactly clear how the eddy momentum flux generates the flow in the deeper layers, although there have been many numerical studies in which the eddy momentum flux is seen to play a role. In those studies, the temporal behavior of the flow is very complicated: many unstable modes interact and determine the final eddy-induced deep motion. Hence, it is difficult to extract a transparent picture of the responsible mechanism. To make progress with a description of this mechanism it is therefore highly desirable to have only one or a few modes that interact with each other and with the mean flow. This situation is only realized at slightly supercritical conditions. Studies on the instability of a zonal jet within a beta-plane channel near

the onset of instability (e.g., Pedlosky, 1970, 1971, 1972) have demonstrated that non-linear interactions of perturbations are indeed able to introduce a non-zero correction to the mean flow.

Hence, the problem of the origin of the deep mean circulation is approached here from a weakly non-linear point of view. Using the results from the bifurcation study of the symmetric double-gyre flow described in Chapter 3, slightly supercritical flows are explored near the first Hopf bifurcation that marks the transition to time-dependence. In Section 4.2, a first example of the rectification of the lower layer flow is analyzed for a slightly supercritical case. The physics of this rectification is studied both in Sections 4.3 and 4.4 by performing a weakly non-linear analysis and by studying the time-dependent behavior at supercritical conditions, respectively. It is demonstrated that non-linear self-interactions of the unstable oscillatory mode associated with the first Hopf bifurcation induce the rectification of the lower layer flow, and the physics of this process is described in detail. A summary and discussion follows in Section 4.5.

4.2 Instability of the double-gyre flow

Some of the results presented in Chapter 3 on the instabilities of the double-gyre flow are repeated here shortly, before analyzing the results of a time integration at slightly supercritical conditions. Based on the results of this time integration, the net effect of time-dependent perturbations on the flow is demonstrated.

4.2.1 First transition to time-dependence

In Section 3.2, branches of stationary solutions for the wind-driven flow were followed as a function of Re, and presented in the form of a bifurcation diagram (Fig. 3.1). This bifurcation diagram is shown again in Figure 4.1a, with the control parameter Re on the horizontal axis and ψ_{SW} as the measure of the stationary solutions on the vertical axis. Details of the diagram that are not relevant to the discussion in this chapter are left out. The stationary solutions all have a motionless second layer, and will be referred to as $\Psi = (\Psi_1, Z_1, \Psi_2, Z_2)$, where $\Psi_2 = Z_2 = 0$. For values of Re smaller than $Re_{H_1} = 17.2$, the double-gyre flow is linearly stable. At the critical boundary for instability represented by the Hopf bifurcation marked H_1 (Fig. 4.1a), the symmetric flow pattern is destabilized by an oscillatory mode. The streamfunction for the stationary solution Ψ_1 at this value of Re is presented in Figure 4.1b, and a snapshot of the most unstable mode that destabilizes this stationary flow is shown in Figures 4.1c-d, for the upper and lower layer. The mode, which displays both horizontal and vertical shear, propagates eastward with time while maintaining a phase difference of approximately 1/4 of a period between the layers. The period of the oscillation is 4.7 months. At $Re = 21.0$, the flow becomes unstable to a second oscillatory mode (not shown in Fig. 4.1a). The patterns of both the oscillatory modes were presented for several phases of the oscillation in Section 3.3, in Figures 3.5 and 3.6. The amplitude of the oscillatory modes is undetermined at criticality, their finite amplitude evolution can be studied by computing the time-dependent behavior of the

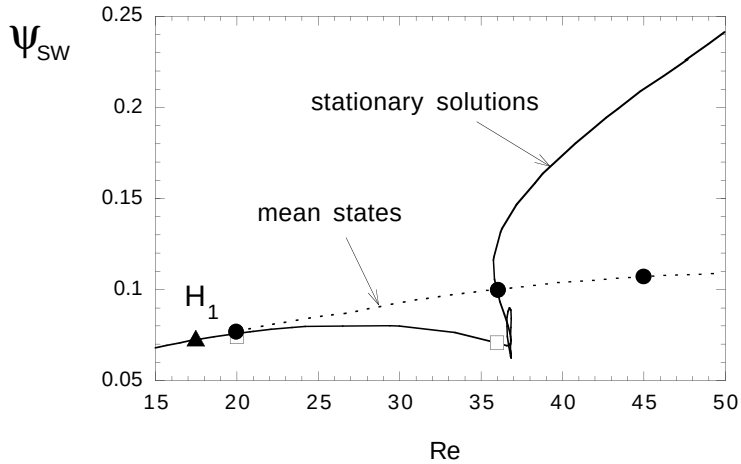

(a)

Figure 4.1: *(a) The bifurcation diagram of the double-gyre wind-driven flow as a function of Re, now showing only the first Hopf bifurcation H_1. On the vertical axis, ψ_{SW} is used again as the measure of the stationary solutions. Solid lines represent stationary solutions. Circles and open squares mark the mean states and the initial conditions of time integrations discussed in Section 4.4, respectively. (b) The upper layer stationary solution Ψ_1 at the first Hopf bifurcation (contour interval is 0.2); (c-d) spatial pattern of the mode that destabilizes the flow at H_1, at phase $\nu t = 0.0$, in the upper and lower layer (the plots are scaled relative to the maximum of the field).*

flow at slightly supercritical conditions.

It is possible that in other parts of the parameter regime different modes than the one associated with H_1 become important in determining the temporal variability of the model. Our choice of parameter regime for the present study is strongly motivated by the fact that we want to isolate a case with only one dominant mode, to keep the non-linear analysis as transparent as possible.

4.2.2 Slightly supercritical flows

Using the time-dependent version of the two-layer quasi-geostrophic model (Section 2.3), several numerical simulations of the time-dependent flow were performed, for different values of Re. As the initial condition, the unstable stationary solution at this specific point in parameter space is used. Next, this solution is perturbed with the calculated pattern of the most unstable mode, having a small amplitude. At $Re = 20$, the stationary solution Ψ is unstable to the oscillatory mode associated with H_1 (Fig. 4.1c-d) only. In Figure 4.2, the evolution of the time-dependent streamfunction $\psi_n(x, y, t)$ is shown for both layers, over a period of 35 years. The streamfunction at the same grid point that is used to define ψ_{SW} in Figure 4.1a is used to represent the flow. At this slightly supercritical value of Re, a stable limit cycle appears. The

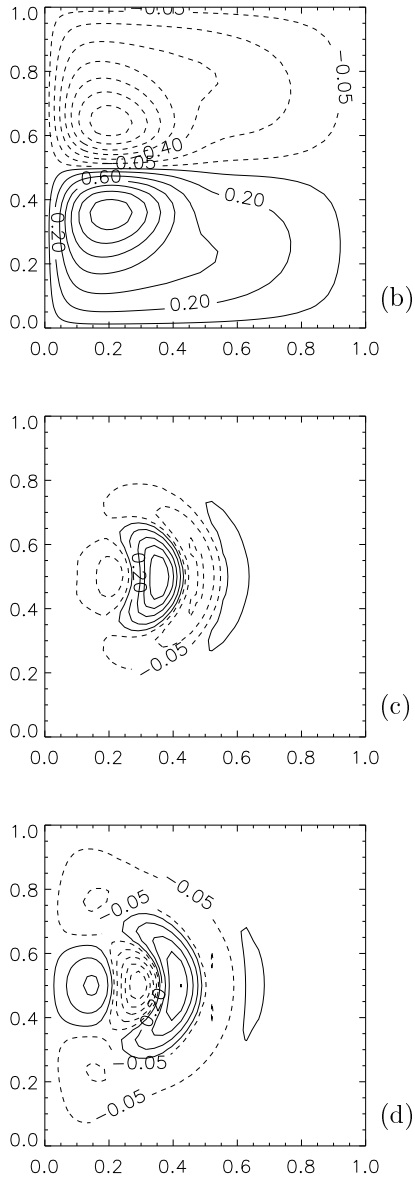

Fig. 4.1, continued.

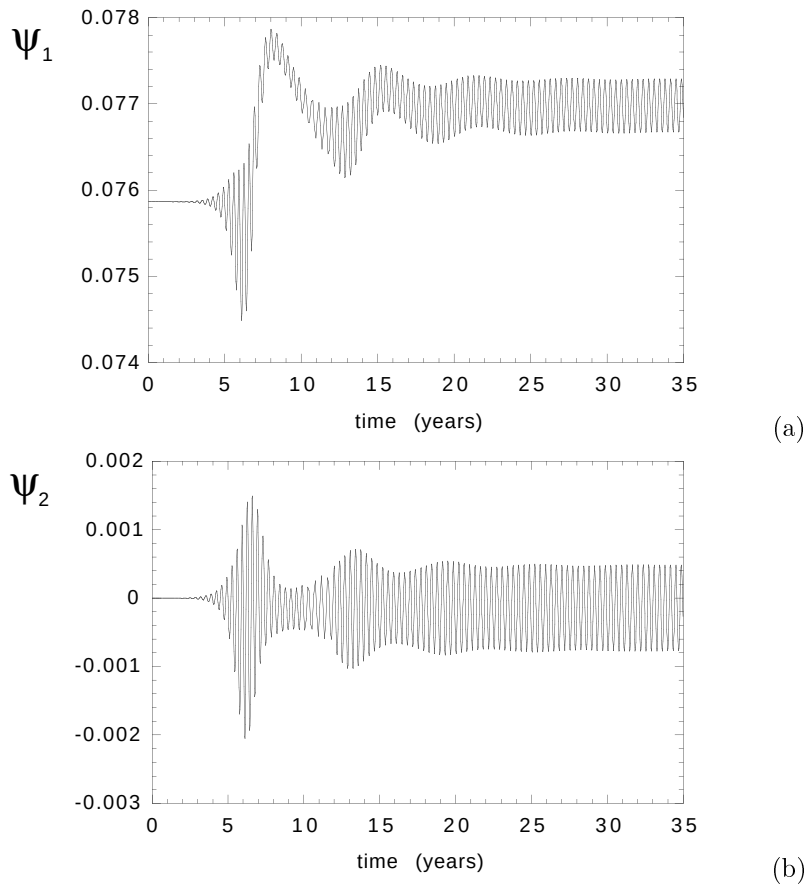

Figure 4.2: *(a) Evolution of the upper layer streamfunction ψ_1 with time, during the time integration at $Re = 20$; (b) as in (a), but for the lower layer streamfunction ψ_2. For both plots, the same grid point in the southwestern part of the basin that is used to define ψ_{SW} is used here to represent the time-dependent behavior of the flow.*

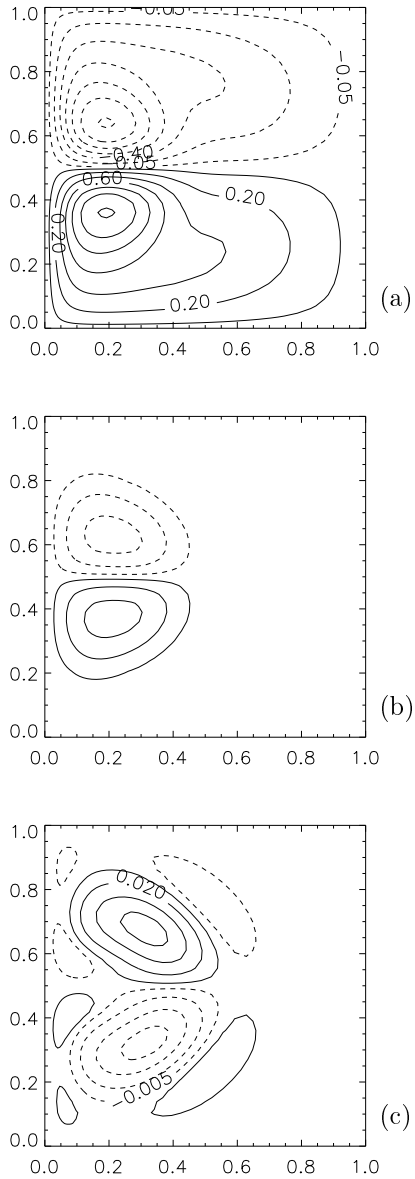

Figure 4.3: *Contour plots of the mean state of the time integration at $Re = 20$, averaged over the period of the limit cycle: (a) the mean flow in the upper layer $\bar{\psi}_1$ (contour interval is 0.2); (b) the mean flow in the lower layer $\bar{\psi}_2$ (contour interval is 0.01). (c) Difference between the mean flow and the unstable stationary solution in the upper layer $\bar{\psi}_1 - \Psi_1$ (contour interval is 0.02).*

oscillation has a period of 4.7 months, which corresponds to the time scale of the mode at the Hopf bifurcation. The limit cycle has equilibrated after approximately 25 years of integration. Note that, in both layers, the average value of the streamfunction at the displayed grid point differs from the initial value. This already shows that the stationary solution is modified by the presence of the oscillatory mode. To indicate the position of the limit cycle in the bifurcation diagram Figure 4.1a, the average value of the upper layer streamfunction at the selected grid point in the southwest is marked by a circle. The initial condition for this time integration, that is, the unstable stationary solution, is marked in this figure by an open square.

In Figures 4.3a-b, the mean state $\bar{\psi}_n(x, y)$, averaged over the period of the limit cycle, is plotted for each layer. It demonstrates that the time-dependent perturbations have altered the flow significantly. In the upper layer, the mean flow $\bar{\psi}_1$ is weaker than the stationary solution Ψ_1 ($\Psi_{1,max} = 1.32$ while $\bar{\psi}_{1,max} = 1.22$). The anomaly $\bar{\psi}_1 - \Psi_1$ (Fig. 4.3c) indicates that although the upper layer flow has strengthened along the western boundary, the velocities in the eastward jet have decreased significantly. The final mean state in the second layer $\bar{\psi}_2$ is non-zero, and thus differs essentially from the unstable stationary solution for which $\Psi_2 = 0$. A weak double-gyre flow has developed in the second layer ($\bar{\psi}_{2,max} = 0.025$).

4.3 Weakly non-linear analysis

The rectification of the unstable stationary flow as discussed in the previous section can be explained by studying the non-linear interactions of the mode in the weakly non-linear regime (i.e., for values of Re just above the first Hopf bifurcation).

4.3.1 Formulation

For each layer n, consider perturbations $\boldsymbol{\varphi}$ on the stationary flow Ψ, such that the total streamfunction $\boldsymbol{\psi} = (\psi_1, \zeta_1, \psi_2, \zeta_2)$ can be written as

$$\boldsymbol{\psi}(x, y, t) = \Psi(x, y) + \boldsymbol{\varphi}(x, y, t) \tag{4.1}$$

Here, $\Psi(x, y)$ is the stationary and $\boldsymbol{\psi}$ the time-dependent solution of the quasi-geostrophic equations. The equations describing the evolution of the perturbations $\boldsymbol{\varphi} = (\phi_1, \eta_1, \phi_2, \eta_2)$ were already formulated in Section 2.1.2, and can be put into the general form

$$(\mathcal{G}\frac{\partial}{\partial t} + \mathcal{L})\boldsymbol{\varphi} + \mathcal{N}(\boldsymbol{\varphi})\boldsymbol{\varphi} = 0 \tag{4.2}$$

where $\mathcal{G}$, $\mathcal{L}$ and $\mathcal{N}(\boldsymbol{\varphi})$ are operators given by

$$\mathcal{G} = \begin{pmatrix} \nabla^2 - F_1 & F_1 \\ F_2 & \nabla^2 - F_2 \end{pmatrix} \tag{4.3a}$$

$$\mathcal{L} = \begin{pmatrix} \mathbf{U_1}\cdot\nabla(\nabla^2 - F_1) - Re^{-1}\nabla^4 + \Pi_{1y}\partial_x - \Pi_{1x}\partial_y & F_1\mathbf{U_1}\cdot\nabla \\ F_2\mathbf{U_2}\cdot\nabla & \mathbf{U_2}\cdot\nabla(\nabla^2 - F_2) - Re^{-1}\nabla^4 + \Pi_{2y}\partial_x - \Pi_{2x}\partial_y \end{pmatrix} \tag{4.3b}$$

$$\mathcal{N}(\boldsymbol{\varphi}) = \begin{pmatrix} \mathbf{u_1}\cdot\nabla(\nabla^2 - F_1) & F_1\ \mathbf{u_1}\cdot\nabla \\ F_2\ \mathbf{u_2}\cdot\nabla & \mathbf{u_2}\cdot\nabla(\nabla^2 - F_2) \end{pmatrix} \tag{4.3c}$$

where the subscripts x and y denote differentiation with respect to that variable, $\partial_n = \partial/\partial n$ and

$$\begin{aligned} \Pi_n &= \nabla^2\Psi_n + (-1)^n\ F_n(\Psi_1 - \Psi_2) + \beta y \\ \mathbf{U_n} &= (-\partial\Psi_n/\partial y, \partial\Psi_n/\partial x) \\ \mathbf{u_n} &= (-\partial\phi_n/\partial y, \partial\phi_n/\partial x) \end{aligned}$$

Note that $\mathcal{N}(\boldsymbol{\varphi})$ is linear in $\boldsymbol{\varphi}$ so that $\mathcal{N}(\boldsymbol{\varphi})\boldsymbol{\varphi}$ is quadratic.

When the perturbations $\boldsymbol{\varphi}$ have an infinitesimally small amplitude, the non-linear terms in (4.3c) are negligibly small. Equation (4.2) then reduces to the linear stability problem

$$(\mathcal{G}\frac{\partial}{\partial t} + \mathcal{L})\boldsymbol{\varphi} = 0 \tag{4.4}$$

which allows solutions of the form $\boldsymbol{\varphi} = A\ \hat{\boldsymbol{\varphi}}(x,y)\ e^{\sigma t}$. The amplitude A is arbitrary at this stage. In this case, the linear stability boundary for the double-gyre flow is the critical value of the Reynolds number Re_c for which $\lambda = 0$. This is just the value of Re at the first Hopf bifurcation H_1 ($Re_c = 17.2$). The patterns $\hat{\boldsymbol{\varphi}}$ associated with the first Hopf bifurcation were already shown for both layers in Figure 4.1c-d.

This linear analysis is only valid while the amplitude of the perturbations is very small, that is, during the initial growth stage. The equilibration of the instabilities has to be determined using a non-linear analysis. At slightly supercritical conditions, we can define ε as a measure of the instability of the flow,

$$Re = Re_c(1 + \varepsilon^2) \quad \text{and} \quad \varepsilon \ll 1 \tag{4.5}$$

Near criticality, the equilibration of the perturbations occurs on a much longer time scale than the growth rate of the oscillatory mode itself. This motivates the introduction of an additional time scale

$$\tau = \varepsilon^2 t$$

to describe the long term evolution of the perturbations on the basic flow (e.g., Eckhaus, 1965; Pedlosky, 1987; Van der Vaart and Dijkstra, 1997). All dependent variables are considered as functions of x, y, t and τ, and the time derivatives transform

according to

$$\frac{\partial}{\partial t} \Longrightarrow \frac{\partial}{\partial t} + \varepsilon^2 \frac{\partial}{\partial \tau}$$

As long as the finite amplitude of the perturbations is small compared to that of the stationary solution, the solution vector $\boldsymbol{\varphi}$ can be expanded as

$$\boldsymbol{\varphi} = \varepsilon \boldsymbol{\varphi}^{(1)} + \varepsilon^2 \boldsymbol{\varphi}^{(2)} + \cdots \tag{4.6}$$

At $\mathcal{O}(\varepsilon)$, the linear stability problem (4.4) is recovered and the solution $\boldsymbol{\varphi}^{(1)}$ is given by

$$\boldsymbol{\varphi}^{(1)} = A\hat{\boldsymbol{\varphi}}(x,y)e^{i\nu t} \tag{4.7}$$

A weakly non-linear analysis shows that only the self-interaction of the unstable mode $\boldsymbol{\varphi}^{(1)}$ contributes to the $\mathcal{O}(\varepsilon^2)$ correction of the stationary solution. When only one unstable mode is present, it can be demonstrated that the second order contribution to the flow $\boldsymbol{\varphi}^{(2)}$ is given by $\boldsymbol{\varphi}^{(2)} = |A|^2\bar{\boldsymbol{\varphi}}$ where $\bar{\boldsymbol{\varphi}}$ is the spatial pattern of the rectification (see Romea, 1977, and the Appendix). This rectification is determined by the equation

$$\mathcal{L}\bar{\boldsymbol{\varphi}} = -2\mathcal{R}(\mathcal{N}(\hat{\boldsymbol{\varphi}})\hat{\boldsymbol{\varphi}}^*) \tag{4.8}$$

where * indicates the complex conjugate, $\mathcal{R}$ denotes the real part and $\hat{\boldsymbol{\varphi}}$ is the spatial pattern of $\boldsymbol{\varphi}^{(1)}$. For the case of one unstable mode, the equilibration amplitude A can be determined from the conditions at $\mathcal{O}(\varepsilon^3)$, the interactions between the unstable mode and the second order correction to the flow.

Equation (4.8) yields that a non-oscillatory contribution $\boldsymbol{\varphi}^{(2)}$ to the flow exists, which can be attributed to the self-interaction of the oscillatory mode $\boldsymbol{\varphi}^{(1)}$. This result strongly motivates further investigation of the right hand side of (4.8), to explain the rectification of the flow by the perturbations. Equation (4.8) can be written out in full as (with $\Psi_2 = \mathbf{U_2} = 0$)

$$\begin{aligned}\mathbf{U_1}\cdot\nabla\left[(\nabla^2 - F_1)\overline{\phi}_1 + F_1\overline{\phi}_2\right] + \frac{\partial \Pi_1}{\partial y}\frac{\partial \overline{\phi}_1}{\partial x} - \frac{\partial \Pi_1}{\partial x}\frac{\partial \overline{\phi}_1}{\partial y} - \frac{1}{Re}\nabla^4\overline{\phi}_1 \\ = -2\,\mathcal{R}(\mathcal{J}(\hat{\phi}_1, \hat{q}_1^*)\ )\end{aligned} \tag{4.9}$$

for the upper layer, and

$$\frac{\partial \Pi_2}{\partial y}\frac{\partial \overline{\phi}_2}{\partial x} - \frac{\partial \Pi_2}{\partial x}\frac{\partial \overline{\phi}_2}{\partial y} - \frac{1}{Re}\nabla^4\overline{\phi}_2 = -2\,\mathcal{R}(\mathcal{J}(\hat{\phi}_2, \hat{q}_2^*)\ ) \tag{4.10}$$

for the lower layer. In these equations, $\overline{\phi}_1$ and $\overline{\phi}_2$ are the non-oscillatory $\mathcal{O}(\varepsilon^2)$ rectifications of the upper and lower layer flow, respectively, while $\hat{q}_n = \nabla^2\hat{\phi}_n + (-1)^n F_n(\hat{\phi}_1 - \hat{\phi}_2)$ and $\mathcal{J}$ is the Jacobian

$$\mathcal{J}(f_1, f_2) \equiv \frac{\partial f_1}{\partial x}\frac{\partial f_2}{\partial y} - \frac{\partial f_2}{\partial x}\frac{\partial f_1}{\partial y}$$

The equations (4.9) and (4.10) are uncoupled, since one can solve for $\bar{\phi}_2$ first and then use that result to determine $\bar{\phi}_1$. The right hand side of (4.10) acts as a forcing on the lower layer and can be written out in full as (the hats have been dropped for convenience)

$$-\mathcal{R}\,[\mathcal{J}(\phi_2, q_2^*)\,] = -\mathcal{R}\,[F_2\ \mathbf{u_2}\cdot\nabla(\phi_1^* - \phi_2^*)] - \mathcal{R}\,[\mathbf{u_2}\cdot\nabla\eta_2^*] \tag{4.11}$$

The interpretation of the two terms in (4.11) leads to a description of how this forcing is generated and, consequently, interpretation of (4.10) leads to an explanation of the origin of the flow in the second layer.

4.3.2 The physics of the lower layer forcing

Both terms on the right hand side of (4.11) represent quantities integrated over the periodic orbit. For clarity, first the instantaneous terms are considered and thereafter the orbit integrated effect. The first term on the right hand side of (4.11) can easily be interpreted, using that $\phi_2 - \phi_1$ is proportional to $\tilde{h}_2$, the thickness anomaly of the second layer associated with the mode (note that $\tilde{h}_1 = -\tilde{h}_2$). So, the first term on the right hand side of (4.11) is proportional to $+\mathbf{u_2}\cdot\nabla\tilde{h}_2$. In Figure 4.4a, a vector plot of the perturbation velocity $\mathbf{u_2}$ is presented, overlying a shaded surface plot of $\tilde{h}_2$. Dark (light) shading represents negative (positive) values of $\tilde{h}_2$. Both fields are shown at the phase $\nu t = 0.0$, for $[x, y] \in [0.0, 0.6] \times [0.2, 0.8]$, the part of the basin where the mode is most dominantly present. Because of the phase difference between the upper and lower layer response, the horizontal perturbation velocity $\mathbf{u_2}$ is not tangent to lines of constant $\tilde{h}_2$. This results in an instantaneous flux of layer thickness. For example, near $[x, y] = [0.3, 0.6]$ the perturbation velocity is northwestward, in the direction of the gradient of the layer thickness anomaly. South of the mid-axis of the basin, at $[x, y] = [0.3, 0.4]$, the perturbation velocity points northeastward and against the direction of $\nabla\tilde{h}_2$. So, north (south) of $y = 0.5$ the flux of anomalous $\tilde{h}_2$ causes the interface to fall (rise) which provides a source of positive (negative) vorticity in the second layer, due to squashing (stretching) of the water column.

Similarly, we can study the instantaneous effect of the second term on the right hand side of (4.11). In Figure 4.4b, the perturbation vorticity η_2 is plotted underlying a vector plot of the horizontal perturbation velocity $\mathbf{u_2}$, also at phase $\nu t = 0.0$. Again, light (dark) shading represents positive (negative) values of η_2. The horizontal perturbation velocity is not tangent to lines of constant perturbation vorticity everywhere. For example, at $[x, y] = [0.3, 0.6]$ the perturbation velocity is northwestward and directed against the gradient of the perturbation vorticity. So, there the perturbation velocity carries positive relative vorticity northwestward, inducing a net Reynolds stress in the lower layer. The opposite occurs on the southern side of the basin, near $[x, y] = [0.3, 0.4]$.

Next, the effect of both contributions during the oscillation is considered. The perturbation streamfunction is non-zero between the western boundary and approximately $[x] = [0.5]$. With time, the individual maxima and minima of the mode propagate eastward, having their largest amplitudes near $[x] = [0.3]$ (see also Fig. 3.5). Considering a frame of reference which is moving eastward with (the extrema of) the

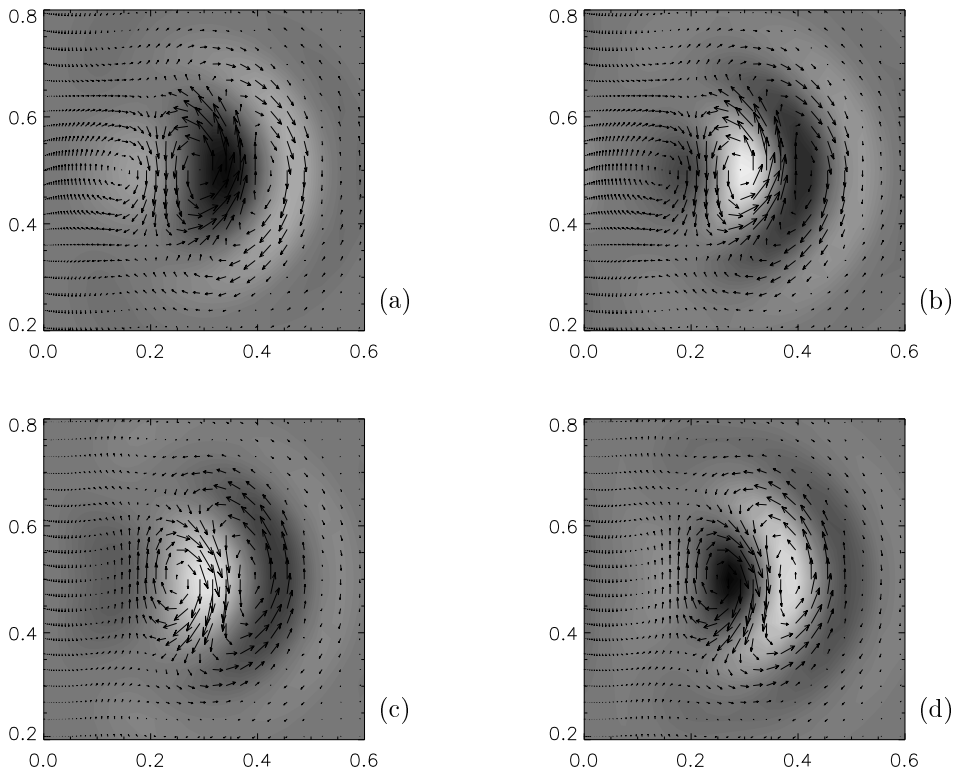

Figure 4.4: *Vector plot at phase* $\nu t = 0.0$ *of the lower layer horizontal velocity* $\mathbf{u_2}$, *combined with a shaded surface plot of (a) the layer thickness perturbation* $\tilde{h}_2 \propto \phi_2 - \phi_1$ *and (b) the perturbation vorticity* η_2. *Light (dark) shading represents positive (negative) values of* $\tilde{h}_2$ *or* η_2. *Note that only part of the basin is shown,* $[x, y] \in [0.0, 0.6] \times [0.2, 0.8]$. *(c-d) As in (a-b), now at phase* $\nu t = 0.125$.

mode, it is clear that the phase differences between the various quantities - like the velocity and gradient of relative vorticity - persist and, consequently, that the contour lines of the different quantities are not tangent at any phase of the oscillation. This is demonstrated in Figures 4.4c-d, which show the same quantities in similar shaded surface and vector plots as the Figures 4.4a-b, only now at phase $\nu t = 0.125$. When Figures 4.4a and 4.4c are compared, it is clear that the minimum of the layer thickness anomaly $\tilde{h}_2$ (the dark shading in the background) found earlier at $[x] = [0.3]$ has moved eastward to $[x] = [0.45]$, and its amplitude has decreased. The northwestward flux of anomalous $\tilde{h}_2$ now occurs around $[x, y] = [0.45, 0.6]$, the northeastward flux of anomalous $\tilde{h}_2$ around $[x, y] = [0.45, 0.4]$. A similar shift can be seen for the Reynolds stress term when Figures 4.4b and 4.4d are compared. For instance, the northwestward flux of positive relative vorticity that was found around $[x, y] = [0.3, 0.6]$ at $\nu t = 0.0$ occurs around $[x, y] = [0.4, 0.6]$ at $\nu t = 0.125$.

At each phase, both the contribution of the vortex stretching and of the Reynolds stress to the vorticity budget are anti-symmetric with respect to $y = 0.5$. This can easily be understood from the symmetry properties of the mode. The perturbation streamfunction ϕ_n is symmetric around $y = 0.5$ (see Figs. 4.1c-d), and hence the vorticity η_n is symmetric as well. As a result, u_n and $\partial\eta_n/\partial y$ are anti-symmetric, while v_n and $\partial\eta_n/\partial x$ are symmetric with respect to $y = 0.5$. Since both the vortex stretching term and the contribution due to the Reynolds stresses thus involve the multiplication of a symmetric and an anti-symmetric term, their patterns will be anti-symmetric. Moreover, at all phases of the oscillation the patterns of both contributions remain of the same sign, that is, there is a positive (negative) vorticity input in the second layer north (south) of $y = 0.5$[†]. However, the local amplitude of the perturbation quantities changes with time, and therefore the longitude where the maximum contribution to the vorticity budget occurs migrates in east-west direction during the oscillation. Note that after half a cycle all the perturbation quantities have changed sign, so both the vortex stretching term and the Reynolds stress term are equal at phase νt and at phase $\nu t + 0.5$.

The orbit integrated patterns of the vortex stretching term, the Reynolds stress term and their sum (the right hand side of (4.11)) are plotted in Figure 4.5. Integrated over the total oscillation period, the combined effect of the vortex stretching and the Reynolds stresses yields an anti-symmetric dipole, which has its maximum at $[x, y] = [0.3, 0.55]$ and its minimum at $[x, y] = [0.3, 0.45]$. Note that in this case the forcing by the vortex stretching is larger than the Reynolds stress contribution.

To clarify the response of the deep flow to the forcing on the right hand side of (4.11), each of the forcing terms can be looked at in terms of an associated (equivalent) vertical velocity (Pedlosky, 1987; Holton, 1992). Since the latter is a more familiar quantity, it may provide a more comprehensive view of the forcing mechanism. An equivalent vertical velocity w_v can be associated with the stretching term, which results in a similar forcing of the second layer as a result of the movement of the

[†]The Reynolds stress term has a small secondary extremum, which is negative (positive) north (south) of $y = 0.5$ at all phases of the oscillation (see Fig. 4.5b)

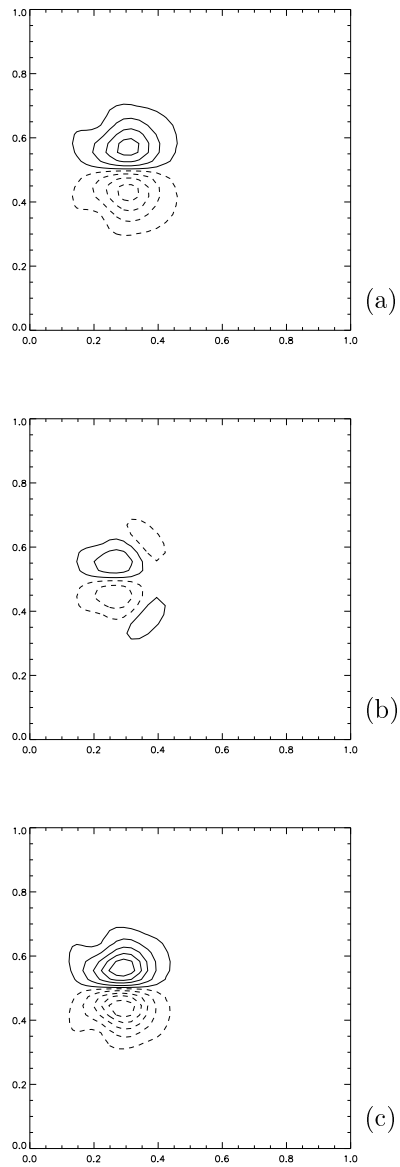

Figure 4.5: *Terms on the right hand side of (4.11) computed from the perturbation streamfunction, and integrated over the oscillation period: (a) the stretching term* $-\mathcal{R}(F_2\mathbf{u_2}\cdot\nabla(\phi_1^* - \phi_2^*)\ )$*; (b) the Reynolds stress term* $-\mathcal{R}(\mathbf{u_2}\cdot\nabla\eta_2^*)$ *and (c) the sum of (a) and (b) (the plots are scaled relative to the maximum of the field of (c), contour interval=0.2).*

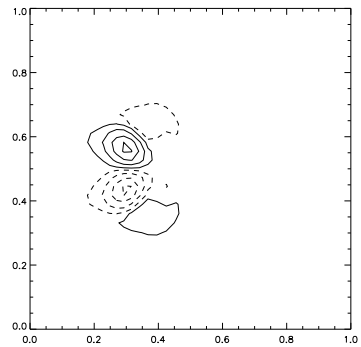

Figure 4.6: *Contour plot of the equivalent vertical velocity $\bar{w}_d$ induced by differential vorticity advection, integrated over the oscillation period.*

interface between the layers. This velocity is given by

$$w_v = -\frac{F_2\ D_2}{D}\left[\mathbf{u_2}\cdot\nabla(\phi_1 - \phi_2)\ \right] \tag{4.12}$$

A positive value of w_v stretches the lower layer and compresses the upper layer. Since w_v and the vortex stretching term in (4.11) differ only by a constant factor D_2/D, the spatial pattern of $\bar{w}_v$, the equivalent vertical velocity integrated over the oscillation period, is identical to that presented in Figure 4.5a. So, $\bar{w}_v$ is upward north of the mid-axis of the basin and downward to the south.

Also the Reynolds stress term can be looked at in terms of an equivalent vertical velocity. Due to so-called differential vorticity advection (the rate of change of the vorticity advection with height) vertical motions can be induced (Holton, 1992). Consider for example the flow below the interface between the two layers in the model. When the relative vorticity above the interface is cyclonic and exceeds the vorticity below the interface (i.e., $\partial\eta/\partial z > 0$), a (relatively) low pressure area will develop below the interface in the second layer. Due to the horizontal pressure differences thus induced below the interface, anomalous horizontal velocities will converge towards the low pressure area, inducing an upward vertical velocity w_d. This equivalent vertical velocity is proportional to

$$w_d \propto \mathbf{u_2}\cdot\nabla(\eta_2 + \beta y) - \mathbf{u_1}\cdot\nabla(\eta_1 + \beta y)$$

Since the term involving βy is linear, it averages out over one cycle of the oscillation. So,

$$\bar{w}_d \propto \overline{\mathbf{u_2}\cdot\nabla\eta_2} - \overline{\mathbf{u_1}\cdot\nabla\eta_1} \tag{4.13}$$

is the orbit integrated effect. The first term on the right hand side is the flux of relative vorticity in the second layer, which was shown in Figure 4.5b but with a minus sign. It is negative (positive) north (south) of the mid-axis of the basin. The integrated effect of the flux of relative vorticity in the first layer, the second term in

(4.13), has a similar spatial pattern since the perturbation streamfunction is similar in both layers, although there is a phase difference (see Fig. 3.5). However, the upper layer perturbation has a larger amplitude so the resulting $\bar{w}_d$ is positive (negative) north (south) of $y = 0.5$. The pattern of $\bar{w}_d$ is presented in Figure 4.6. Around $[x] = [0.3]$, the strongest vertical motions are induced. Again, upward motions are associated with the positive vorticity input shown in Figure 4.5b.

In conclusion, the self-interaction of the mode causes a positive (negative) input of vorticity in the second layer north (south) of $y = 0.5$. The phase difference between ϕ_1 and ϕ_2 leads to a non-zero flux of layer thickness anomaly $\bar{h}_2$, which in turn leads to vortex stretching. Simultaneously, the 'banana shape' of the perturbation leads to a non-zero Reynolds stress. Both forcing terms can be interpreted in terms of equivalent vertical velocities, due to the vortex stretching ($\bar{w}_v$) and as resulting from differential vorticity advection in both layers ($\bar{w}_d$). The net effect of the forcing over a whole period of the oscillation is shown in Figure 4.5c as the right hand side of (4.11). This input of vorticity due to the self-interaction drives a double-gyre flow in the second layer.

4.4 Transient flows at supercritical conditions

In the previous section, the rectification of the stationary solution was shown to originate from the non-linear self-interaction of the unstable mode. Alternatively, we can directly determine the rectification from the interaction of the perturbations present in the time integrations at (slightly) supercritical conditions. Thereto, the total solution $\boldsymbol{\psi}$ is decomposed into a time-mean and deviation field as

$$\boldsymbol{\psi}(x, y, t) = \bar{\boldsymbol{\psi}}(x, y) + \boldsymbol{\psi}'(x, y, t) \tag{4.14}$$

where $\bar{\boldsymbol{\psi}}$ is the flow averaged over a certain time T, i.e.

$$\bar{\boldsymbol{\psi}} = \frac{1}{T} \int_0^T \boldsymbol{\psi}(x, y, t)\ dt$$

and $\bar{\boldsymbol{\psi}}' = 0$. The time averaged vorticity equation for the second layer becomes

$$\begin{aligned} \bar{\mathbf{u}}_{\mathbf{2}} \cdot \nabla \bar{\zeta}_2 + \beta \bar{v}_2 + F_2 \bar{\mathbf{u}}_{\mathbf{2}} \cdot \nabla(\bar{\psi}_1 - \bar{\psi}_2) - \frac{1}{Re} \nabla^4 \bar{\psi}_2 \\ = -F_2 \overline{\mathbf{u}'_{\mathbf{2}} \cdot \nabla(\psi'_1 - \psi'_2)} - \overline{\mathbf{u}'_{\mathbf{2}} \cdot \nabla \zeta'_2} \end{aligned} \tag{4.15}$$

where overbars and primes refer to time-mean and perturbation quantities, respectively. The left hand side of (4.15) contains both linear and non-linear terms involving only the mean state $\bar{\boldsymbol{\psi}}$. The right hand side consists of the non-linear interactions of the perturbations, which act as a forcing on the second layer. In (4.15), $\bar{\psi}_2$ denotes the rectified flow in the lower layer, since the stationary solution Ψ_2 is zero there.

For the weakly non-linear trajectory computed for $Re = 20$ that was shown in Section 4.2.2, the two time-averaged interaction terms on the right hand side of (4.15) are plotted in Figures 4.7a-b, with their sum in Figure 4.7c. This forcing pattern

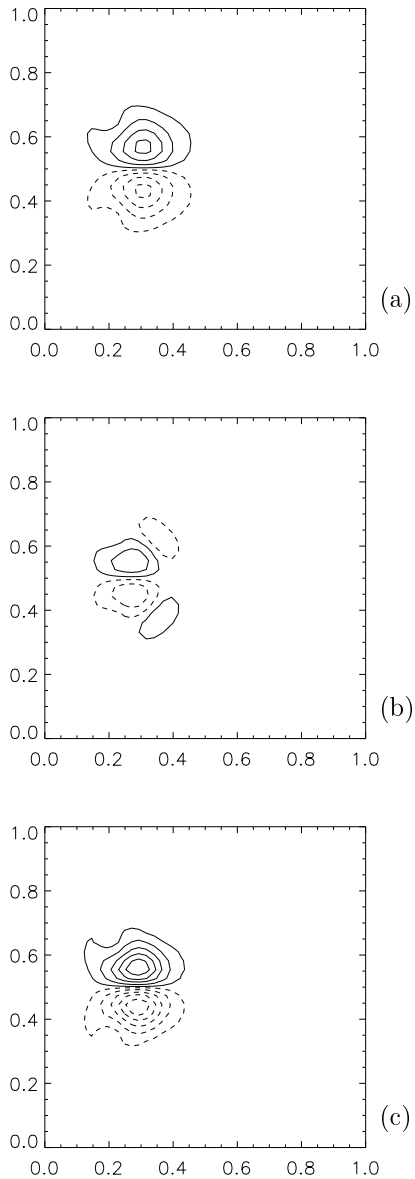

Figure 4.7: *Terms on the right hand side of (4.15), computed from the time integration at $Re = 20$: (a) the stretching term $-F_2\overline{\mathbf{u}'_2 \cdot \nabla(\psi'_1 - \psi'_2)}$; (b) the Reynolds stress term $-\overline{\mathbf{u}'_2 \cdot \nabla \zeta'_2}$ and (c) the total right hand side (the plots are scaled relative to the maximum of the field of (c), contour interval=0.2).*

determined directly from the trajectory can be compared with that derived from the self-interaction of the unstable mode (Figs. 4.5a-c). Both the spatial patterns of the two contributions to the forcing as well as the ratio of the amplitude of the two terms are in very good agreement. In principle, the amplitude at which the mode is found to equilibrate can be compared to the theoretical value that can be derived from the $\mathcal{O}(\varepsilon^3)$ conditions (equation (A4.6) of the Appendix), since there is only one unstable mode in this regime. This calculation is omitted here. The weakly non-linear analysis is sufficient to show that, in accordance with the results in the previous section, the lower layer flow $\bar{\psi}_2$ can be attributed to the self-interaction of one mode.

4.4.1 Mildly non-linear regime

From the results of time integrations performed at higher values of the Reynolds number, it is found that the limit cycle associated with H_1 remains stable and thus dictates the time-dependent behavior of the flow up to $Re = 40$ (see Section 6.2, Fig. 6.2). However, further in parameter space the (unstable) stationary solutions obtained with the continuation technique are substantially different from the solution at $Re = 20$. As was discussed in Section 3.2.1, for decreased lateral friction the stationary solutions become more inertially dominated. The streamfunction Ψ_1 of the unstable stationary solution becomes almost elliptic in east-west direction. In the bifurcation diagram (Fig. 4.1a), the rescaling of the solutions which reflects this change in dominant balance is clearly visible. So, as our second case the results of a time integration at $Re = 36$ are studied, where the limit cycle is still stable but the stationary flow is more inertially dominated as compared to the flow at $Re = 20$. The upper layer streamfunction Ψ_1 for $Re = 36$ is shown in Figure 4.8a, and $\Psi_2 = 0$ again. In the bifurcation diagram, this solution (indicated by an open square in Fig. 4.1a) lies slightly left of the first limit point that is encountered as Re is increased. The time-dependent flow (not shown) displays regular oscillations, now with a period of 3.6 months[‡]. The mean state in the upper and lower layer is shown in Figures 4.8b and 4.8c, respectively, and marked in Figure 4.1a by a small circle. There are large differences between the flow pattern of the mean state and of the unstable stationary solution. The mean state has a more pronounced western boundary current, and its gyres do display east-west asymmetry. Furthermore, the maximum of the upper layer streamfunction has decreased substantially, from $\Psi_{1,max} = 3.9$ to $\bar{\psi}_{1,max} = 1.3$. The time-mean flow in the second layer is an order of magnitude stronger than for the case at $Re = 20$ ($\bar{\psi}_{2,max} = 0.025$ at $Re = 20$; $\bar{\psi}_{2,max} = 0.19$ at $Re = 36$) but has a similar double-gyre pattern. The rectification of the upper layer $\bar{\psi}_1 - \Psi_1$ is shown in Figure 4.8d, the rectification in the second layer is $\bar{\psi}_2$ (Fig. 4.8c). A snapshot of the perturbations ψ_1' and ψ_2' are shown in Figures 4.8e-f, respectively. The patterns still closely resemble those of the unstable mode shown in Figures 4.1c-d. However, the equilibration of the limit cycle now occurs at a much larger amplitude of ψ': the maxima of the perturbations are a factor eight (four) larger for the upper (lower) layer.

[‡]The period of the oscillation agrees well with the results of the linear stability analysis of the unstable stationary flow at this point in parameter space.

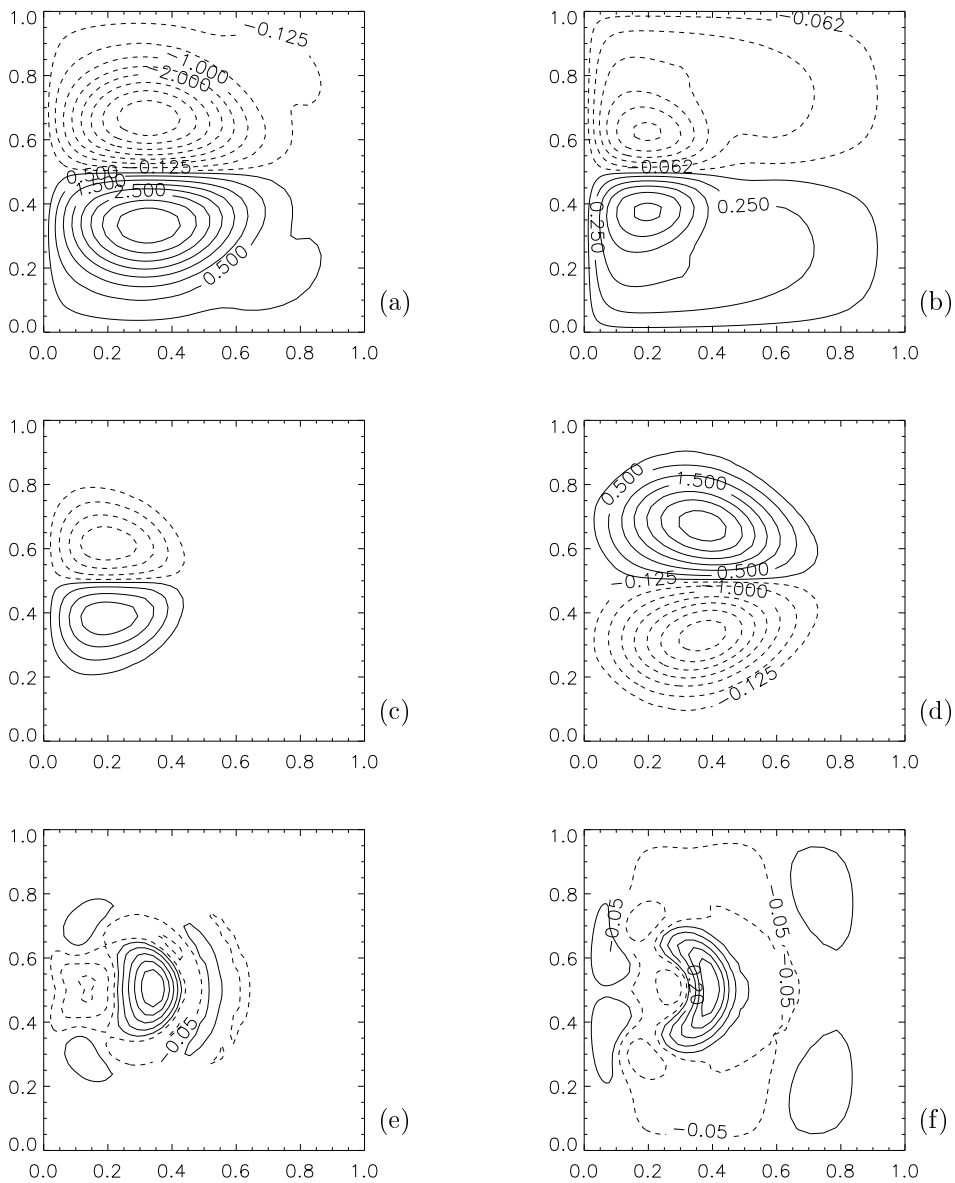

Figure 4.8: *Features of the trajectory at $Re = 36$: contour plot of (a) the upper layer stationary solution Ψ_1 (contour interval is 0.5); (b) the upper layer mean flow $\bar{\psi}_1$ (contour interval is 0.25); (c) the lower layer mean flow $\bar{\psi}_2$ (contour interval is 0.05); (d) the upper layer anomaly $\bar{\psi}_1 - \Psi_1$ (contour interval is 0.5); snapshot of the perturbation streamfunction ϕ'_n in the (e) upper and (f) lower layer (plots (e) and(f) are scaled with the maximum of the field).*

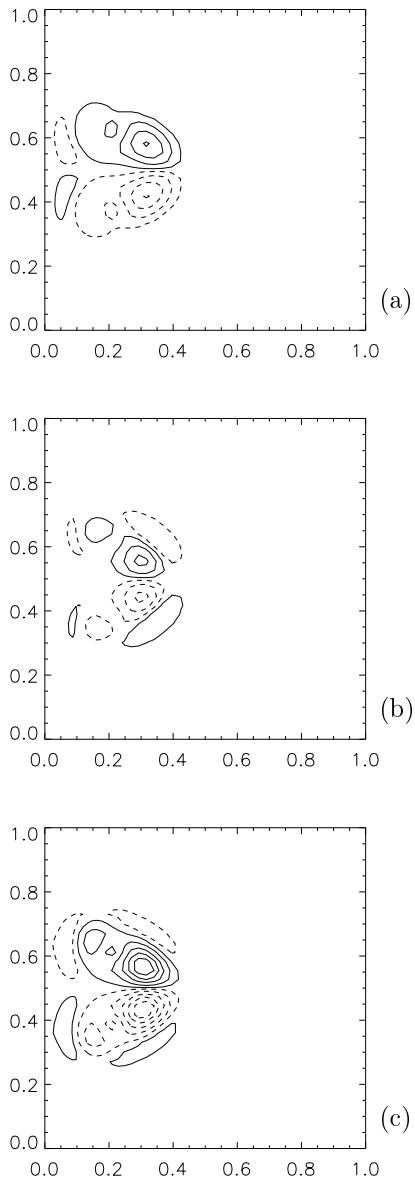

Figure 4.9: *As in Fig. 4.5, but for the time integration at* $Re = 36$*: (a) the stretching term; (b) the Reynolds stress term and (c) the total right hand side of (4.15) (the plots are scaled relative to the maximum of the field of (c), contour interval=0.2).*

Also for this case, the non-linear terms on the right hand side of (4.15) are calculated, integrated over the oscillation period. They are shown in Figures 4.9a-b, with their sum in Figure 4.9c. The patterns of the contribution of the vortex stretching and the Reynolds stresses to the vorticity budget are similar to the forcing derived from the unstable mode (compare Figs. 4.9a-c with Figs. 4.5a-c). The maximum contribution is found at $[x, y] = [0.3, 0.55]$, and again, the stretching term is larger than the Reynolds stress contribution. Although the outermost contours differ slightly, which is a consequence of small modifications of the patterns of ψ'_n (compare Figs. 4.8e-f with Figs. 4.1b-c), also for this case the rectification can be attributed to the non-linear self-interaction of the perturbation.

4.4.2 Strongly non-linear regime

For values of Re larger than 36, past the limit points that mark the rescaling of the stationary solutions (see Fig. 4.1a), trajectories were computed as well. This was done using the mean state at $Re = 36$ as the initial condition and subsequently increase Re, rather than using the unstable stationary solution at that specific value of the Reynolds number. In this way, the stable limit cycle observed for lower values of Re can be traced in parameter space further. For values of the Reynolds number larger than 40, the limit cycle loses its stability and the time-dependent behavior becomes more irregular. As an example, the time-dependent behavior of the flow at $Re = 45$ is shown in Figure 4.10. The first 5 years show some initial effects due to the sudden increase in the Reynolds number from 36 up to 45.

The mean state $\bar{\psi}_n$ (where the time-average is over the last 10 years of the integration) is shown in Figures 4.11a-b for both layers, and is marked in Figure 4.1a by a circle. As compared to the cases discussed above, the amplitude of the time-mean flow in the second layer has again increased ($\bar{\psi}_{2,max} = 0.31$). The time-mean upper layer streamfunction is also larger than before ($\bar{\psi}_{1,max} = 1.47$) as a result of the decreased lateral friction. The perturbations ψ'_n were used again to determine the forcing term acting on the second layer, that is, the right hand side of (4.15). In Figure 4.12a, the pattern of the total forcing term is presented. About one third of this forcing term can be attributed to the Reynolds stresses, and two thirds to the vortex stretching term. The forcing pattern is almost anti-symmetric with respect to $y = 0.5$. Its main feature is a maximum (minimum) north (south) of the mid-axis of the basin, at $[y] = [0.6]$ ($[y] = [0.4]$) and $[x] \in [0.15, 0.35]$. These extrema are wider in the zonal direction than for the two previous cases. A secondary extremum is found at $[x, y] = [0.45, 0.45]$ ($[x, y] = [0.45, 0.55]$). Moreover, between the maximum and the mid-axis of the basin, the forcing term changes sign, at $[x, y] = [0.25, 0.52]$ ($[x, y] = [0.25, 0.48]$). The forcing term is still mainly positive (negative) north (south) of the mid-axis of the basin.

The amplitude of the forcing term is comparable to that of the wind forcing in the upper layer. In dimensional units, the maximum vorticity input in the lower layer is $9.0 \cdot 10^2\ U^2/L^2 = 2.3 \cdot 10^{-13}\ s^{-2}$, whereas the vorticity input by the wind is $2.5 \cdot 10^{-13}\ s^{-2}$ at its maximum. However, the lower layer forcing by the perturbations only acts over part of the domain. In addition, the lower layer is deeper than the upper

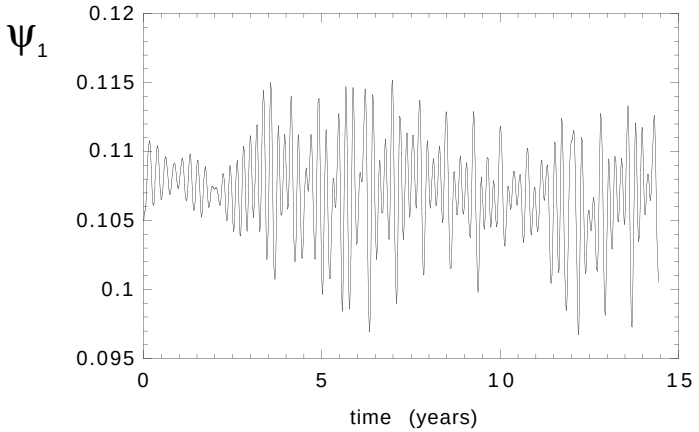

(a)

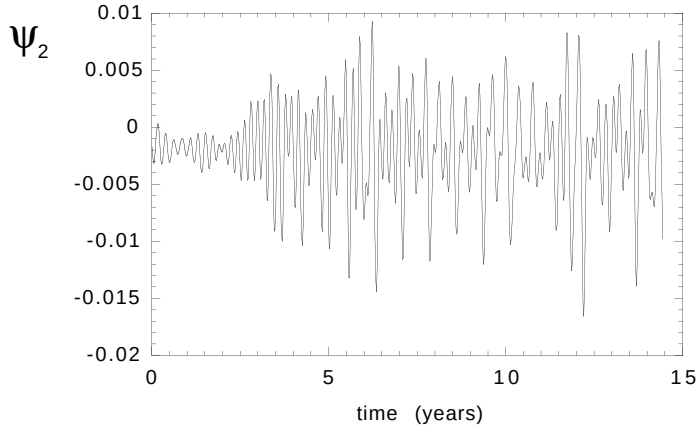

(b)

Figure 4.10: *(a) Evolution of the upper layer streamfunction ψ_1 with time, during the time integration at $Re = 45$; (b) as in (a), but for the lower layer streamfunction ψ_2. For both plots, the same grid point in the southwestern part of the basin that is used to define ψ_{SW} is used here to represent the time-dependent behavior flow.*

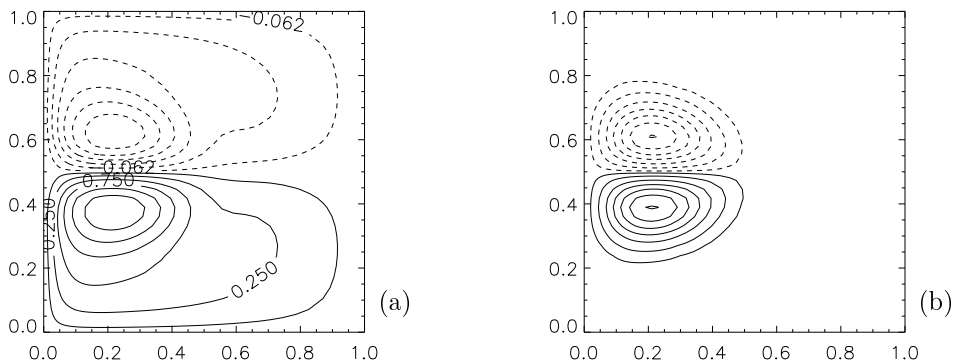

Figure 4.11: *Features of the trajectory at $Re = 45$: flow pattern of (a) the upper layer time-mean flow $\bar{\psi}_1$ (contour interval is 0.25); (b) the lower layer time-mean flow $\bar{\psi}_2$ (contour interval is 0.05).*

layer so that the resulting transport is weaker. In summary, some rough features of the forcing of the second layer persist, even though the time-dependent behavior of the flow is highly irregular for this case. However, it is clear that -not unexpectedly- the observed forcing pattern is far more complicated for this case and can no longer be explained by the self-interaction of the first unstable mode alone.

To explain this forcing of the second layer in more detail, the simulated timeseries are analyzed statistically, using Multivariate Singular Spectrum Analysis (M-SSA Plaut and Vautard, 1994, see also Chapter 6). This statistical analysis provides both the dominant spatial patterns of the variability (the EOF's), the amount of variability each of these EOF's explains and the amplitude of each EOF, which varies with time. Oscillations can be detected as pairs of EOF's. From each EOF and its amplitude one can construct the part of the original ψ'-field that is explained by this specific statistical mode, the so-called reconstructed component. In the analysis, the flow patterns in both the upper and lower layer are used, to retain the phase relation between the upper and lower layer response. By comparing the time scales and spatial patterns of the M-SSA analysis to those obtained from the linear stability analysis, the specific modes that contribute most to the variability can be identified visually. The M-SSA analysis of the time series of ψ' at $Re = 45$ (Fig. 4.10) was done over 200 timesteps of one week, so the total timeseries used for the analysis is approximately four years. The time-dependent flow seems complicated, but only a few modes appear to be responsible for this behavior. There are three dominant oscillating modes, which together explain 89% of the total variance in the simulation. From their spatial patterns and frequencies, it can be derived that these statistical modes are the two baroclinic modes associated with the Hopf bifurcations H_1 and H_2 (Fig. 4.1a) and a barotropic Rossby basin mode, which was already identified within the barotropic model (see Section 3.4.1). So, the patterns of the statistically relevant modes seem to correspond to modes which are destabilizing the stationary solutions.

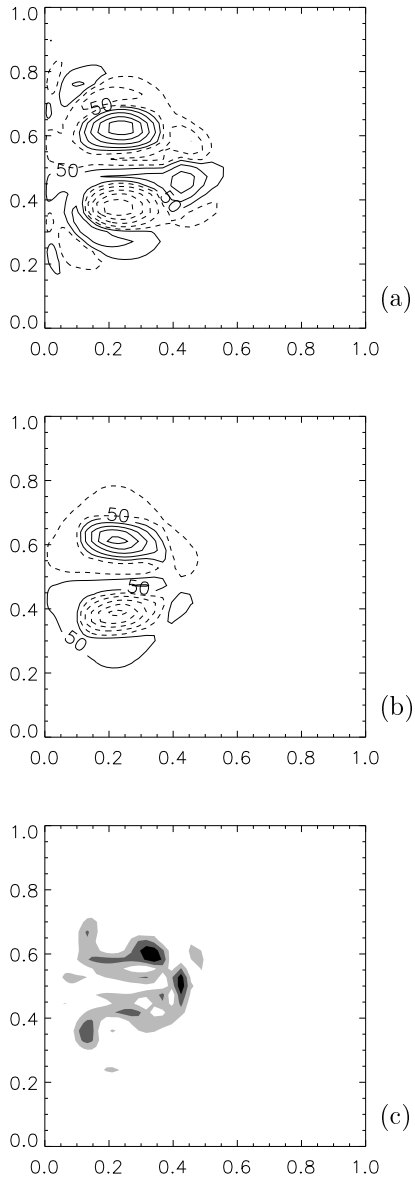

Figure 4.12: *(a) The total right hand side of (4.15), computed from the time integration at* $Re = 45$. *(b) The forcing term on the second layer solely due to the sum of the self-interactions of the three most dominant statistical modes (contour interval for (a) and (b) is 200, note that the forcing term is scaled with* $U^2/L^2 = 2.6{\cdot}10^{-16}\ s^{-2}$*). (c) Difference between (a) and (c), in % of the maximum of (a). Grayscales indicate (from light to dark) differences larger than 10%, 20% and 30%, respectively.*

Now, the self-interaction of each of the three statistical modes can be calculated from their respective reconstructed components. Since the amplitudes of the reconstructed components are time-dependent, the interaction for each mode is determined as the average over the maximum number of complete oscillations in the M-SSA timeseries of four years. The sum of the three self-interaction patterns is plotted in Figure 4.12b. The difference between Figures 4.12a and 4.12b is presented in Figure 4.12c, in % of the maximum of Figure 4.12a. The grayscales in Figure 4.12c indicate (from light to dark) differences larger than 10%, 20% and 30%, respectively. The maximum difference is 38%. Figures 4.12b and c show that almost everywhere in the basin the self-interaction patterns can explain up to 80-90% of the pattern and amplitude of the forcing pattern in Figure 4.12a.

In conclusion, the total forcing of the second layer by the perturbations as obtained from the time integration was shown in Figure 4.12a. This total forcing is the result of complex interactions of both stable and unstable modes. However, from the Figures 4.12b-c it is clear that the structure of the forcing pattern is clearly dominated by the self-interactions of the three statistical modes. Hence, even for this strongly non-linear case it appears that the self-interaction of the perturbations plays a significant role in the time-mean forcing of the deep flow. It should be noted, however, that mutual interactions between the modes associated with H_1 and H_2, that were not accounted for in this analysis, cancel out automatically. This is a consequence of the fact that the spatial patterns of these modes are symmetric and anti-symmetric with respect to $y = 0.5$ and hence are orthogonal (see Figs. 3.5 and 3.6).

4.5 Discussion

The physical mechanism of the forcing of the deep flow, in the absence of interfacial friction, was considered within the two-layer quasi-geostrophic ocean model. Focus was on the parameter regime near the first Hopf bifurcation, where the stationary flow undergoes a transition to time-dependent behavior. This clearly isolates a case where the lower layer is motionless at subcritical conditions, while a time-mean response develops at slightly supercritical conditions. The main new element of the analysis here is a comparison between the mean state of the trajectory and the unstable stationary solution provided by the continuation method. This comparison yields the rectification of the time-mean flow by the time-dependent mode, which is known exactly from the linear stability analysis of the flow.

In the weakly non-linear regime, only one mode contributes to the dynamics of the flow. The self-interaction of this mode was shown to lead to a non-zero time-mean response in the lower layer. First, the non-linear self-interaction induces a direct vorticity input into each layer separately, due to the Reynolds stresses in each layer. Besides, the perturbation causes a net horizontal flux of anomalous layer thickness in the lower layer. The associated vortex stretching acts as a potential vorticity source for the lower layer. Both vortex stretching and Reynolds stress production drive the flow in the lower layer, and can be associated with equivalent vertical velocities. Although the relation between the flow correction in the lower layer and the forcing becomes

more non-linear for a regime further from critical conditions, the basic mechanism as sketched above remains dominant. This analysis adds more clarity to previous work, both to the classical theoretical point of view as well as to the numerical results from eddy-resolving models. The presented weakly non-linear analysis shows exactly how time-dependent features due to instabilities can produce vorticity in the lower layer and, as a consequence, induce a time-mean flow there.

To connect these results with the classical results by Rhines and Young (1982), the closure of geostrophic contours for the stationary solutions was studied for varying Re and F_2. Since for the stationary solutions $\Psi_2 = 0$, the geostrophic contours are defined as lines where $F_2\Psi_1 + \beta y$ is constant. When the upper layer flow Ψ_1 is strong enough, the planetary vorticity gradient is no longer dominant and the contours can close upon themselves. With all parameters except Re fixed, closed geostrophic contours already exist at very small Reynolds numbers, near $Re = 2$. One might conclude that although finite amplitude perturbations may induce motion in the lower layer for $Re > 2$, since then the geostrophic contours are already closed in the lower layer, smaller lateral friction is needed before infinitesimally small perturbations can actually grow on the stationary solution. However, in deriving their theory, Rhines and Young (1982) made the assumption of an inviscid flow, such that its potential vorticity is conserved. Hence, a better comparison between the results for the linear stability limits and the closing of the geostrophic contours can be made by considering stability limits in F_2, when Re is increased. In Chapter 3 (Fig. 3.11), the linear stability boundary for the double-gyre flow was followed in the (Re, δ)-plane, where $\delta = F_2/F_1$. It was found that, for larger values of Re, the stability boundary moves to smaller values of δ, so to smaller F_2. The critical boundary in F_2 for the closing of the geostrophic contours is also expected to decrease with increasing Re, since the maximum of Ψ_1 increases but is still found around the same longitude (near $y = 0.36$). A comparison can be made between the boundary for linear stability $F_{2,ls}$ (that is, the value of F_2 at the first Hopf bifurcation) and the critical value $F_{2,gc}$ where the geostrophic contours close upon themselves, for different values of Re. It is found that the ratio $F_{2,gc}/F_{2,ls}$ goes from 0.23 at $Re = 17.5$ to 0.46 at $Re = 34.5$. So, for a less viscous regime the two boundaries derived for the existence of the deep flow are closer. However, it is not obvious that they will coincide for larger Re.

In the trajectories studied, the time-mean deep flow is forced by transient effects. The question arises whether a similar stationary lower layer flow can be generated by adding a simple interfacial friction term to the equations, with friction coefficient C_i. When this interfacial friction coefficient is chosen such that for the weakly non-linear case ($Re = 20$) the maxima of the streamfunctions in the second layer match, the patterns of the streamfunctions are found to be fairly similar. However, when Re is increased and C_i is kept fixed, the maximum of the streamfunction in the lower layer Ψ_2 is soon much too small in comparison with the mean states of time integrations at the same Reynolds number, while in the upper layer predictions of the maximum value of Ψ_1 are too high. That is, the downward momentum flux from the upper to the lower layer is not large enough. This can be resolved by increasing C_i, but then the appropriate C_i depends strongly on Re which is clearly an undesirable property.

Our results are in agreement with the basin integrated energy budgets as derived

from simulations with numerical models (e.g., Holland, 1978). In numerical simulations with eddy-resolving ocean general circulation models, oscillatory modes due to baroclinic and barotropic instabilities arise spontaneously as a critical Reynolds number is exceeded. Barotropic and baroclinic instabilities both limit the large-scale upper ocean circulation: kinetic energy is transferred downward, filling the deeper ocean with an eddy-induced gyre circulation. This energy transfer is accomplished by the work done by pressure forces acting at the interface, which is the result of either a correlation between vertical velocity and layer thickness (density), i.e. baroclinic instability, or a correlation between vertical velocity and geopotential (barotropic instability). The associated vortex stretching (baroclinic instability) and Reynolds stresses (barotropic instability) provide the vorticity source for the deeper layer flow (Holland, 1978; Holland and Haidvogel, 1980).

Appendix

The equations describing the evolution of perturbations $\boldsymbol{\varphi}$ on a stationary solution are

$$(\mathcal{G}\frac{\partial}{\partial t} + \mathcal{L})\boldsymbol{\varphi} + \mathcal{N}(\boldsymbol{\varphi})\boldsymbol{\varphi} = 0 \qquad (A4.1)$$

where $\boldsymbol{\varphi} = (\phi_1, \eta_1, \phi_2, \eta_2)$ and $\mathcal{G}$, $\mathcal{L}$ and $\mathcal{N}(\boldsymbol{\varphi})$ are the operators defined in (4.3). For slightly supercritical conditions, the equilibration of the instabilities has to be determined using a non-linear analysis. Near criticality, the equilibration occurs on the time scale τ which is much larger than the growth rate of the instability itself, $\tau = \varepsilon^2 t$, where ε is a measure of the instability of the flow (see (4.5)). Hence, when the finite amplitude of the perturbations is small compared to that of the stationary solution, the solution vector $\boldsymbol{\varphi}$ can be expanded as

$$\boldsymbol{\varphi} = \varepsilon\boldsymbol{\varphi}^{(1)} + \varepsilon^2\boldsymbol{\varphi}^{(2)} + \cdots \qquad (A4.2a)$$

where

$$\boldsymbol{\varphi}^{(1)}(x, y, t, \tau) = \sum_{j=1}^{K} A_j(\tau)\ \hat{\boldsymbol{\varphi}}^j(x, y)\ e^{\sigma_j t} + c.c. \qquad (A4.2b)$$

is the general solution of the linear stability problem (with slowly varying amplitude) and c.c. indicates complex conjugate. The eigenvalues $\sigma_j = \lambda_j + i\nu_j$ are ordered according to their real part, with -at the stability boundary- $\lambda_1 = 0$ and $\lambda_j < 0$ for all $j > 1$. The sum is truncated at some value of K for which higher modes are very stable (i.e., for which $\lambda_{K+1} \ll 0$), so K is the number of relevant interacting modes. Since the non-linear operator is quadratic, it follows from the equations at $\mathcal{O}(\varepsilon^2)$ that

$$\boldsymbol{\varphi}^{(2)}(x, y, t, \tau) = \sum_{j=1}^{K}\ \sum_{l=1}^{K} A_j(\tau)A_l(\tau)\tilde{\boldsymbol{\varphi}}^{jl}(x, y)e^{(\sigma_j+\sigma_l)t}$$

$$+A_j(\tau)A_l^*(\tau)\boldsymbol{\varphi}^{jl}(x, y)e^{(\sigma_j+\sigma_l^*)t}] + c.c. \qquad (A4.2c)$$

The second order contribution contains both a slowly (time scale τ) developing part with spatial pattern $\tilde{\boldsymbol{\varphi}}^{jl}$ and a fast oscillating part with frequency 2ν and spatial pattern $\boldsymbol{\varphi}^{jl}$. The coefficient functions $\tilde{\boldsymbol{\varphi}}^{jl}$ and $\boldsymbol{\varphi}^{jl}$ that specify the spatial patterns of the correction can be determined from

$$(\mathcal{G}(\sigma_j + \sigma_l) + \mathcal{L})\tilde{\boldsymbol{\varphi}}^{jl} = -\mathcal{N}(\hat{\boldsymbol{\varphi}}^j)\hat{\boldsymbol{\varphi}}^l$$

$$(\mathcal{G}(\sigma_j + \sigma_l^*) + \mathcal{L})\boldsymbol{\varphi}^{lj} = -\mathcal{N}(\hat{\boldsymbol{\varphi}}^j)\hat{\boldsymbol{\varphi}}^{l*} \qquad (A4.3)$$

When it is assumed that only one mode determines the dynamics to leading order ($K = 1$), it follows from (A4.2c) that at $\mathcal{O}(\varepsilon^2)$ a non-oscillatory finite amplitude contribution is obtained from the self-interaction of the most unstable mode, which is of the form

$$\boldsymbol{\varphi}^{(2)} = \mid A_1 \mid^2\ \boldsymbol{\varphi}^{11} \qquad (A4.4)$$

From the second part of equation (A4.3) the spatial pattern $\boldsymbol{\varphi}^{11}$ of this finite amplitude contribution can be derived. Write $\hat{\boldsymbol{\varphi}} = \hat{\boldsymbol{\varphi}}^1$ for the pattern of the most unstable mode and $\bar{\boldsymbol{\varphi}} = \boldsymbol{\varphi}^{11}$ for the pattern of the rectification. Equation (A4.3) then yields

$$\mathcal{L}\bar{\boldsymbol{\varphi}} = -2\mathcal{R}(\mathcal{N}(\hat{\boldsymbol{\varphi}})\hat{\boldsymbol{\varphi}}^*) \tag{A4.5}$$

where $\mathcal{R}$ indicates the real part.

The amplitude A_1 can be obtained from compatibility conditions at $\mathcal{O}(\varepsilon^3)$. From classical studies of baroclinic instability of channel flows (Pedlosky, 1970) it is known that when only one unstable mode is present the amplitude A_1 satisfies the equation

$$\frac{\partial A_1}{\partial \tau} = \lambda A_1 - \Lambda A_1 |A_1|^2 \tag{A4.6}$$

(the Landau equation). In this equation, λ is the linear growth factor known from the linear stability analysis. The factor Λ contains all the non-linear interactions at $\mathcal{O}(\varepsilon^3)$, i.e. the interactions between the unstable mode and the second order flow correction. So, when only one unstable mode is present, Λ can be determined and thus the non-linear equilibration of the amplitude A_1 of the unstable mode.

Chapter 5

The interaction of a Deep Western Boundary Current and the wind-driven gyres*

Recent modelling and observational studies have indicated that the interaction of the Gulf Stream and the Deep Western Boundary Current (DWBC) in the North Atlantic may induce low-frequency variability at interannual to decadal time scales. To understand the origin of this low-frequency variability, stationary solutions of the coupled wind-driven/DWBC system are computed, again using lateral friction as the control parameter. In addition, the stability of these stationary solutions is assessed. The results are connected to those for purely wind-driven flows by varying the strength of the DWBC transport, to investigate the origin of changes in the bifurcation structure.

5.1 Introduction

Near Cape Hatteras, where the Gulf Stream leaves the North American coast and flows (north-)eastward into the Atlantic, it crosses the Deep Western Boundary Current (DWBC), which flows southward at greater depths (Swallow and Worthington, 1961). The DWBC originates from high latitudes in the North Atlantic, where intermediate and deep water masses are formed through convection (Section 1.1.2). Both observations and numerical studies suggest a strong dynamical interaction between the two currents, resulting in complex behavior of the flow in this cross-over region. An overview of early records of Gulf Stream and deep undercurrent measurements collected between 1961 and 1972 was given by Richardson (1977). Estimates of the

*This chapter is partly based on the paper "*The interaction of a Deep Western Boundary Current and the wind-driven gyres as a cause for low-frequency variability*", by C. A. Katsman, S. S. Drijfhout and H. A. Dijkstra (accepted for publication in *J. Phys. Oceanography*)

undercurrent transport, measured over periods of typically a few weeks, varied between 2 and 50 Sv, with a mean value of 16 Sv. Hogg (1983) showed that the deep circulation in the cross-over area consists of two components: the DWBC flowing southward along the continent and transporting approximately 12 Sv, and two recirculation gyres aligned with the Gulf Stream axis. He argued that these recirculation gyres are driven by eddy momentum fluxes caused by Gulf Stream and DWBC instabilities. In Pickart and Smethie Jr. (1993), it was reported that the shallowest part of the DWBC (at 500-1200 meters depth) is partly entrained by the Gulf Stream and follows an eastward course, whereas the deeper waters (at 2500-3500 meters depth) do cross underneath the Gulf Stream and stay close to the western boundary of the basin. Recent Lagrangian observations obtained with RAFOS floats launched at approximately 800 and 3000 meters depth support this view of the splitting of the DWBC in the cross-over region (Bower and Hunt, 2000a,b). From surveys conducted over the period 1991-1995 a total mean DWBC transport of 19 Sv was deduced, of which 8 Sv is carried in the shallower part, and 11 Sv in the deeper part of the DWBC (Pickart and Smethie Jr., 1998). Current meter observations covering a period of three years were analyzed by Pickart (1994). These observations indicate that on time scales shorter than a year, fluctuations of the velocity of the DWBC can be attributed to pulsing of the DWBC transport and to meandering of the DWBC itself. On interannual time scales, it appears that fluctuations in the DWBC are connected to those of the Gulf Stream.

The observational record is still fairly short, and hence can only give limited information on the characteristics of the variability on longer time scales (Pickart, 1994). In contrast, ocean models can be applied to study the variability of the interacting Gulf Stream and DWBC on both shorter and longer time scales. For example, Thompson and Schmitz Jr. (1989) and Tansley and Marshall (2000) demonstrated the strong impact of the DWBC on both the mean path of the Gulf Stream, and on (the variability of) its separation point in two-layer models. Using a three-layer primitive equation model of the Gulf Stream/DWBC system, Spall (1996a,b) found pronounced low-frequency variability. The circulation in his model comprises a Gulf Stream-like surface circulation and a shallower and deeper DWBC, and its mean state agrees well with the available observations (Pickart and Smethie Jr., 1993). Oscillations with a time scale of approximately 10 years are clearly present in the model simulations. During the high-energy phase of such an oscillation, the DWBC in the second layer is deflected by the Gulf Stream and turns eastward in the cross-over region. During the opposite phase, it is only partly deflected and part of it remains close to the coast and crosses underneath the Gulf Stream. In the upper layer, the Gulf Stream penetrates far into the basin during a high-energy phase, whereas its penetration scale is much less during a low-energy phase. The low-frequency variability is absent when there is no DWBC in the second layer, and Spall (1996b) concludes that the decadal oscillations in his model simulations are caused by interactions of the Gulf Stream and the upper DWBC.

In this chapter, it is investigated how the picture of the internal variability of the wind-driven gyres discussed in Chapter 3 changes when a DWBC is allowed to interact dynamically with the wind-driven flow. A priori, there seem to be several

possibilities depending on whether and how the DWBC modifies the structure of stationary solutions and changes the preferred time scales arising from instabilities on these stationary solutions. These issues are systematically studied within the two-layer quasi-geostrophic model described in Section 2.1, now extended with a DWBC. The DWBC is modelled through open boundary conditions in the lower layer, and its volume transport can be prescribed. Section 5.2 provides a description of the implementation of a DWBC into the two-layer model used in this study, as well as a short discussion of the methods applied by Thompson and Schmitz Jr. (1989); Spall (1996a) and Tansley and Marshall (2000). The stationary solutions for the coupled wind-driven/DWBC system are presented in Section 5.3, and compared to the results for the purely wind-driven flow discussed in Chapter 3. The presence of the DWBC appears to have a large impact on the dynamics of the circulation. First, multiple equilibria disappear when a DWBC is introduced: only one branch of stationary solutions remains. Second, stationary solutions on this unique branch are found to be susceptible to instabilities with intermonthly to interannual time scales. The precise changes in the bifurcation diagram and the changes in the character of the instabilities are investigated in Sections 5.4 and 5.5, respectively, by continuously increasing the strength of the DWBC from zero, and thus connecting the results presented in Section 5.3 with those presented in Section 3.2.

5.2 Implementation of a DWBC

In a wind-driven ocean model, a DWBC can be implemented by prescribing in- and outflow conditions at the lateral boundaries. In this set-up, no feedbacks are possible between the lower limb of the thermohaline circulation (the DWBC) and the upper limb (the Gulf Stream at the surface). Thompson and Schmitz Jr. (1989) used a two-layer primitive equation model to study the interactions between the Gulf Stream and the DWBC, in which realistic coastlines and bottom topography were incorporated. In the lower layer, they forced a DWBC by prescribing an inflow in the northwestern part of the basin. The upper layer is forced both by a surface wind stress and by an inflow in the southwestern part of the basin. The latter transport represents both the wind-driven Sverdrup transport in the North Atlantic Ocean that is not captured by the limited model area as well as waters that originate from the Southern Hemisphere and form the upper limb of the thermohaline circulation. At the outflow boundaries (the eastern boundary in the upper layer and the southern boundary in the lower layer, a radiation condition is applied, which prevents inflow through this boundary (Orlanski, 1976). Spall (1996a,b) simplified this model configuration by defining a flat bottom except for a continental slope in the northwest, and an idealized slanted coastline to represent the American continent. He added a third model layer to simulate the differing behavior of the upper and lower DWBC, in accordance with the observations (Pickart and Smethie Jr., 1993). In that respect, the model is more realistic than that by Thompson and Schmitz Jr. (1989). The inflow conditions he used were similar to those applied by Thompson and Schmitz Jr. (1989). In the upper layer, the outflow is over the whole eastern boundary, whereas in the second

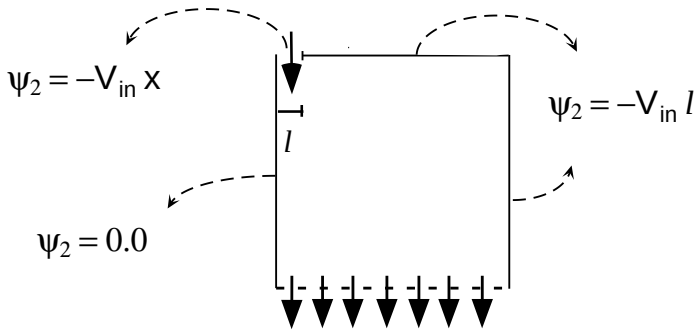

Figure 5.1: *Plan view of the second layer and the applied boundary conditions. V_{in} is a control parameter defining the (dimensionless) inflow velocity of the DWBC in the northwest of the basin, over the (dimensionless) width l.*

and third layer the whole southern boundary is open to allow for the outflow of the DWBC. A radiation condition is used to assure that the in- and outflowing transports match. The two-layer model used by Tansley and Marshall (2000) is more idealized. It has straight coastlines and the possibility to include a continental shelf in the west. In contrast to the models used by Thompson and Schmitz Jr. (1989) and Spall (1996a,b), the surface layer is purely wind-driven. Inflows and outflows are handled by appending sponge layers in the north and south, in which the velocities are relaxed towards prescribed values.

In this study, a DWBC was implemented in the two-layer quasi-geostrophic model in an idealized way. In the upper layer, the flow is purely wind-driven, as in Tansley and Marshall (2000). In the second layer, an inflow is prescribed in the northwestern part of the basin, whereas the outflow is over the full width of the southern boundary. In Figure 5.1, a plan view of the second layer is shown, together with the applied boundary conditions. The inflow is prescribed over a dimensionless width l ($l < 1$), by defining the streamfunction ψ_2 at the northern boundary as

$$\psi_2 = \begin{cases} -V_{in}\ x & \text{for} \quad x \in [0, l] \\ -V_{in}\ l & \text{for} \quad x \in [l, 1] \end{cases} \qquad \text{at } y = 1$$

The (positive) parameter V_{in} controls the strength of the DWBC in the northwest. The value used for l is 0.15, corresponding to a dimensional inflow width of 150 km for the standard model parameters. The dimensional inflow velocity V_{in}^* (in m/s) and the incoming DWBC transport Γ_2^* (in m^3/s) are

$$V_{in}^* = V_{in}\ U; \qquad \Gamma_2^* = V_{in}\ U \cdot l\ L \cdot D_2$$

upper	north	free slip	$\psi_1 = 0$	$\zeta_1 = 0$
layer	south	free slip	$\psi_1 = 0$	$\zeta_1 = 0$
	east	no slip	$\psi_1 = 0$	$\partial\psi_1/\partial x = 0$
	west	no slip	$\psi_1 = 0$	$\partial\psi_1/\partial x = 0$
lower	north	inflow	ψ_2 prescribed	$\zeta_2 = 0$
layer	south	outflow	$\partial\psi_2/\partial y = 0$	$\partial\zeta_2/\partial y = 0$
	east	no slip	$\psi_2 = -V_{in}\ l$	$\partial\psi_2/\partial x = 0$
	west	no slip	$\psi_2 = 0$	$\partial\psi_2/\partial x = 0$

Table 5.1: *Overview of the boundary conditions for the two-layer model in which a DWBC is incorporated. The standard value used for l in this study is $l = 0.15$.*

The net outward transport through the southern boundary is required to amount to the transport coming in through the northern boundary. This yields that the integrals of the meridional velocity $v_2 = \partial\psi_2/\partial x$ over the open northern and southern boundaries must equal:

$$\int_0^l \frac{\partial\psi_2}{\partial x}\bigg|_{y=1} dx = \int_0^1 \frac{\partial\psi_2}{\partial x}\bigg|_{y=0} dx$$

Since ψ_2 has to be continuous along each boundary, it is clear from Figure 5.1 that this condition is satisfied by prescribing $\psi_2 = 0$ at the western boundary and $\psi_2 = -V_{in}\ l$ at the eastern boundary. Furthermore, it is required here that in the south the flow is normal to the boundary:

$$\frac{\partial\psi_2}{\partial y} = 0; \qquad \frac{\partial\zeta_2}{\partial y} = 0 \qquad\qquad \text{at } y = 0$$

In this way, the outflow profile at the southern boundary is not fixed, but can adjust to variations of V_{in} and other model parameters. With these boundary conditions, it is possible that locally the transport through the southern boundary is inward, as long as it is compensated by an outflow elsewhere along this boundary. In practice, this feature has proven not to cause any problems. For the closed boundaries, no-slip conditions are prescribed in the east and west, and free-slip conditions in the north and south, as for the standard model configuration. In Table 5.1, an overview of all the boundary conditions is given.

5.3 Coupled wind-driven/DWBC flows

In this section, the stationary solutions and the stability characteristics of the wind-driven flow obtained when a DWBC is present are presented, and contrasted with those obtained when a DWBC is absent ($V_{in} = 0.0$), discussed in Chapter 3. As the standard value, an inflow of 7.2 Sv is chosen, which corresponds to $V_{in} = 2.1$ or $V_{in}^* = 3.4\ cm/s$. All other parameters are kept the same as for the purely wind-driven flow (Table 2.1). It will be shown that such a weak DWBC (as compared to

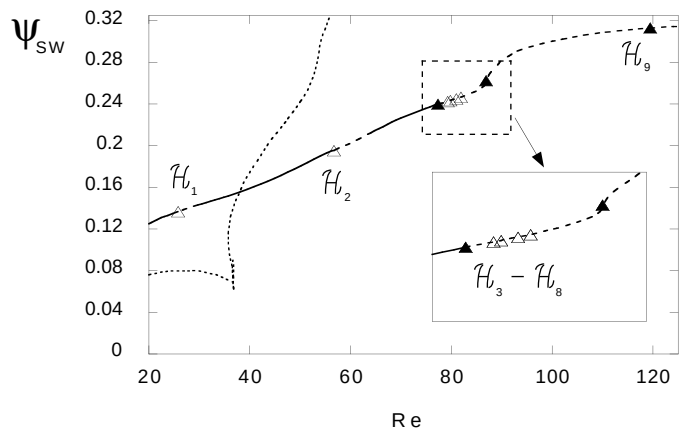

Figure 5.2: *Bifurcation diagram as a function of Re for the coupled wind-driven/DWBC flow ($V_{in} = 2.1$). The same measure ψ_{SW} as used in previous bifurcation diagrams is plotted on the vertical axis. Solid (dashed) lines indicate (un-)stable solution branches. Marked are the Hopf bifurcation points $\mathcal{H}_1$ to $\mathcal{H}_9$ (triangles). Solid triangles are used when the associated modes remain unstable for increasing Re, open triangles for the bifurcation points associated with those modes that stabilize again through a reverse Hopf bifurcation. The dash-dotted curve indicates the stationary solutions found for the purely wind-driven flow, shown earlier in Figure 3.1.*

the observations) already has a large impact on the characteristics of the flow. Re is varied between 20 and 125, so δ_M^* ranges from 37 to 20 km, whereas $\delta_I^* = 32$ km.

The bifurcation diagram for the coupled wind-driven/DWBC flow is shown in Figure 5.2. The stationary solution branches are plotted with Re on the horizontal axis, and the same measure for the solution that was used in the previous bifurcation diagrams, ψ_{SW}, on the vertical axis. For comparison, the stationary solutions found for the purely wind-driven flow are shown in Figure 5.2 as a dash-dotted curve. With a DWBC of the chosen strength, only one branch of solutions is found for the investigated range in Re. The flow first becomes unstable through a Hopf bifurcation (marked $\mathcal{H}_1$ in Figure 5.2) at $Re = 25.8$. However, at $Re = 29.7$ the growth rate of this mode becomes negative again, and the flow stabilizes through a reverse Hopf bifurcation (not explicitly marked in Fig. 5.2, but visible as the transition from a dashed to a solid branch). A stability analysis of the stationary solutions reveals that for $Re \in [20, 125]$ nine different modes destabilize the flow. The time scales of these modes (which will be referred to as B_1 to B_9, B for Boundary Current) vary from 0.7 to 22.3 years at critical conditions. In Figure 5.2, the Hopf bifurcation points where these modes become unstable are marked $\mathcal{H}_1$ to $\mathcal{H}_9$. Six of the oscillatory modes, among which B_1, stabilize again for larger values of Re through a reverse Hopf bi-

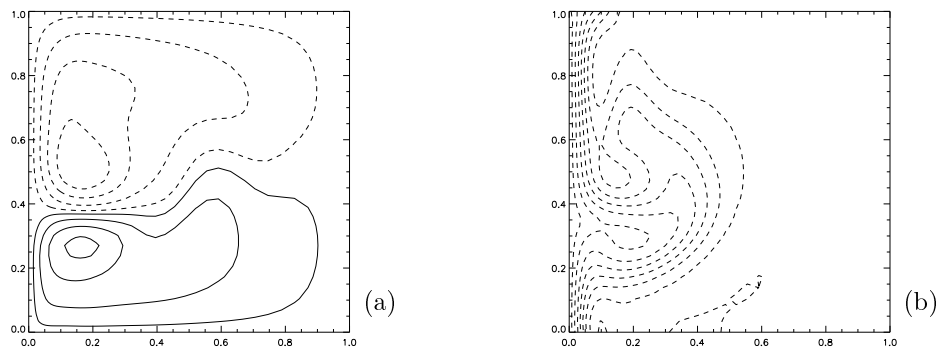

Figure 5.3: *Contour plot of the stationary solution for $Re = 31$, in the (a) upper and (b) lower layer. Contour interval is 0.3 in (a) and 0.05 in (b).*

furcation, but three of them remain unstable. Hopf bifurcations associated with the latter modes ($\mathcal{H}_3$, $\mathcal{H}_8$ and $\mathcal{H}_9$) are marked with solid triangles in Figure 5.2, the others with open triangles. The modes that stabilize again attain maximum dimensional growth rates $\lambda^* = \lambda U/L$ of 0.04 to 1.0 $years^{-1}$.

As an example of the stationary solutions that are found, the linearly stable solution at $Re = 31$ is plotted in Figure 5.3. The upper layer jet flows (north-)eastward, and its separation point lies 125 km south of the zero wind stress curl line (the mid-axis of the basin). This in contrast to the symmetric wind-driven flows, for which separation occurs exactly at the mid-axis of the basin as a result of the symmetry properties of the quasi-geostrophic model. In the second layer, the DWBC mainly follows the western boundary southward, until it reaches the cross-over region where it is deflected eastward. It returns to the coast further south, and then continues along the western boundary again. Despite the obvious simplifications of our model set-up, the stationary solutions show basic features of the Gulf Stream/DWBC interaction simulated by more complicated models. As in Thompson and Schmitz Jr. (1989), the separation point shifts southward due to the presence of the DWBC (Fig. 5.3). The deflection of the DWBC near the cross-over point is also captured by the model.

When the results for the coupled wind-driven/DWBC flow (Fig. 5.2) are compared to those obtained for the purely wind-driven flow (Section 3.2), it is clear that the presence of the DWBC has a strong effect on both the structure of the bifurcation diagram, on the spatial patterns of the stationary solutions and on their stability characteristics. First, when the DWBC is present, regimes of multiple equilibria do not exist. The precise details of this transition towards unique stationary flows is explored in Section 5.4. Second, whereas only intermonthly oscillatory modes destabilize the flow in absence of a DWBC (Section 3.3), interannual to decadal modes are found when a DWBC is present. This preference of the coupled wind-driven/DWBC flow for longer time scale instabilities is explored in Section 5.5.

5.4 Multiple equilibria

The multiple stationary equilibria that were found for the purely wind-driven flow have disappeared when a DWBC of 7.2 Sv is present (compare Figs. 3.1 and 5.2). By gradually increasing the strength of the DWBC from zero, the results of the two cases can be connected and the fate of the multiple equilibria can be studied.

For the purely wind-driven flow, multiple stationary solutions exist in the region $Re \in [Re_{L_2}, Re_{L_3}]$ due to the existence of two limit points and two pitchfork bifurcations (Section 3.2). These multiple equilibria are shown again in Figure 5.4a, a detail of the bifurcation diagram for $V_{in} = 0.0$. Both the limit point L_1, the pitchfork bifurcations P_1 and P_2 and the limit point L_3 that connects the asymmetric solution branches are marked in this figure. The limit point L_2 lies outside the interval in Re shown here. The symmetric solution branch is marked 'S', while asymmetric solutions are marked 'separate north' (smaller ψ_{SW}) or 'separate south' (larger ψ_{SW}), indicating that the jet of the stationary solution separates north or south of the mid-axis of the basin, respectively. In Figure 5.4b, the solution branches are plotted for $V_{in} = 1.0 \cdot 10^{-3}$ (a DWBC transport of 0.003 Sv). The weak DWBC destroys the reflection symmetry of the model with respect to the mid-axis of the basin, and as a result, the pitchfork bifurcations break up. The former symmetric solution branch now connects to the branch of 'separate south'-solutions. The two asymmetric solution branches with jets that separate north of $y = 0.5$ ('separate north') form a closed loop. This closed loop shrinks when V_{in} is increased further (Fig. 5.4c, $\Gamma_2^* = 0.01$ Sv) and eventually disappears completely. So, apparently the stationary solutions with a jet separating north of the mid-axis of the basin can not exist in the presence of a DWBC, and only a branch of solutions with a jet that separates south of the mid-axis of the basin remains. This is consistent with findings by Thompson and Schmitz Jr. (1989) and Tansley and Marshall (2000) that the DWBC pushes the separation point southward.

Despite the disappearance of the 'separate north'-branch, multiple stationary solutions still exist when the DWBC transport is weak, due to the limit points L_3 and L_2. However, when the inflow rate V_{in} is increased further, these limit points on the 'separate south'-branch disappear as well. To show this, the remaining stationary solution branch is plotted as a function of Re in Figure 5.5, for various DWBC transports. For an inflow rate $V_{in} = 0.5$, L_3 (marked by a filled circle in Fig. 5.5) has moved to a larger value of Re, while L_2 (open circle) remains in the same position. For $V_{in} = 1.0$, the limit points are found closer together and have both moved to higher values of Re ($Re_{L_3} = 100.7$ and $Re_{L_2} = 100.2$). Finally, when the DWBC is strong enough, multiple equilibria do not exist anymore; no limit points are found for Re up to 125 for $V_{in} = 2.1$ ($\Gamma_2^* = 7.2$ Sv). So, the regimes of multiple equilibria that were found for the purely wind-driven flow are no longer present when a DWBC is introduced.

This result is in agreement with the discussion in Section 3.2.1 that the limit points are a manifestation of a transition from a frictionally dominated to an inertially dominated flow regime, which is characteristic of flows with internal symmetry. The presence of the DWBC destroys the internal symmetry of the flow, and as a result the

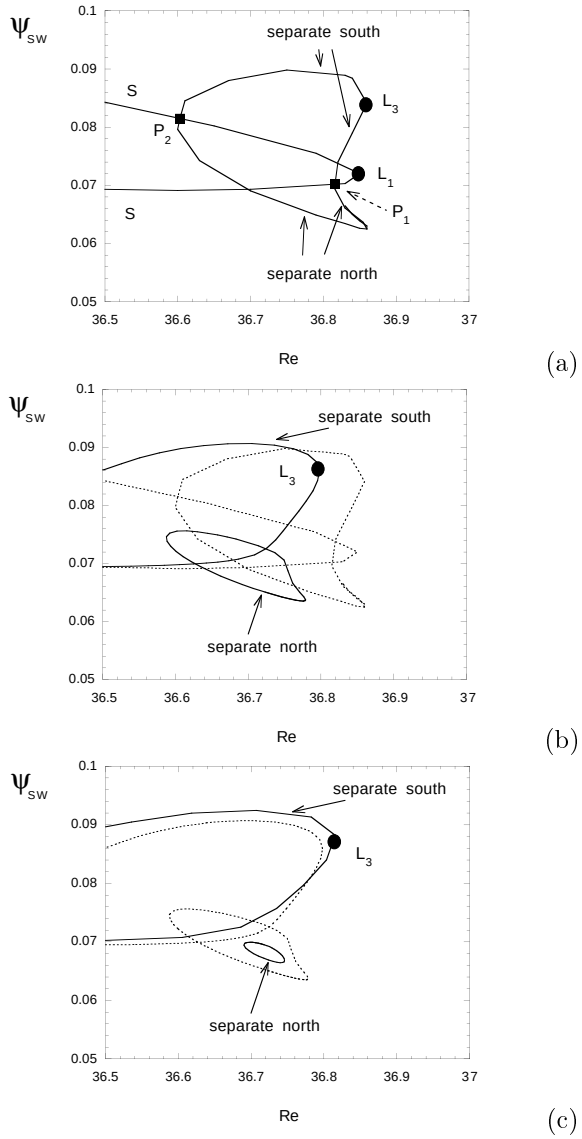

Figure 5.4: *Detail of the bifurcation diagram for $Re \in [36.5, 37.0]$, for cases without a DWBC and with a very weak DWBC: (a) $V_{in} = 0.0$, (b) $V_{in} = 1.0 \cdot 10^{-3}$ and (c) $V_{in} = 3.0 \cdot 10^{-3}$ ($\Gamma_2^* \in [0.0, 0.01]$ Sv). In (b) and (c), the solutions of the previous panel are shown as well for comparison (dash-dotted curve). 'S' marks a symmetric solution branch, 'separate north' ('separate south') marks a solution branch with a jet that separates north (south) of the mid-axis of the basin. The bifurcation points P_1, P_2 and L_1 and L_3 are marked as well.*

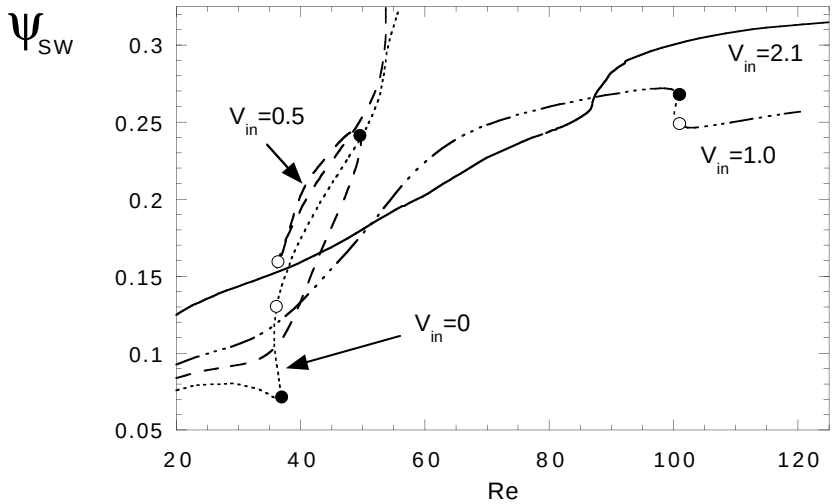

Figure 5.5: *Bifurcation diagram for Re between* 20 *and* 125*, for* $V_{in} = 0.0,\ 0.5,\ 1.0$ *and* 2.1 *(dotted, dashed, dash-dotted and solid branches, respectively). The limit points* L_2 *and* L_3 *are marked by an open and a filled circle.*

transport of vorticity across the mid-axis of the basin is no longer zero. Hence, the input of vorticity by the wind can be partly redistributed internally, whereas it needed to be dissipated in each gyre separately for the symmetric flows. As a consequence, no sudden rescaling of the solution occurs when Re is increased.

5.4.1 Flow patterns

As the strength of the DWBC is increased, the spatial patterns of the stationary solutions change substantially. Examples of stationary flows for increasing V_{in} and $Re = 31$ are shown in Figure 5.6. For $V_{in} = 0.0$, the stationary solution at $Re = 31$ is symmetric (Fig. 5.6a-b). The separation point of the upper layer jet shifts southward with increasing V_{in}, as in Thompson and Schmitz Jr. (1989). It shifts over a distance of 35 km for $V_{in} = 0.5$ (Fig. 5.6c) and over 250 km for $V_{in} = 3.0$ (Fig. 5.6g). The jet direction changes to northeastward for increasing inflow rates, and stationary meanders develop. The upper layer streamfunction Ψ_1 decreases with increasing V_{in}.

In the second layer, the undercurrent follows the coastline until it reaches the cross-over region. There, part of the flow continues along the coast and part gets deflected eastward and crosses the midlatitude jet east of the recirculation cells in the upper layer. For higher inflow rates, the DWBC is deflected less far into the basin in the cross-over region. As is clear from Figure 5.6g, a rather weak DWBC transport (in comparison with the observed transport) already induces a large southward shift of the separation point for the basin of 1000×1000 km used here. Therefore, larger DWBC transports were not considered.

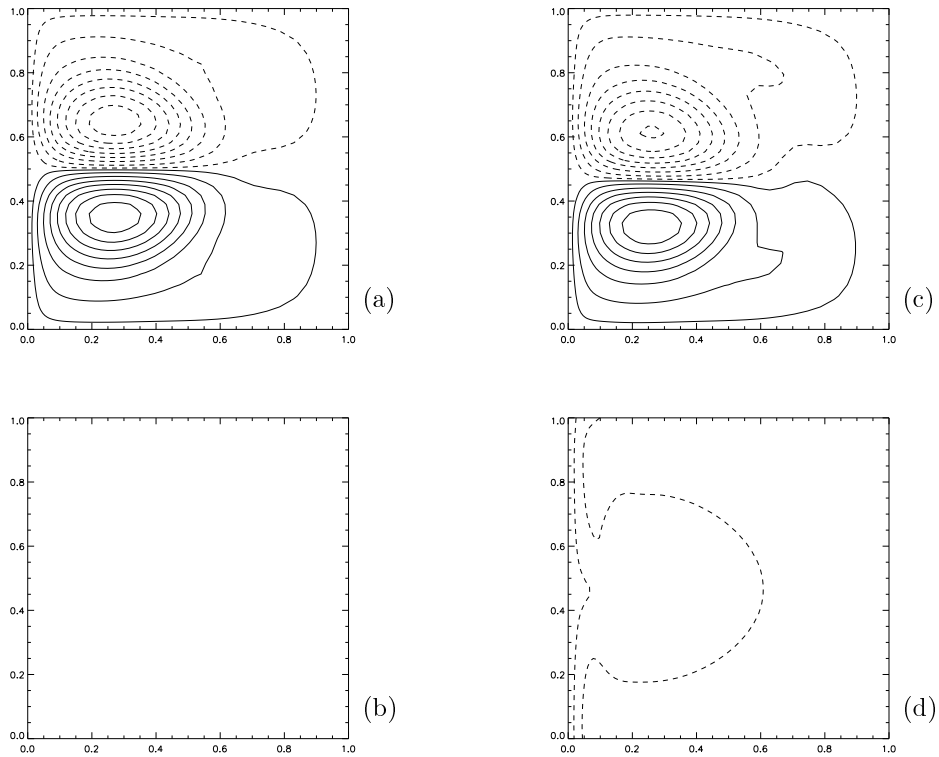

Figure 5.6: *Streamfunction of the stationary solution in the upper and lower layer (upper and lower panels) for a fixed Reynolds number ($Re = 31$) and increasing DWBC transport: (a-b) $V_{in} = 0.0$, (c-d) $V_{in} = 0.5$, (e-f) $V_{in} = 1.5$, and (g-h) $V_{in} = 3.0$ ($\Gamma_2^* \in [0.0, 10.0]$ Sv). Contour interval is 0.3 in the upper and 0.05 in the lower layer. Recall that the stationary solution for $Re = 31$ and $V_{in} = 2.1$ was already shown in Fig. 5.3.*

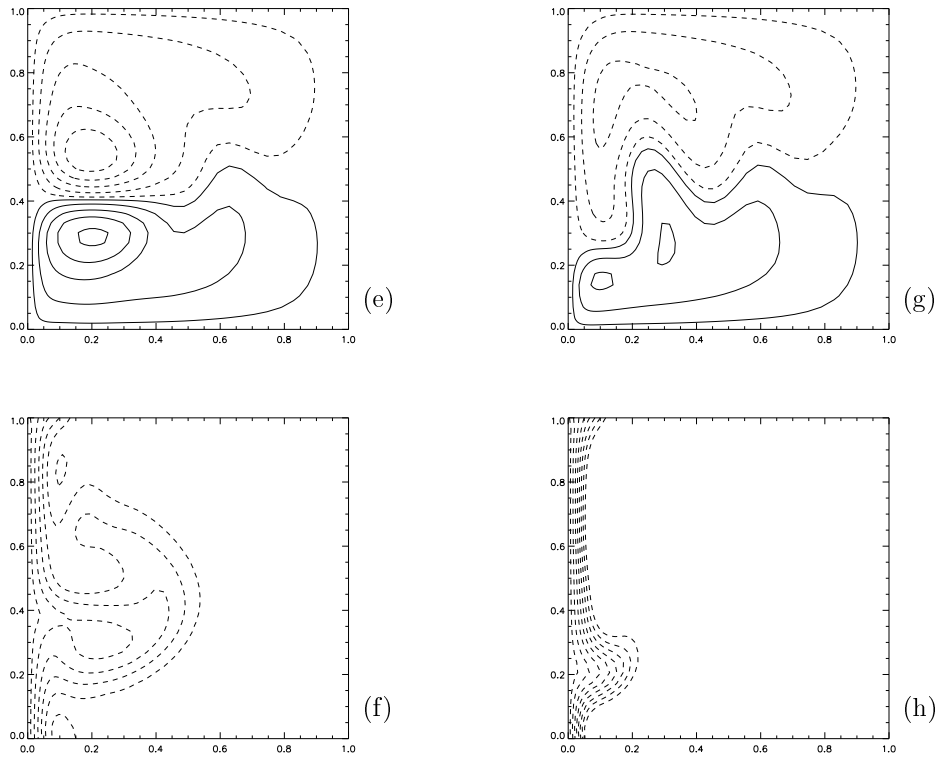

Fig. 5.6, continued.

5.4.2 Vorticity balance

When a DWBC is introduced, the symmetric solution branch connects to the 'separate south'-branch (see Fig. 5.4b) and hence one might expect to obtain a stationary solution with a jet that separates south of the mid-axis of the basin, associated with a stronger subtropical gyre and a southeastward directed jet, as for the purely wind-driven case (Fig. 3.9c). However, for non-zero V_{in} the subpolar gyre of the solution is stronger than the subtropical gyre (Fig. 5.6c). For higher values of V_{in} the maximum of the upper layer streamfunction reduces but the subpolar gyre remains strongest (Figs. 5.6e-g). This strengthening of the subpolar gyre can be explained by considering the conservation of potential vorticity for the coupled wind-driven/DWBC flow. As long as the DWBC is weak, its presence mainly alters the potential vorticity balance through changes in the tilt of the interface between the two layers. In the western boundary layer the interface rises, whereas it falls over the rest of the domain (recall that the lower layer depth is proportional to $\Psi_1 - \Psi_2$, and $\Psi_2 < 0$). This downward displacement of the interface over a large part of the domain tends to reduce the potential vorticity of the flow, and additional positive relative vorticity is required to conserve potential vorticity. This is consistent with a stronger subpolar and a weaker subtropical gyre in the upper layer. As a result of the difference in strength of the two gyres, the path of the jet shifts to a northeastward direction.

The strong decrease in Ψ_1 with increasing V_{in} can only partly be explained. Since the presence of the DWBC results in a stationary solution which is no longer symmetric with respect to the zero wind stress curl line, solutions with $V_{in} \neq 0$ are able to advect vorticity across the mid-axis of the basin. This allows for a partial internal redistribution of the input of vorticity by the wind, as explained in Section 3.2.1, which reduces the transport in the upper layer. However, this effect can not account for the reduction of the upper layer transport for $V_{in} = 3.0$ to about 65% of the transport predicted by Sverdrup theory. Also for this reason, a lower value of V_{in} was chosen as the standard value. For $V_{in} = 2.1$, the strength upper layer transport is close to that predicted by Sverdrup theory (see Fig. 5.3a).

For the stationary solution in Figure 5.6e-f, with $V_{in} = 1.5$, various terms in the vorticity balance are plotted in Figures 5.7 and 5.8, for the upper and lower layer, respectively. Note that again the contour interval is different for high and low absolute values. The input of vorticity by the wind stress curl INP_1 is not shown (it is the same as for the wind-driven flows discussed in Section 3.2.1, and was plotted in Fig. 3.3a). The other terms are defined as

$$\begin{aligned} BETA_1 &= \beta\frac{\partial\Psi_1}{\partial x} & BETA_2 &= \beta\frac{\partial\Psi_2}{\partial x} \\ ADV_1 &= \mathbf{U_1}\cdot\nabla Z_1 & ADV_2 &= \mathbf{U_2}\cdot\nabla Z_2 \\ DISS_1 &= -\frac{1}{Re}\nabla^2 Z_1 & DISS_2 &= -\frac{1}{Re}\nabla^2 Z_2 \\ STR_1 &= -F_1\mathbf{U_1}\cdot\nabla(\Psi_1-\Psi_2) & STR_2 &= F_2\mathbf{U_2}\cdot\nabla(\Psi_1-\Psi_2) \end{aligned} \tag{5.1}$$

In the upper layer, the vorticity balance yields

$$BETA_1 + ADV_1 + STR_1 + DISS_1 + INP_1 = 0.0$$

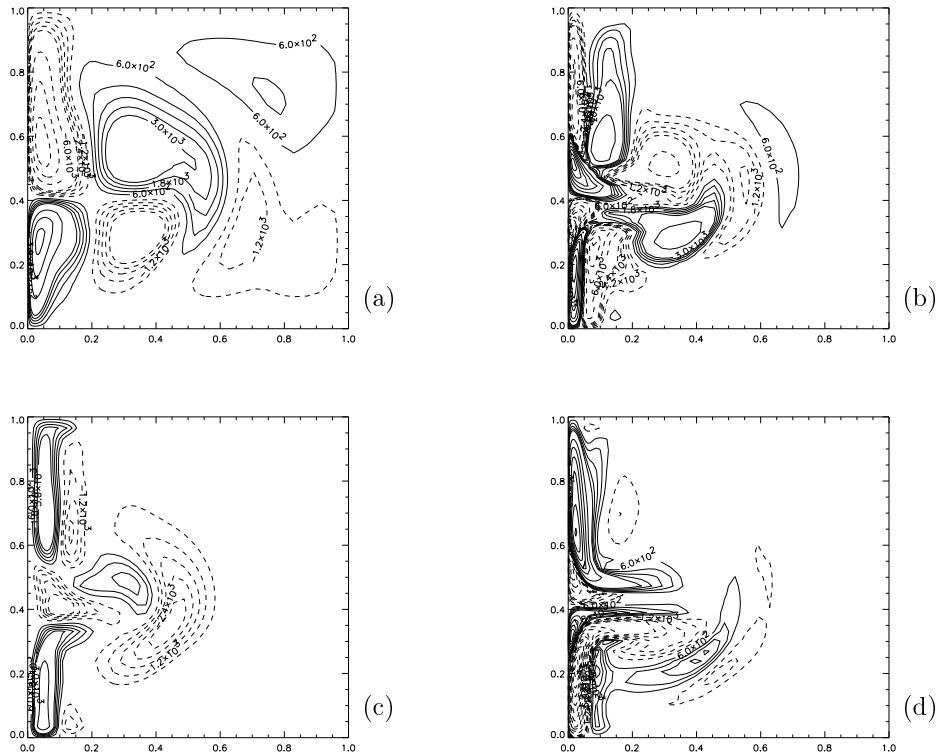

Figure 5.7: *Different terms in the vorticity balance for the upper layer, for the stationary solution at* $Re = 31$ *and* $V_{in} = 1.5$ *in Fig. 5.6e: (a) the advection of planetary vorticity* $BETA_1$*; (b) the advection of relative vorticity* ADV_1*; (c) the stretching term* STR_1 *and (d) the dissipation of vorticity* $DISS_1$ *(see (5.1) for definitions). The contour interval is* $6 \cdot 10^2$ *for absolute values lower than* $3 \cdot 10^3$*, and* $3 \cdot 10^3$ *otherwise. The wind forcing* $INP_1 = \alpha_\tau \partial \tau^x / \partial y$ *is not shown.*

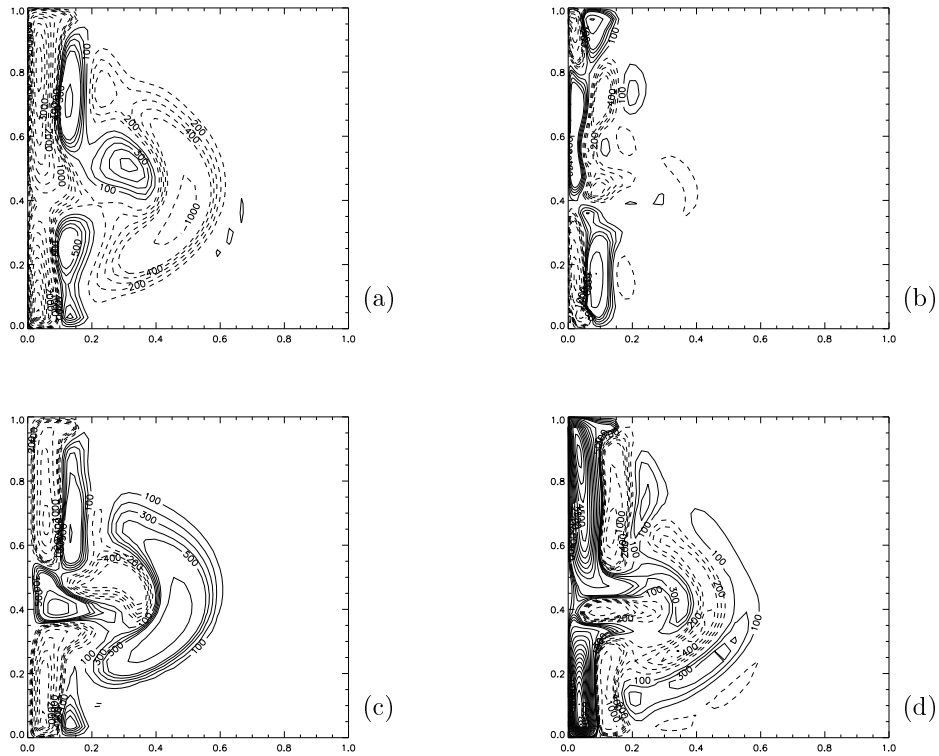

Figure 5.8: *As in Fig. 5.7, but for the stationary solution in the lower layer (Fig. 5.6f): (a) the advection of planetary vorticity* $BETA_2$*; (b) the advection of relative vorticity* ADV_2*; (c) the stretching term* STR_2 *and (d) the dissipation of vorticity* $DISS_2$*. The contour interval is* $1 \cdot 10^2$ *for absolute values lower than* $5 \cdot 10^2$*, and* $5 \cdot 10^2$ *otherwise.*

whereas for the lower layer

$$BETA_2 + ADV_2 + STR_2 + DISS_2 = 0.0$$

In the upper layer, three different flow regimes can be identified. For $x > 0.5$, in the eastern half of the basin, the flow is approximately in Sverdrup balance. That is, $BETA_1 \simeq -INP_1$. However, due to the presence of the DWBC, the deviations from this balance are larger than for the purely wind-driven case, in particular due to a small contribution from ADV_1 (Fig. 5.7b). Closer to the western boundary, for $x \in [0.1, 0.5]$, an approximate balance exists between the advection of planetary and of relative vorticity (Fig. 5.7a and b), as for the purely wind-driven flow at low Re (Fig. 3.3). However, the contributions from STR_1 and $DISS_1$ can not be entirely neglected. As expected, the DWBC mainly affects the vorticity balance near the western boundary of the domain. Although, as for the purely wind-driven case, the advection of relative vorticity and dissipation are the dominant terms (Figs. 5.7b and d), stretching effects become important there. In the northwest, the advection of planetary and of relative vorticity have the same sign (Figs. 5.7a-b), and are primarily balanced by the stretching term and the dissipation (Figs. 5.7c-d). In contrast,the stretching term has the same sign as $BETA_1$ and ADV_1 in the southwest. These three terms are all compensated by the dissipation (Fig. 5.7d).

In the second layer, two regions can be distinguished. For $x < 0.1$, the main balance is between the advection of planetary vorticity $BETA_2$ and the stretching term STR_2 on one hand, and the dissipation $DISS_2$ on the other hand (Figs. 5.8a,c and d). Near the center of the basin, where the DWBC is deflected as it passes underneath the upper layer jet, the dominant balance is between the $BETA_2$ and STR_2 (Figs. 5.8a and c). The contribution of the dissipation is of lesser importance. The advection of relative vorticity ADV_2 is not a dominant term in the vorticity balance in the second layer for this solution.

5.5 Internal modes of variability

It was shown in Section 5.3 that not only the structure of the stationary solutions changes when a DWBC is introduced, but that also the stability characteristics of the coupled wind-driven/DWBC flow differ from those of the purely wind-driven flow. In this section, focus is on the fate of the intermonthly modes found for the wind-driven flow and on the origin of the low-frequency mode found for the coupled wind-driven/DWBC flow, as the strength of the DWBC is increased continuously.

5.5.1 The stabilization of intermonthly modes

The three Hopf bifurcations that were found to destabilize the symmetric, purely wind-driven flow occur at $Re = 17.2$, $Re = 21.0$ and $Re = 26.5$, respectively. So, they all have positive growth rates at $Re = 31$, which is used here as the standard value for the Reynolds number while V_{in} is changed. In Figure 5.9a, the dimensional growth rate $\lambda^* = \lambda\ U/L$ of these modes is plotted against V_{in}^*. It appears that

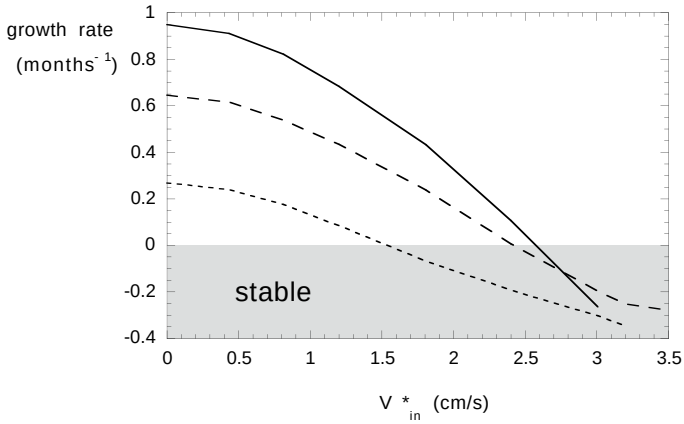

(a)

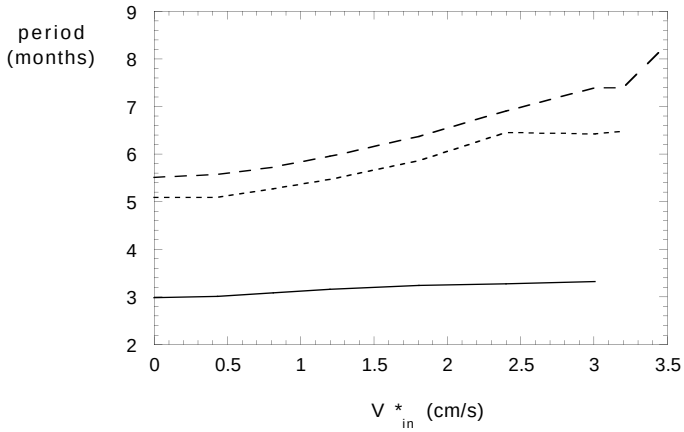

(b)

Figure 5.9: *(a) Dimensional growth rates $\lambda^* = \lambda U/L$ of the modes that destabilize the purely wind-driven flow, for a fixed Reynolds number ($Re = 31$) and increasing V^*_{in}. A solid, dashed and dotted line are used for the growth rate of the modes associated with H_1, H_2 and H_3 in Fig. 3.1a, respectively. (b) As in (a), but for the dimensional period $p^* = 2\pi L/\nu U$ of the modes.*

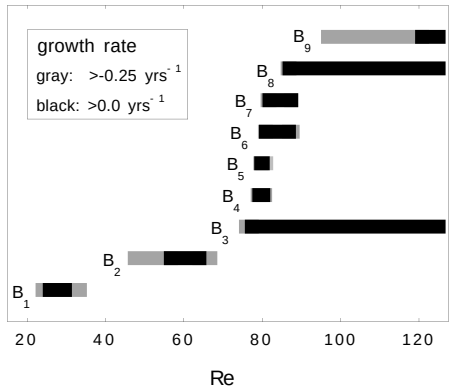

Figure 5.10: *Intervals in Re where the nine most unstable modes for the coupled wind-driven/DWBC flow, associated with the Hopf bifurcations $\mathcal{H}_1$ to $\mathcal{H}_9$ in Fig. 5.2, have positive growth rates ($\lambda^* > 0$, black) or are only marginally damped ($\lambda^* > -0.25$ $years^{-1}$, gray).*

increasing the strength of the DWBC strongly damps these three modes, and for $V_{in}^* > 2.7$ cm/s (and $Re = 31$) none of the three modes is able to destabilize the flow anymore. As V_{in}^* is increased, the periods of the modes increase slightly (Fig. 5.9b).

The stationary solutions become stable with respect to these baroclinic modes as a result of changes in the solutions themselves. When there is a weak DWBC or no inflow at all, well developed recirculation gyres exist that give rise to a sharp jet (Fig. 5.6). As a consequence, the vertical shear $|\vec{u}_1 - \vec{u}_2|$, which was shown to be the energy source for the instability process (Section 3.3.1), is quite large (up to 40 cm/s). When the strength of the DWBC is increased, the vertical shear is reduced. For $V_{in} = 1.5$, the maximum shear is 25 cm/s while for $V_{in} = 3.0$ the sheaR in the eastward jet is about 10 cm/s. This decrease is mainly caused by the decrease in amplitude of Ψ_1, and partly by the deflection of the DWBC in the cross-over region that occurs for lower V_{in}. One might expect that the stationary flow can be destabilized again by these modes when the vertical shear of the stationary solution increases, for example at larger Re. However, when Re is increased while V_{in} is kept fixed at the value $V_{in} = 2.1$, the coupled wind-driven/DWBC flow remains stable to this type of perturbations with an intermonthly time scale, as was shown in Section 5.3. Hence, the interannual modes that were found to destabilize the coupled wind-driven/DWBC are not simply a modification of these intermonthly modes.

5.5.2 The appearance of low-frequency variability

For $V_{in} = 2.1$, nine different modes were found to destabilize the coupled wind-driven/DWBC flow (Section 5.3). In Figure 5.10, the intervals in Re where each of these nine modes has a positive growth rate ($\lambda^* > 0$, black) or is only marginally damped ($\lambda^* > -0.25$ $years^{-1}$, gray) are plotted. Six of the oscillatory modes have

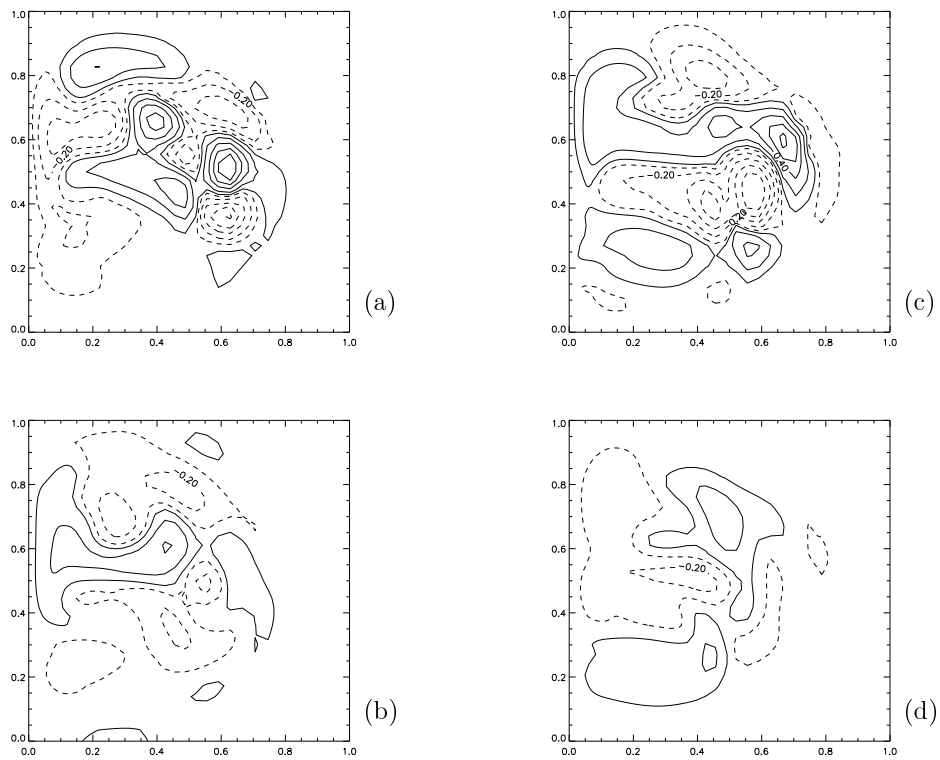

Figure 5.11: *Snapshots of the modes B_3 and B_8, in the upper and lower layer (upper and lower panels) at phase $\nu t = 0.0$; (a-b) B_3 (period $p^* = 0.7$ years at criticality) and (c-d) B_8 ($p^* = 1.4$ years). For both modes, the plots are scaled with the maximum of the perturbation streamfunction ϕ_1 in the upper layer.*

positive growth rates only over a small interval in Re, and hence are expected to be of lesser importance for the variability. In contrast, the modes B_3, B_8 and B_9 are expected to contribute to the time-dependent behavior of the flow over a larger interval in Re. So, only the characteristics of these latter modes are discussed here in detail. Contour plots of the perturbation streamfunction of the modes B_3 and B_8, in both the upper and lower layer, are shown in Figure 5.11 for one phase of the oscillation ($\nu t = 0.0$). For each mode, the fields are scaled with the maximum of the upper layer perturbation streamfunction ϕ_1.

At $\mathcal{H}_3$ ($Re = 77.4$), the stationary flow is destabilized by the mode B_3, which has a period of 8.2 months at criticality. Its main features are the $\mathcal{O}(150)$ km anomalies in the strip between $[x, y] = [0.4, 0.7]$ and $[x, y] = [0.6, 0.4]$, in both layers (Fig. 5.11a-b). During a cycle, these anomalies propagate southeastward in this strip. A phase difference exists between the response in the two layers: the lower layer leads the upper

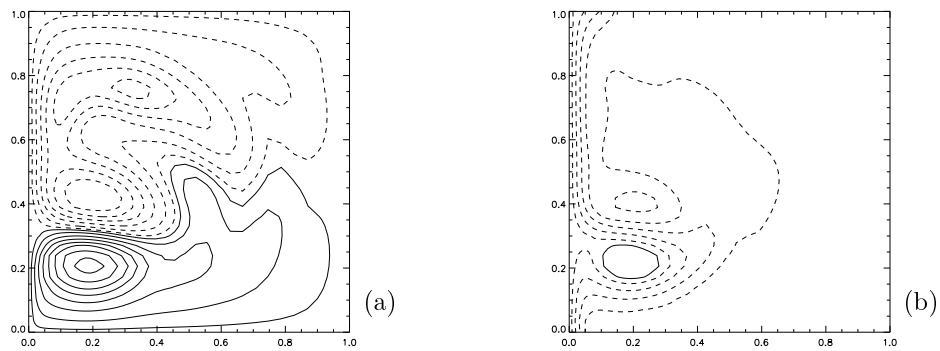

Figure 5.12: *Spatial pattern of the stationary solution at $Re = 78$ (near $\mathcal{H}_3$ and $\mathcal{H}_8$) in (a) the upper and (b) the lower layer. Contour intervals are 0.2 and 0.05, respectively.*

layer. In Figure 5.12a-b, the stationary solution at $Re = 78$, near the bifurcation point, is shown. The upper layer jet of the stationary solution has a strong meander in the area where B_3 shows the strongest response, while there is only a weak circulation in the lower layer in this region.

At $\mathcal{H}_8$ ($Re = 87.0$), an oscillatory mode with a time scale of 1.4 years destabilizes the stationary flow (B_8, Fig. 5.11c-d). The stationary solution at this Reynolds number has not changed much compared to that in Figure 5.12a-b and is therefore not shown. The mode shows a response on somewhat larger spatial scales than B_3, and the strongest anomalies develop near the center of the domain. During the cycle they propagate (north-)westward with the return flow of the subpolar gyre (see Fig. 5.12a-b), and decay near the western boundary around $[x, y] = [0.1, 0.8]$. Again, a phase difference exists between the response in the two layers, with the lower layer leading the upper layer. Both B_3 and B_8 mainly affect the midlatitude jet around the center of the basin.

The third oscillatory mode for which the stationary flow remains unstable for increasing Re, B_9, has a period of 5.1 years at criticality (Fig. 5.13). This mode destabilizes the flow at the bifurcation point $\mathcal{H}_9$, located at $Re = 120.8$. This Reynolds number corresponds to a lateral friction coefficient $A_H = 130\ m^2/s$. The most important features of the mode are two large-scale anomalies centered at $[x, y] = [0.2, 0.25]$ and $[0.2, 0.4]$ at phase $\nu t = 0.0$. These are aligned with the recirculation gyres of the stationary solution at this Reynolds number, shown in Figure 5.14. The positive anomaly which at phase $\nu t = 0.0$ is present in the northern recirculation gyre at $[x, y] = [0.2, 0.4]$, first propagates (south-)eastward (Fig. 5.13c). In the second layer, the propagation of the anomaly is similar (Fig. 5.13b and d). Subsequently, this positive anomaly returns to the western boundary following a (south-)westward course (Fig. 5.13e-h). A negative anomaly follows the same path as the positive anomaly half a cycle later (not shown, the spatial pattern at phase $\nu t = 0.5$ is the same as in

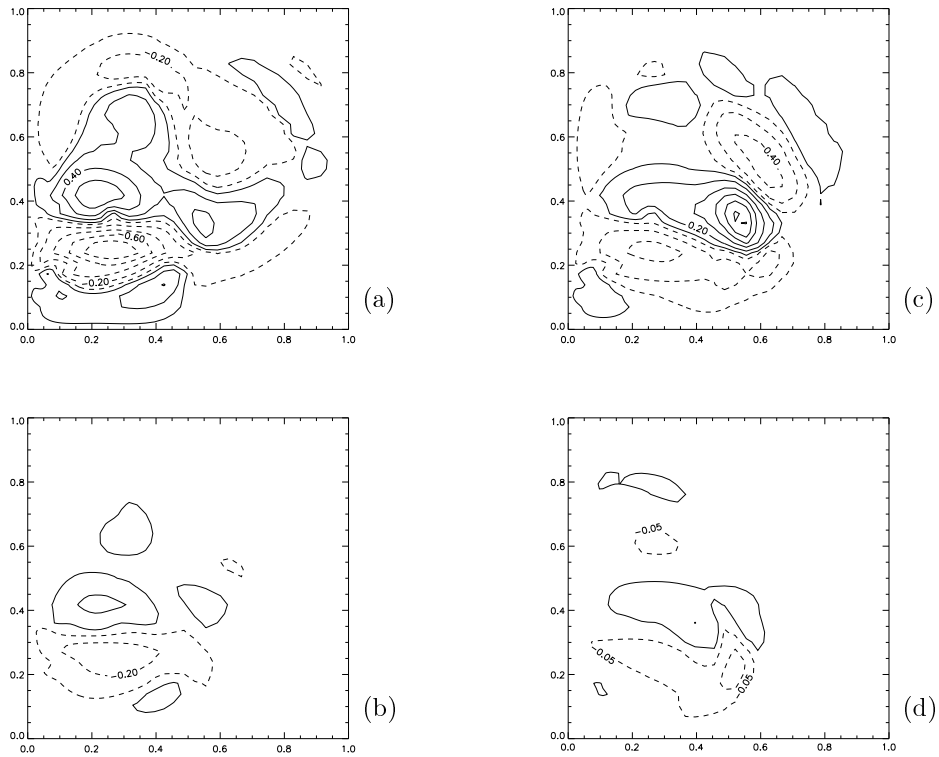

Figure 5.13: *Contour plots of the streamfunction of the mode B_9, for the upper and lower layer (upper and lower panels), at four phases of the oscillation 1/8 period apart: (a-b) $\nu t = 0.0$; (c-d) $\nu t = 0.125$; (e-f) $\nu t = 0.25$; (g-h) $\nu t = 0.375$. Since the amplitude of the mode is arbitrary, all plots are scaled with the maximum of (a), the perturbation in the upper layer at phase $\nu t = 0.0$. The contour interval is 0.2.*

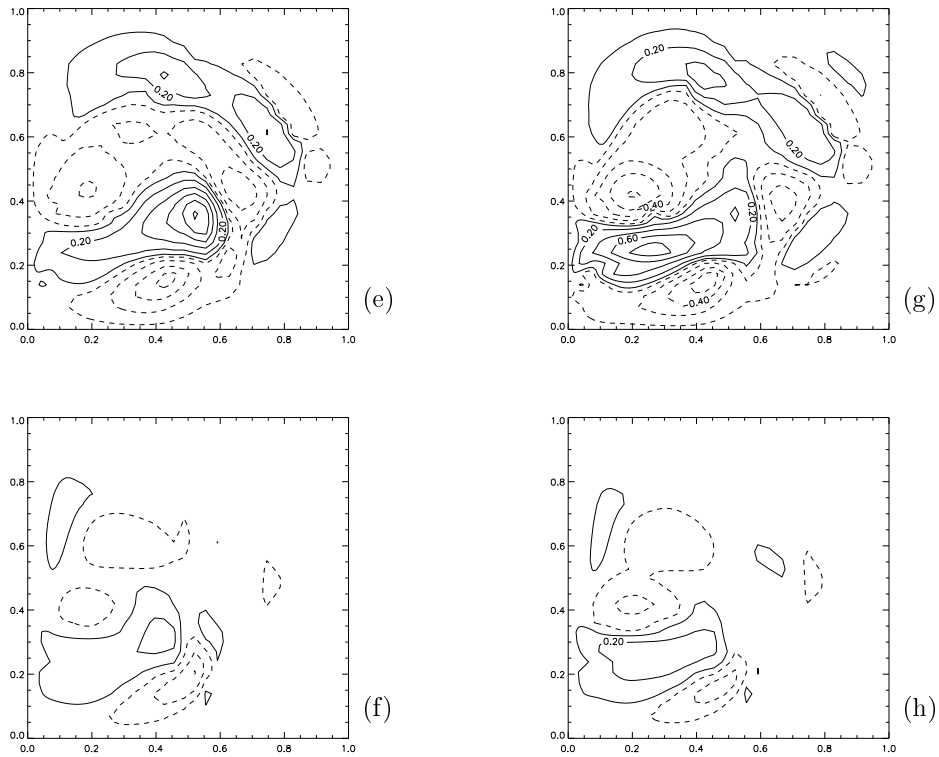

Fig. 5.13, continued.

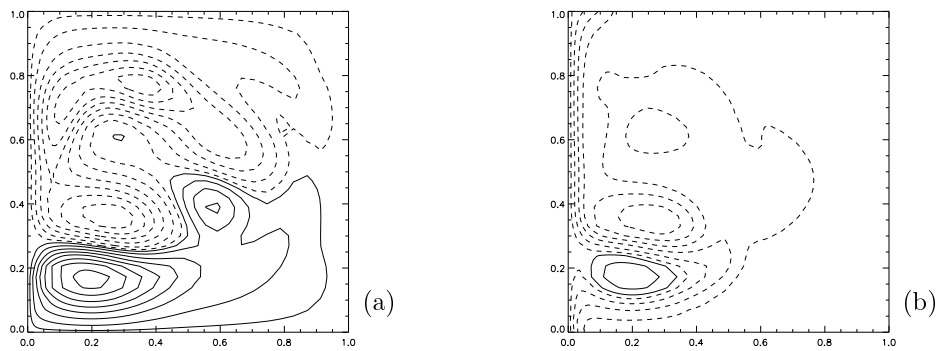

Figure 5.14: *As in Fig. 5.12, but for* $Re = 121$ *(near* $\mathcal{H}_9$*).*

Fig. 5.13a-b but with a minus-sign). This interannual mode has its strongest response in a region where both the surface and the deeper circulation are strong, that is, in the cross-over region.

Summarizing the results presented in this section, the coupled wind-driven/DWBC flow becomes unstable to different modes of variability than the purely wind-driven flow. These new modes have intermonthly to interannual time scales. Furthermore, other modes on time scales of years to decades exist which are only marginally damped over large intervals in Re.

5.6 Discussion

In this chapter, a DWBC was introduced to the wind-driven double-gyre system to explore the impact of its presence on the internal dynamics of the flow. The main motivation for this study has been to understand results in the paper by Spall (1996b), where decadal variability is found in a numerical model of the Gulf Stream/DWBC system. Changes in structure of stationary solutions and instabilities have been monitored, using both the lateral friction and the strength of the DWBC as control parameters. For the purely wind-driven flow, the stationary flows are destabilized at large friction through baroclinic instabilities, and as a result, intermonthly time scales of variability are introduced (Chapter 3). The presence of the DWBC has a significant impact on the characteristics of this wind-driven flow. First, stationary solutions for the coupled Gulf Stream/DWBC flow are unique, whereas multiple stationary solutions were found for the purely wind-driven flow. Second, its presence strongly favors instabilities with interannual time scales.

A comparison of the results presented in this chapter with observations of the variability of the Gulf Stream/DWBC system, as described by for example Pickart (1994), does not seem appropriate at this stage. First, it can not be expected that the idealized model is capable of capturing the important details of the flow. Neglected

features like bottom topography and the shape of the coastline will certainly modify the flow, even though they may not be essential to the basic physical mechanisms behind the variability. A second difficulty is that, with respect to the low-frequency variability, the observational records are still simply too short. An interesting issue that can be addressed, however, is whether an internal low-frequency mode like the one discussed in this chapter may play a role in the variability of Gulf Stream/DWBC system as modelled by Spall (1996b). The mode B_9 is, based solely on its period, the most interesting mode of variability for comparison with the low-frequency behavior found by Spall (1996b). In Spall (1996b), the dominant time scale of variability is 10 years, which is considerably longer than the interannual time scale of the low-frequency mode B_9 discussed here (5.1 *years* at criticality). However, the time scale of the mode probably increases with the basin size, which is larger in Spall (1996b) than in this study (3500×2500 km versus 1000×1000 km). Tansley and Marshall (2000) also used quite a small basin to study the interaction between the Gulf Stream and the DWBC (1920×960 km), and mainly found variability on interannual time scales, as in our study. Next, consider the spatial pattern of the flow associated with the extreme phases of the decadal oscillation described by Spall (1996b). In his three-layer model, the Gulf Stream penetrates far into the basin and is flanked by eddy-driven recirculation gyres during the high-energy phase of the oscillation. At intermediate depth, in the second model layer, recirculation gyres exist. These are aligned with the Gulf Stream above, and the upper DWBC is entrained into these recirculation gyres. During the opposite phase, when the kinetic energy of the flow is relatively low, the Gulf Stream penetrates less far into the basin. Only part of the upper DWBC is entrained in the (now weaker) recirculation gyres, while part of it is unaffected and continues southward. These high- and low-energy phases can be compared with the oscillatory flow that arises by adding the low-frequency mode B_9 (Fig. 5.13) to the stationary solution for the coupled wind-driven/DWBC flow at high Re (Fig. 5.14). In the upper layer, adding the low-frequency mode at phase $\nu t = 0.0$ (Fig. 5.13a), weakens the recirculation gyres (the strongest anomalies, near $[x, y] = [0.2, 0.25]$ and $[0.2, 0.4]$, have the opposite sign as the stationary flow). As a result, the upper layer jet penetrates less far into the basin. During the opposite phase ($\nu t = 0.5$), the sign of the perturbation streamfunction of the mode is reversed, and the recirculation gyres are strengthened. In the lower layer, the perturbation at $\nu t = 0.0$ (Fig. 5.13b) moderates the deflection of the DWBC. The opposite occurs half a period later: the sign of the anomaly reverses, and stronger deflection occurs. Moreover, the changes in the separation point of the upper layer jet induced by this mode are similar. For the stationary solution at $Re = 121$, the separation point of the upper layer jet is located at $y = 0.28$ (see Fig. 5.14a). At phase $\nu t = 0.0$, the low-energy phase, the upper layer perturbation streamfunction (Fig. 5.13a) is negative at that latitude and hence the separation point shifts southward during this phase, as in Spall (1996b). The opposite occurs at phase $\nu t = 0.5$. To summarize, based on the spatial characteristics, the high- and low-energy phase of the oscillation described by Spall (1996b) resemble the $\nu t = 0.5$ and $\nu t = 0.0$ phases of the low-frequency internal mode of variability described in this study, respectively. However, it can not be concluded from these results that the decadal variability found by Spall

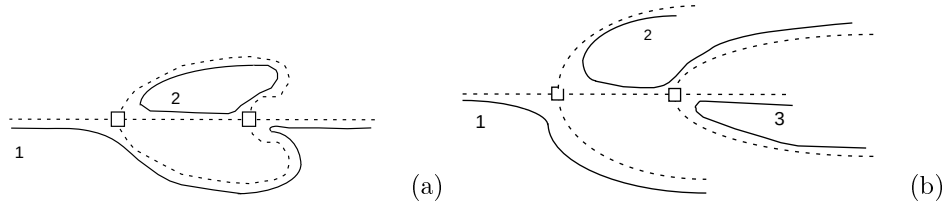

Figure 5.15: *Schematic bifurcation diagram of the breaking up of the two pitchfork bifurcations (marked by squares) when a weak DWBC is introduced, for (a) the standard parameter setting discussed in Section 5.4 ($F_1 = 850$); (b) a parameter regime where the asymmetric solutions are not connected by a limit point ($F_1 \leq 450$). In these figures, dashed lines indicate the solution branches for the purely wind-driven flow, solid lines show the branches in the presence of a weak DWBC. For clarity, the limit points L_1 and L_2 have been omitted.*

(1996b) is caused by an internal mode similar to the one denoted here as B_9. For that, the robustness of this low-frequency internal mode to a larger basin size, to the defined layer depths and the stratification needs to be tested. Moreover, to assess the importance of this low-frequency mode it needs to be verified that it indeed contributes substantially to the time-dependent behavior of the flow (in Chapter 6, it will be shown that this is indeed the case). Nevertheless, it is remarkable that an internal mode is found for the coupled wind-driven/DWBC flow, which shows many similarities with the dominant patterns of variability in Spall (1996b), whereas such a mode is absent for the purely wind-driven flow.

In Section 5.4, it was shown that the branches of solutions with a jet that separates north of the mid-axis of the basin form a closed loop and eventually disappear when a DWBC is introduced. As a result, a unique branch of stationary solutions is obtained when the DWBC is strong enough. However, this closed loop of 'separate north'-solutions that shrinks and eventually disappears exists due to the fact that the asymmetric solutions are connected by the limit point L_3 (see Fig. 5.4). In Section 3.4.2, it was shown that the presence of this connecting limit point depends strongly on the value of F_1. For lower values of F_1 than the standard value of 850, the limit point moves towards higher values of Re, thus enlarging the interval in Re where asymmetric solutions exist. For $F_1 \leq 450$ the limit point was not found at all in the explored regime in Re. Thus, the effects of introducing a DWBC on the structure of the stationary solutions was explored for $F_1 = 450$ as well. In Figure 5.15a, the breaking up of the two pitchfork bifurcations is sketched both for the standard case ($F_1 = 850$) and for a case for which the asymmetric solutions are not connected ($F_1 = 450$). The limit points L_1 and L_2 have been omitted in this sketch for clarity. Dashed lines represent the solution branches when a DWBC is absent, and solid lines are the solution branches when a weak DWBC is introduced. In Figure 5.15a, the closed loop of 'separate north'-solutions that disappear when V_{in} is increased is marked branch #2. Branch #1 is the branch that survives when V_{in} is increased ('separate south' in Fig. 5.4). When a DWBC is introduced in a parameter regime

where the asymmetric solutions are not connected by a limit point (Fig. 5.15b), the pitchfork bifurcations break up in a similar way as for the standard case. However, since L_3 does not exist, one ends up with three separate branches. The formerly symmetric branch at low Re (branch #1 in Fig. 5.15b) connects to a branch of solutions that separates south of $y = 0.5$. Also for high Re, the formerly symmetric branch connects to the branch of solutions with a more southerly separation point and forms branch #3. The two branches with solutions that separate north of $y = 0.5$ connect again, but now do not form a closed loop (branch #2). When the strength of the DWBC is increased, the latter branch moves quickly to high values of Re, so that it is less likely to be reached by time integrations. The limit point of branch #3 does not move to higher Re with increasing V_{in}, so that for low F_1 multiple equilibria do exist in the presence of a DWBC.

Chapter 6

The contributions of internal modes to the variability*

In previous chapters, the internal modes to which both purely wind-driven and coupled wind-driven/DWBC flows become unstable were discussed. These oscillatory modes are known to dominate the specific time and spatial scales of the variability near the onset of instability. It needs to be investigated though to what extent they contribute to the time-dependent behavior far into the unstable regime. To this end, transient flows at high and low friction are analyzed statistically in this chapter. In this way, the contributions of various internal modes to the variability of the flow are assessed. In particular, the origin of the displayed low-frequency variability is discussed.

6.1 Introduction

In Chapters 3 and 5, the internal variability of both purely wind-driven flows and coupled wind-driven/DWBC flows was studied on the basis of stationary solutions for the flow and the oscillatory modes that destabilize them. It was presumed that these internal modes control the variability of the flow to a large degree, and that the approach thus provides a framework for the interpretation of the results of time integrations (Section 2.3). For slightly supercritical conditions, when the flow is unstable to one mode only, this presumption is certainly valid. Then, the time-dependent behavior of the flow can be predicted from the structure of the bifurcation diagram (see Chapter 4). However, it needs to be established whether also at higher forcing the displayed variability can to a large extent be attributed to internal modes.

In this chapter, the results of time integrations performed at various parameter settings are analyzed using statistical techniques, to identify the statistical modes

*This chapter is partly based on the paper "*The interaction of a Deep Western Boundary Current and the wind-driven gyres as a cause for low-frequency variability*", by C. A. Katsman, S. S. Drijfhout and H. A. Dijkstra (accepted for publication in *J. Phys. Oceanography*)

that contribute most to the variability. These statistical modes are compared to the results of the linear stability analyses, to identify the contributions of various internal modes. In this way, time-stepping techniques and dynamical systems analyses are combined. A few earlier studies exist in which the results of time integrations with simple, wind-driven models are interpreted from a dynamical systems point of view. However, in none of these studies the internal modes of variability were explicitly derived and incorporated in the analysis.

McCalpin and Haidvogel (1996) used an equivalent barotropic quasi-geostrophic model on a computational domain of $3600 \times 2800\ km$ to study the internal variability of the wind-driven circulation. They calculated transient flows for differing strengths and shapes of the wind stress forcing, at low friction. These transient flows display variability on decadal and intermonthly to annual time scales. The low-frequency variability is associated with irregular transitions between a high-, a medium- and a low-energy state. During a high-energy state, the jet penetrates much farther into the basin than during a medium- or low-energy state. Primeau (1998a) repeated this study, and in addition determined the stationary solutions for this wind-driven flow using continuation techniques. He found that multiple stationary solutions for the flow existed in the parameter regime investigated by McCalpin and Haidvogel (1996), and that approximately 30% of the total variability could be explained in terms of transitions between some of these (apparently unstable) equilibria. McCalpin and Haidvogel (1996) found that for asymmetric wind forcing such low-frequency transitions occur less frequently. Primeau (1998a) was able to explain this behavior by demonstrating that specific unstable stationary solutions ceased to exist in that particular parameter regime.

Another systematic study of the internal variability of wind-driven flows in quasi-geostrophic models was performed by Berloff and McWilliams (1999), who calculated transient flows for decreasing lateral friction. They applied symmetric and asymmetric double-gyre wind forcing patterns to both equivalent barotropic and baroclinic models on a domain of $3840 \times 3840\ km$. For all model configurations, a similar picture emerged from the time integrations: the flows are stationary in the high friction regime, and then become periodic, quasi-periodic and finally chaotic as the lateral friction is decreased. The transition to periodic behavior is interpreted by Berloff and McWilliams (1999) to be the result of a Hopf bifurcation, associated with an oscillation on an intermonthly time scale. The quasi-periodic behavior is characterized by an intermonthly and an interannual time scale, and is assumed to be caused by the existence of a second Hopf bifurcation. However, they did not verify these conjectures by calculating the stability characteristics of the flow explicitly. For lower friction, the transient flows display irregular transitions between distinct gyre patterns, which occur on decadal time scales. These gyre patterns differ mainly in the zonal extent of the midlatitude jet, which changes from approximately $1000\ km$ to $600\ km$ during a transition from a high-energy to a low-energy state. These low-frequency transitions become more dominant as lateral friction is decreased, as is clear from energy spectra of the time series.

A similar study for wind-driven flows in a baroclinic and a barotropic model was performed by Meacham (2000), but on a smaller domain of $1024 \times 2048\ km$. The flows

were again found to evolve from stationary to periodic on intermonthly time scales as friction was decreased. He showed that at sufficiently large forcing, as in Berloff and McWilliams (1999), irregular large-amplitude vacillations on a decadal time scale arise, that are robust to asymmetric forcing. Again, these vacillations are associated with changes in the penetration scale of the midlatitude jet. This variability on longer time scales becomes more and more important as friction is decreased.

Recent work by Qiu (2000) showed that large-scale interannual changes of the Kuroshio Extension system are also characterized by an oscillation between an elongated and a contracted state. It should be noted that the seven year TOPEX/Poseidon data set which he analyzed is fairly short to be able resolve these interannual time scales properly. Nonetheless, it is noteworthy that observations indicate that this type of low-frequency behavior, characterized by changes in the penetration scale of the midlatitude jet, is not only occurring in numerical simulations.

In this chapter, time integrations performed at high and low Reynolds numbers are presented, both for purely wind-driven and for coupled wind-driven/DWBC flows. In contrast to earlier studies, now the origin of the variability can be investigated by determining the contributions of various internal modes to the time-dependent behavior. To calculate the transient flows, an implicit time-stepping code is used. In most cases, the (unstable) stationary solution computed with the continuation method is used as the initial condition for the time integrations, perturbed with the most unstable eigenmode for this specific solution. A statistical analysis is used to extract both the dominant time scales and the associated spatial patterns of variability (Multivariate Singular Spectrum Analysis or M-SSA, see for example Plaut and Vautard, 1994). In the analysis, both the upper and lower layer flow patterns are used, sampled at intervals of one or two weeks. Hence, the phase relation between the response in the upper and lower layer is retained, and both high- and low-frequency signals can be distinguished. The time scales and spatial patterns obtained from the M-SSA analysis are inspected visually and compared to the results of the linear stability analysis, to identify the specific internal modes that contribute substantially to the variability.

An interesting remark regarding the origin of low-frequency variability was made by Spall (1996b), on the basis of his simulations of the Gulf Stream/Deep Western Boundary Current (DWBC) system (Chapter 5). He attributes the decadal time scale variability in his simulations to eddy-mean flow interactions. The presence of the upper DWBC appears essential for the occurrence of this low-frequency variability, since it is absent when the upper DWBC transport is set to zero. However, he remarks that the high- and low-energy states and patterns of low-frequency variability in his simulations are very similar to the results by McCalpin and Haidvogel (1996). Moreover, the low-frequency variability discussed by Berloff and McWilliams (1999) and Meacham (2000) is also characterized by high- and low-energy states associated with changes in the zonal penetration scale of the Gulf Stream. Since the latter were obtained using a purely wind-driven model, the mechanism that causes the low-frequency variability has to differ for the two cases. The similarities in the low-frequency variability simulated by McCalpin and Haidvogel (1996) and Spall (1996b) illustrate that it is difficult to extract the responsible physical mechanism just from the dominant spatial patterns of the low-frequency variability. However, the identification

of this underlying mechanism is crucial for a full understanding of the variability and its sensitivity to physical parameters.

In general, low-frequency variability can be caused by various mechanisms. First, the existence of multiple unstable solutions, between which the flow fluctuates irregularly, is a possible cause for low-frequency variability. This mechanism was discussed by Primeau (1998a) to explain the time-dependent behavior found by McCalpin and Haidvogel (1996). Second, internal modes with interannual to decadal time scales may exist, that give rise to the low-frequency variability. A third possible cause is that non-linear interactions of high-frequency signals (that is, eddy-mean flow or eddy-eddy interactions) result in low-frequency variability. This mechanism is, according to Spall (1996b), responsible for the low-frequency variability in his Gulf Stream/DWBC simulations. On the basis of the results of the dynamical systems analysis, i.e. the structure of the stationary solutions in parameter space and their stability characteristics, these three mechanisms can be distinguished. In this chapter, the origin of low-frequency variability is explicitly addressed by analyzing the transient flow characteristics of two time integrations at low friction in detail. The parameter setting for these two integrations is the same, except for the absence or presence of a DWBC. In both cases, low-frequency variability is expected to arise. Based on the results presented in Chapters 3 and 5, it is hypothesized that for the purely wind-driven flow, non-linear interactions of high-frequency modes are responsible, since no low-frequency modes were detected and multiple stationary equilibria were not found for high Re either. In contrast, for the coupled wind-driven/DWBC flow internal modes on interannual time scales, in particular the mode B_9 discussed in Chapter 5, are expected to play a role.

In Section 6.2, transient purely wind-driven flows for low and moderate Reynolds numbers are analyzed. They are found to display only high-frequency variability, in agreement with the simulations of Berloff and McWilliams (1999) and Meacham (2000) at high friction. The time-dependent behavior of coupled wind-driven/DWBC flows is analyzed in Section 6.3. For these flows, both high- and low-frequency variability is found to play a role. In Section 6.4, the low-frequency variability of the flow in two simulations at high Re is analyzed, which only differ by the fact that a DWBC is present or absent. The analysis of the statistical characteristics of these transient flows leads to the conclusion that interaction of the wind-driven gyres with the DWBC induces a preference for variability on specific interannual time scales, whereas the purely wind-driven flow displays low-frequency variability over a broader spectral band.

6.2 Purely wind-driven flows

Three Hopf bifurcations were detected for the purely wind-driven case, associated with the destabilization of the flow by three oscillatory modes (Section 3.3). The characteristics of these modes, which will be referred to as W_1 to W_3 (W for wind-driven), are recapitulated in Table 6.1. The results of time integrations of these purely wind-driven flows for $Re \in [20, 60]$ were analyzed using M-SSA. In Figure 6.1, the

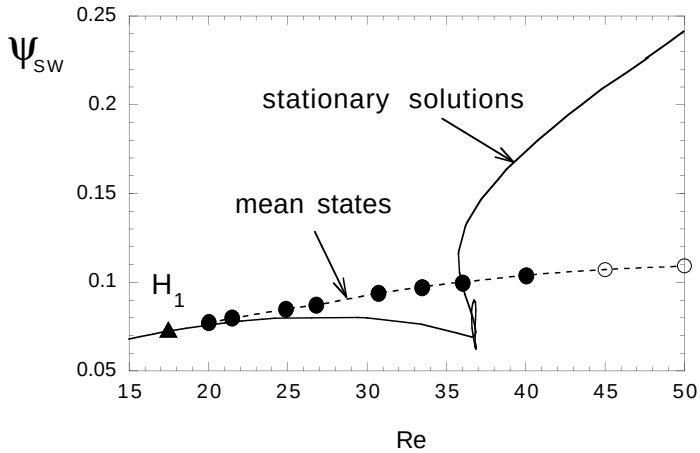

Figure 6.1: *Stationary solutions (solid curves) and mean states of time integrations (circles) as a function of Re for the purely wind-driven flow. The circles marking the time-mean states are filled when the variability is solely due to the mode W_1 (i.e., they outline the stable periodic orbit arising from H_1) and open otherwise.*

mean states of the time integrations (circles) are plotted as a function of Re, together with the stationary solutions (solid line). On the vertical axis, ψ_{SW} is plotted again as the measure of the stationary solutions. The value of ψ_1 at the same grid point is shown for the mean states. For $Re < 40$ the periodic orbit associated with H_1 is stable. That is, all the variability in the time series is due to the mode W_1, which is indicated in Figure 6.1 by filled circles. Note that the mean states of the time integrations do not show the strong increase in transport and rescaling associated with the transition to a more inertially dominated flow regime. As expected, the time-dependent flows are able to redistribute part of the input of vorticity by the wind internally by advection of vorticity across the zero wind stress curl line (see also Section 3.2.1). As a result, the mean transport is on the order of the transport predicted by Sverdrup theory.

For $Re > 40$, the time-dependent behavior becomes more complicated. The periodic orbit associated with H_1 has become unstable, so that more than one oscillatory

	Hopf bifurcation	period (months)	spatial pattern perturbation streamfunction
W_1	$H_1: \ Re = 17.2$	4.3	symmetric (Fig. 3.5)
W_2	$H_2: \ Re = 21.0$	8.2	anti-symmetric (Fig. 3.6)
W_3	$H_3: \ Re = 26.5$	6.0	symmetric (Fig. 3.7)

Table 6.1: *Characteristics of the three oscillatory modes W_1, W_2 and W_3 that destabilize the purely wind-driven double-gyre flow.*

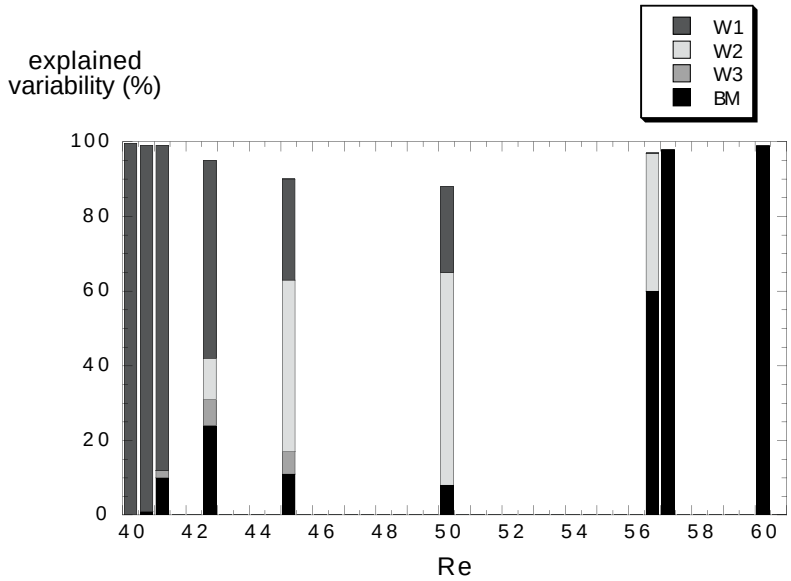

Figure 6.2: *Stack histogram of the percentage of the total variability in the purely wind-driven transient flows that is explained by specific internal modes (from Schmeits, 2000).*

mode contributes to the variability. The results of the M-SSA analysis for Re larger than 40 are displayed in Figure 6.2. In this stack histogram, the percentage of the total variability in the time series that is explained by specific internal modes is presented. Despite the irregular behavior displayed in the time series (see for example Fig. 4.10 for the time series at $Re = 45$), it is found that the time-dependent behavior can still be explained by only a few modes. For increasing Re, the mode W_1 becomes less important. A substantial contribution from W_2 is detected (it explains up to 55% of the total variability), as well as a minor contribution from W_3 (2 to 8%). Moreover, a contribution from a barotropic mode, denoted by BM, is detected. This latter mode is identified as the barotropic Rossby basin mode which was found to destabilize the flow in the (equivalent) barotropic model (Section 3.4.1). It even becomes the only mode that determines the variability of the transient flow at $Re = 57$ and $Re = 60$. For an inviscid ocean in a confined basin, the Rossby basin modes are the free mode solutions of the model. They are the equivalent of free Rossby waves in an unbounded ocean (Dijkstra, 2000). Variability on longer than intermonthly time scales was not found in this relatively high friction regime.

6.3 Coupled wind-driven/DWBC flows

Also for coupled wind-driven/DWBC flows, several time integrations have been performed. The prescribed DWBC transport is 7.2 Sv, the standard value used in Chapter 5. It was shown in Section 5.3 that nine different modes destabilize the flow along the unique branch of stationary solutions that was detected (Fig. 5.2), and that six of them stabilize again as Re is increased. In Table 6.2, the characteristics of these nine modes are summed up. The spatial patterns of the three modes that remain unstable for increasing Re (B_3, B_8 and B_9) were shown in Figures 5.11 and 5.13.

Various Reynolds numbers are explored, at which the flow is expected to behave differently based on the results of the linear stability analysis. At $Re = 62$, oscillations with a time scale of 2.6 years are anticipated, since in that regime the flow is only unstable to the oscillatory mode B_2. At $Re = 80$, more complicated behavior is expected at various time scales, since the modes B_3, B_4 and B_5 have positive growth rates and B_6 and B_7 are only marginally damped. Finally, at $Re = 110$, the near-annual modes B_3 and B_8 are expected to be important. In Figure 6.3, 25-year time series for these three cases ($Re = 62$, $Re = 80$ and $Re = 110$) are shown. Note that for $Re = 62$, the first 10 years of the integration, during which the perturbations on the flow are still very small and hence not visible in the time series, are not shown. For $Re = 80$, the first 5 years are omitted for the same reason.

At $Re = 62$, the flow unexpectedly displays regular high-frequency oscillations with a period of 3.2 months, in stead of the expected oscillations with the features of B_2. A plot of the streamfunction anomaly (Fig. 6.4), obtained by subtracting the time-mean state from a snapshot of ψ_1 and ψ_2, shows a perturbation signal mainly along the northern boundary. It consists of wave-like disturbances with a meridional scale of approximately 300 km in the zonal direction that propagate westward. Moreover, the mean state of the integration is quite different from the stationary solution at

	Hopf bifurcation	period ($years$)	reverse Hopf bifurcation	max. growth rate (yrs^{-1})	spatial pattern
B_1	$\mathcal{H}_1$: $Re = 25.8$	4.4	$Re = 29.7$	0.12	
B_2	$\mathcal{H}_2$: $Re = 56.7$	2.6	$Re = 64.0$	0.18	
B_3	$\mathcal{H}_3$: $Re = 77.4$	0.7	–	2.8	Fig. 5.11a-b
B_4	$\mathcal{H}_4$: $Re = 79.3$	22.3	$Re = 80.3$	0.11	
B_5	$\mathcal{H}_5$: $Re = 79.8$	3.0	$Re = 80.2$	0.08	
B_6	$\mathcal{H}_6$: $Re = 81.0$	4.7	$Re = 86.9$	0.04	
B_7	$\mathcal{H}_7$: $Re = 81.9$	0.9	$Re = 87.4$	1.0	
B_8	$\mathcal{H}_8$: $Re = 87.0$	1.4	–	6.1	Fig. 5.11c-d
B_9	$\mathcal{H}_9$: $Re = 120.8$	5.1	–	0.12	Fig. 5.13

Table 6.2: *Characteristics of the nine oscillatory modes B_1 to B_9 that destabilize the coupled wind-driven/DWBC flow. For the modes that remain unstable with increasing Re, the growth rate at $Re = 125$ is stated.*

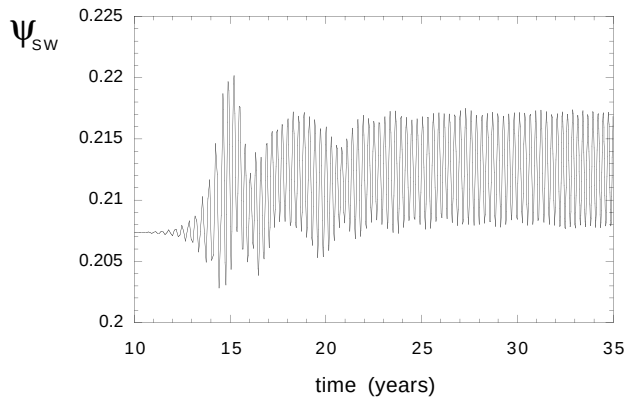

(a)

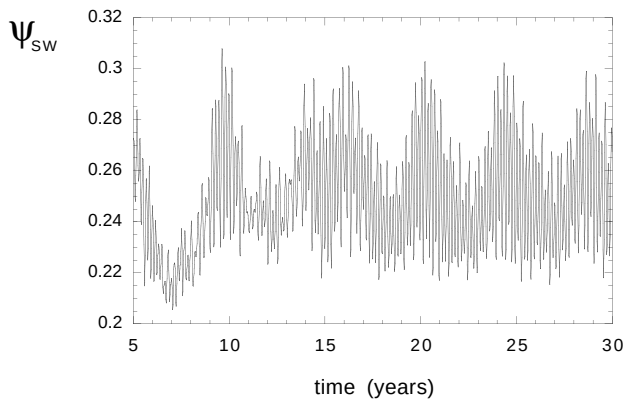

(b)

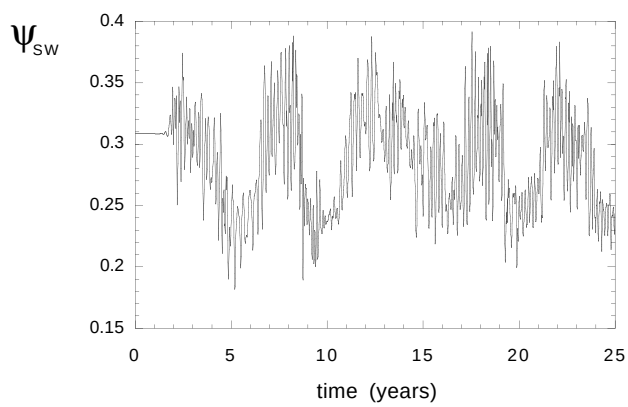

(c)

Figure 6.3: *Time series for the measure ψ_{SW} of the solution for (a) $Re = 62$, (b) $Re = 80$ and (c) $Re = 110$. Note that in (a) the first 10 years of the integration, during which the perturbations are still very small, are not shown. In (b), the first 5 years are left out.*

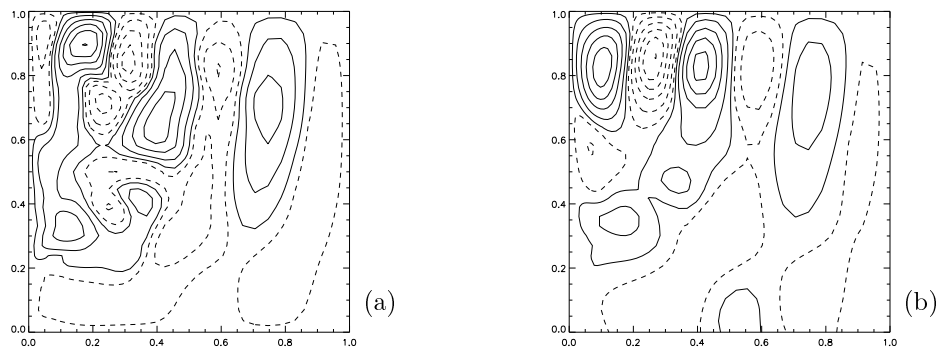

Figure 6.4: *Snapshot of the anomalous streamfunction in the (a) upper and (b) lower layer from the time integration at $Re = 62$ (both plots are scaled with their maximum, contour interval is 0.2).*

$Re = 62$ used as the initial condition (not shown). The origin of this oscillation was explored by combining the results of time integrations at different parameter settings and of the dynamical systems analysis, and will be discussed at the end of this section.

For higher values of Re, the time-dependent behavior of the flow is less regular (Figs. 6.3b-c) and it is obvious from the time series that both low-frequency and high-frequency variability now play a role. With M-SSA, the dominant statistical modes of variability for these time series are determined. At $Re = 80$, almost all the variability (93% of the total) can be attributed to only three oscillatory modes. These are identified as the same oscillation as shown in Figure 6.4 (27% of the total variability), the barotropic Rossby basin mode BM that also contributed to the variability of the purely wind-driven flow (60%), and the interannual mode B_6 (6%). For this time series, the dominant time scales of variability are 3.0 months, 2.0 months and 4.9 years, respectively. Apparently, the other modes that are unstable at $Re = 80$ (B_3, B_4 and B_5 in Table 6.2) are less important.

For $Re = 110$ the signal looks even noisier, but again only a few statistical modes (in this case four) already explain a large part (70%) of the simulated variability. These are identified as the oscillation shown in Figure 6.4, the barotropic Rossby basin mode and the modes B_6 and B_9. The associated dominant time scales are 2.4 months, 2.0 months, 3.6 years and 4.9 years. The low-frequency modes are more important at this Reynolds number: the contributions of the four modes to the total variability are 3%, 37%, 10% and 20%, respectively. The remaining 30% of the variability is divided between many different modes, which were not investigated in detail. Note that the expected substantial contribution of B_3 and B_8 is in fact negligible. Furthermore, B_9 is linearly stable at this value of Re, but its signal is clearly present in the (non-linear) evolution of the transient flow. The results of the M-SSA analysis of the time series in Figure 6.3 are summarized in the stack histogram in Figure 6.5.

Some of the statistical modes found with the M-SSA analysis can easily be identi-

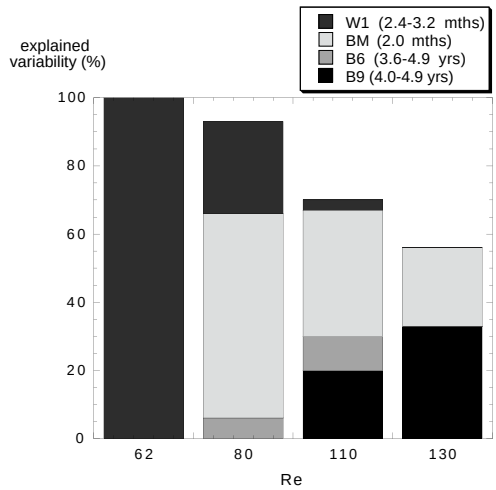

Figure 6.5: *Stack histogram of the percentage of the total variability in the coupled wind-driven/DWBC transient flows that is explained by specific internal modes. The associated time scales are provided in the legend.*

fied with modes known from the linear stability analysis (B_6, B_9 and the barotropic Rossby basin mode). The perturbation shown in Figure 6.4 is found to have a less obvious but very interesting origin: it appears to be the (modified) mode W_1, which was shown in Figure 3.5. This is clear from Figure 6.6, in which contour plots of the perturbation streamfunction for W_1 are shown for increasing values of V_{in}. The spatial patterns of the stationary solutions change for increasing inflow rates (see Fig. 5.6), and so do the patterns of the modes. For increasing strength of the DWBC, the mode W_1 resembles the snapshot from the time integration more and more (compare Figs. 6.6g-h and 6.4). The dominant time scale of the statistical mode of 3.2 to 2.4 months is also similar to that of the mode W_1 at high Reynolds numbers. So apparently, W_1 contributes substantially to the variability of the coupled wind-driven/DWBC flows. This seems surprising, since it was demonstrated in Section 5.5.1 that the mode W_1 does not become unstable anywhere along the branch of stationary solutions traced for coupled wind-driven/DWBC flows. This implies that the periodic orbit initially arising from the bifurcation point H_1 is now disconnected from the branch of stationary solutions, and has undergone a so-called cyclic-fold bifurcation as V_{in} was increased. A cyclic-fold bifurcation is basically a limit point for periodic solutions: the periodic orbit exists only for parameter values α larger (or smaller) than a critical value α_c (Nayfeh and Balachandran, 1995). If this is the case, it should be possible to find this cyclic-fold bifurcation by following the periodic orbit as a function of Re. This can be done by performing several time integrations, while using the transient flow shown in Figure 6.3 as the initial condition. Based on the results for $Re = 80$ and $Re = 110$, it seems that the periodic orbit loses its stability for higher Re (its contribution to the variability decreases, see Fig. 6.5), so

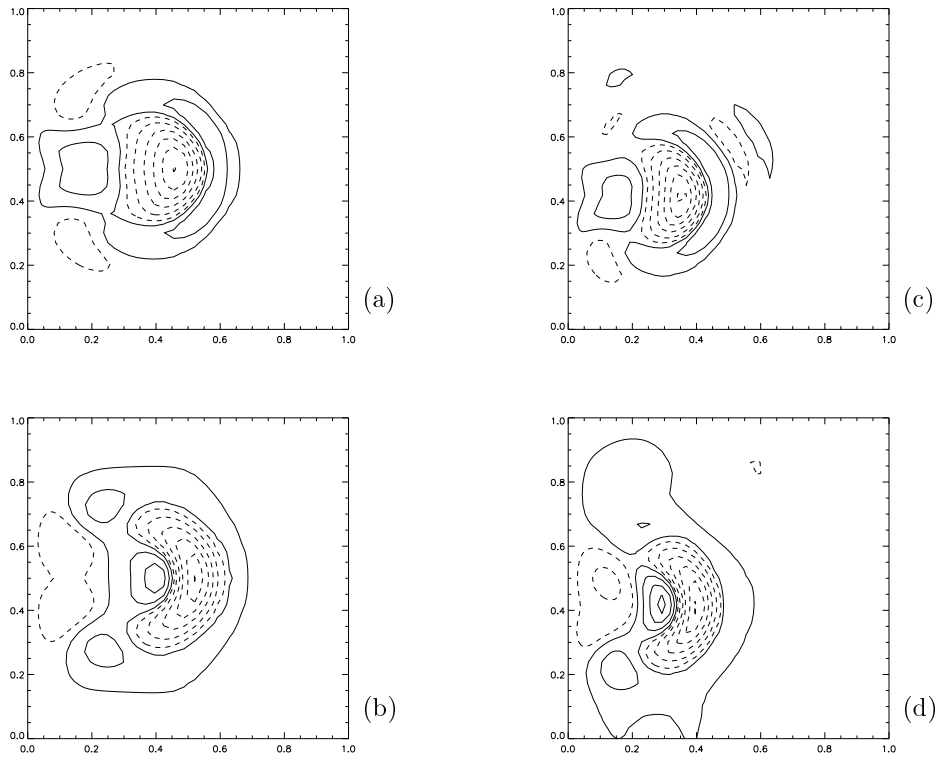

Figure 6.6: *Contour plot of the perturbation streamfunction of the oscillatory mode* W_1, *for* $Re = 31$ *and increasing* V_{in}. *Shown are contour plots for the upper and lower layer (upper and lower panels), at phase* $\nu t = 0.0$, *for (a-b)* $V_{in} = 0.0$; *(c-d)* $V_{in} = 1.5$; *(e-f)* $V_{in} = 2.0$ *and (g-h)* $V_{in} = 2.3$ ($\Gamma_2^* \in [0.0, 7.7]$ Sv). *All plots are scaled with their maximum, the associated stationary solutions were shown in Fig. 5.6.*

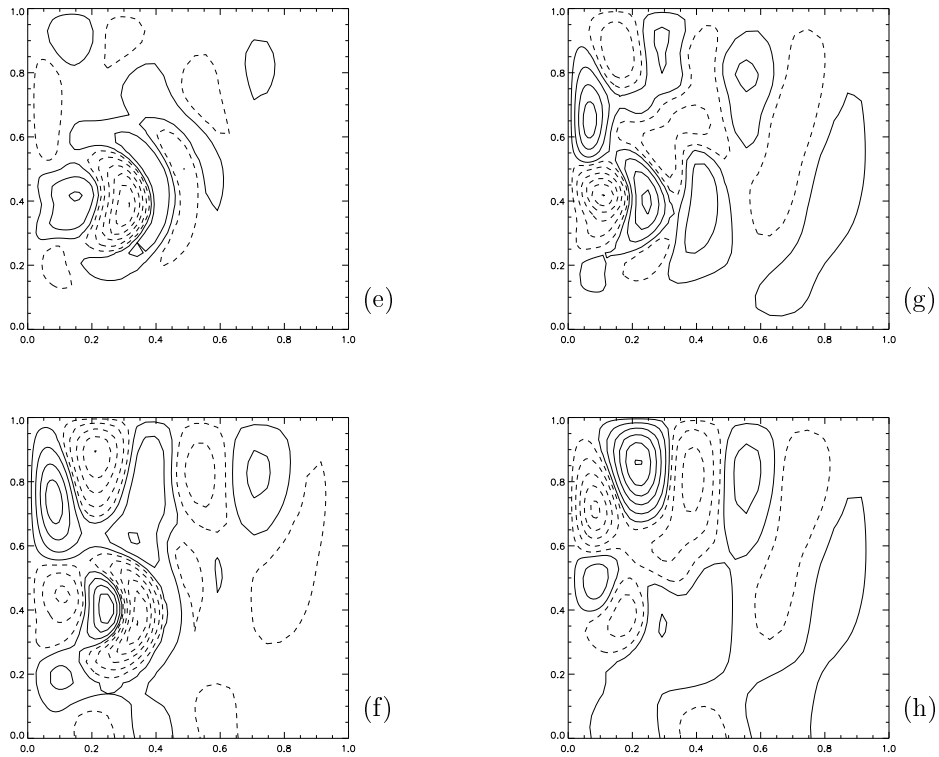

Fig. 6.6, continued.

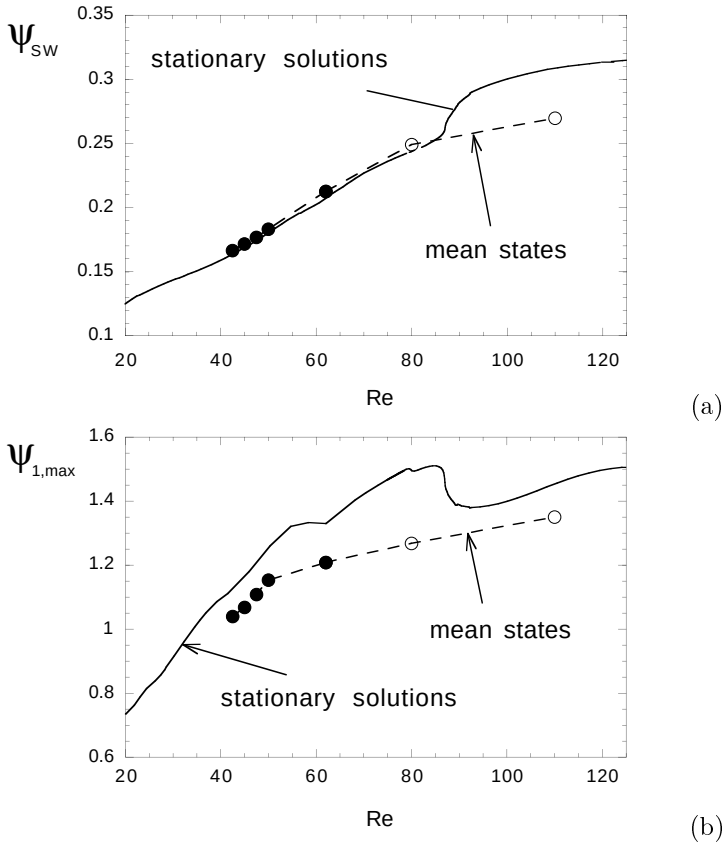

Figure 6.7: *Stationary solutions and mean states of time integrations as a function of Re, for the case with a DWBC ($V_{in} = 2.1$). In (a), ψ_{SW} is used as the measure of the solutions; in (b) the maximum of the upper layer streamfunction is plotted. The circles denote the mean states of the various time integrations, and are filled when the variability is solely due to the modified mode W_1, and open otherwise.*

the cyclic-fold bifurcation is expected to be found at low Re. Indeed, for Re down to 42, oscillatory behavior like shown in Figure 6.3a is found, but the amplitude of the oscillations decreases. For $Re < 42$, the transient flow converges towards the branch of stationary solutions, so the cyclic-fold bifurcation is located at $Re_c = 42$. In can thus be concluded that a large part of the variability of the coupled wind-driven/DWBC flows is due to the (modified) baroclinic mode W_1.

The results presented in this section are summarized in Figure 6.7, in which the mean states of the time integrations (circles) and the branch of stationary solutions for $V_{in} = 2.1$ are plotted. Filled circles indicate where the variability is entirely due to the modified internal mode W_1, open circles are used when other modes contribute to the simulated variability as well. Figure 6.7a gives the impression that the time-mean states and the stationary solutions are fairly similar, since in this case ψ_{SW} is not a good choice for the measure of the solutions. The substantial differences between the mean states and the stationary solutions are clearer in Figure 6.7b, in which the maximum of ψ_1 is used as the measure of the solutions.

6.4 Low-frequency variability

For the purely wind-driven flow, only the high friction regime was explored in Section 6.2. It is expected that, in accordance with the results by McCalpin and Haidvogel (1996), Berloff and McWilliams (1999) and Meacham (2000), low-frequency variability will arise in transient flows at lower friction. Also for the coupled wind-driven/DWBC flow the contributions of low-frequency modes seem to increase with increasing Re (Fig. 6.5). Hence, in this section the behavior of a transient wind-driven flow is compared to that of a transient coupled wind-driven/DWBC flow, both at low friction ($Re = 130$ or $A_H = 125\ m^2/s$). For both cases, the last 42 years of the time integration are used for the M-SSA analysis, sampled at intervals of one week.

For the wind-driven flow ($V_{in} = 0.0$), the time series for ψ_{SW} and for the upper layer kinetic energy are shown in Figure 6.8. Both high-, medium- and low-energy states are visited. Time-mean states, averaged over a high- and a low-energy period (years 27 to 29 and years 39 to 41, respectively), are shown in Figure 6.9a-d. In line with the results by McCalpin and Haidvogel (1996), Berloff and McWilliams (1999) and Meacham (2000), a high-energy state (low-energy state) is characterized by stronger (weaker) recirculation cells and a larger (smaller) penetration scale of the midlatitude jet.

The M-SSA analysis of the time series reveals that four statistical modes dominate the time-dependent behavior displayed in Figure 6.8. Together, they explain 46% of the variability. These statistical modes have time scales of 2.0 months, 10 years, 6.7 years and 2.0 months, respectively, and explain 20%, 15%, 8% and 3% of the total variability (Table 6.3). The high-frequency modes are identified again as barotropic Rossby basin modes, similar to the modes found in the higher friction regime (Section 6.2). The spatial pattern of the low-frequency mode with the time scale of 10 years is shown in Figure 6.10, at phase $\nu t = 0.0$. It hardly propagates, and simply seems to display the difference between the high- and the low-energy states. The low-frequency

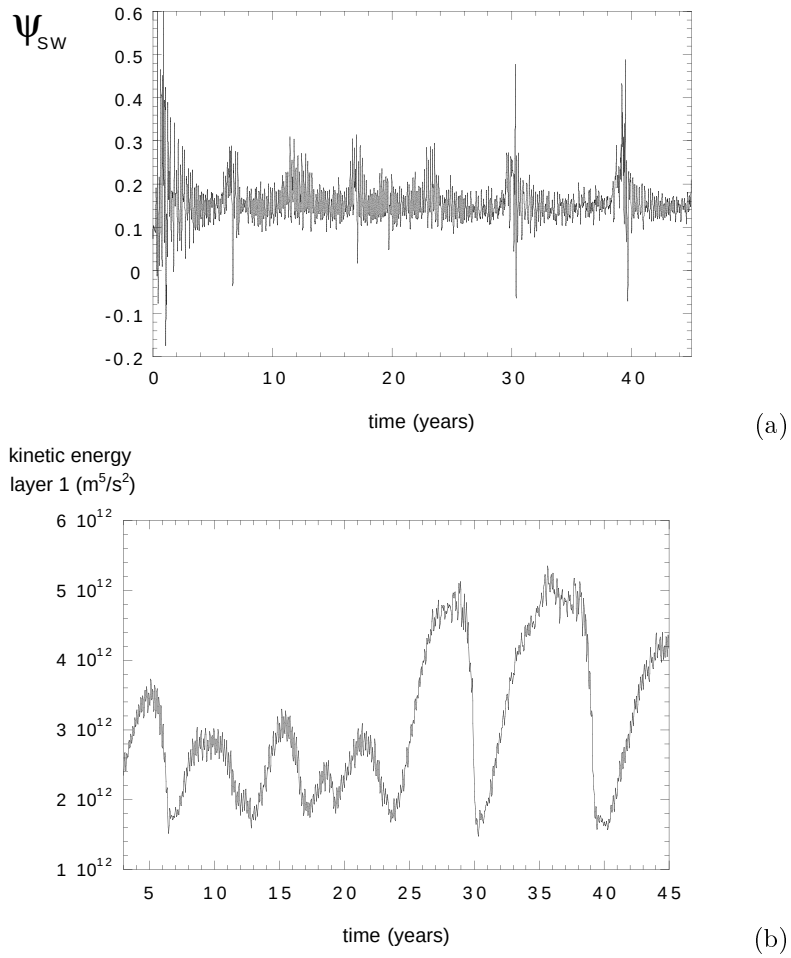

Figure 6.8: *Time series for (a) ψ_{SW} and (b) the upper layer kinetic energy (for the last 42 years of the total time series), for the purely wind-driven flow ($V_{in} = 0.0$) at $Re = 130$.*

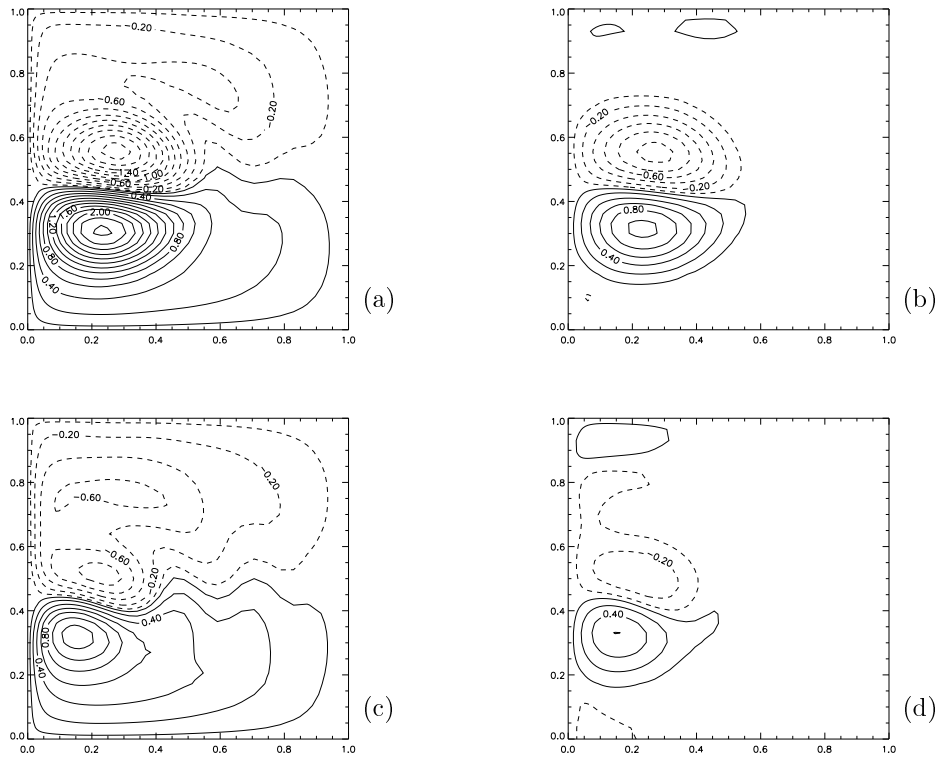

Figure 6.9: *Time-mean states for the upper and lower layer, for (a-b) a high-energy state (average over years 27 to 29) and (c-d) a low-energy state (average over years 39 to 41). Contour interval is 0.2 in all plots.*

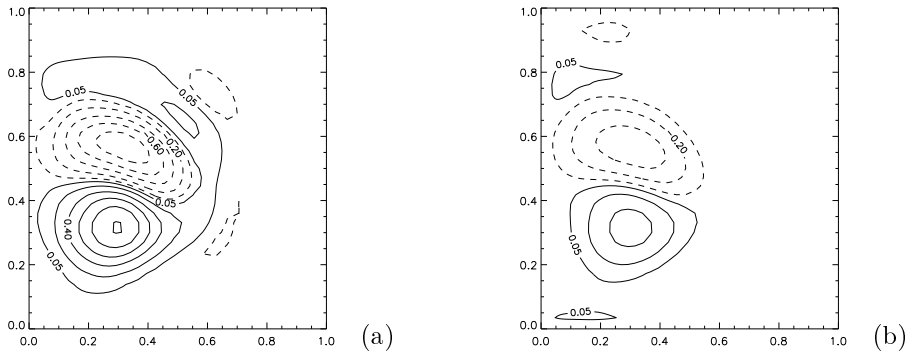

Figure 6.10: *Snapshot of the spatial pattern of the second most dominant statistical mode from the M-SSA analysis of the purely wind-driven flow in Fig. 6.8, which has a time scale of 10 years and explains 15% of the total variability, in (a) the upper and (b) the lower layer. The plots are scaled with the maximum of the field in (a).*

mode with the time scale of 6.7 years exhibits similar behavior. Their patterns do not correspond to any of the unstable modes that were detected. Moreover, multiple unstable equilibria do not exist in this parameter regime (Section 5.3). Hence it can be concluded that in this case the simulated low-frequency variability must be due to non-linear interactions of high-frequency signals.

For the coupled wind-driven/DWBC flow at $Re = 130$, the time series for ψ_{SW} is shown in Figure 6.11a. During the first few years of the integration, perturbations on the initial state are still very small and hence hardly visible. In the remainder of the time series, both high- and low-frequency variability signals are clearly present. Similar behavior is observed in time series of the kinetic energy of the upper layer (Fig. 6.11b). In Figure 6.12, mean states averaged over periods when the upper layer

	dominant time scale	explained variability	identification with internal mode
wind-driven	2.0 months	20% + 3%	Rossby basin mode
($V_{in} = 0.0$)	10 years	15%	–
	6.7 years	8%	–
coupled wind-driven/DWBC	4.0 years	33%	B_9 (Section 5.5)
($V_{in} = 2.1$)	2.0 months	15% + 8%	Rossby basin mode

Table 6.3: *Dominant time scales and percentage of the total variability in the time series at $Re = 130$ that can be attributed to various internal modes, based on the M-SSA analysis.*

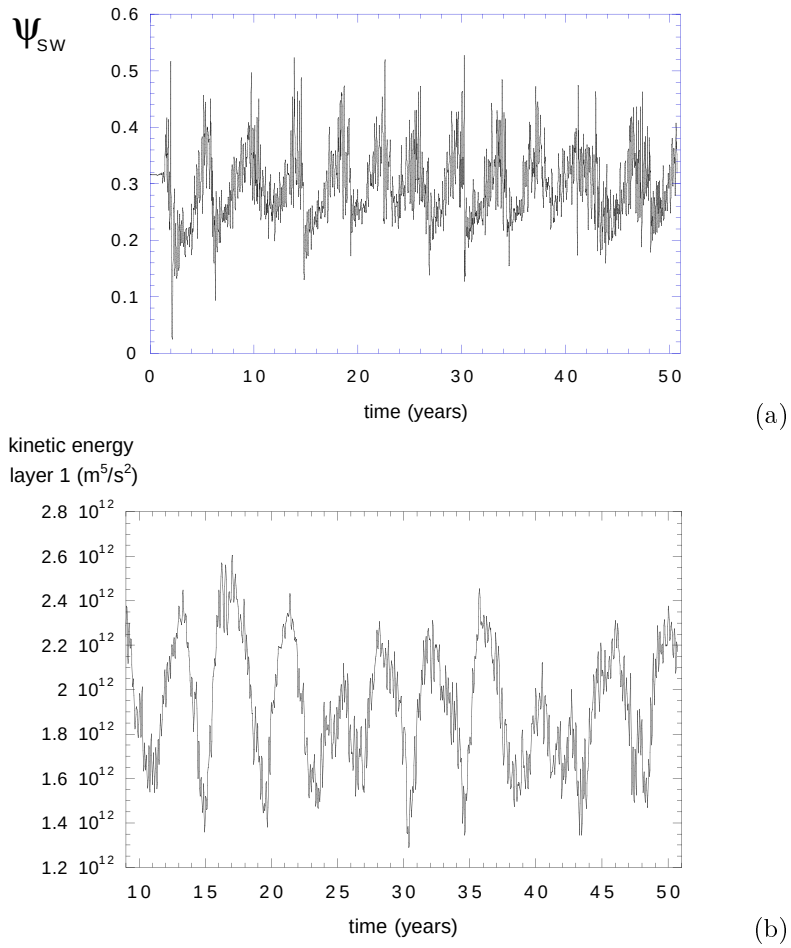

Figure 6.11: *As in Fig. 6.8, but for the coupled wind-driven/DWBC flow* ($V_{in} = 2.1$) *at* $Re = 130$.

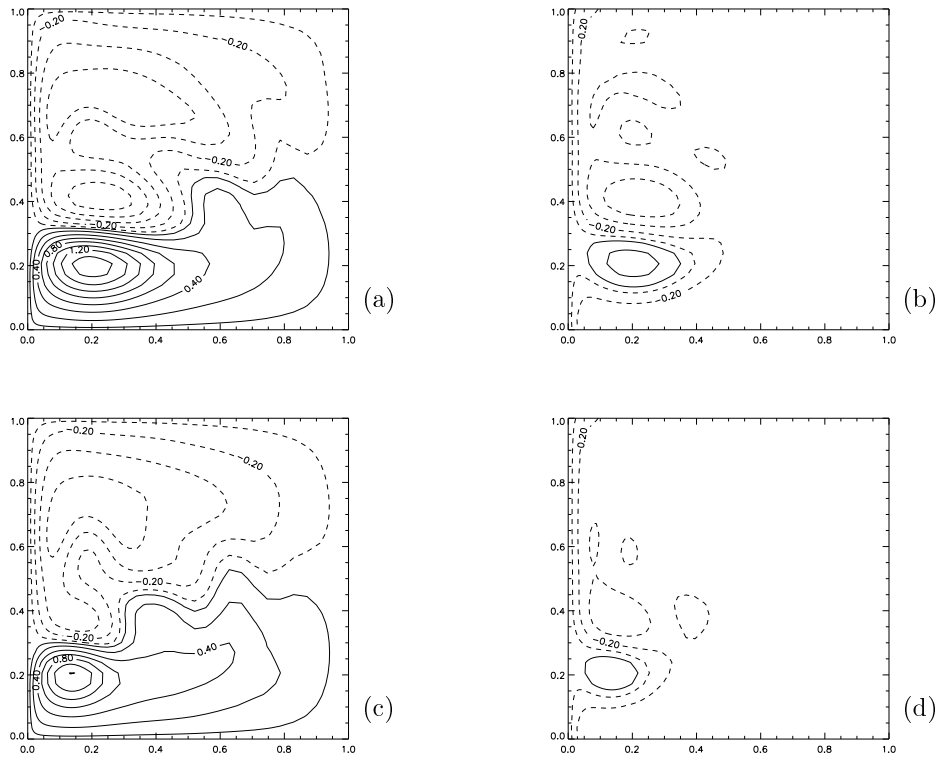

Figure 6.12: *Time-mean states for the upper and lower layer, for (a-b) a high-energy state (average over years 16 to 18) and (c-d) a low-energy state (average over years 38 to 40). Contour interval is 0.2.*

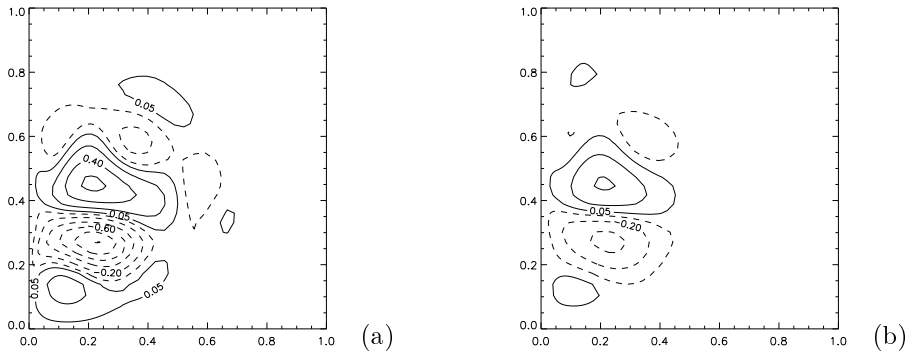

Figure 6.13: *Snapshot of the spatial pattern of the most dominant statistical mode from the M-SSA analysis of the coupled wind-driven/DWBC flow in Fig. 6.11, in (a) the upper and (b) the lower layer. The plots are scaled with the maximum of the field in (a).*

kinetic energy is relatively high (a-b) and relatively low (c-d) are shown (averages are over years 16 to 18 for the high-energy state and over years 38 to 40 for the low-energy state). Again the penetration scale of the midlatitude jet is larger for the high-energy state, and the DWBC is deflected more in the cross-over region.

The most dominant statistical mode of variability in the time series shown in Figure 6.11 is an oscillation with a time scale of 4.0 years, which explains 33% of the total variability. In Figure 6.13, a snapshot of the spatial pattern of this statistical mode is shown. Its spatial pattern resembles that of the linearly unstable mode B_9 shown in Figure 5.13: its main features are two anomalies of opposite sign in both layers, centered at $[x, y] = [0.25, 0.25]$ and $[x, y] = [0.25, 0.45]$. Moreover, the propagation of the mode is similar to that of B_9 (not shown). Apparently, the time scale of the mode is slightly modified at these supercritical conditions (recall that at criticality, the period of B_9 is 5.1 *years*). The second and third most dominant statistical mode are both oscillations with a time scale of 2.0 months, and explain 8% and 15% of the total variability. These are again identified as barotropic Rossby basin modes. So, in agreement with the hypothesis stated in the introduction, an internal mode seems to give rise to the simulated low-frequency variability for the coupled wind-driven/DWBC flow.

More support for this conclusion is obtained by analyzing the spectra of the time series of the upper layer kinetic energy. For both the coupled wind-driven/DWBC flow and the purely wind-driven flow, this spectrum is shown in Figure 6.14a-b. On the horizontal axis, the dimensionless frequency f is plotted. The dimensional period p^* (in seconds) associated with a particular frequency f is $p^* = L/(Uf)$. The highest frequency that is resolved if $f = 50$, which corresponds to a period p^* of 2 weeks (two times the sample interval used in the M-SSA analysis), but only the frequencies $f < 20$

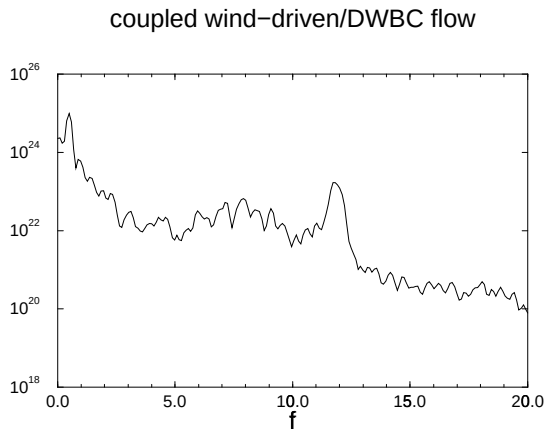

(a)

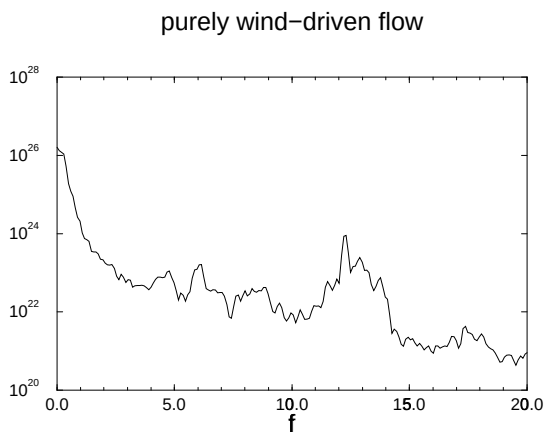

(b)

Figure 6.14: *Spectra of the time series for the upper layer kinetic energy (a) for the coupled wind-driven/DWBC flow in Fig. 6.11b and (b) for the purely wind-driven flow in Fig. 6.8b. On the horizontal axis, the dimensionless frequency f is plotted. The dimensional period p^* (in seconds) associated with f is $p^* = L/(Uf)$. The highest frequency that is resolved is $f = 50.0$, or $p^* = 2$ weeks. The range in f shown here is $f \in [0.0, 20.0]$, corresponding to periods p^* larger than 5 weeks.*

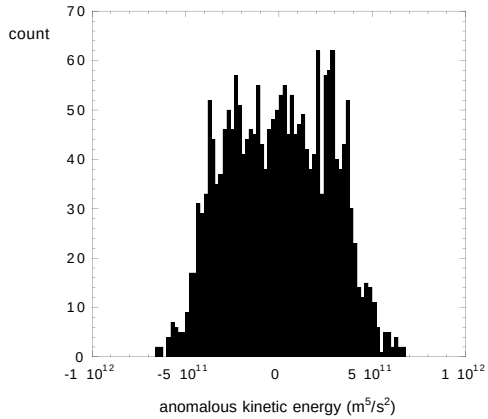

(a)

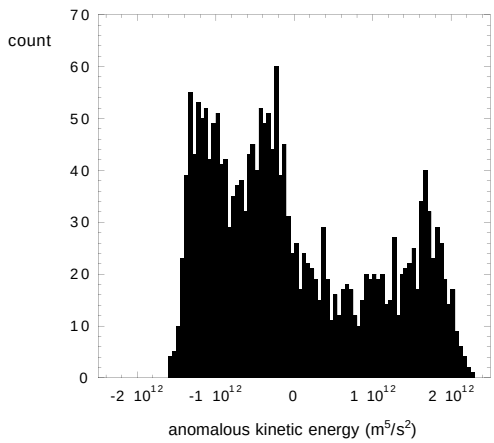

(b)

Figure 6.15: *Histograms of the distribution of the upper layer kinetic energy with respect to its mean value, (a) for the coupled wind-driven/DWBC flow in Fig. 6.11b and (b) for the purely wind-driven flow in Fig. 6.8b.*

are displayed in this figure ($p^* > 5$ *weeks*). For $V_{in} = 2.1$, a distinct low-frequency peak is found near $f = 0.5$, which corresponds to a period of 4 years. This signal is related to the dominant mode of variability derived from the M-SSA analysis, which was identified as the mode B_9 (Table 6.2). Another peak in the spectrum is found around $f = 12$ or $p^* = 2$ *months*, which is the signal of the barotropic Rossby basin modes. For the purely wind-driven flow, the Rossby basin modes also give a clear signal in the intermonthly frequency band (Fig. 6.14b). In the low-frequency band, the spectrum has no distinct low-frequency peak. So, the internal mode of variability B_9 appears to dictate the time scale of the low-frequency variability for the coupled wind-driven/DWBC flow, whereas for the purely wind-driven flow there seems to be no preferred low-frequency time scale.

Further support for this conclusion was found by plotting a histogram of the anomalous kinetic energy distribution for the time series in Figures 6.11b and 6.8b. These plots were constructed by dividing the range in kinetic energy visited during the 42 years of the time series into 100 bins of equal width, and subsequently counting the number of samples in each bin. The coupled wind-driven/DWBC flow does not show a preference for a specific state (Fig. 6.15a), because every phase of the low-frequency oscillation has comparable kinetic energy. In contrast, the kinetic energy distribution for the purely wind-driven flow (Fig. 6.15b) shows three distinct peaks, indicative of irregular transitions between the high-, medium- and low-energy states in Figure 6.8b. Unlike for the coupled wind-driven/DWBC flow, for the wind-driven flow the mean value of the kinetic energy is not the one that is visited most often. This again indicates that the low-frequency variability for the wind-driven flow is not caused by an internal mode, but by non-linear interactions of high-frequency signals.

6.5 Discussion

Throughout this thesis, the internal variability of the wind-driven ocean circulation is studied by calculating stationary solutions, and subsequently determining the most unstable modes that destabilize these flows. It is expected that these modes to a large extent control the time- and spatial characteristics of the variability, near the stability boundary as well as further into the unstable regime. As a consequence, they are thought to provide a foundation for the interpretation of the time-dependent behavior of the flow. In this chapter, this assumption was verified by analyzing the results of a series of time integrations, for both purely wind-driven and coupled wind-driven/DWBC flows. With the help of statistical techniques, the most dominant time scales and spatial patterns of the variability of the transient flows were determined. These were compared to the characteristics of the internal modes known from the linear stability analysis of the stationary solutions, to assess the importance of various internal modes for the variability of the transient flows. For the time series considered, almost all the important statistical modes of variability (explaining more than a few % of the total variability) could ultimately be identified as being internal modes of the system. This certainly justifies the approach used in this thesis. Note, however, that the specific contributions of the various internal modes depend on the parameter

setting used, as was shown in Figures 6.2 and 6.5. Moreover, not all the unstable internal modes that were detected contribute to the variability of the transient flows. This implies that the non-linear evolution of the circulation cannot be predicted from the stationary solutions and their stability characteristics alone beyond the onset of instability. However, the results of the dynamical systems analysis are very useful for interpreting and deducing the origin of the internal variability simulated in time integrations.

A demerit of the applied approach that was already discussed in Section 2.3 is that the stability of periodic orbits is not considered. As a consequence, sometimes the simulated variability has surprising features, which at first do not seem related to the linearly unstable modes. The existence of the isolated periodic orbit associated with W_1 is a good example of the occurrence of variability that could not be anticipated from the results presented in Chapter 5, since periodic orbits are not traced in parameter space. However, the explanation of its origin that was given in Section 6.3 illustrates the complementary role of the dynamical systems analysis and the time integrations. Moreover, it demonstrates the advantage of using a hierarchy of models, in which new physical processes are introduced step by step.

In the transient flows at low friction discussed in Section 6.4, low-frequency variability is found independent of the presence of the DWBC. As was shown in Figures 6.14 and 6.15, the spectral characteristics are quite different in the two cases. When a DWBC is present, a single internal mode of variability dominates the low-frequency variability. When a DWBC is absent, non-linear eddy-eddy and eddy-mean flow interactions are responsible for the low-frequency variability. Transitions between high- and low-energy states are involved in this low-frequency variability, but the M-SSA analysis of the time series indicates that no particular low-frequency oscillatory mode stands out.

Since low-frequency variability is found in transient flows under a wide range of parameter settings and in different model configurations (McCalpin and Haidvogel, 1996; Berloff and McWilliams, 1999; Meacham, 2000, and this study), all lacking a DWBC, it is on hindsight actually quite surprising that in the study by Spall (1996b) low-frequency variability is absent when the DWBC transport in the second layer is set to zero. Possibly, the presence of the third layer in his model influences the variability characteristics. In addition, the in- and outflows in the upper layer, which represent the sum of the Sverdrup transport not captured by the limited model domain and the upper limb of the thermohaline circulation (see Section 5.2) may also affect the internal variability. As a result, the stability characteristics of the surface flow in the case studied by Spall (1996b) may very well be different from those of the purely wind-driven flows. If this change in stability results in weaker non-linear interactions between high-frequency signals in the simulations performed by Spall (1996b), it would explain the lack of low-frequency variability in the absence of an upper DWBC. When this upper DWBC is present, an internal mode like the one discussed in Chapter 5 may be responsible for the low-frequency oscillations described by Spall (1996b). To confirm this conjecture a dynamical systems analysis could be performed using a three-layer model in a similar configuration as used by Spall (1996b).

Chapter 7

Discussion

The main objective of this thesis was to study the origin and characteristics of the internal variability of the wind-driven ocean circulation. To this end, the dynamical behavior of the flow was explored using an idealized two-layer quasi-geostrophic ocean model, in which a double-gyre circulation was forced by prescribing a steady, zonal wind stress at the surface. The subject was approached from a dynamical systems point of view, by calculating the stationary solutions for the flow while varying a control parameter. In most cases, the strength of the lateral friction was used. In addition, the internal modes that destabilize these stationary flows were determined, which give rise to time-dependent behavior.

In Chapter 3, the dynamics of the idealized double-gyre system was studied. By exploiting the simplifications of the quasi-geostrophic system, in particular its internal symmetry, the solution structure (i.e., the possible stationary solutions as a function of a control parameter) was explored for changing values of the lateral friction coefficient. Branches of both symmetric and asymmetric double-gyre solutions were traced. It was found that, at relatively low friction, the circulation is destabilized by baroclinic instabilities that introduce internal variability on intermonthly time scales. The results obtained for this symmetric configuration provide a foundation for further studies in this thesis. Starting from this known, simple reference case, model parameters were changed continuously. In this way, a connection was made between different physical models, meanwhile studying the (changes in the) dynamics. This appeared more illuminating than just comparing the results for two model settings. In Chapter 3, the impact of allowing for baroclinic instabilities was investigated in this way, by continuously transforming the baroclinic model into a barotropic model.

In Chapter 4, it was illustrated how dynamical systems analysis and time integrations can be combined to explain the underlying physics of a fundamental oceanographic problem. In that chapter, the rectification of the mean flow by time-dependent eddies was addressed. Based on the results of the linear stability analysis, a slightly supercritical parameter regime could be chosen. It was demonstrated how non-linear

interactions of the baroclinic instabilities change the mean flow, by performing a weakly non-linear analysis. The knowledge of both the stationary solutions, the most unstable internal modes and the mean state of the time integrations made it possible to derive a clear picture of the rectification process, in particular of the generation of a deep mean flow.

In Chapter 5, a Deep Western Boundary Current (DWBC) was introduced in the symmetric wind-driven system studied in Chapter 3. Its presence appeared to have a large impact, both on the stationary solutions for the flow as well as on the internal modes that destabilize them. By establishing a continuous connection between the wind-driven flows and the coupled wind-driven/DWBC flows, the changes in the dynamics due to the presence of the subsurface current could be analyzed in detail. It was shown that the presence of a DWBC results in stationary solutions with a mid-ocean jet that all separate south of the zero wind stress curl line. Moreover, it was demonstrated that its presence induces a preference for instabilities on longer time scales, as was seen earlier in more realistic models of the Gulf Stream/DWBC cross-over.

Finally, the results of various time integrations were analyzed in Chapter 6, on the basis of the dynamical systems analyses performed in previous chapters. It was demonstrated that, even far from the onset of instability, a large part of the variability displayed by the transient flows could be attributed to internal modes. This holds for both purely wind-driven and for coupled wind-driven/DWBC flows. Moreover, different physical mechanisms that give rise to low-frequency variability were distinguished, using the combined knowledge of a dynamical systems and a statistical analysis. To a large extent, the time-dependent behavior of the flows can be explained on the basis of the bifurcation structure.

Obviously, the range of parameters considered and the idealization of the wind stress and geometry make it difficult to compare the results presented in this thesis with those of state-of-the-art eddy-resolving Ocean General Circulation Models (OGCM's) or observations. To make progress in building an interpretation framework for the time-dependent behavior of the wind-driven ocean circulation, the robustness of the (qualitative features of the) results needs to be addressed using more realistic model configurations. For the (equivalent) barotropic circulation this has recently been done by applying a hierarchy of models. The circulation in the barotropic quasi-geostrophic model discussed in Chapter 3 served as the reference case for these studies. Within this model, multiple equilibria exist due to spontaneous symmetry-breaking through a pitchfork bifurcation. Time-dependent behavior is first introduced through an oscillatory Rossby basin mode with an intermonthly time scale.

In Dijkstra and Molemaker (1999), it was demonstrated that these multiple equilibria persist in an equivalent barotropic configuration, both in a quasi-geostrophic and in a shallow-water model. In the latter case, the equilibria exist as a result of a perturbed pitchfork bifurcation, since the shallow-water model does not have the internal symmetry properties the quasi-geostrophic model has. As for the quasi-geostrophic model, the circulation in the shallow-water model is first destabilized by a barotropic basin mode with an intermonthly time scale. The results are in qualitative

agreement with the results obtained by Speich *et al.* (1995), who performed a similar study. Subsequently, Dijkstra and Molemaker (1999) incorporated realistic continental geometry. In addition, a more realistic wind forcing was prescribed, which was derived from the Hellerman and Rosenstein (1983) data set. Naturally, the stationary solutions for the flow are modified by these alterations, but still the multiple equilibria as well as the basin mode survive.

The full extent of the North Atlantic Ocean was considered in Schmeits and Dijkstra (2000), who used a barotropic shallow-water model with realistic continental geometry on a horizontal resolution of 0.5°. They also found multiple equilibria due to the perturbed pitchfork bifurcation, which has its origin in the symmetry-breaking in the quasi-geostrophic model. These multiple stationary solutions differ with respect to the separation behavior of the model Gulf Stream. Besides the multiple equilibria, Schmeits and Dijkstra (2000) detected a Hopf bifurcation that marks the transition to oscillatory behavior. For the most realistic model configuration, this mode has a time scale of six months, and is located in the region where the Gulf Stream separates from the coast. It is found to be a modification of the ocean basin modes that were detected for the barotropic quasi-geostrophic model in a square basin (Chapter 3). So it can be concluded that, with regard to the barotropic circulation, the idealized quasi-geostrophic model on a small, square domain already encompasses the essential internal dynamics that determine the underlying solution structure and the stability properties of the circulation in a barotropic model of the full North Atlantic Ocean.

For baroclinic layer models, such a series of studies has not yet been performed. However, the subsurface layers of such layer models are not forced directly by the surface wind stress, and are only set into motion by interfacial stresses or time-dependent motions (Pedlosky, 1996). As a consequence, without interfacial friction between the layers, the stationary solution structure for the circulation in a two-layer model is exactly the same as that for the circulation in an equivalent barotropic model with the same parameter setting, and qualitatively the same as that for the circulation in a barotropic model. As was shown in Chapter 3, multiple equilibria due to symmetry-breaking exist in both the baroclinic and the barotropic quasi-geostrophic model. Since these equilibria persist throughout the hierarchy of barotropic models that was studied, the same can be expected for the baroclinic case.

However, it was shown in Chapter 3 that the presence of an active second layer drastically changes the stability characteristics of the flow, and consequently its transition to time-dependence. The robustness of the baroclinic modes thus needs to be established by studying more realistic model configurations. Most of the results obtained so far support the conclusion that the results presented here for a small, square ocean basin are representative for the qualitative behavior of purely wind-driven flows. The baroclinic modes persist when the applied wind forcing is non-symmetric (Dijkstra and Katsman, 1997), and are also among the first to destabilize the flow in a two-layer shallow-water model (S. Wolting and J.J. Nauw-van der Vegt, personal communication). In addition, there are indications that the baroclinic modes also survive when the basin size is increased. Berloff and McWilliams (1999) studied the circulation in a two-layer quasi-geostrophic model on a much larger computational domain than used in this thesis. They showed that the transition to time-dependence

is marked by an oscillatory mode with similar features as the internal modes discussed in Chapter 3. Nonetheless, more work is needed to determine the impact of for example more realistic geometry, wind forcing pattern, bottom topography and vertical resolution on the bifurcation structure.

Furthermore, the results presented in Chapter 5 demonstrate the sensitivity of the baroclinic modes to the presence of a Deep Western Boundary Current. Its presence significantly distorts the spatial pattern of the stationary solutions and thus their stability. This indicates that in the North Atlantic Ocean the wind-driven and the thermohaline-driven part of the circulation interact in a fundamental way, so that separating them is not justified. It demonstrates that for a proper representation of the circulation in this area both the wind-driven and the thermohaline circulation have to be incorporated. In particular, one needs to allow for feedbacks between the (strength of the) wind-driven surface flows and the DWBC, that are not accounted for in the model configuration used in this study.

In this thesis, the variability of the wind-driven circulation was addressed from a dynamical systems point of view. This choice was motivated by the expectation that the results would provide a framework for the interpretation of the time-dependent behavior of the circulation. The details of the contributions of various modes to the internal variability depend on the specific parameter setting that is chosen, so that the time-dependent behavior can not be predicted on the basis of the bifurcation diagram. However, within the context of the idealized two-layer quasi-geostrophic model, the origin of a large part of the variability displayed by transient flows could indeed be explained on the basis of the dynamical systems analysis, even far into the unstable regime (Chapter 6). When only transient flows are computed, as was done by for example Berloff and McWilliams (1999), explaining the variability is more difficult. They also interpret the variability in transient flows at various strengths of the lateral friction from a dynamical systems point of view, but do not calculate the instabilities for the flow explicitly. Based partly on results presented in Chapter 3, the first transitions to periodic and quasi-periodic behavior are linked to the occurrence of Hopf bifurcations. However, they need to fall back on a spectral analysis of the time series in the low friction regime, where the flow behaves chaotically. Subsequently, statements can only be made on changes in the spectral characteristics of the flow with changing strength of the friction. In contrast, the analysis presented in Chapter 6 allows for a more specific analysis of changes in the contributions of various internal modes.

For the large-dimensional system studied in this thesis, only the stability of stationary solutions was investigated. As explained in Chapter 2, it is not feasible to follow periodic solutions in parameter space, although this would be more appropriate beyond the first Hopf bifurcation which marks the transition to time-dependence. Consequently, isolated periodic orbits that possibly exist can not be detected. This is a weakness of the approach which is not easily evaded at present. As a result, time integrations may display substantial variability at time and spatial scales unpredicted by the linear stability analysis of the stationary solutions. Two such isolated periodic orbits contributed to the variability in the transient flows presented in Chapter 6.

For these cases, the origin of the variability could still be recovered by analyzing time series and continuation results at various parameter settings in detail. However, this may not always be possible in general.

To trace periodic orbits and analyze their stability in a systematic way, perhaps a so-called reduced model can be applied. In such a model, which is deduced from the full ocean model, the number of degrees of freedom is drastically decreased. The resulting mathematical problem is much easier to handle so that it can be applied to trace periodic orbits through parameter space. The obvious difficulty in constructing such a reduced model is to decide *a priori* how to reduce the number of degrees of freedom, while keeping the qualitative behavior of the reduced model unimpaired. Many attempts have been made, which basically come down to a projection of the full model equations on to a set of basis functions. A large disadvantage of most attempts is that the choice of these basis functions is not based on knowledge of the dynamics of the flow. It is currently investigated whether it is possible to construct a reliable reduced model based on the stationary solutions for the flow and on the most unstable internal modes (P.C.F. van der Vaart *et al.*, personal communication), to circumvent this disadvantage.

Ultimately, one would like to be able to identify the origin of variability in simulations with state-of-the-art eddy-resolving OGCM's or in observations on the basis of the results of the dynamical systems analysis. For this, one first needs to determine the most unstable internal modes for the flow in a realistic model configuration, then trace these modes to simpler model configurations, and study their basic physics within the context of this idealized model. The same can be attempted the other way around, by increasing the complexity of models from a simple, well-understood starting-point. In this thesis, this strategy was used when studying the impact of the Deep Western Boundary Current on the wind-driven circulation. The advantage of this 'bottom-up' approach is that the obtained knowledge of the characteristics of the internal modes gives directions for analyzing large data sets. This 'bottom-up' approach proved to be quite successful in the study by Schmeits and Dijkstra (2000). The 0.5° resolution barotropic model of the North Atlantic Ocean they used is, apart from the lack of stratification, fairly realistic. It can be viewed as the end point of the systematic analysis of the dynamics of the barotropic wind-driven circulation, which was started by studying the flow in the idealized quasi-geostrophic model (Chapter 3). In this realistic model, the transition to time-dependence is marked by an ocean basin mode on an intermonthly time scale. It was attempted to identify this mode with variability of the Gulf Stream. Output from an eddy-resolving OGCM was found to display significant variability on a time scale of nine months. The nine-month mode and the modified ocean basin mode have many features in common. This gives an indication that the nine-month variability in the Gulf Stream region as found in the OGCM may be explained as arising through internal ocean dynamics. Also in satellite data of the Gulf Stream region a statistically significant propagating mode of variability with a time scale close to nine months was found. However, the connection of the internal basin mode with the nine month variability in the observations is less obvious (Schmeits and Dijkstra, 2000).

In conclusion, it was shown in this thesis that the dynamical systems analysis of the wind-driven circulation provides valuable information on the solution structure and its stability characteristics. On the basis of this dynamical systems analysis, the relevant physical processes that cause internal variability can be studied in detail, for example by exploring the relatively simple behavior near the stability boundary and by continuously connecting parameter regimes which involve different physics. Although the transient properties of the circulation can not be predicted on the basis of this dynamical systems analysis away from the stability boundary, the results facilitate the interpretation of the variability in time integrations. In this respect, the combination of dynamical systems and time series analysis is a particularly powerful tool for investigating the characteristics, the origin and the sensitivity of the internal variability of the ocean circulation. It is expected that in the near future the variability of the circulation can be explored using more realistic models. Such an analysis will contribute to our understanding of the observed variability of the ocean circulation.

Bibliography

Acheson, D. J. (1990). *Elementary fluid dynamics*. Clarendon Press, Oxford. 397 pp.

Apel, J. R. (1988). *Principles of ocean physics*. Academic Press, London, 2nd edition. 631 pp.

Barnier, B., Hua, B. L., and LeProvost, C. (1991). On the catalytic role of high baroclinic modes in eddy-driven large-scale circulations. *J. Phys. Oceanography*, **21**, 976–997.

Berloff, P. S. and McWilliams, J. C. (1999). Large-scale, low-frequency variability in wind-driven ocean gyres. *J. Phys. Oceanography*, **29**, 1925–1949.

Bower, A. S. and Hunt, H. D. (2000a). Lagrangian observations of the Deep Western Boundary Current in the North Atlantic Ocean. Part 1: Large-scale pathways and spreading rates. *J. Phys. Oceanography*, **30**, 764–783.

Bower, A. S. and Hunt, H. D. (2000b). Lagrangian observations of the Deep Western Boundary Current in the North Atlantic Ocean. Part 2: The Gulf Stream - Deep Western Boundary Current Crossover. *J. Phys. Oceanography*, **30**, 784–804.

Broecker, W. S. (1991). The great ocean conveyor. *Oceanography*, **4**, 79–89.

Bryan, K. (1963). A numerical investigation of a nonlinear model of a wind-driven ocean. *J. Atm. Sci.*, **20**, 594–606.

Cessi, P. (1988). A stratified model of the inertial circulation. *J. Phys. Oceanography*, **18**, 662–682.

Cessi, P. and Ierley, G. R. (1995). Symmetry breaking and multiple equilibria in quasi-geostrophic, wind driven flows. *J. Phys. Oceanography*, **25**, 1196–1205.

Cessi, P., Ierley, G. R., and Young, W. R. (1987). A model of the inertial recirculation driven by potential vorticity anomalies. *J. Phys. Oceanography*, **17**, 1640–1652.

Cushman-Roisin, B. (1994). *Introduction to geophysical fluid dynamics*. Prentice-Hall, Inc., New Jersey. 320 pp.

Dijkstra, H. A. (2000). *Nonlinear physical oceanography. A dynamical systems approach to the large scale ocean circulation and El Niño.* Kluwer Academic Publishers, Dordrecht, the Netherlands. 456 pp.

Dijkstra, H. A. and Katsman, C. A. (1997). Temporal variability of the wind-driven quasi-geostrophic double gyre ocean circulation: Basic bifurcation diagrams. *Geophys. Astrophys. Fluid Dynamics*, **85**, 195–232.

Dijkstra, H. A. and Molemaker, M. J. (1999). Imperfections of the North-Atlantic wind-driven ocean circulation: continental geometry and windstress. *J. Marine Res.*, **57**, 1–28.

Dijkstra, H. A. and Neelin, J. D. (1995). On the attractors of an intermediate coupled ocean-atmosphere model. *Dyn. Atm. Oceans*, **22**, 19–48.

Dijkstra, H. A., Molemaker, M. J., van der Ploeg, A., and Botta, E. F. F. (1995). An efficient code to compute nonparallel flows and their linear stability. *Comp. Fluids*, **24**, 415–434.

Eady, E. T. (1949). Long waves and cyclone waves. *Tellus*, **13**, 33–52.

Eckhaus, W. (1965). *Studies in non-linear stability theory.* Springer Verlag, Berlin. 117 pp.

Ekman, V. W. (1905). On the influence of the earth's rotation on ocean-currents. *Arkiv för Matematik, Astronomi och Fysik*, **2:11**, 52 pp.

Gill, A. E. (1983). Eddies in relation to climate. In A. R. Robinson, editor, *Eddies in Marine Science*, pages 441–444. Springer Verlag, New York.

Guckenheimer, J. M. and Holmes, P. J. (1983). *Nonlinear Oscillations, Dynamical systems and Bifurcations of vector fields.* Springer, New York, 3rd edition. 453 pp.

Haidvogel, D. B., Robinson, A. R., and Rooth, C. G. H. (1983). Eddy-induced dispersion and mixing. In A. R. Robinson, editor, *Eddies in Marine Science*, pages 481–491. Springer Verlag, New York.

Hasselmann, K. (1976). Stochastic climate models, Part I: theory. *Tellus*, **28**, 473–485.

Hellerman, S. and Rosenstein, M. (1983). Normal monthly wind stress over the world ocean with error estimates. *J. Phys. Oceanography*, **13**, 1093–1104.

Hogg, N. G. (1983). A note on the deep circulation of the western North Atlantic: its nature and its causes. *Deep-Sea Research*, **30**, 945–961.

Holland, W. R. (1977). Oceanic General Circulation Models. In E. P. Goldberg, I. N. McCave, J. J. O'Brien, and J. H. Steele, editors, *The sea: ideas and observations on progress in the study of the seas*, volume VI, pages 3–44. Wiley and Sons, Inc., New York.

Holland, W. R. (1978). The role of mesoscale eddies in the general circulation of the ocean - numerical experiments using a wind-driven quasi-geostrophic model. *J. Phys. Oceanography*, **8**, 363–392.

Holland, W. R. and Haidvogel, D. B. (1980). A parameter study of the mixed instability of ocean currents. *Dyn. Atm. Oceans*, **4**, 185–215.

Holland, W. R. and Lin, L. B. (1975a). On the generation of mesoscale eddies and their contribution to the oceanic general circulation. I. A preliminary numerical experiment. *J. Phys. Oceanography*, **5**, 642–657.

Holland, W. R. and Lin, L. B. (1975b). On the generation of mesoscale eddies and their contribution to the oceanic general circulation. II. A parameter study. *J. Phys. Oceanography*, **5**, 658–669.

Holland, W. R., Harrison, D. E., and Semtner Jr., A. J. (1983). Eddy-resolving models of large-scale ocean circulation. In A. R. Robinson, editor, *Eddies in Marine Science*, pages 379–403. Springer Verlag, New York.

Holton, J. R. (1992). *An introduction to dynamic meteorology*, volume 48 of *Int. Geophysics Series*. Academic Press Inc., San Diego, 3rd edition. 507 pp.

Hurlburt, H. E. and Hogan, P. J. (2000). Impact of 1/8° to 1/64° resolution on Gulf Stream model-data comparisons in basin-scale subtropical Atlantic Ocean models. *Dyn. Atm. Oceans*, **32**, 283–329.

Ierley, G. R. and Sheremet, V. A. (1995). Multiple solutions and advection-dominated flows in the wind-driven circulation. Part I: Slip. *J. Marine Res.*, **53**, 703–737.

Jiang, S., Jin, F. F., and Ghil, M. (1995). Multiple equilibria and aperiodic solutions in a wind-driven double-gyre, shallow-water model. *J. Phys. Oceanography*, **25**, 764–786.

Katsman, C. A., Dijkstra, H. A., and Drijfhout, S. S. (1998). The rectification of wind-driven flow due to its instabilities. *J. Marine Res.*, **56**, 559–587.

Katsman, C. A., Drijfhout, S. S., and Dijkstra, H. A. (2001). The interaction of a Deep Western Boundary Current and the wind-driven gyres as a cause for low-frequency variability. *J. Phys. Oceanography*. Accepted for publication.

Keffer, T. (1985). The ventilation of the world's oceans: maps of the potential vorticity field. *J. Phys. Oceanography*, **15**, 509–523.

Keller, H. B. (1977). Numerical solution of bifurcation and nonlinear eigenvalue problems. In P. H. Rabinowitz, editor, *Applications of bifurcation theory*. Academic Press, New York. 389 pp.

Legras, B. and Ghil, M. (1985). Persistent anomalies, blocking, and variations in atmospheric predictability. *J. Atm. Sci.*, **42**, 433–471.

Lozier, M. S. (1997). Evidence for large-scale eddy-driven gyres in the North Atlantic. *Science*, **277**, 361–364.

McCalpin, J. D. (1995). The statistics and sensitivity of a double-gyre model: the reduced gravity, geostrophic case. *J. Phys. Oceanography*, **25**, 806–824.

McCalpin, J. D. and Haidvogel, D. B. (1996). Phenomenology of the low-frequency variability in a reduced-gravity, quasigeostrophic double-gyre model. *J. Phys. Oceanography*, **26**, 739–752.

McDowell, S., Rhines, P. B., and Keffer, T. (1982). North Atlantic potential vorticity and its relation to the general circulation. *J. Phys. Oceanography*, **12**, 1417–1436.

Meacham, S. P. (2000). Low-frequency variability in the wind-driven circulation. *J. Phys. Oceanography*, **30**, 269–293.

Moro, B. (1987). On the inertial motion of a homogeneous ocean. *Dyn. Atm. Oceans*, **11**, 1–17.

Moro, B. (1988). On the non-linear Munk model, I: Steady flows. *Dyn. Atm. Oceans*, **12**, 259–287.

Moro, B. (1990). On the non-linear Munk model, II: Stability. *Dyn. Atm. Oceans*, **14**, 203–227.

Munk, W. H. (1950). On the wind-driven ocean circulation. *J. Meteor.*, **7**, 79–93.

Munk, W. H., Groves, G. W., and Carrier, G. F. (1950). Note on the dynamics of the Gulf Stream. *J. Marine Res.*, **9**, 218–238.

Nayfeh, A. H. and Balachandran, B. (1995). *Applied Nonlinear Dynamics.* John Wiley and Sons, Inc., New York. 685 pp.

Niiler, P. P. (1987). The observational basis for large scale circulations. In H. Abarbarnel and W. R. Young, editors, *General circulation of the ocean*, pages 1–54. Springer Verlag, New York.

Orlanski, I. (1976). A simple boundary condition for unbounded hyperbolic flows. *J. Comput. Phys.*, **21**, 251–269.

Pedlosky, J. (1964). The stability of currents in the atmosphere and the ocean: Part 1. *J. Atm. Sci.*, **21**, 201–219.

Pedlosky, J. (1970). Finite amplitude baroclinic waves. *J. Atm. Sci.*, **27**, 15–30.

Pedlosky, J. (1971). Finite amplitude baroclinic waves with small dissipation. *J. Atm. Sci.*, **28**, 587–597.

Pedlosky, J. (1972). Limit cycles and unstable baroclinic waves. *J. Atm. Sci.*, **29**, 55–63.

Pedlosky, J. (1987). *Geophysical Fluid Dynamics.* Springer Verlag, New York, 2nd edition. 710 pp.

Pedlosky, J. (1996). *Ocean Circulation Theory.* Springer Verlag, New York. 453 pp.

Peixoto, J. P. and Oort, A. H. (1992). *Physics of Climate.* AIP Press, New York. 520 pp.

Philander, S. (1989). *El Niño, La Niña and the Southern Oscillation.* Academic Press, New York. 289 pp.

Phillips, N. A. (1954). Energy transformations and meridional circulations associated with simple baroclinic waves in a two-level, quasi-geostrophic model. *Tellus*, **6**, 273–286.

Pickart, R. S. (1994). Interaction of the Gulf Stream and Deep Western Boundary Current where they cross. *J. Geophysical Res.*, **99 C12**, 25,155–25,164.

Pickart, R. S. and Smethie Jr., W. M. (1993). How does the Deep Western Boundary Current cross the Gulf Stream? *J. Phys. Oceanography*, **23**, 2602–2616.

Pickart, R. S. and Smethie Jr., W. M. (1998). Temporal evolution of the Deep Western Boundary Current where it enters the sub-tropical domain. *Deep-Sea Research*, **I 45**, 1053–1083.

Plaut, G. and Vautard, R. (1994). Spells of low-frequency oscillations and weather regimes in the northern hemisphere. *J. Atm. Sci.*, **51**, 210–236.

Primeau, F. W. (1998a). *Multiple equilibria and low-frequency variability of wind-driven ocean models.* Ph.D. thesis, MIT & Woods Hole Oceanographic Institution.

Primeau, F. W. (1998b). Multiple equilibria of a double-gyre ocean model with super-slip boundary conditions. *J. Phys. Oceanography*, **28**, 2130–2147.

Qiu, B. (2000). Interannual variability of the Kuroshio Extension system and its impact on the wintertime SST field. *J. Phys. Oceanography*, **30**, 1486–1502.

Rhines, P. B. and Holland, W. R. (1979). A theoretical discussion of eddy-driven mean flows. *Dyn. Atm. Oceans*, **3**, 289–325.

Rhines, P. B. and Schopp, R. (1991). A theory of wind-driven circulation: quasi-geostrophic simulations and theory for nonuniform winds. *J. Phys. Oceanography*, **21**, 1438–1469.

Rhines, P. B. and Young, W. R. (1982). The wind-driven circulation. I: Mid-ocean gyres. *J. Marine Res.*, **40S**, 559–596.

Richardson, P. L. (1977). On the crossover between the Gulf Stream and the western boundary undercurrent. *Deep-Sea Research*, **24**, 139–159.

Robinson, A. R. (1983). *Eddies in Marine Science*. Springer Verlag, New York. 609 pp.

Robinson, A. R. and McWilliams, J. C. (1974). Baroclinic instability of the open ocean. *J. Phys. Oceanography*, **4**, 281–294.

Romea, R. D. (1977). The effects of friction and β on finite amplitude baroclinic waves. *J. Atm. Sci.*, **34**, 1689–1695.

Schmeits, M. J. (2000). *Bimodality and internal variability of the Gulf Stream and the Kuroshio*. Ph.D. thesis, Utrecht University.

Schmeits, M. J. and Dijkstra, H. A. (2000). Physics of the 9-month variability in the Gulf Stream region: combining data and dynamical systems analyses. *J. Phys. Oceanography*, **30**, 1967–1987.

Schmitz Jr., W. J. and Holland, W. R. (1986). Observed and modeled mesoscale variability near the Gulf Stream and the Kuroshio extension. *J. Geophysical Res.*, **91**, 9624–9638.

Semtner, A. J. and Holland, W. R. (1978). Intercomparison of quasi-geostrophic simulations of the western North Atlantic circulation with primitive equation results. *J. Phys. Oceanography*, **8**, 735–754.

Seydel, R. (1988). *From equilibrium to chaos: practical bifurcation and stability analysis*. Springer Verlag, New York. 367 pp.

Spall, M. A. (1996a). Dynamics of the Gulf Stream/Deep Western Boundary Current Crossover. Part I: Entrainment and recirculation. *J. Phys. Oceanography*, **26**, 2152–2168.

Spall, M. A. (1996b). Dynamics of the Gulf Stream/Deep Western Boundary Current Crossover. Part II: Low-frequency internal oscillations. *J. Phys. Oceanography*, **26**, 2169–2182.

Speich, S., Dijkstra, H. A., and Ghil, M. (1995). Successive bifurcations of a shallow water model, applied to the wind-driven circulation. *Nonlinear Proc. Geophys.*, **2**, 241–268.

Stommel, H. (1948). The westward intensification of wind-driven ocean currents. *Trans. Amer. Geophysical Union*, **29**, 202–206.

Stommel, H. (1957). A survey of ocean current theory. *Deep-Sea Research*, **4**, 149–184.

Stommel, H. (1958). The abyssal circulation. *Deep-Sea Research*, **5**, 80–82.

Stowe, K. S. (1979). *Ocean Science*. John Wiley and Sons, Inc., New York. 610 pp.

Sverdrup, H. U. (1947). Wind-driven currents in a baroclinic ocean; with application to the equatorial current in the eastern Pacific. *Proc. Natl. Acad. Sci. Wash.*, **33**, 318–326.

Swallow, J. C. and Worthington, L. V. (1961). An observation of a deep countercurrent in the western North Atlantic. *Deep-Sea Research*, **8**, 1–19.

Tansley, C. E. and Marshall, D. P. (2000). On the influence of bottom topography and the Deep Western Boundary Current on Gulf Stream separation. *J. Marine Res.*, **58**, 297–325.

Thompson, J. D. and Schmitz Jr., W. J. (1989). A limited-area model of the Gulf Stream: design, initial experiments and model-data comparison. *J. Phys. Oceanography*, **19**, 791–814.

Van der Vaart, P. C. F. and Dijkstra, H. A. (1997). Sideband instabilities of mixed barotropic/baroclinic waves growing on a midlatitude zonal jet. *Phys. Fluids*, **9**, 615–631.

Veronis, G. (1966). Wind-driven ocean circulation – Part II: Numerical solution of the nonlinear problem. *Deep-Sea Research*, **13**, 31–55.

Worthington, L. V. (1981). The water masses of the world ocean: some results of a fine-scale census. In B. A. Warren and C. Wunsch, editors, *Evolution of physical oceanography*, pages 42–69. MIT Press, Cambridge.

Samenvatting

De stromingen in de oceaan worden aangedreven aan het zeeoppervlak, deels door de krachten die worden uitgeoefend door de wind, en deels door de uitwisseling van warmte en vocht (het netto effect van regen en verdamping) met de atmosfeer. De wind is de belangrijkste drijvende kracht voor de circulatie aan het oppervlak, maar beïnvloedt alleen de bovenste duizend meter van de oceaan rechtstreeks. De warmte- en vochtfluxen veranderen daarentegen de dichtheid van het water aan het zeeoppervlak en kunnen aanleiding geven tot verticale bewegingen (convectie) en menging met het water op grotere diepte. Deze door dichtheidsverschillen aangedreven stromingen, de thermohaliene circulatie genoemd, brengen de diepe oceaan in beweging. Als gevolg van de grote warmtecapaciteit van (oceaan-)water hebben de stromingen en veranderingen daarin een belangrijk effect op ons klimaat. Zo is bijvoorbeeld de Golf Stroom verantwoordelijk voor het relatief milde klimaat in West-Europa. Voor klimaatstudies is het dan ook essentiëel om de (variabiliteit van de) oceaancirculatie te begrijpen, en om de robuustheid van deze variabiliteit te onderzoeken.

Er bestaat tegenwoordig een redelijk goed beeld van de kenmerken van de grootschalige oceaancirculatie. Voor grote delen van de oceaan zijn deze kenmerken echter afgeleid van metingen van de temperatuur en het zoutgehalte van het water op basis van eenvoudige dynamische en thermodynamische overwegingen. Directe metingen van stroomsnelheden zijn nog altijd schaars en zijn vaak slechts momentopnames. Als gevolg van deze beperkte beschikbaarheid van directe metingen over langere periodes is over de variabiliteit van de circulatie nog relatief weinig bekend. Oceanografen maken mede daarom veelvuldig gebruik van computermodellen om de stromingen te simuleren. Ook kan de configuratie van zo'n model worden afgestemd op het specifieke probleem dat bestudeerd wordt. Zo worden de thermohaliene en de windgedreven component van de stroming gescheiden bestudeerd. Dit is mogelijk omdat veranderingen in de thermohaliene circulatie op veel langere tijdschalen spelen (in de orde van tientallen jaren tot eeuwen) dan veranderingen in de windgedreven circulatie (maanden tot jaren). Voor het bestuderen van de snelle veranderingen in de windgedreven circulatie kan dus volstaan worden met het voorschrijven van een constante dichtheidsverdeling waarvan verondersteld wordt dat deze is bepaald door de (niet beschouwde) thermohaliene component van de circulatie. Wanneer het doel van de modelsimulatie is om de waargenomen circulatie in detail na te bootsen moeten uiteraard zowel de windgedreven als de thermohaliene component worden meegenomen.

De windgedreven oceaancirculatie

Figuur 1.1 (pag. 3) is een schets van de windgedreven oppervlaktecirculatie in de oceaan. Kenmerkend voor deze circulatie zijn de reusachtige wervelstructuren over de hele breedte van de oceaan, die op zowel het noordelijk als het zuidelijk halfrond te vinden zijn. Deze reuzenwervels, de *gyres*, zijn asymmetrisch in oost-west richting. Langs de continenten aan de westkant van het oceaanbekken zijn geconcentreerde grenslaagstromingen te vinden. Wanneer twee zulke grenslaagstromingen elkaar ontmoeten buigen ze samen af naar het oosten, en vormen intense oostwaartse stromingen tussen twee gyres in (jetstromen of *mid-ocean jets*). Voorbeelden hiervan zijn de Golf Stroom in de Noord-Atlantische Oceaan, de Kuroshio in de Stille Oceaan en de Agulhas Stroom in de Indische Oceaan (de laatste is niet expliciet benoemd in Fig. 1.1). Typische snelheden in deze jetstromen zijn in de orde van 1 m/s, veel sneller dan in het centrum van de gyres (~ 0.01 m/s).

Sverdrup (1947) gaf als eerste een verklaring voor het bestaan van grootschalige gyres door te laten zien hoe de circulatie in de open oceaan samenhangt met het ruimtelijke patroon van de passaatwinden aan het zeeoppervlak. De westelijk versterking van de gyres bleek een gevolg van de aanwezigheid van continenten die het oceaanbekken omsluiten (Stommel, 1948; Munk, 1950). Voortbouwend op deze eerste analytische resultaten voor geïdealiseerde omstandigheden zijn in latere jaren veel studies van de windgedreven circulatie uitgevoerd, met meer geavanceerde computermodellen.

De directe invloed van de wind op de oceaancirculatie is zoals gezegd beperkt tot de bovenste duizend meter van de oceaan. De thermohalien gedreven stromingen in de diepzee zijn in het algemeen veel zwakker dan die aan het oppervlak (stroomsnelheden zijn typisch enkele cm/s). Er bestaat echter een relatief snelle onderzeese stroming die bekend staat als de 'Diepe Westelijke Onderstroom' (de *Deep Western Boundary Current*, afgekort tot DWBC) waarvan de gemiddelde snelheid ongeveer 20 cm/s is. Deze stroming vindt zijn oorsprong in de noordelijke Atlantische Oceaan. Op hoge breedten (in de Groenland en de Labrador Zee) wordt het warme, zoute oppervlaktewater sterk afgekoeld door de atmosfeer. De dichtheid van het water aan het oppervlak wordt daardoor groter dan die van het water op grotere diepten en als gevolg zakt het oppervlaktewater naar de diepzee. Dit nu koude, zoute water stroomt vervolgens langs het Amerikaanse continent zuidwaards en vormt de DWBC. Op ongeveer $35°NB$ kruist deze diepzeestroming de Golf Stroom, die daar de kust verlaat en in noordoostwaartse richting de Noord-Atlantische Oceaan in stroomt. Recente metingen en modelstudies geven aan dat de aanwezigheid van de DWBC zowel het gemiddelde pad als de variabiliteit van de Golf Stroom sterk beïnvloedt. Deze wisselwerking is op dit moment nog niet volledig begrepen.

Interne variabiliteit

Het is bekend dat en dat de oceaancirculatie grote variaties vertoont op diverse tijd- en ruimtelijke schalen, en dus dat Figuur 1.1 een te simpel beeld schetst van de stromingen aan het zeeoppervlak. De aanwezigheid van deze variaties, aangeduid met de algemene term *eddies* (wervels), heeft een significant effect op de gemiddelde circulatie. Eddies zijn bovendien van groot belang voor het warmtetransport in de oceaan, voor

menging en voor het energieverlies door wrijving (Robinson, 1983). Met behulp van satellieten kan tegenwoordig een goede indruk verkregen worden van de variabiliteit van de oppervlaktecirculatie door zeer nauwkeurig de hoogte van het zeeoppervlak te meten. Heuvels en dalen in het oppervlak weerspiegelen het bestaan van hoge- en lagedrukgebieden die, net als in de atmosfeer, de circulatie bepalen. Figuur 1.2 (pag. 7) laat zien waar de grootste variaties in de hoogte van het zeeoppervlak te vinden zijn. Uit deze satellietmetingen blijkt dat vooral de intense oostwaartse jetstromen zeer variabel zijn (de donkere gebieden in Figuur 1.2). Dus ligt het voor de hand om bij het bestuderen van de windgedreven oceaancirculatie aandacht te besteden aan zulke jetstromen geflankeerd door twee gyres (het twee-gyre systeem of *double-gyre system*).

Variaties in de oppervlaktecirculatie kunnen verschillende oorzaken hebben. Zo kan de oceaan bijvoorbeeld passief reageren op veranderingen in de atmosferische forcering (de windsterkte). Een tweede mogelijkheid is dat de variaties ontstaan door terugkoppelingen tussen veranderingen in de circulatie in de atmosfeer en in de oceaan. Een bekend voorbeeld van zulke gekoppelde variabiliteit waarbij zowel de oceaan als de atmosfeer een actieve rol spelen is het verschijnsel El Niño. Tenslotte kunnen ook interne processen in de oceaan aanleiding geven tot variabiliteit. Alleen dit laatste type variabiliteit wordt in dit proefschrift bestudeerd, door in het oceaanmodel de atmosferische forcering constant te houden en daarmee de twee andere types uit te sluiten.

Deze *interne variabiliteit* is een gevolg van het feit dat de gemiddelde circulatie (de basisstroming) instabiel is. Dit betekent dat oneindig kleine verstoringen, die in werkelijkheid en in modellen altijd aanwezig zijn, kunnen aangroeien tot grotere, niet-stationaire eddies. Deze verstoringen destabiliseren de stroming, en maken hem tijdsafhankelijk en variabel. Er kan onderscheid gemaakt worden tussen zogenaamde *barotrope* en *barocliene* instabiliteit, op grond van het fysische mechanisme dat aan de instabiliteit ten grondslag ligt. De instabiliteit wordt barotroop genoemd wanneer de verstoringen aangroeien door kinetische energie te onttrekken aan de basisstroming: bij barocliene instabiliteit is de potentiële energie van de basisstroming de bron voor de groei van de verstoringen.

Dit proefschrift

In dit proefschrift wordt alleen de windgedreven component van de oceaancirculatie bestudeerd. Met behulp van een eenvoudig computermodel wordt het gedrag van een geïdealiseerd twee-gyre systeem onderzocht. Het model bestaat uit twee niet-mengbare lagen water van verschillende dichtheid. Dit twee-lagen model is een ruwe weergave van de verticale dichtheidsverdeling in de oceaan, met warm oppervlaktewater en een koude diepzee (zie Figuur 2.1 op pag. 14 voor een schets van dit twee-lagen model). De bovenste laag van het model wordt aangedreven door een constante wind, de onderste laag kan indirect worden aangedreven door bewegingen van het grensvlak tussen de twee lagen. De grootschalige basisstroming in dit twee-lagen model kan in principe zowel barotroop als baroclien instabiel worden. De circulatie dient als een prototype voor de waargenomen twee-gyre systemen in de oceaan. Juist door zijn eenvoud is het model zeer geschikt voor het uitvoeren van uitgebreide proces-

en gevoeligheidsstudies, maar niet voor het in detail nabootsen van de waargenomen circulatie. Daarom ook worden de resultaten voornamelijk kwalitatief bediscussiëerd.

In de meeste studies wordt de interne variabiliteit van de windgedreven circulatie bestudeerd door het tijdsafhankelijke gedrag van de stroming te simuleren. Aan de hand van de wiskundige vergelijkingen die de ontwikkeling van de stroming in de tijd beschrijven en het stromingspatroon op een eerder tijdstip kan het stromingspatroon op een later tijdstip wordt berekend. De resultaten van zo'n *tijdsintegratie* kunnen achteraf uitgebreid geanalyseerd worden met behulp van statistische technieken. In dit proefschrift is gekozen voor een andere aanpak, waarbij gebruik wordt gemaakt van het feit dat interne variabiliteit een gevolg is van de instabiliteit van de stroming. Deze methode is gebaseerd op wiskundige technieken die zijn ontwikkeld binnen de dynamische systeem theorie. Eerst wordt berekend welk stationair (tijdsonafhankelijk) stromingspatroon hoort bij een bepaalde combinatie van modelparameters, zoals de sterkte van de wind en van de wrijving. Met behulp van een *continueringsmethode* kunnen takken van zulke stationaire oplossingen voor de circulatie worden getraceerd terwijl één specifieke parameter van het model (de controleparameter genaamd) wordt veranderd. Op deze manier worden alle mogelijke oplossingen voor het stromingspatroon in kaart gebracht, en kan bepaald worden of er voor dezelfde set van parameters meerdere stationaire stromingspatronen mogelijk zijn (meervoudige evenwichten of *multiple equilibria*). De analyse wordt altijd gestart vanuit een situatie met een stabiele stroming, door of een zwakke forcering of sterke wrijving te veronderstellen. Vervolgens wordt bepaald welke specifieke interne modes de basisstroming het eerst destabiliseren wanneer de verhouding tussen de forcering en de wrijving wordt vergroot. In dit proefschrift wordt meestal de eddy-viscositeit van de stroming (de stroperigheid) gebruikt als controleparameter. Deze eddy-viscositeit is een maat voor de wrijving ten gevolge van kleinschalige processen die in het model niet worden opgelost, en is veel groter dan de moleculaire viscositeit van oceaanwater.

Vervolgens wordt de stabiliteit van deze stromingspatronen onderzocht, door te berekenen of oneindig kleine verstoringen op deze stroming in de tijd uitdempen danwel aangroeien. Ook de belangrijkste eigenschappen van deze specifieke verstoringen (de *interne modes*), zoals het ruimtelijke patroon en -in het geval van een oscillerende verstoring- de frequentie of tijdschaal, kunnen worden bepaald. De snelst groeiende (meest instabiele) interne modes zullen naar verwachting een dominante bijdrage leveren aan de interne variabiliteit, en kunnen in detail bestudeerd worden. Omgekeerd kan men proberen het tijdsafhankelijk gedrag zoals gesimuleerd met behulp van tijdsintegraties te interpreteren op basis van de opgedane kennis over de interne modes.

De belangrijkste vragen die in dit proefschrift aan de orde komen zijn:

- Wat zijn de kenmerken van de twee-gyre circulatie en van de interne modes die deze circulatie destabiliseren?
- Hoe veranderen deze instabiliteiten de grootschalige stromingspatronen?
- Hoe beïnvloedt de aanwezigheid van de Deep Western Boundary Current de windgedreven circulatie en de variabiliteit?

- Kan de variabiliteit gesimuleerd in tijdsintegraties begrepen worden aan de hand van de resultaten van deze dynamische systeem analyse?

Resultaten

In hoofdstuk 3 worden de mogelijke stationaire stromingspatronen voor het geïdealiseerde twee-gyre systeem in kaart gebracht, als functie van de eddy-viscositeit. De analyse start in een parametergebied waar de circulatie zeer visceus en dus stabiel is. Voor hoge eddy-viscositeit blijkt er een uniek stationair stromingspatroon te bestaan met twee gyres en een oostwaartse jetstroom in het midden van het bekken. Dit patroon is perfect symmetrisch in de noord-zuid richting. Voor lagere eddy-viscositeit bestaan er meervoudige symmetrische en asymmetrische evenwichten. Nog voor redelijk hoge wrijving wordt de twee-gyre circulatie instabiel ten opzichte van drie oscillerende modes, die allemaal variabiliteit introduceren op tijdschalen van enkele maanden. Deze interne modes zorgen er voor dat de oostwaartse jetstroom gaat meanderen, en locaal wordt versterkt of verzwakt. Een analyse van de energiebalans van deze interne modes laat zien dat het alledrie barocliene instabiliteiten zijn.

Met behulp van de continueringsmethode kan het barocliene twee-lagen model eenvoudig veranderd worden in een zogenaamd equivalent barotroop model door de tweede laag oneindig diep te maken. Deze laag is dan dynamisch niet meer actief, en de circulatie kan alleen nog barotroop instabiel worden. De stabiliteitseigenschappen van de circulatie in het equivalent barotrope model zijn dan ook heel anders dan in het twee-lagen model: de eerder gevonden barocliene instabiliteiten verdwijnen wanneer de dikte van de tweede laag wordt vergroot en de circulatie is ook voor lagere eddy-viscositeit nog stabiel. Op de stationaire circulatiepatronen heeft de aan- of afwezigheid van barocliene effecten geen invloed, omdat de tweede laag in beide gevallen bewegingsloos is.

Dit laatste is een bekend fenomeen in laagmodellen van de windgedreven oceaancirculatie: voor stationaire windgedreven stromingen geldt dat alleen de bovenste laag direct in beweging wordt gezet door de wind aan het zeeoppervlak. Wanneer de stroming tijdsafhankelijk is zijn daarentegen ook de diepere lagen in beweging, mits ze niet oneindig diep zijn. Dit betekent dat de aanwezigheid van tijdsafhankelijke verstoringen een fundamentele verandering teweeg brengt in de circulatie. In de meeste modelsimulaties is het tijdsafhankelijk gedrag van de stroming erg gecompliceerd en is het moeilijk een helder beeld te krijgen van de fysische processen die deze veranderingen veroorzaken. In hoofdstuk 4 wordt dit probleem onderzocht aan de hand van tijdsintegraties die zijn uitgevoerd voor een waarde van de eddy-viscositeit waarvoor de circulatie nét instabiel is. Daar is het tijdsafhankelijk gedrag erg simpel en voorspelbaar: de stroming oscilleert door de aanwezigheid van één bekende verstoring, namelijk de meest instabiele interne mode. Ook de beginconditie van de tijdsintegratie (het nu instabiele stationaire stromingspatroon) en het gemiddelde van de tijdsafhankelijke stroming zijn bekend. Met deze ingrediënten kan de oorsprong van de veranderingen in de circulatie ten gevolge van de aanwezigheid van tijdsafhankelijke verstoringen, en in het bijzonder de drijvende kracht voor de circulatie in de diepere laag van het model, eenvoudig bestudeerd worden. Uit de analyse in

hoofdstuk 4 blijkt dat de veranderingen worden veroorzaakt door onderlinge interacties tussen de oscillerende modes. Deze interacties veroorzaken bewegingen van het grensvlak tussen de twee lagen en drijven uiteindelijk de stroming op grotere diepte aan.

Naar aanleiding van recente observaties dat de DWBC de variabiliteit van de Golf Stroom beïnvloedt wordt in hoofdstuk 5 een DWBC toegevoegd aan het windgedreven twee-gyre systeem. Opnieuw worden de stationaire stromingen bepaald als functie van de eddy-viscositeit, maar ook de grootte van het transport van de DWBC wordt gebruikt als controleparameter. In dit eenvoudige twee-lagen model blijkt de aanwezigheid van de DWBC een voorkeur te introduceren voor variabiliteit op langere tijdschalen, in overeenstemming met eerdere, meer geavanceerde modelstudies. In het systeem met een DWBC zijn interne modes met een tijdschaal van enkele jaren het meest instabiel, terwijl modes met een tijdschaal van enkele maanden de variabiliteit van de puur windgedreven stroming domineren. Eén van de gedetecteerde interne modes voor het windgedreven/DWBC systeem heeft verrassend veel kenmerken gemeen met de dominante patronen van variabiliteit die gevonden zijn in meer realistische simulaties van de circulatie in de Noord-Atlantische Oceaan. Ook in deze geavanceerde modellen zou een interne mode dus ten grondslag kunnen liggen aan de gesimuleerde variabiliteit.

Van de interne modes die zijn besproken in hoofdstuk 3 en 5 is bekend dat ze de interne variabiliteit van de circulatie domineren in de buurt van de stabiliteitsgrens. In hoofdstuk 6 wordt onderzocht of interne modes nog steeds een significante bijdrage leveren aan de variabiliteit wanneer de eddy-viscositeit relatief laag is, in een parametergebied ver voorbij de stabiliteitsgrens. Een andere mogelijkheid is dat complexe interacties tussen de aanwezige tijdsafhankelijke verstoringen variabiliteit veroorzaken met 'nieuwe' karakteristieke tijdschalen en patronen. Voor zowel het puur windgedreven systeem als voor het windgedreven/DWBC systeem zijn daarom tijdsintegraties uitgevoerd en geanalyseerd met behulp van statistische technieken. Hiermee kunnen de meest voorkomende patronen en tijdschalen voor variaties in de stroming bepaald worden. De kenmerken van deze statistische modes zijn vervolgens vergeleken met die van de interne modes, om te proberen de oorsprong van de variabiliteit te achterhalen. In alle bestudeerde gevallen kon een groot deel van de variabiliteit zo worden toegeschreven aan diverse interne modes.

Wat opvalt in de tijdsintegraties voor relatief lage eddy-viscositeit is dat, ongeacht de aan- of afwezigheid van de DWBC, de dominante tijdschaal voor de variabiliteit in de orde van enkele jaren is. De onderliggende oorzaak voor deze laag-frequente variabiliteit blijkt echter in de twee gevallen heel verschillend te zijn. In het gecombineerde windgedreven/DWBC systeem zijn het interne modes die de laag-frequente variabiliteit veroorzaken, met een bijbehorende specifieke voorkeurstijdschaal. In de puur windgedreven stroming zijn niet-lineaire interacties tussen hoog-frequente signalen de oorzaak. Dit leidt tot laag-frequente variabiliteit over een breder scala aan tijdschalen. Door de resultaten van de dynamische systeem analyse en de tijdsintegraties te combineren is het mogelijk deze oorzaken te onderscheiden, wat van belang is voor een beter begrip van de gevoeligheid van deze laag-frequente variabiliteit voor veranderingen in de modelparameters.

Conclusie

In dit proefschrift zijn de structuur van mogelijke stationaire oplossingen en de stabiliteitseigenschappen van een windgedreven twee-gyre systeem bepaald, met behulp van een dynamische systeem analyse. Aan de hand van de resultaten van deze analyse kunnen de oorsprong en de robuustheid van de interne variabiliteit en de onderliggende fysische processen die deze variabiliteit veroorzaken in detail worden bestudeerd. Bovendien biedt de zo verworven kennis een kader voor de interpretatie van het tijdsafhankelijk gedrag van de circulatie. Door in de toekomst deze combinatie van analysetechnieken toe te passen voor het bestuderen van de circulatie in meer realistische modellen, waarin bijvoorbeeld ook de thermohalien geforceerde component wordt opgenomen, kan een beter begrip worden verkregen van de variabiliteit van de waargenomen oceaancirculatie.

List of publications

Dijkstra, H. A. and Katsman, C. A. (1997) Temporal variability of the wind-driven quasi-geostrophic double gyre ocean circulation: Basic bifurcation diagrams, *Geophys. and Astrophys. Fluid Dynamics*, **85**, 195–232.

Katsman, C. A., Dijkstra, H. A., and Drijfhout, S. S. (1998) The rectification of wind-driven flow due to its instabilities, *J. Marine Res.*, **56**, 559–587.

Dijkstra, H. A., Schmeits, M. J. and Katsman, C. A. (1999) Variability of the North-Atlantic wind-driven ocean circulation, *Surveys in Geophysics*, **20**, 463–503.

Katsman, C. A., Dijkstra, H. A. and Schmeits, M. J. (2000) Applications of continuation methods on physical oceanography. In D. Henry and A. Bergeon, editors, *Continuation methods in Fluid Dynamics. Contributions to the ERCOFTAC/EUROMECH Colloquium 383, Aussois, France, 6.-9. September 1998*, pages 155–166, Vieweg, Braunschweig/Wiesbaden.

Katsman, C. A., Drijfhout, S. S., and Dijkstra, H. A. (2001) The interaction of a Deep Western Boundary Current and the wind-driven gyres as a cause for low-frequency variability, accepted for publication in *J. Phys. Oceanography.*

Dankwoord

Deze pagina is eigenlijk de belangrijkste pagina van dit proefschrift, ook al is het één van de laatste. Niet alleen omdat vrijwel iedereen hier begint met lezen, maar vooral ook omdat de mensen om je heen nu eenmaal belangrijker zijn -voor je ontwikkeling als onderzoeker en als mens- dan het preciese onderwerp en de resultaten van het onderzoek.

Allereerst wil ik mijn beide co-promotoren, Henk Dijkstra en Sybren Drijfhout, bedanken voor hun bijdrage. Soms tot verbazing van outsiders is de samenwerking in dit driemanschap altijd prima geweest. Discussies leidden eigenlijk nooit tot dilemma's, omdat het altijd minstens 'twee-tegen-één' was. Plannen die bij nader inzien toch niet zo geweldig bleken werden in deze mini-democratie in een vroeg stadium resoluut van tafel geveegd, en vervangen door een overvloed aan nieuwe ideeën. Henk's belangstelling en enthousiasme voor de resultaten is aanstekelijk te noemen. Bovendien zorgde hij met de PIONIER-groep voor een stimulerende werkomgeving van onderzoekers die op elkaars werk konden voortbouwden. Zijn recente opmerking dat vierkante bakken nu 'uit' zijn zie ik dan ook als een compliment. Sybren zorgde er voor dat ik de fysische kant van het werk niet uit het oog verloor, en me bleef verplaatsen in collega's die niet vertrouwd waren met de wiskundige technieken die door ons werden gebruikt. De huidige samenwerking met Woods Hole Oceanographic Institution is mede te danken aan zijn adviezen om na te denken over 'de Toekomst' in een fase dat ik daar zelf nog niet zo mee bezig was.

Will de Ruijter bleef als promotor meer op de achtergrond, maar was altijd geïnteresseerd in de voortgang van het onderzoek. Op de valreep kreeg ik van hem de kans eindelijk een echte oceanograaf te worden aan boord van de Pelagia: een onvergetelijke ervaring. Met Herman ('positivo') Ridderinkhof en de rest van de ACSEX-bemanning bracht ik vier wonderbaarlijke weken door op de Indische Oceaan.

Door op twee verschillende instituten te werken heb ik vier jaar lang van twee walletjes kunnen eten. Dat ik me nooit een halve medewerker heb gevoeld is de verdienste van de medewerkers van beide onderzoeksgroepen, en weegt ruimschoots op tegen de overmaat aan werkbesprekingen en colloquia die ik soms te verwerken kreeg. In het bijzonder wil ik hier Gerbrand Komen noemen, die als hoofd Oceanografisch Onderzoek van het KNMI niet alleen mijn werk van dichtbij volgde maar ook de werkkamer met het mooiste uitzicht afstond aan zijn promovendi.

Behalve het uitzicht zijn ook de collega's binnen van het grootste belang voor het plezier in je werk. In Villa Orta woonde ik op zolder, samen met Wilco Hazeleger (ongeëvenaard in het vertalen van Sybren's aantekeningen) en Femke Vossepoel (niets is beter tegen (promotie-)stress dan een rondje Beerschoten). Op het IMAU deelde ik mijn kamer met Meinte Blaas (samen met Margreet de initiator van het tussen-de-middag-zwemmen: ontspannen en toch met je vak bezig zijn) en later met Maurice Schmeits (statistisch gezien de beste collega).

De verre reizen voor congres- en werkbezoeken zijn de krenten in de pap van het OiO-schap. Goed gezelschap maakt het alleen maar leuker. Paul van der Vaart en ik reden 1000 kilometer door Australië voor we eindelijk onze eerste welverdiende kangoeroe tegen kwamen. In San Antonio ging een oude wens in vervulling: met Janine Nauw en Lianke te Raa bezocht ik een NBA-wedstrijd. We moeten nog een keer terug als er wél cheerleaders zijn. Mathijs Schouten en ik liepen samen de wacht aan boord van de Pelagia, en hij bleek een uitstekend tosti-bakker tijdens het CTD-en. Dank ook aan Jeroen Molemaker (hij hielp me op gang met de continueringscode), Ernst van der Avoird (hij deed mijn werk nog eens dunnetjes over en haalde er zo een aantal fouten uit) en de rest van de PIONIERs en OO-ers voor hun bijdragen.

Tenslotte wil ik alle vrienden en familie bedanken voor hun belangstelling voor mijn werk, en vooral ook voor de afleiding die ze boden naast het werk. Bert Jan: bedankt voor het doorlezen van de Nederlandse samenvatting en het verbeteren van mijn kromme Nederlands. Omdat je al zo lang ik me kan herinneren op mij past ben je geknipt voor je rol als paranimf.

De eerste stap voor dit proefschrift is eigenlijk gezet door mijn ouders: mijn fascinatie voor de zee is begonnen tijdens onze zeiltochten op het Wad. Pappa en mamma: jullie steun, vertrouwen, aandacht en trots betekenen veel meer dan ik ooit hier kwijt kan.

Tenslotte, Han, bedankt voor het meedenken over, meeleven met en relativeren van het belang van het maken van dit proefschrift, maar vooral ook voor je aanwezigheid de afgelopen jaren. Een allesomvattend 'dank je wel' voor jou.

Caroline Katsman

maart 2001

Curriculum Vitae

Caroline Antoinette Katsman werd geboren op 16 september 1971 in Roden (Drente). Na de lagere school aldaar begon ze in 1983 aan haar VWO opleiding aan het Praedinius Gymnasium te Groningen, en in 1989 haalde ze haar eindexamen. Het daaropvolgende schooljaar bracht ze door in Gol (Noorwegen), als student *friluftsliv* aan de Hallingdal Folkehøgskule.

In 1990 begon ze aan haar studie Natuurkunde aan de Universiteit Utrecht. Na het afleggen van het propaedeutisch examen in januari 1992 vervolgde ze haar universitaire opleiding als student Meteorologie en Fysische Oceanografie. Van augustus tot en met december 1993 verbleef ze opnieuw in Noorwegen, dit keer als uitwisselingsstudent aan de *Universitetet i Bergen*. Daar hield ze zich een semester lang voornamelijk bezig met de oceanografie van polaire gebieden. In juni 1996 studeerde ze af als fysisch oceanograaf op een onderzoek naar de variabiliteit van de windgedreven oceaancirculatie. Dit afstudeerproject vormde de basis voor het werk dat in dit proefschrift wordt gepresenteerd.

Van augustus 1996 tot oktober 2000 werkte ze als Onderzoeker in Opleiding in dienst van NWO aan haar promotieonderzoek. Tijdens dit onderzoeksproject maakte ze deel uit van twee verschillende onderzoeksgroepen: de afdeling Oceanografisch Onderzoek van het KNMI in De Bilt en het Instituut voor Marien en Atmosferisch onderzoek Utrecht (IMAU) van de Universiteit Utrecht. De dagelijkse begeleiding van dit project was in handen van dr. S. S. Drijfhout (KNMI) en dr. H. A. Dijkstra (IMAU). In het kader van haar onderwijstaak was ze twee keer gedurende enkele maanden interim-coördinator van de Wetenschapswinkel Natuurkunde (Universiteit Utrecht).

Sinds 1 maart jl. heeft ze een aanstelling als postdoc, mede gefinancierd via het FOm/v Stimuleringsprogramma van de Stichting FOM. Binnen dit onderzoeksproject maakt ze opnieuw deel uit van twee verschillende onderzoeksgroepen. Naast haar werk op het IMAU zal zij een éénjarig bezoek brengen aan Woods Hole Oceanographic Institution (Woods Hole, USA).